

The University of Nottingham

UNITED KINGDOM · CHINA · MALAYSIA

# Active magnetic shielding systems for wearable magnetoencephalography

by

Niall Holmes M.Sci.

Thesis submitted to the University of Nottingham

for the degree of Doctor of Philosophy

October 2019

# Contents

**Abstract** **viii**

**Acknowledgements** **xi**

**Introduction** **1**

**1 Magnetoencephalography** **6**

1.1 Introduction . . . . . 6

1.2 Neuronal currents . . . . . 7

1.2.1 Action potentials . . . . . 9

1.2.2 Post-synaptic potentials . . . . . 10

1.3 Measurable effects in MEG . . . . . 13

1.3.1 Evoked responses . . . . . 14

1.3.2 Spontaneous rhythms . . . . . 14

1.3.3 Induced responses . . . . . 16

1.4 The MEG forward problem . . . . . 18

1.5 The MEG inverse problem . . . . . 25

1.5.1 Lead fields . . . . . 25

1.5.2 Beamforming . . . . . 26

1.6 MEG hardware . . . . . 29

1.6.1 SQUIDs . . . . . 30

1.6.2 Commercial SQUID based MEG systems . . . . . 33

1.6.3 Limitations of SQUID systems . . . . . 34

1.7 On-scalp MEG . . . . . 37

1.7.1 High $Tc$ SQUIDs . . . . . 38

1.7.2 Nitrogen vacancy centre . . . . . 39

1.7.3 Optically pumped magnetometers . . . . . 39

**2 Optically-Pumped Magnetometers 40**

2.1 Introduction . . . . . 40

2.2 The QuSpin OPM . . . . . 44

2.3 Optical Pumping . . . . . 47

2.4 Maintaining spin polarisation . . . . . 53

2.5 Bloch equations of spin polarisation . . . . . 57

2.6 Sensor array operation . . . . . 62

2.7 Requirements for OPMs used in MEG . . . . . 66

**3 Magnetic Shielding** **67**

3.1 Introduction . . . . . 67

3.2 Passive magnetic shielding . . . . . 69

3.2.1 Flux shunting . . . . . 70

3.2.2 Eddy-current cancellation . . . . . 73

3.2.3 De-gaussing . . . . . 75

3.2.4 Practical considerations . . . . . 77

3.3 Active shielding . . . . . 79

3.3.1 Electromagnetic coils . . . . . 80

3.3.2 Feedback controllers . . . . . 83

3.3.3 Practical considerations . . . . . 86

**4 Bi-planar coil active shielding system** **88**

4.1 Introduction . . . . . 88

4.2 Theory of bi-planar coil design . . . . . 90

4.2.1 Magnetic field equation . . . . . 90

4.2.2 Evaluating the stream function . . . . . 92

4.2.3 Harmonic Minimisation . . . . . 95

4.2.4 Power dissipation term . . . . . 96

4.2.5 Optimising Stream Functions . . . . . 97

4.3 Methods . . . . . 99

4.3.1 Coil design and construction . . . . . 99

4.3.2 Automated field nulling procedure . . . . . 101

4.3.3 Field mapping to assess nulling performance . . . . . 102

4.3.4 Stability of null over time . . . . . 104

4.3.5 Demonstrating the allowed range of motions . . . . . 105

4.3.6 Measurement of retinotopy: data acquisition . . . . . 108

4.3.7 Measurement of retinotopy: data analysis . . . . . 110

4.4 Results . . . . . 114

4.4.1 Coil designs . . . . . 114

4.4.2 Coil construction . . . . . 124

4.4.3 Field mapping to assess nulling performance . . . . . 126

4.4.4 Stability of null over time . . . . . 128

4.4.5 Demonstrating the allowed range of motions . . . . . 130

4.4.6 OPM-MEG demonstration: measurement of retinotopy . . 132

4.5 Discussion . . . . . 135

4.5.1 Coil design . . . . . 135

4.5.2 Coil construction . . . . . 136

4.5.3 Field cancellation method . . . . . 136

4.5.4 Artefact reduction . . . . . 138

4.6 Other demonstrations of OPM-MEG . . . . . 140

**5 Balanced, bi-planar field and field gradient coils 143**

5.1 Introduction . . . . . 143

5.2 Design theory . . . . . 147

5.3 Methods . . . . . 153

5.3.1 Coil design and construction . . . . . 153

5.3.2 Comparing design methods . . . . . 155

5.3.3 Static field nulling . . . . . 155

5.3.4 Field mapping . . . . . 157

5.3.5 Dynamic field nulling . . . . . 157

5.3.6 Investigating interactions with the shielded room . . . . . 160

5.4 Results . . . . . 165

5.4.1 Coil designs . . . . . 165

5.4.2 Comparing design methods . . . . . 167

5.4.3 Field mapping . . . . . 169

5.4.4 Dynamic field nulling . . . . . 171

5.4.5 Investigating interactions with the shielded room . . . . . 174

5.5 Discussion . . . . . 177

5.5.1 Coil design and construction . . . . . 177

5.5.2 Static and dynamic field nulling . . . . . 178

5.5.3 Interactions with the shielded room . . . . . 180

**6 Matrix coils** **182**

6.1 Introduction . . . . . 182

6.2 Background . . . . . 184

6.3 Theory . . . . . 188

6.3.1 Matrix equation formulation . . . . . 188

6.3.2 Matrix regularisation and inversion . . . . . 191

6.3.3 Choosing optimal regularisation parameter . . . . . 193

6.4 Methods . . . . . 195

6.4.1 Prototype matrix coil design . . . . . 195

6.4.2 Comparison to bi-planar coil designs . . . . . 196

6.4.3 Moving the homogeneous region . . . . . 199

6.4.4 Mu-metal interactions . . . . . 201

6.4.5 Building coils into the MSR . . . . . 201

6.5 Results . . . . . 205

6.5.1 Comparison to bi-planar coil designs . . . . . 205

6.5.2 Moving the homogeneous region . . . . . 215

6.5.3 Mu-metal interactions . . . . . 221

6.5.4 Combining coils with the MSR . . . . . 237

6.6 Discussion . . . . . 240

6.6.1 Comparison to six-coil system . . . . . 240

6.6.2 Moving the homogeneous region . . . . . 241

6.6.3 Mu-metal interactions . . . . . 241

6.6.4 Combining coils with the MSR . . . . . 242

6.7 Prototype construction . . . . . 244

6.7.1 Coil construction . . . . . 244

6.7.2 Electronics system . . . . . 245

6.7.3 Field nulling methods . . . . . 246

6.7.3.1 Field mapping and optical tracking . . . . . 246

6.7.3.2 Reference array . . . . . 247

**Conclusion** **247**

# Abstract

Magnetoencephalography (MEG) is a functional brain imaging technique which combines high spatial and temporal resolution to provide unique insights into the workings of the human brain. State-of-the-art commercial MEG systems utilise an array of superconducting sensors to measure magnetic fields generated by neuronal currents. These magnetic fields are around one billion times smaller than the magnetic field of the Earth, requiring systems to be housed inside a magnetically shielded room (MSR).

The limitations imposed by the superconducting sensors leave a source-to-sensor separation of around 2-4 cm, diminishing the signal-to-noise ratio. The participant must also move less than 5 mm during a session. This restricts access to subject groups such as children, and patients with movement disorders. High installation and operational costs have also prevented widespread clinical use of the technology.

The miniaturisation and commercialisation of optically-pumped magnetometers (OPMs), which can be placed directly onto the scalp, has stimulated interest in the development of wearable MEG. By measuring fields closer to the source, an increase in spatial resolution can be achieved and the OPMs can remain fixed in position with respect to the brain during movements. As a result, they present promise as the building blocks of a functional brain imaging system with high spatial resolution, high temporal resolution and good tolerance to participant

motion.

For high-sensitivity usage, the OPMs must operate in a region of zero magnetic field within a range of ±5 nT. MSRs are constructed from ferromagnetic materials, leaving a remnant magnetic field of several tens of nT in magnitude, with spatial variation around 10 nT/m which confounds OPM operation.

This thesis describes the development of a series of active magnetic shielding systems for operation inside a MSR. Bi-planar systems based on design methods previously employed in magnetic resonance imaging (MRI) are used to design coils capable of generating three uniform field components and spatial field gradients which are homogeneous over a volume of $0.4 \times 0.4 \times 0.4$ m$^3$ at the centre of the coils. The six-coil, bi-planar system described here formed a crucial element of an OPM-based MEG system and allowed participants to make head movements of ±35° and ±10 cm.

Although successful, the construction and siting of these coils was a significant challenge. By exploiting shared symmetry of pairs of field and field gradient coils the number of coils required could be halved from six to three. Dynamic stabilisation of the remnant field inside a MSR was also achieved via operation of the coils in a feedback loop to adapt the system to interference generated by a nearby railway line. Interactions between the coils and the high-permeability walls of the MSR which result in degradation of the homogeneity from predicted performance are also investigated.

Finally, a simulation study of new type of coil design where individual currents are applied to a series of small unit coils in order to approximate myriad current distributions is presented. This so-called 'matrix coil' is highly flexible in concept, being able to produce homogeneous magnetic field and field gradient components at multiple locations (the bi-planar field and gradient coils can only produce useful fields at the centre of the set) and readily incorporate interactions with the

high-permeability walls of the MSR. Upon its successful construction the matrix coil would provide a crucial step towards achieving full ambulatory motion in MEG experiments.

# Acknowledgements

I would like to extend a huge thanks to my supervisor, Professor Richard Bowtell for all of your time, support and guidance throughout. I'd also like to thank Professor Matt Brookes for your support and constant enthusiasm. I have thoroughly enjoyed the last three years and would like to thank you both for giving me the opportunity to work on this project.

Thanks to everyone here in Nottingham for making the centre such a welcoming environment. To all members of the MEG team. To Elena, for everything you have done to make the entire OPM-MEG project such a success; the photoshoots will keep on coming. To Ryan, for expanding our scope, and the puppy party in Philadelphia (don't tell Elena - she'll be jealous!). To Gill, despite the hour-long MEG virtual reality experiences. To Alan, without your help I think we would still be trying construct the first coil! To Lesley, for navigating us through the stresses of international shipping. And crucially, to Jim, for teaching me the importance of using different coloured wires.

To Vishal Shah for your drive, determination and incredible sensors, but mostly as without you we would still be sat on the floor turning the dials on 8 different power supplies before every recording.

To the team at UCL. To Professor Gareth Barnes, for your unwavering enthusiasm. To Tim, for your time spent continually travelling to Nottingham to make measurements, and your help constructing the second set of coils (but also

puppies...).

To David, Nick, Stephen, Eliot, Max and everyone at Magnetic Shields for your work translating the prototypes into a commercially viable system. Seeing this happen so quickly is something I am extremely proud of.

Thanks to Nick, Jamie, Joe, Ashley, Nathan, Jack and Michael Henry Allies from the ever-changing cast of the sitcom that has been life in Beeston over the past three years - you made them so memorable.

Thank you Siân for always brightening my day, it has been amazing to share this journey with you. To Mum, Dad and Dom, for many trips to Leicester Space Centre and the Science Museum, for proof-reading the thesis, and for your never-ending support.

# Introduction

The human brain has been described by theoretical physicist Michio Kaku as "the most complicated object in the known universe". The processing power required for simple actions, such as coordinated movement, requires a complex process of information transfer. Neuroscientific research via non-invasive imaging allows us to obtain insights into the working of the human brain from a wide spectrum of ages and abilities, across disease and mental health conditions. This is invaluable to furthering our understanding of the human brain. In general, two types of brain imaging are performed: structural and functional.

Structural imaging of the brain using either magnetic resonance imaging (MRI) or X-Ray computed tomography (CT), non-invasively provides researchers and clinicians with a 'snapshot' of brain structure with very high spatial resolution (on the order of 1 mm or better). MRI exploits the large quantities of water within the body to produce images with very high spatial resolution, without using ionising radiation [Lauterbur, 1973, Mansfield and Grannell, 1973]. X-Ray CT passes a high-intensity X-Ray beam through the body forming images by measuring the attenuation of this beam by different media [Hounsfield, 1973]. Despite the success of MRI and X-Ray CT, little can be gleaned about the function of the brain from assessment of structural images.

Underpinning the brain's ability to communicate with itself and the rest of the body is the passing of electrical currents along neurons. Directly measuring

these currents, or physiological changes related to them, allows for measurement of brain function.

Functional magnetic resonance imaging (fMRI) exploits the different magnetic properties of oxygenated and deoxygenated blood to provide functional measurements with high spatial resolution [Ogawa et al., 1990]. However, the temporal resolution is restricted due to the timescale of blood flow. As a result, many processes in the brain occur at a much higher frequency than can be temporally resolved using fMRI. The requirement that a participant lie perfectly still inside a MRI scanner restricts the subject groups that can be scanned and paradigms that can be performed. Direct, high-bandwidth measurements of the effects of the neuronal currents themselves, from a participant that is free to move, is required for establishing a complete picture of the working brain.

Electroencephalography (EEG) uses electrodes placed on the scalp to record electrical potentials generated by neuronal currents [Berger, 1934]. EEG is routinely employed in clinical and academic work due to its ease of set-up, high temporal resolution and low-cost. However, due to the high electrical impedance of the skull, the potentials are distorted, and 'smeared out' across the scalp surface restricting the spatial resolution that can be achieved. Although participant movements are permitted (as the electrodes remain fixed in position with respect to the head), interfering signals from muscles in the neck and other parts of the body further suppress the brain signal [Muthukumaraswamy, 2013].

By contrast, the magnetic fields produced by neuronal currents pass almost unimpeded through the skull and scalp, making magnetoencephalography (MEG) an attractive prospect [Cohen, 1968, Hämäläinen et al., 1993]. MEG combines high spatial resolution (typically 5 mm) with high temporal resolution (around 1 ms) [Hansen et al., 2010]. Muscle artefacts are still generated, but due to a tighter spatial signature their reduction via signal processing is a simpler task [Muthuku-

maraswamy, 2013]. No electrical contact is needed for a magnetometer, so set-up time and the comfort of a participant can be significantly improved.

The neuromagnetic signal is very weak, around 1 billion times smaller than the magnetic field of the Earth [Hämäläinen et al., 1993]. Its detection is therefore a significant engineering challenge. As a result, commercially available MEG systems employ a fixed array of superconducting sensors which operate at a temperature of 4 K [Hansen et al., 2010]. These sensors are placed inside a dewar of liquid helium and the participant places their head inside a 'helmet'. In addition to the high installation cost of a system and the operational costs required for the replenishment of liquid helium (itself a dwindling resource) in the dewar, the one-size-fits-all design has two key disadvantages: participant motion is limited to <5 mm, and as the neuromagnetic signal decays with the square of distance, weaker signals are measured from those with smaller heads (e.g. infants).

Recent developments in the commercialisation and miniaturisation of optically pumped magnetometers (OPMs) offer an exciting opportunity to develop wearable MEG systems [Shah and Wakai, 2013]. OPMs do not require cryogenic cooling, and can be placed directly on the scalp. The sensor array is then able to move with the head and can be tailored to each participant as in EEG. The increased proximity of sensors to the brain manifests as an increase in signal strength and spatial resolution when compared to EEG and a conventional MEG system [Boto et al., 2016, Iivanainen et al., 2017].

The potential for wearable systems with high spatial resolution, high temporal resolution and increased participant comfort due to high movement tolerance provides an opportunity for a 'step-change' in MEG technology, and in neuroscience in general. By providing access to subject groups that would be inconceivable with current technologies (such as infants and those with movement disorders),

coupled with the potential for implementing previously inaccessible neuroscientific experiments (such as spatial navigation tasks or controlled virtual reality experiences) a vast array of data could be obtained to further our understanding of the human brain.

A major challenge with the operation of an OPM on a moving participant is the narrow dynamic range. High-sensitivity recordings of magnetic field can only be made in the range of $\pm 5$ nT within a bandwidth of 1-100 Hz with miniaturised, commercially-available sensors [Shah et al., 2018]. Reduction of the background magnetic fields in which the sensor operates (e.g. generated by the Earth's magnetic field of 20-60 $\mu$T), further than the level sufficient for a conventional MEG system, is required for OPM recordings.

This thesis describes the design and construction of a series of electromagnetic coil systems which provide cancellation of the remnant magnetic field inside a magnetically shielded room (MSR). Development of OPM-based MEG systems at the University of Nottingham and University College London was aided by the work presented here.

The thesis is divided into six chapters:

- **Chapter 1**: An overview of the basic physics of MEG is given. The focus is on deriving formulae for the strength of the MEG signal due to neuromagnetic fields, and the hardware which is required to detect these very weak magnetic fields. The OPM is introduced as a potential candidate for integration into a wearable MEG system.

- **Chapter 2**: The physics of a commercially available OPM with characteristics suitable for MEG is outlined. Signal equations are derived which highlight the environmental requirement that the sensor operates around a zero-field resonance, within a range of $\pm 5$ nT.

- **Chapter 3**: Both passive and active magnetic shielding techniques are introduced. Due to a remnant magnetic field of several tens of nT inside a passively shielded enclosure, active shielding solutions comprised of electromagnetic coil systems are required to provide the zero-field environment for OPM operation.

- **Chapter 4**: The design, construction and evaluation of a bi-planar coil system featuring six individual coils that can be used to cancel the remnant field over a volume spanning the participants head, at the start of an experimental session is described. The bi-planar design permits movements within a $40 \times 40 \times 40\ \mathrm{cm}^3$ region at the centre of the two planes. The degree of motion which can be accommodated, stability of the field cancellation and MEG data from a movement-based paradigm are reported.

- **Chapter 5**: Although successful, the six-coil system proved challenging to construct. By exploiting the shared symmetry of coil designs, the same performance can be readily achieved with only three coils. Temporal changes in the magnetic field due to underground trains running near the installation site were cancelled by dynamically varying the coil currents in a continually running high-speed feedback loop. Interactions with the high-permeability walls of the MSR which degrade coil performance are also investigated.

- **Chapter 6**: With a bi-planar coil system, the region over which the participant is free to move is fixed in the centre of the coils. By applying a different current to a series of small unit coils, an arbitrary magnetic field at varying positions can be produced. Simulated results and development of a prototype system are presented. Such a system would allow simpler coil construction and could potentially permit full ambulatory motion of a participant.

# Chapter 1

# Magnetoencephalography

## 1.1 Introduction

Magnetoencephalography (MEG) provides non-invasive measurements of brain function with high spatial and temporal resolution [Hämäläinen et al., 1993]. MEG applications are widespread: rich datasets provide valuable insights into many aspects of neuroscience [Baillet, 2017].

The first MEG recordings were performed by David Cohen in 1968 using an inductive coil with 2 million turns [Cohen, 1968]. Significant advancements since that time have been made, with whole-head MEG systems, featuring state-of-the-art superconducting sensors, having been commercially available for many years [Hansen et al., 2010].

This chapter outlines the basic principles of MEG, from signal generation by neuronal currents to signal detection and data analysis. Limitations of state-of-the-art commercial MEG systems employing superconducting magnetic field detectors are discussed, and the benefits of measuring MEG on the scalp with a 'wearable' array of magnetic field sensors are presented.

## 1.2 Neuronal currents

The cortex contains around 100 billion neurons. These are specialised cells responsible for the processing and transfer of information within the brain via the passing of small electrical currents. These electrical currents are essential for mediating brain function. As with any electrical current, an associated magnetic field is also generated. It is these magnetic fields which are of interest in MEG.

A sketch of a single neuron is shown in Figure 1.1. It depicts four sections: the soma containing the cell nucleus; dendrites which extend from the soma to receive stimulation from nearby cells; the axon hillock, beneath the soma where neuronal currents are initiated and the axon, a long structure which carries currents away from the soma, and towards other cells. Grey matter in the brain is formed of dendrites and the soma, whilst the white matter is mainly formed from the axons as they extend to allow communication between different regions.

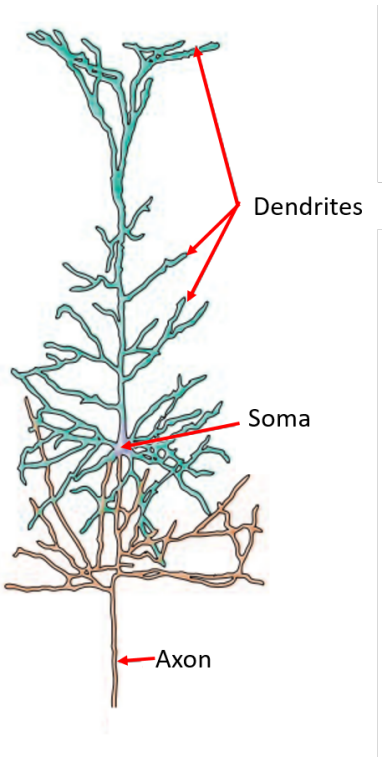



Figure 1.1: *Outline of a single neuron, the key communication unit of the brain. Figure adapted from [Purves et al., 2004].*

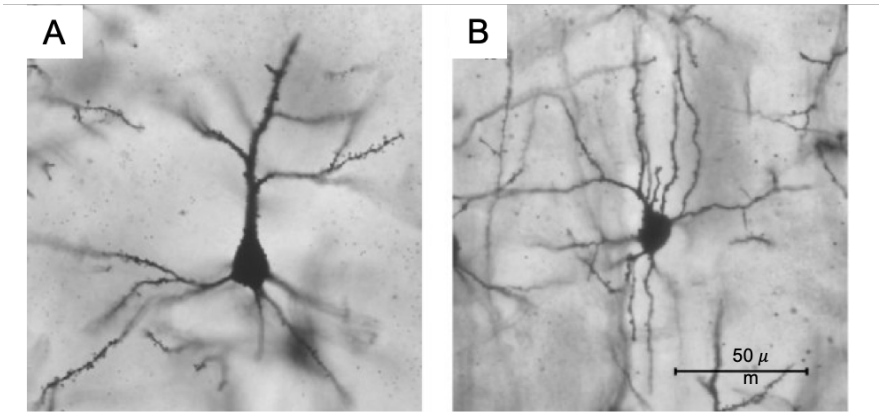



Figure 1.2: *Different types of neuronal structure imaged with light microscopy following Golgi staining. A) The asymmetric structure of a pyramidal neuron. B) The dendrites form a symmetric configuration in a stellate neuron. Figure adapted from [Churchill et al., 2004].*

Neurons are enclosed by an insulating membrane, this divide between intracellular and extracellular tissue results in a different concentration of ions of (mainly) potassium, sodium and chlorine ($K^+$, $Na^+$ and $Cl^-$ respectively) between the two regions. This imbalance of charged ions results in a potential difference between the two regions of $\Delta V$ = -70 mV (intracellular relative to extracellular). A change in this potential difference at the soma, brought about by ion influx at the dendrites, can result in electrical current flow in the form of an 'action potential' [Hämäläinen et al., 1993].

Neurons can have different shapes and are often referred to either as 'pyramidal' or 'stellate'. The pyramidal neurons have an asymmetric, extended dendritic structure, which is oriented perpendicular to the cortical surface as shown in Figure 1.2A. As a consequence, the dendrites coherently guide current flow along the cell, which allows for a magnetic field to be generated. The dendritic structure of stellate neurons is highly symmetric, as shown in Figure 1.2B resulting in no coherent direction of current flow. As a result, these cells are likely to be of limited influence in a MEG measurement as the magnetic fields generated by such structures will likely cancel each other out [Hämäläinen et al., 1993].

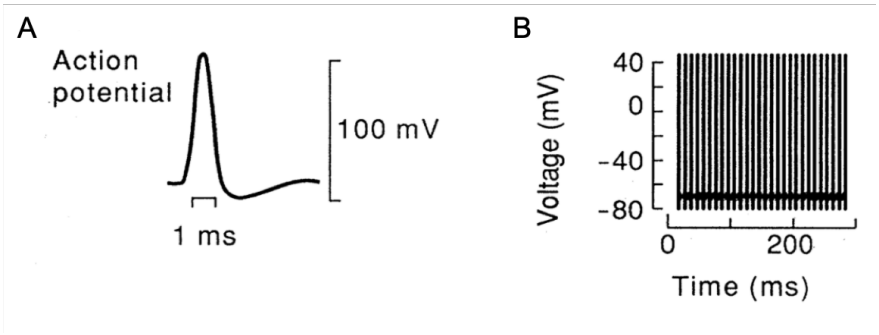



Figure 1.3: *The action potential. A) Characterised as a short-lived increase in potential difference following depolarisation of the neuron due to open ion channels. B) Repeated stimulated firing of the action potential shows an increase in frequency of the potential but not an increase in the amplitude. Figure adapted from [Hämäläinen et al., 1993].*

### 1.2.1 Action potentials

If the potential difference across the membrane at the axon hillock reaches a threshold level of $\Delta V$ = -55 mV then ion channels open resulting in $K^+$ flowing out of the neuron and $Na^+$ ions flowing into the neuron. The permeability of the membrane to $Na^+$ ions changes, resulting in a flow of ions which raises the potential difference to $\Delta V$ = +40 mV in a period of around 1 ms. This triggers the action potentials to pass down the axon. As the potential rises, permeability of the membrane to $K^+$ ions greatly increases such that the cell is repolarised by a flow of $K^+$ ions restoring the potential difference to $\Delta V$ = -70 mV. This process is outlined in Figure 1.3.

As the action potential passes down the axon, the processes of depolarisation at the leading edge and repolarisation at the trailing edge, can be modelled as two current dipoles with opposing orientations. This creates a quadrupolar current source [Hämäläinen et al., 1993].

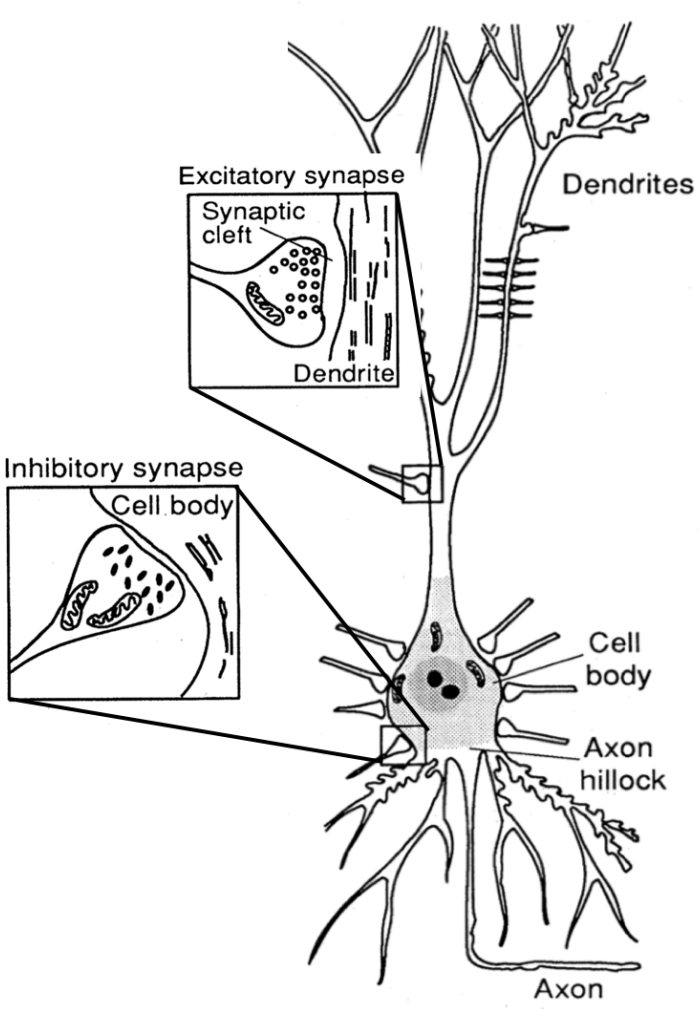



Figure 1.4: *Excitatory and inhibitory synapses. The excitatory synapses mainly form at the dendrites and the inhibitory synapses form at the cell body. Figure adapted from [Hämäläinen et al., 1993].*

### 1.2.2 Post-synaptic potentials

When an action potential reaches the end of an axon, chemical transmission between two neurons can occur. These interactions occur in connections, or 'synapses' between two neurons. Two types of synapse, excitatory and inhibitory, are shown in Figure 1.4. Excitatory synapses (mainly found on dendrites) make the post-synaptic neuron more likely to fire by decreasing the potential difference $\Delta V$, and inhibitory synapses (mainly located on the soma) increase $\Delta V$ making the neuron less likely to fire.

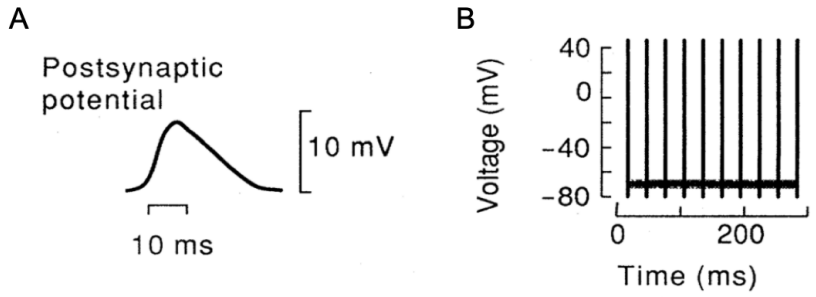



Figure 1.5: *The post-synaptic potential. Longer in duration but smaller in amplitude than an action potential and excitatory or inhibitory in nature. Caused by a terminating action potential opening ion channels into the post-synaptic neuron resulting in either hyperpolarisation or depolarisation of the neuron. Again the frequency but not the amplitude of the potential is increased via stimulated firing. Figure adapted from [Hämäläinen et al., 1993].*

The process of transmission of signal from a pre-synaptic neuron to a post-synaptic neuron begins when an action potential reaches the end of the axon of the pre-synaptic neuron. This event stimulates the release of chemicals known as neurotransmitters into the space between the axon and the dendrite of the post-synaptic neuron (the 'synaptic cleft'). These neurotransmitters stimulate the opening of ion channels in the wall of the post-synaptic neuron causing ions to flow in or out of the neuron. This imbalance of ions again causes a change in the potential difference which produces a post-synaptic potential.

If the ion channels which are opened allow the flow of $Na^+$ ions into the neuron then a depolarisation occurs as before and the post-synaptic potential is a excitatory potential. If the ion channels allow $K^+$ ions to flow out of the cell or $Cl^-$ ions into the neuron then a hyperpolarisation occurs and the post-synaptic potential is inhibitory. The probability of a neuron firing an action potential depends on the sum of these excitatory and inhibitory events. Both cause a current to flow along the dendrites and into the soma on a timescale of about 10 ms as shown in Figure 1.5. This event can be approximated by a current dipole and is referred to as the primary current.

In order to balance ion flows in depolarisation and repolarisation, current must flow in the extracellular space around the neuron. This current flow is therefore on average in the opposite direction to the primary current and highly dependent on the electrical conductivity of the surrounding region. This is referred to as the volume current and has little effect on the measured magnetic field as detailed later [Hämäläinen et al., 1993].

## 1.3 Measurable effects in MEG

Considering both the structure of pyramidal neurons and the timescales of post-synaptic potentials (10 ms c.f. 1 ms for an action potential) significant coherence of current flow can be achieved between the post-synaptic potentials in groups of pyramidal neurons [Baillet, 2017]. This synchronous firing will constructively interfere and generate a measurable effect which can be measured in a MEG experiment as shown in Figure 1.6. Three main effects are commonly investigated: Evoked responses, spontaneous rhythms and induced responses [Hansen et al., 2010]. Robust effects producing a known response in the vast majority of participants are useful tools when evaluating the performance of a MEG system.

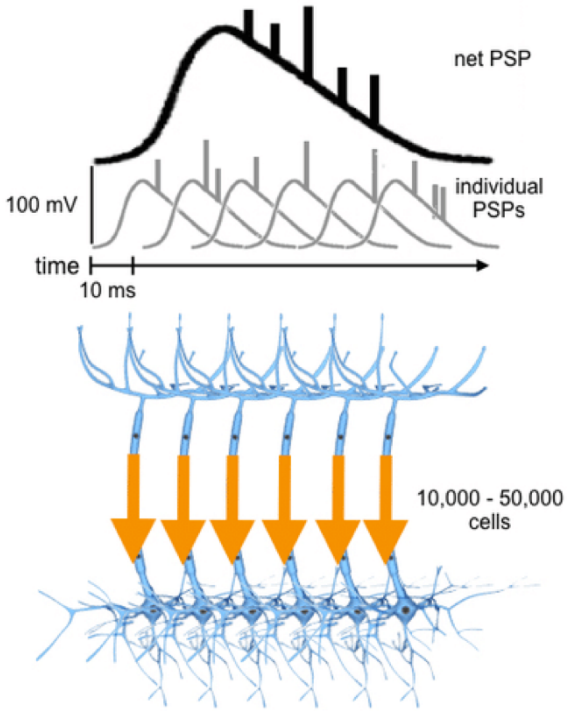



Figure 1.6: *Synchronous firing of around 10,000 pyramidal neurons to form the MEG signal. The post-synaptic potentials (PSPs) interfere constructively due to their long timescale. Adapted from [Baillet, 2017].*

### 1.3.1 Evoked responses

Presentation of a sensory stimulus typically generates a measurable neuromagnetic response, e.g. stimulating motion in a finger via controlled application of an electrical current to the median nerve [Hari et al., 1993]. A visual flicker generates a visual response. [Ahlfors et al., 1992]. A repeated audible tone generates an auditory response [Hari et al., 1987]. Each process produces a repeatable, measurable response in the brain. The resulting neuromagnetic signal is not only time-locked to the stimulus, but also phase-locked to it, so averaging data recorded over many repeats of the stimulus will reduce the noise in the data, leaving a clear response as outlined in Figure 1.7 [Hansen et al., 2010].

These time-and-phase-locked signals are known as evoked responses. They are a useful marker of healthy brain function, as changes in latency or the temporal morphology can indicate a number of neurological or physiological disorders such as multiple sclerosis [Rossini and Rossi, 1998].

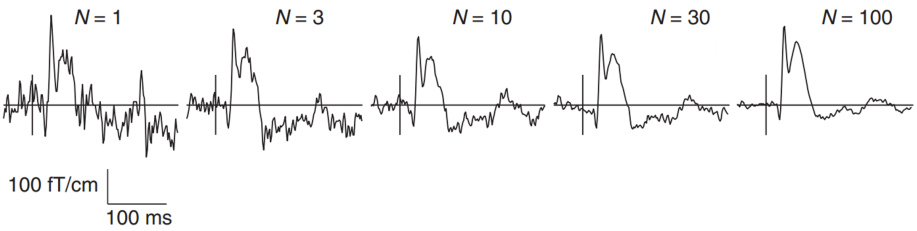



Figure 1.7: *Evoked response from electrical stimulation of the median nerve. Response is observed in the somatosensory region of the brain. Averaging over N trials improves the signal to noise ratio of the response although its characteristics are observable in a single trial recording. Figure adapted from [Hansen et al., 2010]*

### 1.3.2 Spontaneous rhythms

The background activity of the brain results in continually firing neuronal currents without any stimulation, forming spontaneous rhythms. Recordings of elec-

trical activity in the human brain were performed by Hans Berger and constituted the first electroencephalography (EEG) experiment. In his experiments he discovered a change in the amplitude of an oscillatory rhythm, of frequency ≈8-13 Hz when a participant opened and closed their eyes [Berger, 1934]. This became known as the alpha rhythm and following Berger's work a series of oscillatory rhythms were discovered.

The frequencies of brain rhythms are typically split into five 'bands' (sometimes referred to as the 'Berger bands')

- Delta <4 Hz
- Theta 4-8 Hz
- Alpha 8-13 Hz
- Beta 13-30 Hz
- Gamma >30 Hz

Each band is responsible for a different process, as the rhythms continually occur without external stimulation. Most MEG studies therefore require sensitivity to changing magnetic fields with at least a 1-100 Hz bandwidth, but there is also evidence of higher frequency effects [Baillet, 2017]. These rhythms are thought to aid connectivity between regions, but also to promote local activity. Their coupling across frequency bands facilitates the process of information transfer, via stimulation of neuronal firings over short and long-range connections [Hipp et al., 2012, Engel et al., 2013, Donner and Siegel, 2011].

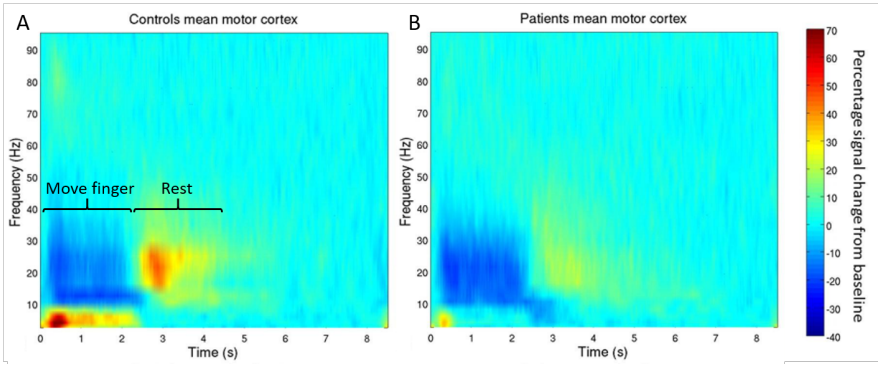



Figure 1.8: *Induced response during a single finger abduction. The oscillatory power in the beta band decreases during the finger movement and a post-movement beta rebound is observed during rest. The size of this beta rebound is diminished in schizophrenia patients compared to healthy controls. Adapted from [Robson et al., 2016].*

### 1.3.3 Induced responses

Changes in spontaneous brain rhythms can be 'induced' by an external stimulus. In general the frequency of the neural oscillations is unaffected, but the amplitude is modulated [Pfurtscheller and Lopes Da Silva, 1999]. As spontaneous rhythms occur naturally, the induced effects are time-locked, but not phase-locked to the external stimulus. To analyse the data a time-series recording is filtered to the frequency band of interest and the amplitude envelope is then calculated. Averaging this envelope over trials allows stimulus-induced changes in oscillatory power with respect to a baseline level (when the participant is not performing any task) to be clearly shown.

For example, the movement/sensory induced beta response is a robust response that is elicited when a participant makes a movement (or receives a somatosensory stimulus). During the movement (for example abducting a single finger out with an open palm) the amplitude of the beta oscillations decreases compared to the baseline level. After the movement ceases there is a 'post stimulus beta rebound' during which the amplitude increases above the baseline level. This decrease in beta power is thought to be due to the brain region responsible for the finger

removing itself from the wider brain network during the movement, the rebound following movement cessation then being responsible for re-integrating this region to the wider network [Donner and Siegel, 2011].

Figure 1.8 shows an example beta rebound signal on a time-frequency spectrogram (TFS). The TFS is a common tool for displaying temporally rich MEG data in which time is shown along the $x$-axis and frequency on the $y$-axis. Colour information provides an indicator of the oscillatory amplitude. The percentage change from baseline in beta band activity during the post stimulus period has been shown to be diminished in patients with schizophrenia, providing promise as a clinically relevant biomarker which is simple to measure [Robson et al., 2016].

## 1.4 The MEG forward problem

As discussed previously, the synchronous firing of post-synaptic currents in pyramidal neurons constructively adds to generate a measurable magnetic field. In order to determine the hardware required for a MEG system (and allow for accurate data modelling and analysis) a mathematical model of the neuronal magnetic field is required. This is referred to as the MEG forward problem, where the magnetic field at a detector placed outside the head is calculated from a known current density inside the brain. The magnetic field generated by a current density $\boldsymbol{J}$ can be described using Maxwell's equations

$$\begin{aligned} \nabla.\boldsymbol{E} &= \frac{\rho}{\epsilon} \\ \nabla.\boldsymbol{B} &= 0 \\ \nabla \times \boldsymbol{E} &= -\frac{\partial \boldsymbol{B}}{\partial t} \\ \nabla \times \boldsymbol{B} &= \mu_0\left(\boldsymbol{J} + \epsilon\frac{\partial \boldsymbol{E}}{\partial t}\right) \end{aligned} \tag{1.4.1}$$

where, $\mu_0$ is the permeability of free space, $\epsilon$ is the permittivity of the medium and $\rho$ is the charge density in the medium. As most neuronal activity occurs within the 1-100 Hz frequency range, a quasistatic approximation without charge accumulation can be made, resulting in

$$\begin{aligned} \nabla \times \boldsymbol{E} &= 0 \\ \nabla \times \boldsymbol{B} &= \mu_0 \boldsymbol{J}. \end{aligned} \tag{1.4.2}$$

Defining a volume, $G$ in which the current density exists then the magnetic field measured by a detector at position $\boldsymbol{r}(x, y, z)$ outside the volume, produced by current density $\boldsymbol{J}(\boldsymbol{r}'(x, y, z))$ inside the volume is given by the Ampere-Laplace law as

$$\boldsymbol{B}(\boldsymbol{r}) = \frac{\mu_0}{4\pi} \int_G \boldsymbol{J}(\boldsymbol{r}') \times \frac{\boldsymbol{r} - \boldsymbol{r}'}{|\boldsymbol{r} - \boldsymbol{r}'|^3} \, dV'. \tag{1.4.3}$$

Decomposing the current density into separate components corresponding to the primary ($\boldsymbol{J_p}$) and volume ($\boldsymbol{J_v}$) currents as

$$\boldsymbol{J}(\boldsymbol{r}') = \boldsymbol{J_p}(\boldsymbol{r}') + \boldsymbol{J_v}(\boldsymbol{r}') \tag{1.4.4}$$

allows the volume current to be further expressed in terms of an electrical potential, $V$, (as the volume current results from the effects of the electric field on the medium) as [Sarvas, 1987]

$$\boldsymbol{J_v}(\boldsymbol{r}') = \sigma \boldsymbol{E}(\boldsymbol{r}') = -\sigma \nabla V(\boldsymbol{r}'), \tag{1.4.5}$$

where $\sigma$ is the electrical conductivity of the medium. The resulting current density is then given by

$$\boldsymbol{J}(\boldsymbol{r}') = \boldsymbol{J_p}(\boldsymbol{r}') - \sigma \nabla V(\boldsymbol{r}') \tag{1.4.6}$$

and the magnetic field, assuming a constant value of $\sigma$ throughout the volume, becomes

$$\boldsymbol{B}(\boldsymbol{r}) = \frac{\mu_0}{4\pi} \int_G \boldsymbol{J_p}(\boldsymbol{r}') \times \frac{\boldsymbol{r} - \boldsymbol{r}'}{|\boldsymbol{r} - \boldsymbol{r}'|^3} \, dV' - \sigma \frac{\mu_0}{4\pi} \int_G \nabla V(\boldsymbol{r}') \times \frac{\boldsymbol{r} - \boldsymbol{r}'}{|\boldsymbol{r} - \boldsymbol{r}'|^3} \, dV'. \tag{1.4.7}$$

If $\sigma$ varies throughout the medium then the volume current integral can be performed over several 'compartments', followed by summation of the results. The conductivity profile has no effect on the magnetic field generated by the primary current. Applying vector calculus identities to the volume current term, we can write [Sarvas, 1987]

$$\nabla V(\boldsymbol{r}') \times \frac{\boldsymbol{r}-\boldsymbol{r}'}{|\boldsymbol{r}-\boldsymbol{r}'|^3} = \nabla \times V(\boldsymbol{r}') \frac{\boldsymbol{r}-\boldsymbol{r}'}{|\boldsymbol{r}-\boldsymbol{r}'|^3}. \tag{1.4.8}$$

Then applying the generalised Stokes theorem to convert the volume integral to a surface integral gives the generated field as [Geselowitz, 1967]

$$\boldsymbol{B}(\boldsymbol{r}) = \frac{\mu_0}{4\pi} \int_G \boldsymbol{J_p}(\boldsymbol{r}') \times \frac{\boldsymbol{r}-\boldsymbol{r}'}{|\boldsymbol{r}-\boldsymbol{r}'|^3}\, dV' - \sigma \frac{\mu_0}{4\pi} \int_S \hat{\boldsymbol{n}}(\boldsymbol{r}') \times \nabla V(\boldsymbol{r}') \frac{\boldsymbol{r}-\boldsymbol{r}'}{|\boldsymbol{r}-\boldsymbol{r}'|^3}\, dS', \tag{1.4.9}$$

where $S$ denotes the surface of the volume $G$ and $\hat{\boldsymbol{n}}(\boldsymbol{r}')$ is a vector perpendicular to this surface at $\boldsymbol{r}'$.

A common approach in MEG analysis is to assume that the volume has uniform conductivity and is bound by a spherical surface. This is often referred to as the single sphere model [Hämäläinen et al., 1993]. If only the radial component of the field is considered, i.e. $B_r(\boldsymbol{r}) = \boldsymbol{B}(\boldsymbol{r}) \cdot \hat{\boldsymbol{e_r}}(\boldsymbol{r})$ where $\hat{\boldsymbol{e_r}}(\boldsymbol{r})$ is the radial unit vector at position $\boldsymbol{r}$, then upon inspection of the volume current term it follows that

$$\hat{\boldsymbol{n}}(\boldsymbol{r}') \times (\boldsymbol{r}-\boldsymbol{r}') \cdot \hat{\boldsymbol{e_r}}(\boldsymbol{r}) = [\hat{\boldsymbol{n}}(\boldsymbol{r}') \times \boldsymbol{r} - \hat{\boldsymbol{n}}(\boldsymbol{r}') \times \boldsymbol{r}'] \cdot \hat{\boldsymbol{e_r}}(\boldsymbol{r}) = 0 \tag{1.4.10}$$

since ($\hat{\boldsymbol{n}}(\boldsymbol{r}')$ is parallel with $\boldsymbol{r}'$ so $\hat{\boldsymbol{n}}(\boldsymbol{r}') \times \boldsymbol{r}' = 0$, and $\hat{\boldsymbol{n}}(\boldsymbol{r}') \times \boldsymbol{r}$ is perpendicular to $\hat{\boldsymbol{e_r}}(\boldsymbol{r}')$ so $(\hat{\boldsymbol{n}}(\boldsymbol{r}') \times \boldsymbol{r}) \cdot \hat{\boldsymbol{e_r}} = 0$. As the volume current term drops out in the single sphere approximation the radial field can be expressed just in terms of the primary current [Sarvas, 1987]

$$B_r(\boldsymbol{r}) = \frac{\mu_0}{4\pi} \int_G \boldsymbol{J_p}(\boldsymbol{r}') \times \frac{\boldsymbol{r}-\boldsymbol{r}'}{|\boldsymbol{r}-\boldsymbol{r}'|^3} \cdot \hat{\boldsymbol{e_r}}(\boldsymbol{r})\, dV'. \tag{1.4.11}$$

To estimate the magnitude of the magnetic field produced by neuronal currents, the current density can be approximated by a current dipole, $\boldsymbol{Q}$ inside the volume

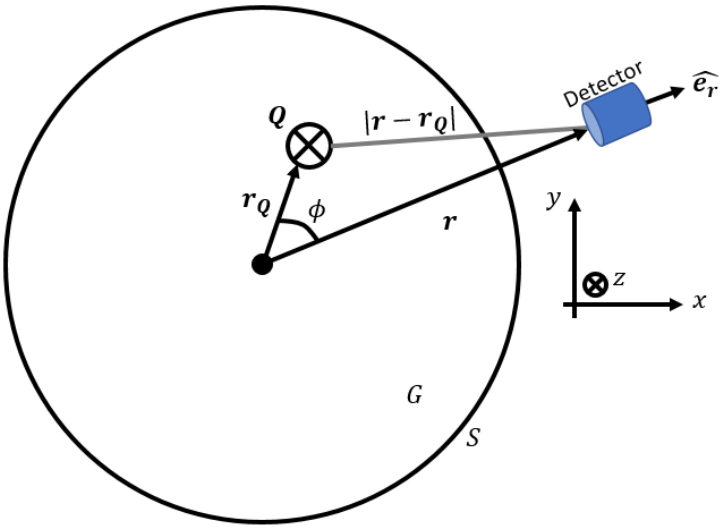



Figure 1.9: *The single-shell forward model. The magnetic field measured by a detector at position* $\boldsymbol{r}$ *generated by a dipole source at position* $\boldsymbol{r_Q}$ *oriented along the* $z$ *axis inside the volume* $G$*.*

$G$ at position $\boldsymbol{r_Q}$ [Sarvas, 1987]. Concentrating the current source to a single point allows expression of $\boldsymbol{J_p}$ using a dirac delta function as

$$\boldsymbol{J_p}(\boldsymbol{r}') = \boldsymbol{Q}\delta(\boldsymbol{r}' - \boldsymbol{r_Q}). \tag{1.4.12}$$

It then follows that the radial component of the measured magnetic field is

$$B_r(\boldsymbol{r}) = \frac{\mu_0}{4\pi}\int_G \boldsymbol{Q}\delta(\boldsymbol{r}' - \boldsymbol{r_Q}) \times \frac{\boldsymbol{r} - \boldsymbol{r}'}{|\boldsymbol{r} - \boldsymbol{r}'|^3} \cdot \hat{\boldsymbol{e}}_{\boldsymbol{r}}(\boldsymbol{r})\, dV', \tag{1.4.13}$$

and finally,

$$B_r(\boldsymbol{r}) = \frac{\mu_0}{4\pi}\boldsymbol{Q} \times \frac{\boldsymbol{r} - \boldsymbol{r_Q}}{|\boldsymbol{r} - \boldsymbol{r_Q}|^3} \cdot \hat{\boldsymbol{e}}_{\boldsymbol{r}}(\boldsymbol{r}). \tag{1.4.14}$$

In this model a radial source produces no measurable $B_r$ field. Constraining the orientation of $Q$ to the $z$ direction as shown in Figure 1.9 and evaluating the field

inside a single $x-y$ plane of the volume $G$ for analysis allows the expression to be reduced to

$$B_r(\boldsymbol{r},\phi) = \frac{\mu_0}{4\pi}\frac{|\boldsymbol{Q}||\boldsymbol{r_Q}|\sin(\phi)}{(|\boldsymbol{r}|^2+|\boldsymbol{r_Q}|^2-2|\boldsymbol{r}||\boldsymbol{r_Q}|\cos(\phi))^{3/2}}. \tag{1.4.15}$$

The magnitude of the vector quantities are expressed as $|\boldsymbol{A}|$ and the angle between $\boldsymbol{r}$ and $\boldsymbol{r_Q}$ is $\phi$. As a result the measured field varies anti-symmetrically with respect to the angle $\phi$ for fixed values of $\boldsymbol{r}$, $\boldsymbol{r_Q}$ and $\boldsymbol{Q}$. The angle $\phi$ which produces the maximum measured field is found by differentiating and given as the solution to

$$\cos(\phi) = \frac{-(|\boldsymbol{r}|^2+|\boldsymbol{r_Q}|^2)+\sqrt{|\boldsymbol{r}|^4+|\boldsymbol{r_Q}{}^4|+14|\boldsymbol{r}|^2|\boldsymbol{r_Q}|^2}}{2|\boldsymbol{r}||\boldsymbol{r_Q}|}. \tag{1.4.16}$$

An estimate of the variation of the maximum resulting magnetic field which is measured at the surface of the volume $G$ with source depth, is plotted in Figure 1.10. Here, the 'head' is modelled as a spherical volume with a radius of 10 cm. An on-scalp detector was assumed such that $|\boldsymbol{r}| = 10$ cm. A source magnitude of $|\boldsymbol{Q}| = 10$ nAm was used (typically values of 1-10 nAm are assumed for MEG modelling). The depth of the dipole, $|\boldsymbol{r_Q}|$ is varied between 1 cm and 9 cm (where 1 cm approximates the cortical surface and 9 cm reflects deep sources such as the hippocampus). For each value the angle giving the maximal field was calculated using equation [1.4.16].

The magntitude of the produced magnetic field from this single-sphere approximation varies between 3,000 fT to 10 fT as the depth of the 10 nAm source increases from 1-9 cm. This represents a magnetic field which is around 1 billion times smaller than the magnetic field of the Earth (20-80 $\mu$T) and thus MEG represents a significant engineering challenge.

For completeness, the remaining (tangential) components of the magnetic field

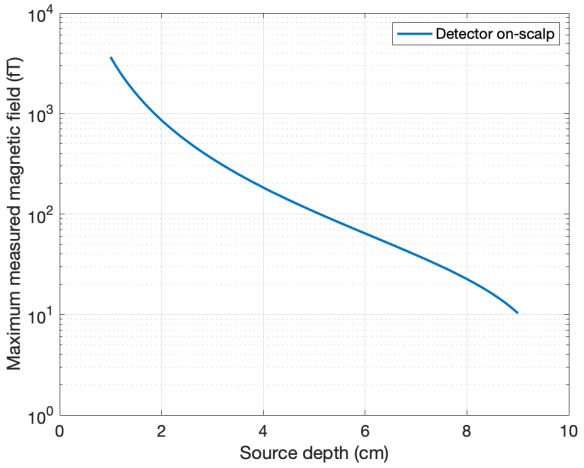



Figure 1.10: *The maximum magnetic field measured on the scalp from a single-shell forward model. Assuming the head is a sphere of radius 10 cm containing a current dipole of strength 10 nAm. The field is plotted as a function of the source depth for depths of 1 cm to 9 cm.*

$\boldsymbol{B}(\boldsymbol{r})$ can be obtained by expressing $\boldsymbol{B}(\boldsymbol{r})$ in terms of a magnetic scalar potential $U(\boldsymbol{r})$ (since $\nabla \times \boldsymbol{B} = 0$ outside the head where $\boldsymbol{J} = 0$) as

$$\boldsymbol{B}(\boldsymbol{r}) = -\mu_0 \nabla U(\boldsymbol{r}). \tag{1.4.17}$$

The expression for $U(\boldsymbol{r})$ is derived by Sarvas through evaluation of a line integral of $\nabla U$ along the radius $\boldsymbol{r} + t\hat{\boldsymbol{e}_r}$ with $0 < t < \infty$ ($U$ vanishes at $\infty$) [Sarvas, 1987]. Sarvas defines the integral as

$$U(\boldsymbol{r}) = -\int_0^\infty \nabla U(\boldsymbol{r} + t\hat{\boldsymbol{e}_r}) \cdot \hat{\boldsymbol{e}_r}\, dt \tag{1.4.18}$$

with solution

$$U(\boldsymbol{r}) = -\frac{1}{4\pi} \frac{\boldsymbol{Q} \times \boldsymbol{r_Q} \cdot \boldsymbol{r}}{F}. \tag{1.4.19}$$

Here, $F = a(ar + \boldsymbol{r}^2 - \boldsymbol{r_Q}.\boldsymbol{r})$, $\boldsymbol{a} = \boldsymbol{r} - \boldsymbol{r_Q}$ and the vector magnitudes $|\boldsymbol{a}|$ and $|\boldsymbol{r}|$ are given as $a$ and $r$ respectively.

Using equation 1.4.17, the complete magnetic field vector outside the spherical conductor model generated by a current dipole can be expressed as [Sarvas, 1987]

$$\boldsymbol{B}(\boldsymbol{r}) = \frac{\mu_0}{4\pi F^2}(F\boldsymbol{Q} \times \boldsymbol{r_Q} - \boldsymbol{Q} \times \boldsymbol{r_Q} \cdot \boldsymbol{r}\nabla F). \tag{1.4.20}$$

Although simplistic, this so-called 'single-sphere' head model is commonly used in MEG analysis. More accurate models include the 'multiple-sphere' head model where a different sphere is chosen for each detector giving a series of overlapping volumes which better approximates the brain's geometry [Huang et al., 1999]. Boundary element model (BEM) analysis can also be employed, by extracting the scalp, skull and brain surfaces from a participant's anatomical MRI such that the exact structure is known [Stenroos et al., 2014]. BEMs are very accurate, but computationally expensive. With parallel or cluster-based processing becoming widely available, such methods are increasingly being employed. Modelling of the additional components of the magnetic field can readily be applied in these cases. As the MEG measurements described in this thesis concentrate on simple paradigms with sensor coverage limited to specific brain regions, the single-sphere head model is used.

## 1.5 The MEG inverse problem

In a MEG experiment it is necessary to reconstruct the neuronal current distribution which generated the magnetic fields detected outside the head. This is the MEG inverse problem. It is mathematically ill-posed as field cancellation means there is an infinite number of different current distributions which would produce the same magnetic field pattern [Hämäläinen et al., 1993]. A considered approach, taking into account the MEG forward modelling described previously and several other assumptions is therefore required when addressing this problem.

### 1.5.1 Lead fields

The magnetic field detected at sensor $i$ of a set of $N$ sensors at time $t$ is expressed as $m_i(t)$. A model of this field, as would be generated by a dipole of unit strength at position $\boldsymbol{r}'$, at each detector is given as $l_i(\boldsymbol{r}')$. Calculated using the forward model, this is referred to as the 'lead field' [Van Veen et al., 1997]. Multiplying this lead field by the actual dipole strength at position $\boldsymbol{r}'$ and time $t$, $q(\boldsymbol{r}', t)$ and integrating over the volume of interest $V$ gives $m_i(t)$ as

$$m_i(t) = \int_V l_i(\boldsymbol{r}') \cdot q(\boldsymbol{r}', t)\ dV. \tag{1.5.1}$$

This is known as the generative model for MEG. If the volume of interest is the brain volume as extracted from a MRI scan of the participant, then a simple approach is to discretise the brain into a series of voxels (typically cubes of side length 2 - 4 mm are used). Assuming a single dipole exists in each of $j = 1$ to $M$ voxels, the measured field $m_i(t)$ is given as [Vrba and Robinson, 2001]

$$m_i(t) = \Sigma_{j=1}^{M} l_{i,j} \cdot q_j(t), \tag{1.5.2}$$

where $l_{i,j}$ is the lead field at detector $i$ generated by a unit dipole in voxel $j$. For all $N$ detectors and all $M$ voxels the matrix equation

$$\boldsymbol{m}(t) = \boldsymbol{L}\boldsymbol{q}(t) \tag{1.5.3}$$

can be written. $\boldsymbol{m}(t)$ is a $(N \times 1)$ vector of the magnetic fields at each detector as measured by the MEG system, $\boldsymbol{L}$ is the lead field matrix with dimensions $(N \times M)$ constructed using the forward model. The underlying neuronal current distribution $\boldsymbol{q}(t)$ is then a $(M \times 1)$ vector.

In typical MEG analysis $M$ can be on the order of $10^4$ (typical brain size discretised to a 4 mm grid) and $N$ is typically around 200-300 sensors. As a result the matrix $\boldsymbol{L}$ is a non-square matrix which is unlikely to have full rank (number of linearly independent columns) so inversion in the form of $\boldsymbol{q}(t) = \boldsymbol{L}^{-1}\boldsymbol{m}(t)^T$ (where $T$ denotes the transpose of a matrix) is not possible without applying additional constraints.

### 1.5.2 Beamforming

Many solutions to the inverse problem exist, here particular attention is paid to the beamformer solution as results using this method are presented in Chapter 4. Originally developed for radar and communications, the mathematical framework is also applicable to MEG [Van Veen and Buckley, 1988, Van Veen et al., 1997]. The beamformer aims to find an *estimate* of the current density, $\hat{q}_\Theta$, at a given position and orientation, denoted by $\Theta$. The estimate is formed from a weighted sum of sensor measurements given by

$$\hat{q}_\Theta(t) = \boldsymbol{w}_\Theta^T \boldsymbol{m}(t) \tag{1.5.4}$$

where, $\boldsymbol{w}_\Theta$ is vector of weights of dimension $(N \times 1)$ for dipole position and orientation $\Theta$ [Van Veen et al., 1997, Vrba and Robinson, 2001]. The weights vector is chosen such that activity at $\Theta$ is emphasised and all other activity is suppressed [Van Veen et al., 1997]. The weights are derived based on a minimisation of the variance of $\hat{q}_\Theta$, but with a linear constraint that the signals which are generated at $\Theta$ remain. The minimisation is expressed as

$$\min_{\boldsymbol{w}_\Theta} |\langle \hat{q}^2_\Theta(t) \rangle| \text{ subject to } \boldsymbol{w}^T_\Theta \boldsymbol{l}_\Theta = 1, \tag{1.5.5}$$

where $\boldsymbol{l}_\Theta$ is the lead field for the magnetic field measured at $N$ sensors from a dipole at location $\Theta$, a column of the matrix $L$ and $\langle \hat{q}^2_\Theta(t) \rangle$ denotes the expectation value of $\hat{q}^2_\Theta(t)$ over time. $\hat{q}^2_\Theta(t)$ is expressed as

$$\hat{q}^2_\Theta(t) = \boldsymbol{w}^T_\Theta \boldsymbol{m}(t)[\boldsymbol{w}^T_\Theta \boldsymbol{m}(t)]^T = \boldsymbol{w}^T_\Theta \boldsymbol{m}(t)\boldsymbol{m}(t)^T \boldsymbol{w}_\Theta. \tag{1.5.6}$$

The covariance matrix, $\boldsymbol{C}$ contains a measure of the covariance of data recorded across all channels. $\boldsymbol{C}$ is a square matrix of dimension $(N \times N)$, which can be approximated as $\langle \boldsymbol{m}(t)\boldsymbol{m}(t)^T \rangle$. The solution for $\boldsymbol{w}_\Theta$ is then given as

$$\boldsymbol{w}^T_\Theta = \frac{\boldsymbol{l}^T_\Theta \boldsymbol{C}^{-1}}{\boldsymbol{l}^T_\Theta \boldsymbol{C}^{-1} \boldsymbol{l}_\Theta}. \tag{1.5.7}$$

If $\boldsymbol{C}$ is close to singular then regularisation is required to provide a stable solution of $\boldsymbol{C}^{-1}$. Typically, a Tikhonov regularised matrix, $\boldsymbol{C_r}$, of the form $\boldsymbol{C_r} = \boldsymbol{C} + \mu \boldsymbol{I}$ is used. $\mu$ is a regularisation parameter, usually some small percentage of the maximum eigenvalue of $\boldsymbol{C}$, and $\boldsymbol{I}$ is the identity matrix (regularisation of this type is applied in Chapter 6 to design electromagnetic coils).

Although the source orientation is unknown, a common approach is to assume the source is azimuthally constrained (as a radial source would produce no magnetic

field in the single-sphere model) and to vary the angle $\phi$ (as introduced in the forward model derivation) between 0 and $\pi$ defining a new weights vector for each value of $\phi$. The maximum signal to noise ratio for a given location is then estimated by comparing the 'pseudo $Z$ statistic' from each value of $\phi$ [Vrba and Robinson, 2001]. The pseudo $Z$ statistic for a dipole at position $\boldsymbol{r_Q}$ is given as

$$Z_{\boldsymbol{r_Q},\phi} = \frac{\boldsymbol{w}^T_{\boldsymbol{r_Q},\phi}\boldsymbol{C}\boldsymbol{w}_{\boldsymbol{r_Q},\phi}}{\boldsymbol{w}^T_{\boldsymbol{r_Q},\phi}\boldsymbol{I}\boldsymbol{w}_{\boldsymbol{r_Q},\phi}}. \tag{1.5.8}$$

In an MEG experiment involving induced responses it is common to compare changes in brain activity during stimulation. Trials are separated into two periods: baseline brain activity, known as the 'control window' and a period where the stimulation occurs, known as the 'active window'. A separate covariance matrix is formed for each window. These are written as $\boldsymbol{C_a}$ and $\boldsymbol{C_c}$ for the active and control periods, respectively. The contrast between the two periods is calculated for each location $\Theta$ (taking the orientation which gives the maximum SNR) using a pseudo-$T$-statistic as [Vrba and Robinson, 2001]

$$T_\Theta = \frac{\boldsymbol{w}^T_\Theta\boldsymbol{C_a}\boldsymbol{w}_\Theta - \boldsymbol{w}^T_\Theta\boldsymbol{C_c}\boldsymbol{w}_\Theta}{2\boldsymbol{w}^T_\Theta\boldsymbol{C_c}\boldsymbol{w}_\Theta}. \tag{1.5.9}$$

Computing this statistic for each position in the brain allows a 'heatmap' of brain activity to be formed, which highlights regions where the contrast between active and resting brain activity is highest [Vrba and Robinson, 2001]. For example, it would be expected that during a finger movement task the contrast would be highest over the motor cortex, specifically in the finger and hand region.

## 1.6 MEG hardware

The MEG forward problem indicates that the neuromagnetic signals of interest are of the order 10-3,000 fT in magnitude at the scalp surface within a frequency range of around 1-100 Hz [Hämäläinen et al., 1993]. This signal is many orders of magnitude smaller than biomagnetic signals generated by other parts of the body, such as those produced by the beating heart, movements of the eyes and muscles, as well as signals generated by the movement of magnetic particles that have been lodged in the lungs by inhalation. Magnetic fields generated by urban sources such as cars, trams, trains and electrical equipment also create interfering magnetic fields at magnitudes much larger than the brain signals [Vrba, 2000]. The relative magnitudes of these sources compared to the sensitivity of several magnetometers are shown in Figure 1.11. Housing the MEG system inside a magnetically shielded room (MSR) can attenuate external sources (as discussed in Chapter 3), but the biomagnetic interference still requires consideration.

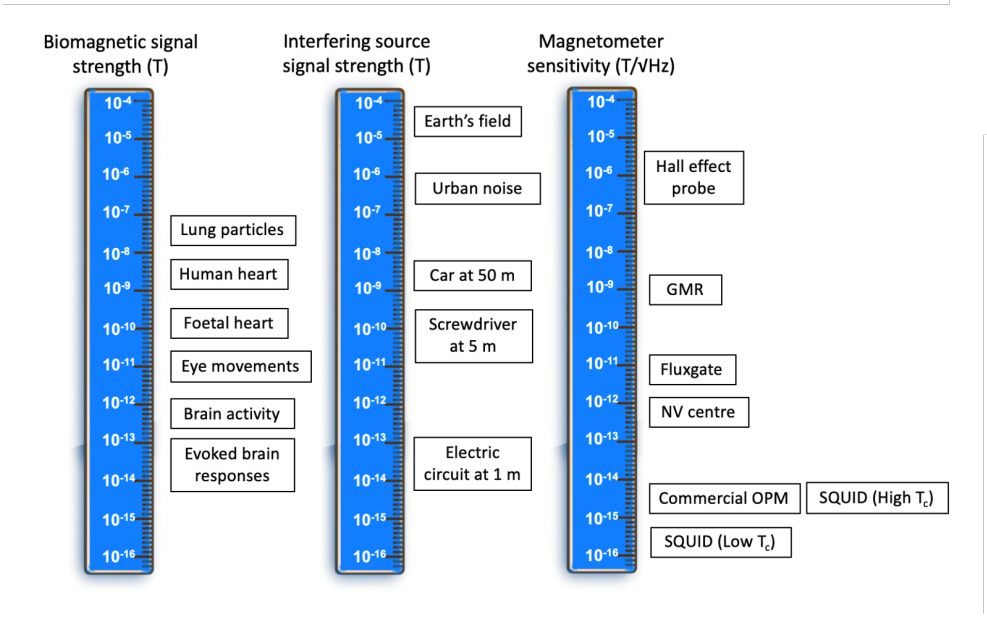



Figure 1.11: *Magnetic field strengths of biomagnetic signals, interfering sources and the sensitivity of various magnetometers. Values for biomagnetic and interfering sources taken from [Hämäläinen et al., 1993] and [Hansen et al., 2010]. Magnetometer sensitivities taken from [Seltzer, 2008].*

The MEG forward, and consequently inverse problem requires high-quality measures of the very small magnetic fields generated by the brain. Commonly used magnetometers such as Hall effect probes, giant magnetoresistance (GMR) sensors or fluxgates have a sensitivity of roughly 1 $\mu$T/$\sqrt{Hz}$, 1 nT/$\sqrt{Hz}$ and 0.1 pT/$\sqrt{Hz}$, respectively, which is insufficient for MEG experiments. The state-of-the-art sensor for measuring very weak magnetic fields in commercial and research applications is the superconducting quantum interference device (SQUID), which typically has a sensitivity of 2-5 fT/$\sqrt{Hz}$ [Vrba, 2000].

### 1.6.1 SQUIDs

SQUID sensors are the key components of current commercial MEG systems. The SQUID was first developed in 1964 [Jaklevic et al., 1964, Zimmerman et al., 1970] and the first MEG measurements were performed by Cohen in 1972 [Cohen, 1972]. Whole-head systems became the norm in the early 2000s [Vrba, 2000].

Superconductivity is a phenomenon arising when certain materials are cooled to a low enough temperature such that they have no electrical resistance. Current can then pass through the material unimpeded [Bardeen et al., 1957]. The temperature at which this occurs is material-dependent and referred to as the 'critical temperature' $T_c$. Superconductivity has vast applications such as in MRI where the continually flowing current in superconductive wires allows the generation of large magnetic fields, which would not be achievable with resistive electromagnets.

Described by the Bardeen, Cooper and Schrieffer (BCS) theory, electrons in the material 'pair-up' when the critical temperature is reached and can be described with a single macroscopic wavefunction, as many of these boson-like pairs can exist in the same quantum state [Bardeen et al., 1957]. In a ring of superconducting material the wavefunction is constant throughout the ring leading to the

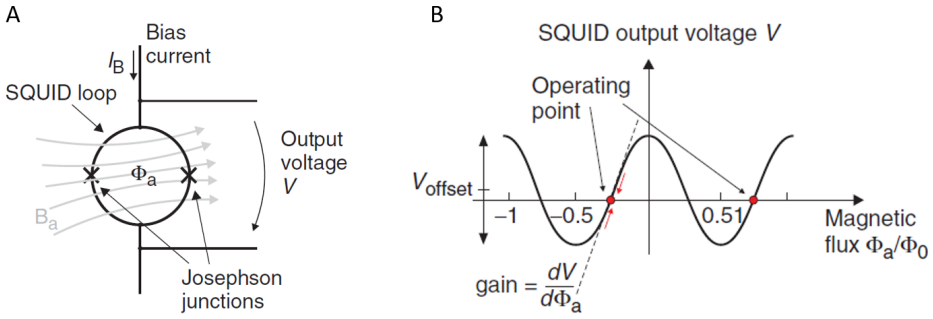



Figure 1.12: *Schematic and voltage characteristic of a SQUID formed from a superconducting ring broken by two Josephson junctions. A) An applied magnetic field $B_a$ results in an induced flux $\Phi_a$ inside the ring which can be measured if a known bias current $I_B$ is applied to the SQUID. B) In negative feedback operation the field dependent voltage is held around an operating point by applying a flux which opposes $\Phi_a$ to avoid ambiguous measurements of a periodic function. Figure adapted from [Hämäläinen et al., 1993] and [Hansen et al., 2010].*

quantisation of flux passing through it. This flux quantum is equal to $\Phi_0 = 2.07$ Wb and induces a current in the ring. This so-called 'shielding current' maintains a constant flux throughout the ring. The value of the shielding current depends on the applied flux and the inductance of the ring.

A measurement of the shielding current of a superconducting ring placed in a magnetic field would therefore provide a measure of the applied field, but doing so would break the ring and flux quantisation would disappear as the quantum coherence is destroyed. If however, the ring is broken by only a very thin layer of electrically insulating material then the wavefunction can tunnel through the insulator as shown in Figure 1.12A [Josephson, 1962]. These so-called Josephson junctions give rise to a flux-dependent resistance across the SQUID. If a known bias current is applied then a change in flux will be reflected in the voltage measured across the ring (see Figure 1.12) [Hansen et al., 2010].

The voltage versus flux characteristic of a SQUID is a sinusoidal function if the change in flux is less than an integer step of $\Phi_0$ [Hämäläinen et al., 1993].

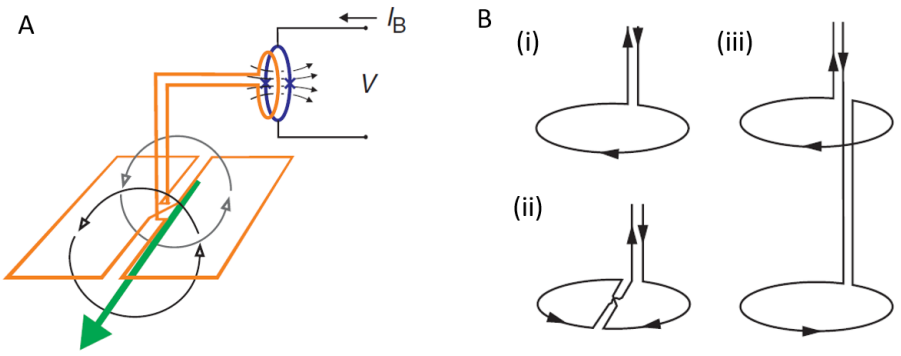



Figure 1.13: *Pickup coils and flux transformers to enhance sensitivity. A) The flux transformer allows the induced flux generated by a current (shown in green, e.g. from a neuron) to be gathered over a larger area by a pickup coil (orange) and then transferred to the SQUID (blue). B) Different pickup coil arrangements. i) simple magnetometer measuring the flux over a single loop. ii) Planar gradiometer which measures the difference in flux gathered by the two loops, this system is sensitive to sources directly beneath the coils and reduces the strength of interfering fields. iii) Axial gradiometer, the difference in field is measured at two points with increased radial separation from the head, again reducing the strength of interfering sources. Figure adapted from [Hansen et al., 2010]*

The periodic response of $\Phi_0$ makes a magnetic field measurement ambiguous [Hämäläinen et al., 1993]. As a result SQUIDs are often run in a negative feedback mode, where a 'flux-locked loop' involves applying additional flux that opposes the flux which is induced in the ring in order to keep the SQUID at a known operating point as shown in Figure 1.12B. The size of the feedback signal is therefore equivalent to the negative of the applied flux in the SQUID and can be used as a measure of the magnetic field [Hansen et al., 2010]. By operating SQUIDs in this mode, field values which exceed a single flux quantum can be measured.

To increase sensitivity, SQUIDs are generally inductively coupled to a superconducting pickup coil using a flux transformer, which can collect flux from a larger area (typically 1-2 cm) than a SQUID (around 1 mm) as shown in Figure 1.13A [Vrba, 2000, Vrba and Robinson, 2001]. Adding a second 'compensation' coil

connected in series with the pickup coil can decrease the effects of interfering sources. These 'gradiometer' configurations comprise two loops wound in opposite directions, such that the measured flux reflects the gradient of the magnetic field passing through the two coils [Vrba and Robinson, 2001]. Axial and planar gradiometers are shown in Figure 1.13B. Sources which are far away from the gradiometer produce fields that are nearly homogeneous in magnitude over the coils due to the slower rate of decay of magnetic fields and gradients with increasing distance from the source meaning a gradiometric measurement is almost zero. Fields from nearby sources (i.e. the brain signals) decay more quickly with distance and their gradient is larger and consequently their signal is boosted relative to that from distant sources of interference.

### 1.6.2 Commercial SQUID based MEG systems

Commercial systems contain around 200-300 sensors with the pickup coils and SQUIDs contained in a dewar filled with liquid helium as shown in Figure 1.14A [Hansen et al., 2010]. These dewars require filling with around 50-100 litres of liquid helium which has to be replenished as the supply boils off. A vacuum separates the dewar and sensors from the surface of the MEG system. The participant then places their head inside a 'helmet' which contains the pickup coils (the SQUIDs are displaced further inside the dewar) providing coverage of the whole brain.

The Canadian thin films (CTF) MEG system (CTF, Coquitlam, BC, Canada) at the University of Nottingham is shown in Figure 1.14B and contains 275 axial gradiometers as well as a reference array positioned away from the head, providing synthetic third-order cancellation of magnetic interference.

The head is localised within the helmet via head position indicator (HPI) coils attached to known reference points on the head of the participant [Gross et al.,

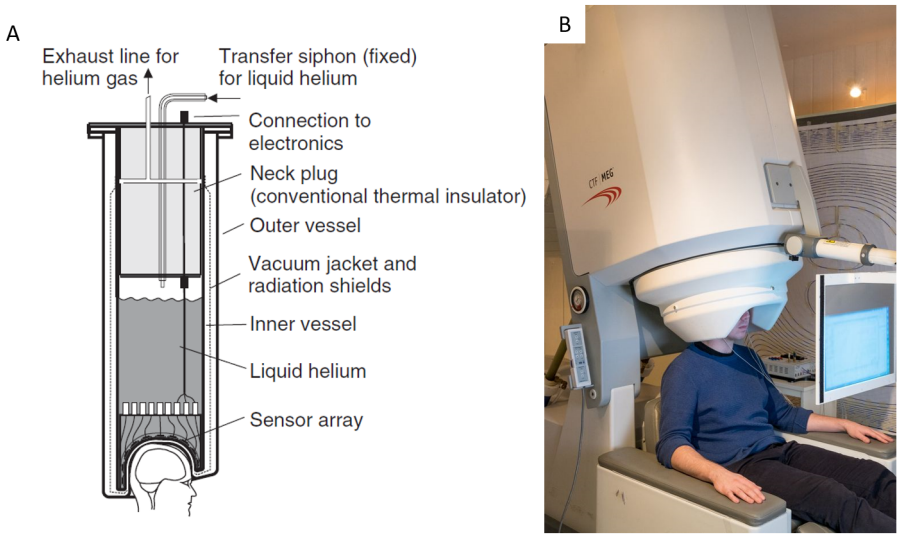



Figure 1.14: *Whole-head coverage MEG system. A) Sketch of the liquid helium dewar used to house the SQUIDs and the pickup coils. Adapted from [Hansen et al., 2010] B) The CTF-MEG system at the University of Nottingham with seated participant, the dewar can also be tipped so that the participant can be scanned supine.*

2013]. Current at a known frequency is passed through these coils generating a magnetic field. The data measured by the SQUIDs thus reveals the position of the HPI coils relative to the SQUID array. The head and HPI coil locations are digitised using either a Polhemus digitiser or optical methods and coregistered to the MRI, giving the position of the brain with respect to the sensors as required for inverse modelling [Gross et al., 2013]. This can either be done at the beginning and end of a scan to ensure the particpant has not significantly moved during a session or continuously so that the head position can be dynamically updated.

### 1.6.3 Limitations of SQUID systems

SQUID gradiometer configurations are commonly used in commercial MEG systems [Hansen et al., 2010, Gross et al., 2013]. This, along with the MSR allows for significant reduction of the magnetic field interference arising from unwanted

sources, thus maximising the brain signal and minimising the interference. However, the low $T_c$ materials require cryogenic cooling to a temperature of 4 K using liquid helium, placing several limitations on SQUID-based MEG systems:

- To ensure the surface of the helmet is at room temperature there must be a vacuum between the head and the pickup coils producing a minimum scalp to sensor distance of roughly 2 cm. This results in a decrease in signal magnitude with a $1/r^2$ dependence.
- As the sensors are fixed in position, the same system is used to scan all head sizes and consequently the scalp-to-sensor distance increases further for children, as a result of their smaller head-size. Signal-to-noise ratio therefore, is a function of head size making it difficult to scan children.
- The fixed sensor positions reduce the available paradigms due to the immovable nature of the system, making experiments addressing social interaction and spatial navigation challenging.
- The spatial frequencies of the measured fields are reduced due to the large scalp to sensor distance, again translating to a limiting factor in the spatial resolution that can be achieved.
- In a typical scan head movements of no more than $\approx 5$ mm are permitted [Gross et al., 2013]. Although several approaches for compensating for head movement within the confines of the helmet have been developed [Nenonen et al., 2012, Taulu et al., 2005, Wehner et al., 2008], large motion of the head away from the helmet remains a problem due to loss of signal, which cannot be compensated for in post-processing.
- Liquid helium is a costly and finite resource. Although modern systems have recycling facilities a refill is periodically required (two times a week, or once a year with a recycling system) resulting in significant running costs.

- MSRs are expensive and difficult to site, requiring a solid foundation in a large room to accommodate multiple metal layers.

As a result, it is desirable to develop a MEG system which is cost-effective and universal. The ability to scan across the lifespan from newborns to adults would provide a wealth of neuroscientific information. Scanning participants who cannot remain still during experiments such as most patient populations (especially those with Tourette's syndrome or Parkinson's disease) and infants would be of great interest. Although use of a MSR is most likely still a requirement, any reduction in operational or installation costs would permit greater takeup of MEG technology: for example, presently (2019) only 10 MEG facilities are currently operating in the UK but many more sites could benefit from access to a MEG system. On-scalp sensing of magnetic fields by a system which is tailored to the individual, based on a liquid-helium-free sensor could overcome these disadvantages.

## 1.7 On-scalp MEG

The variation in signal strength with source depth when measuring MEG signals is shown in Figure 1.15 for three cases: firstly, measuring the magnetic fields with detectors placed on the scalp, secondly with a detector positioned 2 cm from the scalp (as in the majority of cases for a SQUID sensor) and finally for a sensor placed 4 cm from the scalp (this spacing or even larger could occur for a child). The maximal measured field was calculated using the forward model parameters outlined in Section 1.4. An order of magnitude difference in magnitude is observed for these fairly small changes in scalp to sensor distance.

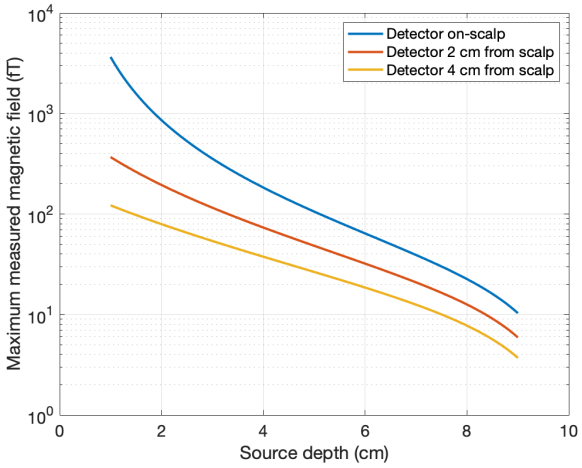



Figure 1.15: *The maximum magnetic field measured by a magnetic field sensor using a single-shell forward model for different scalp-to-sensor distances. The model assumes the head is a sphere of radius 10 cm with a dipole strength of 10 nAm. The measured field is plotted as a function of the source depth for depths of 1 cm to 9 cm.*

Quantitative studies into the benefits of recording MEG signals closer to the brain than can be achieved with SQUID-based systems have been performed in simulation. Boto and colleagues employed a beamformer study comparing the simulated data from a CTF-MEG system to a hypothetical on-scalp array. Results showed an increase in signal to noise ratio (SNR) by around a factor of 4 could be achieved if a detector with similar sensitivity to a SQUID could

be placed a few mm from the scalp surface [Boto et al., 2016]. Improvements in spatial resolution over the cortex were also observed due to the sampling of higher spatial frequencies that can be achieved.

Iivanainen and colleagues produced similar results comparing a Neuromag (Elekta, Stockholm, Sweden) whole-head, SQUID-based MEG system to simulated on-scalp arrays using BEM forward models and minimum-norm inversion methods. This work shows the theoretical improvements in SNR, spatial resolution and information content of the on-scalp array versus the SQUID system [Iivanainen et al., 2017]. These improvements are lesser for deeper sources, but still outperform SQUID systems in most cases.

In order to detect MEG signals on the scalp, a different type of magnetic field sensor is required, which is not limited by the need for liquid helium. From Figure 1.11 three candidate sensors are highlighted: the High-$T_c$ SQUID, the nitrogen vacancy (NV) centre and the optically pumped magetometer (OPM).

### 1.7.1 High $Tc$ SQUIDs

By forming the main ring of the SQUID with a material which has a higher $T_c$ than in a standard SQUID, the device can be cooled using liquid nitrogen instead of liquid helium. This increases the dewar temperature to 77 K and reduces the insulation requirements needed between the scalp and the sensor, resulting in around 1 mm separation [Andersen et al., 2017, Riaz et al., 2017]. Development of a 7-channel High-$T_c$ SQUID system is ongoing with evoked and induced responses being measured using devices with sensitivities of around 50 fT/$\sqrt{Hz}$ [Pfeiffer et al., 2019]. Whilst promising, such a system would still require a dewar for operation meaning that the subject would have to remain still, thus limiting its prospects in providing MEG measurements on infants or those with movement disorders.

### 1.7.2 Nitrogen vacancy centre

A nitrogen impurity at the site of a carbon atom inside a diamond leaves a vacancy in the lattice structure. This NV centre has a simple quantum structure which through the use of a microwave source and a laser can form a magnetically sensitive state with long coherence time at room temperature [Rondin et al., 2014]. NV centres have been used to perform magnetic resonance experiments with high spatial resolution, producing images of proteins and within a single cell [Shi et al., 2015, Wang et al., 2019]. A miniaturised version of the technology could be applied to on-scalp MEG, but the current sensitivity of >100 pT/$\sqrt{Hz}$ makes them ill-suited at present [Dale and Morley, 2017]. The requirement for a microwave source near the head of a participant is a potential disadvantage.

### 1.7.3 Optically pumped magnetometers

The OPM exploits the properties of a gas of alkali atoms via a process called optical pumping. A magnetically sensitive state can be prepared and interrogated using laser light [Budker and Jackson Kimball, 2011]. The OPM operates without cryogenic cooling, but requires heating to an atomic species dependent temperature (e.g. 150°C for Rubidium-87) in order to achieve coherence times suitable for magnetometry [Allred et al., 2002].

The first MEG measurements with an OPM occurred in 2006 [Xia et al., 2006] but recent developments in miniaturising OPMs have led to commercially available sensors (QuSpin Inc., Colorado, USA) with a scalp to sensor distance (6 mm), external temperature (<45°), footprint (13 mm × 9 mm), bandwidth (1-130 Hz) and sensitivity (<15 fT/$\sqrt{Hz}$) which are all suitable for on-scalp MEG [Shah et al., 2018]. The construction of a multi-channel, OPM-based, MEG system presents an exciting challenge.

# Chapter 2

# Optically-Pumped Magnetometers

## 2.1 Introduction

Optically-pumped magnetometers (OPMs) have the potential to vastly impact on the field of magnetoencephalography (MEG) and neuroscience in general [Boto et al., 2016, Iivanainen et al., 2017]. With flexible sensor placement, myriad opportunities for neuroscientific and clinical investigations on participants who are free to move become available. In order to develop an OPM-based MEG system, careful consideration of the physics which govern optical magnetic field measurements must be taken.

Optical magnetometers with high sensitivity were first developed in the 1960s by applying light sources which are resonant with atomic transitions to atomic populations. This generates a magnetically sensitive system which can be probed to obtain a measure of local magnetic field [Bell and Bloom, 1957, Bell and Bloom, 1961]. Optical magnetometers have been developed with a sensitivity which rivals, and sometimes exceeds, that of superconducting quantum interfer-

ence devices (SQUIDs), the state-of-the-art devices for detection of very weak magnetic fields [Dupont-Roc et al., 1969, Kominis et al., 2003]. Despite these achievements in sensitivity, early systems were bulky and required housing on an optical laboratory bench.

Recent developments in the field have allowed the miniaturisation of optical magnetometers and these have prompted an interest in applying the technology to MEG [Shah et al., 2007, Schwindt et al., 2007, Knappe et al., 2010]. Significant advancements in microfabrication techniques have lead to multiple sensor designs, all with noise levels on the order of a few tens of femtotesla, comparable in most cases with the noise levels of a SQUID.

The first MEG measurement using OPMs which was reported was of an auditory evoked response in 2006 [Xia et al., 2006]. Multiple MEG experiments have since been performed, involving measurement of evoked effects following auditory or somatosensory stimulation [Borna et al., 2017, Boto et al., 2017, Johnson et al., 2013, Johnson et al., 2010, Sander et al., 2012]. Changes in the alpha and beta rhythms have also been observed [Boto et al., 2017, Kamada et al., 2015, Sander et al., 2012]. OPMs have also been used to detect biomagnetic signals generated by both adult [Bison et al., 2009, Kamada et al., 2012] and foetal heartbeats [Batie et al., 2018].

The final step towards realising the potential of OPMs as a neuroscientific tool was the commercialsiation of sensors leading to production in large quantities such that whole-head MEG systems can be built. QuSpin Inc. (Louisville, Colorado, USA) was setup in 2012 as a spin-out company from sensor-development work performed at the National Institute of Standards and Technology (NIST) and are producing commercially available, off-the-shelf OPMs, with the sensitivity needed to perform MEG experiments [Shah et al., 2018]. FieldLine Inc. (Boulder, Colorado, USA) are also manufacturing OPMs for MEG applications,

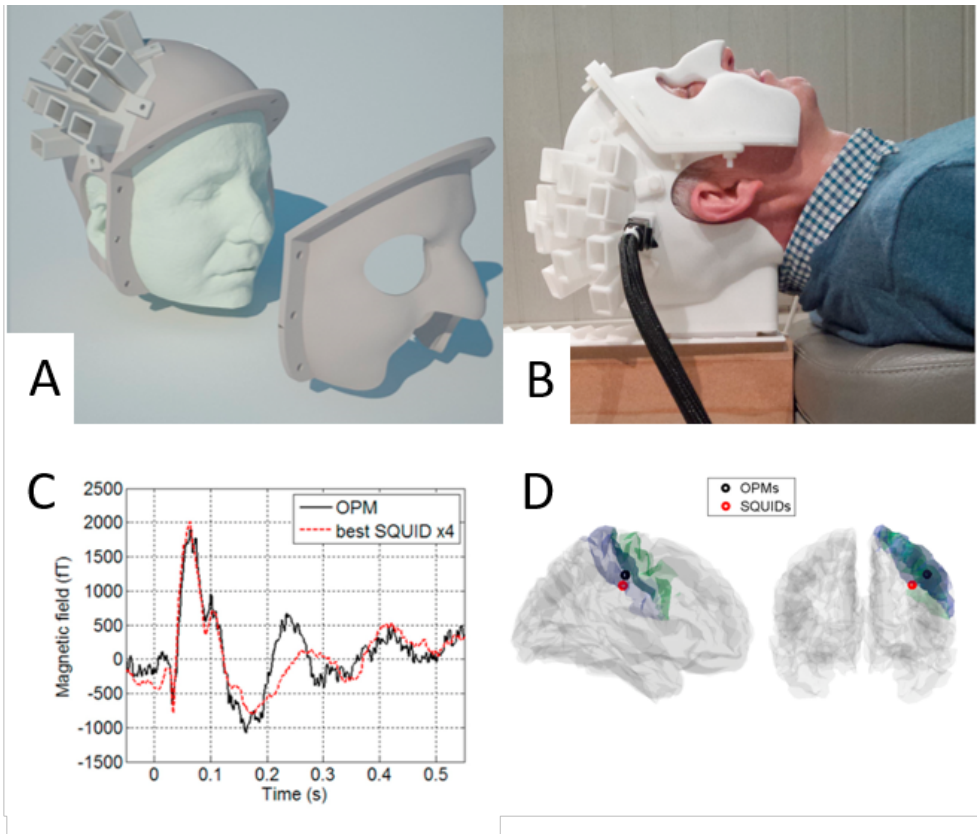



Figure 2.1: *On-scalp MEG recordings made with a single QuSpin OPM sensor. A) The scanner-cast designed based on the MRI scan of a participant with 13 slots for OPM placement. B) Participant lying down wearing the scanner-cast with OPM (thick black cable). C) The evoked response obtained via stimulation of the median nerve, the OPM signal is four times the size of the SQUID sensor with the highest magnitude. D) Source localisation comparing SQUID recordings to the OPM recording showing good agreement. Figure adapated from [Boto et al., 2017].*

though this thesis concentrates on the QuSpin device. Through the availability of such devices the construction of a multi-channel MEG system based on a standard, reproducible magnetic field sensor is achieveable.

Boto and colleagues used a single QuSpin OPM sensor placed inside a 'scanner-cast' to perform source-localised measurements of an evoked response generated via stimulation of the median nerve [Boto et al., 2017]. The scanner-cast was 3D-printed based on a magnetic resonance imaging (MRI) scan of a participant such that the sensor position and orientation with respect to the brain was known, as shown in Figure 2.1A. They moved a single sensor across 13 different positions and

recorded brain activity produced by median nerve stimulation at each position (Figure 2.1B). An increase in signal of four times was observed when comparing results to a SQUID recording as shown in Figure 2.1C. Through combining all 13 datasets, source localisation was achieved as shown in Figure 2.1D.

This chapter outlines the relevant theory which governs the principle of operation of the QuSpin sensor allowing detection of weak magnetic fields around a zero-field resonance.

## 2.2 The QuSpin OPM

OPMs exploit the quantum mechanical property of spins in an ensemble of alkali atoms to measure very small magnetic fields [Budker and Jackson Kimball, 2011]. The QuSpin OPM is a vector magnetometer with a simple operational procedure [Shah et al., 2018]:

- A vapour of alkali atoms is formed inside a glass cell via heating.
- Optical pumping is used to prepare the ensemble of atoms in a magnetically sensitive state by placing a laser such that its circularly-polarised beam passes through the cell; the angular momentum of the laser light is transferred to the single unpaired electron of the alkali metal atom which drives a transition between energy levels.
- Once all the spins in the system have been 'optically pumped' the absorption of the laser light is minimised; the intensity of the transmitted laser light is detected on the other side of the glass cell by a photodetector and is maximal when the ensemble has been optically pumped.
- This so-called 'dark state', where the atoms do not interact with the circularly polarised laser light source, only exists when the magnetic field experienced by the cell is precisely zero in the direction perpendicular to the laser beam.
- If the cell is in a non-zero magnetic field environment then the atoms in the ensemble interact with the field and then are re-pumped, resulting in a drop in the intensity of the transmitted laser light.
- By monitoring the intensity of the transmitted light using a photodiode, the magnetic field experienced by the atoms can be inferred. The photodiode signal is referred to as a zero-field resonance with a Lorentzian line shape.

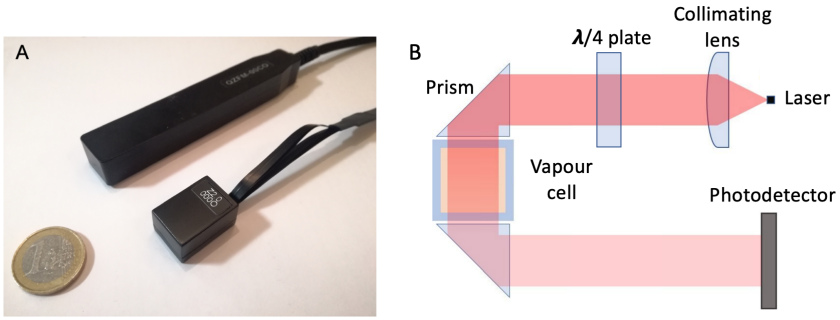



Figure 2.2: *The QuSpin OPM. A) Housings of the Gen-1 and Gen-2 QuSpin zero-field magnetometers, a coin is shown in the picture for size reference. B) Operational diagram of the OPM. Laser light is collimated and reflected through a glass cell containing a vapour of alkali atoms. Some light is absorbed and the rest passes through the cell to a photodetector. The magnetic field experienced by the cell can be inferred by monitoring the change in intensity of the light. Figure adapted from [Shah et al., 2018].*

The first generation QuSpin OPMs contain a $3 \times 3 \times 3$ mm$^3$ glass cell which is filled with rubidium-87 ($^{87}$Rb) atoms. This cell is housed in a sensor head which has dimensions of $13 \times 19 \times 110$ mm$^3$ and sits 6 mm from the external face of the unit. Second generation QuSpin OPMs which follow the same principle of operation but have a smaller sensor head with dimensions $12.4 \times 16.6 \times 24.4$ mm$^3$ are also available. Sensor housings are shown in Figure 2.2 A.

The cell is resistively heated to 150°C to produce a vapour with a high number density of rubidium atoms. A diode laser which emits light of wavelength 795 nm is also placed in the sensor head and provides the optical pumping. The laser light is circularly polarised, collimated and reflected through 90 degrees before passing through the cell, a second reflection directs the beam to a photodiode which monitors the intensity of the transmitted laser light. This process is shown in Figure 2.2 B.

The sensor head also contains three orthogonal coils around the cell. In two directions these coils are formed from pairs of rectangular coils connected in series. A single rectangular coil is then used along the radial axis in the Gen-1

sensor, the Gen-2 sensor has three pairs of coils. Currents are applied to the coils to generate $B_x$, $B_y$ and $B_z$ fields which offset background magnetic fields up to 50 nT in magnitude via an automated 'field-zeroing' process [Shah and Hughes, 2015]. A modulation signal is applied to the cell using these coils in order to gain directional sensitivity.

The sensor head is attached to a cable of 6.5 m length, which runs to an electronics box. Communication with the sensor electronics for system setup is achieved via a USB virtual serial port.

## 2.3 Optical Pumping

Optical pumping is the process via which the alkali atoms can be prepared in a magnetically sensitive state. It involves the transfer of angular momentum from the laser light to the atoms such that a large fraction of the atoms subsequently occupy the same energy level [Happer, 1972]. The total angular momentum of an atom ($\boldsymbol{F}$) is a vector quantity with magnitude given by $|\boldsymbol{F}| = \sqrt{F(F+1)}\,\hbar$ where $F$ is an integer dimensionless quantum number (similar relationships hold for the other angular momenta) and is described as the sum of the nuclear angular momentum ($\boldsymbol{I}$) and the electron angular momentum ($\boldsymbol{J}$) as

$$\boldsymbol{F} = \boldsymbol{J} + \boldsymbol{I}, \tag{2.3.1}$$

where, for $^{87}$Rb the nuclear spin quantum number is $I = 3/2$. The angular momentum of the electron is then further comprised of its orbital angular momentum ($\boldsymbol{L}$) and its spin ($\boldsymbol{S}$) as

$$\boldsymbol{J} = \boldsymbol{L} + \boldsymbol{S}. \tag{2.3.2}$$

Considering just the single valence electron of the $^{87}$Rb atom, its ground state has orbital angular momentum described by the quantum number $L = 0$ and the first excited state has $L = 1$. The electron has spin described by the spin quantum number $S = 1/2$.

As well as the orbital structure of the atomic energy levels, fine structure appears due to interaction between the spin and the orbital angular momentum. The allowed values of the quantum number $J$ are found by taking integer steps in the range $|L - S| \leq J \leq |L + S|$. Using this formalism, the $L = 0$ state has only a single fine structure level at $J = 1/2$, but when $L = 1$ two levels are obtained

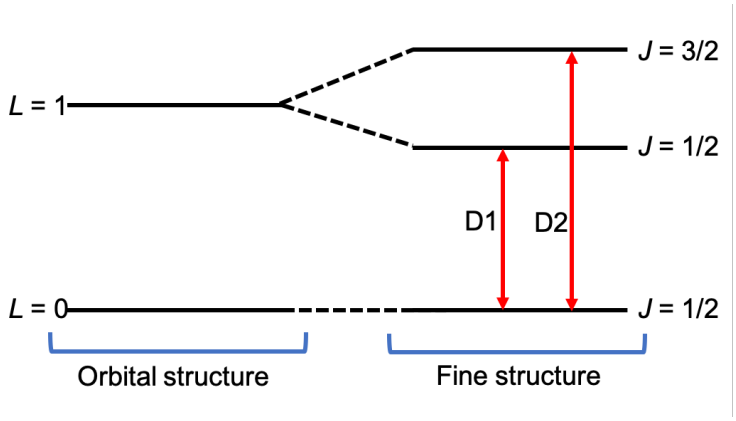



Figure 2.3: *Fine structure. Splitting of the orbital energy levels of the ground and first excited state due to interaction between the electron spin and orbital angular momentum for an alkali atom. The D1 and D2 transitions between states occur when a photon of light with a specific energy is absorbed by an atom.*

with $J = 1/2$ and $J = 3/2$. As a result, two transitions exist from the ground state ($L = 0$, $J = 1/2$). The transition to the first excited state ($L = 1$, $J = 1/2$) is labelled the D1 transition, whilst the transition to the second excited state ($L = 1$, $J = 3/2$) is the D2 transition. The fine structure splitting of the orbital energy levels is shown in Figure 2.3.

Transitions can occur if the electron absorbs energy from a photon of laser light that is equal to the energy difference between the ground state and the excited state. The energy of a single photon is calculated as

$$E = h\nu = \frac{hc}{\lambda} \tag{2.3.3}$$

Where, $h$ is Planck's constant, $\nu$ is the frequency of the incident light, $c$ is the speed of light in a vacuum and $\lambda$ is the wavelength of the incident light. For the D1 transition of $^{87}$Rb the required wavelength is 795 nm (the wavelength used by the laser in the QuSpin sensor).

Interactions between the electron ($S$) and nuclear ($I$) spins results in additional splitting of the fine structure levels into the hyperfine structure of the energy

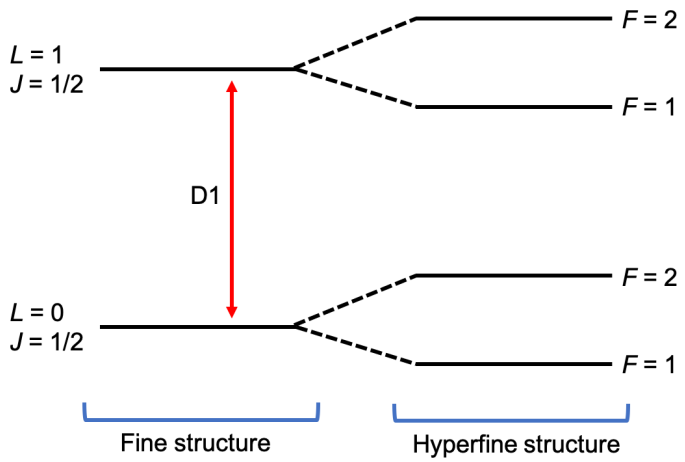



Figure 2.4: *Hyperfine structure. Splitting of the fine structure states in the ground and excited states due to interaction between electron and nuclear spins. Shown here for the D1 transition only.*

levels, since $\boldsymbol{F} = \boldsymbol{I} + \boldsymbol{J}$. Restricting the analysis to the D1 transition of rubidium where in the ground state and the excited state $J = 1/2$ and $I = 3/2$, the hyperfine structure is split into levels where $F = I \pm J$, i.e. there are $F = 1$ and $F = 2$ hyperfine levels for the ground and excited states. These hyperfine levels are shown in Figure 2.4.

A final splitting of the energy levels occurs following an interaction of the atom with an external magnetic field, the Zeeman splitting. This additional splitting of the hyperfine levels occurs along a quantisation axis which, with approximately zero applied magnetic field, is the direction of the laser beam as it passes through the atomic vapour. The projection is described in steps of $m_F = [-F, -F + 1, \ldots, F - 1, F]$ resulting in $m_F = [-1, 0, 1]$ for the $F = 1$ hyperfine states and $m_F = [-2, -1, 0, 1, 2]$ for the $F = 2$ hyperfine states as shown in Figure 2.5.

The energy difference due to Zeeman splitting between adjacent $m_F$ states is given by

$$\Delta E = g_F \mu_B B, \tag{2.3.4}$$

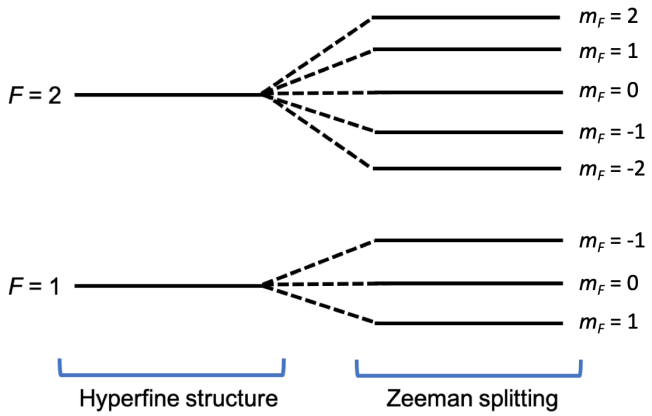



Figure 2.5: *Zeeman splitting. Further splitting of the energy levels of the hyperfine states due to interaction with a magnetic field.*

where $g_F$ is the hyperfine Lande g-factor, $\mu_B$ is the Bohr magneton and $B$ is the magnetic field. The electron spin precesses in this magnetic field at the Larmor frequency,

$$\omega = \gamma B \tag{2.3.5}$$

where $\gamma$ is the gyromagnetic ratio, which for the unpaired electron in $^{87}$Rb is given as

$$\frac{\gamma_F}{2\pi} = \frac{g_F \mu_B}{\hbar}. \tag{2.3.6}$$

For $^{87}$Rb in the $F = 1$ state $g_F = -1/2$, and for the $F = 2$ state $g_F = +1/2$. Note that with opposite signs of $g_F$, the $F = 1$ and $F = 2$ states precess in opposite directions with

$$\left|\frac{\gamma_F}{2\pi}\right| = 7 \text{ Hz/nT}. \tag{2.3.7}$$

A D1 transition is induced following exposure of the valence electron to the 795 nm laser light. If circularly polarised light (i.e. light in which all photons have the

same spin projection along the beam propagation direction) then additional angular momentum is transferred to the atom. Photons in a right-handed circularly polarised light beam all have angular momentum of +1 along the beam direction and can induce transitions which obey a selection rule such that a transfer of angular momentum $\Delta m_F = m_{Ffinal} - m_{Finitial} = +1$ will occur.

After absorption of laser light the atom will return to the ground state following emission of photon. Once the atom has returned to the ground state it can then be re-pumped provided the selection rule can still be obeyed. This process repeats for all atoms in the ensemble eventually driving atoms into a state with the highest spin angular momentum ($F = 2$, $m_F = +2$) as shown in Figure 2.6. This final state is the so-called 'dark state' of the atom where it does not absorb the laser light, as any further transitions would violate the selection rules of the system. The intensity of light detected at the photodiode will be a maximum when all atoms are in this dark state.

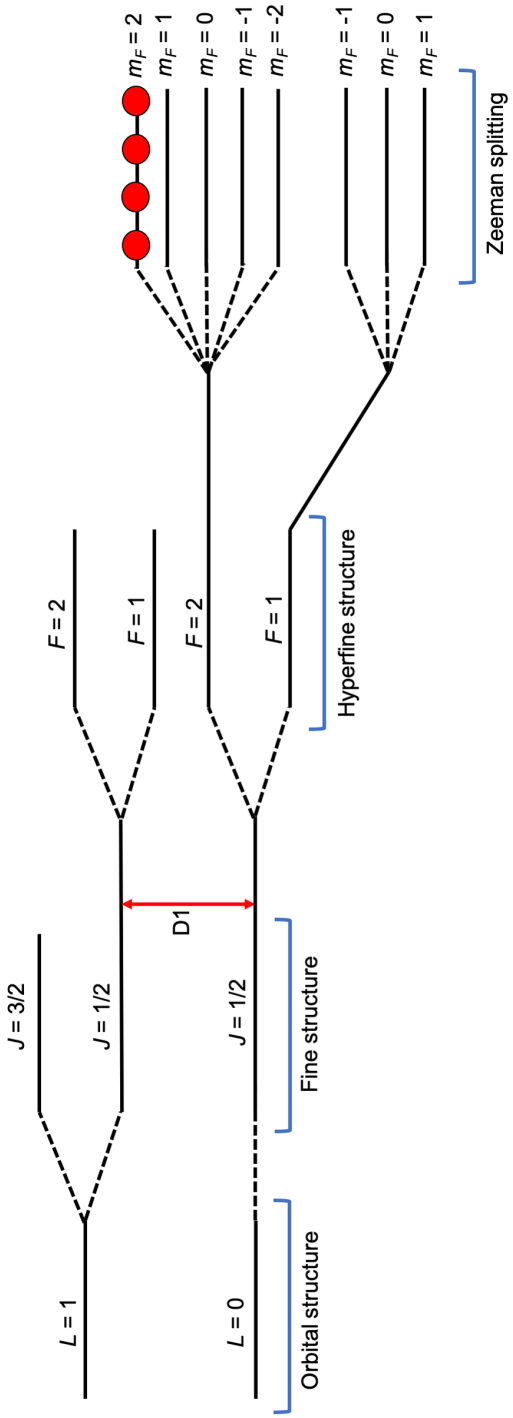



Figure 2.6: *Optical pumping. Energy level diagram capturing the final state of atoms (red circles) following optical pumping on the D1 transition line with left handed circularly polarised light.*

## 2.4 Maintaining spin polarisation

Atomic magnetometers rely on coherent precession of the ensemble of spins inside the cell in a magnetic field to make measurements. This coherence needs to be maintained over meaningful timescales to form the basis of a useful sensor.

The coherence of the precessing spins within the system can be destroyed via several processes including spin-exchange collisions between atoms, spin destruction collisions, collisions of atoms with the walls of the glass cell and interactions with the laser [Kornack, 2005]. Here, particular focus is given to the spin-exchange collisions as they are considered to be the dominant factor which limits the sensitivity of atomic magnetometers [Savukov and Romalis, 2005].

A spin-exchange collision between two Rubidium atoms preserves the total angular momentum, (i.e. the sum of $m_F$ of the two atoma before and after the collision is equal) but may change the hyperfine levels of the atoms as shown in Figure 2.7 [Savukov and Romalis, 2005]. In this example, two spins initially point in the same direction and precess in the same direction since they are in the same $F$-state. After the spin-exchange collision, one of the spins changes its $F$-state and now precesses in the opposite direction due to the change in sign of the gyromagnetic ratio between the $F = 1$ and $F = 2$ states. This difference in precessional frequency contributes to the decoherence of the system. The relaxation rate due to spin-exchange collisions, $R_{se}$, is given as

$$R_{se} = \frac{1}{T_{se}} \tag{2.4.1}$$

where $T_{se}$ is the time between spin-exchange collisions.

In the case where the atoms within the cell experience a low magnetic field, and there is a sufficient atomic density (typically $10^{14}$ atoms are present in a cell of

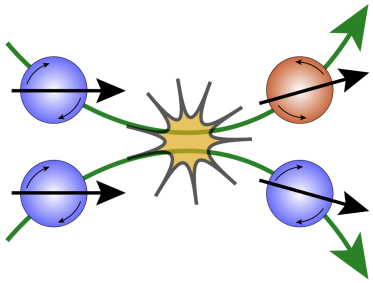


Figure 2.7: *Spin-exchange collisions. Following a spin-exchange collision, the total angular momentum is conserved but the atoms may switch between the $F = 1$ and $F = 2$ (denoted by red and blue) hyperfine levels which precess in opposite directions causing decoherence. Figure taken from [Seltzer, 2008].*

volume $3 \times 3 \times 3$ mm$^3$), a high spin exchange rate can be achieved such that

$$R_{se} \gg \gamma_e B. \tag{2.4.2}$$

Here, $\gamma_e$ is the isolated electron gyromagnetic ratio given as

$$\frac{\gamma_e}{2\pi} = \frac{g_s \mu_B}{\hbar} = 28 \text{ Hz/nT}, \tag{2.4.3}$$

where $g_s \approx 2$ is the Lande $g$-factor for an electron.

With a high rate of spin-exchange collisions, the atoms rapidly switch between the $F = 1$ and $F = 2$ states which have opposing precessional frequencies as shown in Figure 2.8. Although the atoms precess by a small amount each time, there are more $F = 2$, $m_F$ sub-levels which leads to a coherent, net positive precession of the spins at a slightly decreased precessional frequency given as [Kornack, 2005, Savukov and Romalis, 2005]

$$\omega_0 = \frac{\gamma_e B}{Q(P)}, \tag{2.4.4}$$

where $Q(P)$ is referred to as the nuclear slowing down factor which captures the

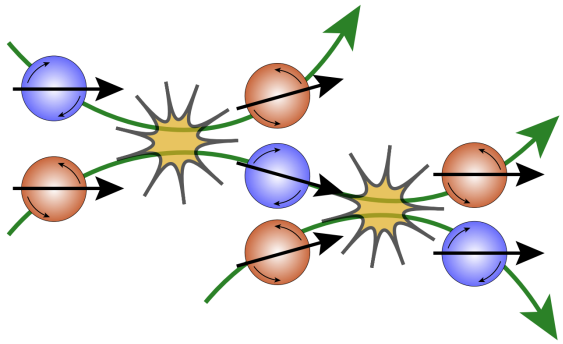


Figure 2.8: *Spin-exchange relaxation free regime. With a high density of atoms, and a low magnetic field, the time between spin-exchange collisions is much shorter than the period of the precessional frequency. The atoms rapidly switch between hyperfine levels, causing a coherent precession of the $F = 1$ and $F = 2$ states (denoted by red and blue). Figure taken from [Seltzer, 2008].*

decrease in the precessional frequency. $Q(P)$ is a function of the total polarisation of the system.

If the system is fully polarised, with all the atoms in the highest angular momentum state ($m_F = 2$ of the $F = 2$ hyperfine state), then spin-exchange collisions have no effect at re-distributing the spins, because the other $m_F$ levels cannot accommodate that amount of angular momentum. When the polarisation of the system decreases, and the distribution of spins across the $m_F$ levels increases, the value of $Q(P)$ becomes larger due to the atoms rapidly moving between the two hyperfine levels, decreasing the average precessional frequency.

For $^{87}$Rb (where $I = 3/2$) the slowing down factor is expressed as [Appelt et al., 1998, Seltzer, 2008]

$$Q(P) = \frac{6 + 2P^2}{1 + P^2}, \tag{2.4.5}$$

such that for an unpolarised system, $Q(P = 0) = 6$ and $Q(P = 1) = 4$ for a polarised system.

This coherently precessisng polarisation following suppresion of decoherence due

to spin-exchange collisions is the basis of a spin-exchange relaxation free (SERF) magnetometer [Allred et al., 2002]. With the suppression of spin exchange, SERF magnetometers have dramatically longer coherence times, and can be operated at much higher atomic densities increasing the signal size.

## 2.5 Bloch equations of spin polarisation

The spin polarisation, $\boldsymbol{P}$ which is established in the SERF regime is sensitive to changes in the magnetic field experienced by the cell. As in MRI, the behaviour of the polarisation can be described via the Bloch equations [Bloch, 1953]. In this case, the rate of change of the polarisation with time is given as [Ledbetter et al., 2008, Shah and Romalis, 2009]:

$$\frac{d\boldsymbol{P}}{dt} = \frac{1}{Q(P)}\left[\gamma \boldsymbol{P} \times \boldsymbol{B} - (\boldsymbol{P} - P_0\ \hat{\boldsymbol{z}})\frac{1}{T}\right], \tag{2.5.1}$$

where $\gamma = \gamma_e$ is the gyromagnetic ratio of the electron, $Q(P)$ is the nuclear slowing down factor, $T$ is a time constant which characterises the effects of the optical pumping rate ($R$) and the relaxation ($T_2$) of the system (mainly due to spin-exchange and spin destruction collisions), taking the form $T = (R + 1/T_2)^{-1}$. $P_0$ is the equilibrium polarisation obtained due to optical pumping when the magnetic field experienced by the cell is zero.

In this instance, it is assumed that the pumping laser beam is oriented along the $z$-axis, so the light transmitted through the cell is sensitive to the vector component of the polarisation $P_z$. Expanding the equation in the steady state ($d\boldsymbol{P}/dt = 0$) into vector components gives

$$\begin{aligned} P_x &= \frac{B_y/(\gamma T) + B_x B_z}{(1/(\gamma T)^2 + B_x^2 + B_y^2 + B_z^2} P_0' \\ P_y &= \frac{-B_x/(\gamma T) + B_y B_z}{(1/(\gamma T)^2 + B_x^2 + B_y^2 + B_z^2} P_0' \\ P_z &= \frac{(1/(\gamma T)^2 + B_z^2}{(1/(\gamma T)^2 + B_x^2 + B_y^2 + B_z^2} P_0', \end{aligned} \tag{2.5.2}$$

where $P_0' = P_0 RT$. For a vector magnetometer measuring field changes along the axis which is perpendicular to the laser ($x$ in this case), we set the values of $B_y$

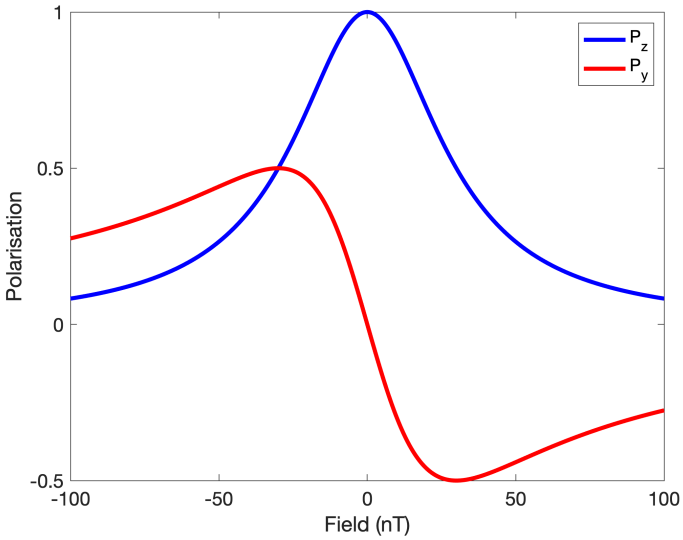



Figure 2.9: *Solution to the Bloch equations in the steady state. The polarisation along the z-direction has the form of a Lorentzian zero-field resonance curve whilst the polarisation along the y-direction has the form of a dispersion curve. The magnetic field $B_x$ can be inferred from these curves. As in the QuSpin sensor the value of $1/\gamma T$ was set to 30 nT.*

and $B_z$ to zero, thus simplifying the above to

$$\begin{aligned} P_x &= 0 \\ P_y &= \frac{-\gamma T B_x}{1+(\gamma T B_x)^2} P_0' \\ P_z &= \frac{1}{1+(\gamma T B_x)^2} P_0' \end{aligned} \tag{2.5.3}$$

If $P_z$ is evaluated as a function of $B_x$ then a Lorentzian lineshape is obtained. This is the zero-field resonance of the system. The full width at half maximum of the Lorentzian is given as $2/\gamma T$ (which takes a value of around 30 nT for the QuSpin sensors). $P_y$ when evaluated as a function of $B_x$ has the form of a dispersion curve. Both lineshapes are shown in Figure 2.9. Although the Lorentzian contains magnetic field information, the systems are sensitive to low-frequency 1/f noise, and the symmetric lineshape makes it difficult to distinguish between positive and negative magnetic fields [Shah et al., 2018].

The addition of an oscillating magnetic field in the direction to which measurement sensitivity is required (i.e. $B_x$) can be used to obtain a more accurate measurement of magnetic field [Cohen-Tannoudji et al., 1970, Kastler, 1973]. The relaxation rate of the atomic vapour is of the order 100 Hz (which also defines the bandwidth of the sensor). Modulating the amplitude of the polarisation at a frequency much larger than this relaxation rate (923 Hz is used in the QuSpin sensors) is done by applying an oscillating current to electromagnetic coils which surround the cell. The total field experienced by the cell therefore features an oscillating term with magnitude $b_x$, described as $\boldsymbol{B}_{mod} = b_x \cos(\omega t)\ \hat{\boldsymbol{x}}$, where $\omega$ is the angular frequency of the modulation. In this case, the expression for the rate of change of polarisation is re-defined as

$$\frac{d\boldsymbol{P}}{dt} = \frac{1}{Q(P)}\left[\gamma \boldsymbol{P} \times [\boldsymbol{B} + b_x \cos(\omega t)\ \hat{\boldsymbol{x}}] - (\boldsymbol{P} - P_0\ \hat{\boldsymbol{z}})\frac{1}{T}\right] \tag{2.5.4}$$

Now the previously defined steady state solution is invalid due to the time-varying term in $B_x$. Evaluation of the polarisation $P_z$ in this case (still assuming $B_y = B_z = 0$) gives a value of [Shah and Romalis, 2009, Tierney et al., 2019]

$$P_z = \frac{\gamma T B_x}{1 + (\gamma T B_x)^2}\ J_0\Big(\frac{\gamma b_x}{Q(P)\ \omega}\Big) J_1\Big(\frac{\gamma b_x}{Q(P)\ \omega}\Big)\ P_0' \sin(\omega t), \tag{2.5.5}$$

where $J_n$ are Bessel functions of the first kind. These functions are evaluated to a constant term depending on the ratio of $\gamma b_x / Q(P)$ to $\omega$, and the effect of all constants can be combined into a constant of proportionality. Lock-in detection of the photodiode voltage, $V$, at the known modulation frequency allows detection of the final signal of the form

$$V \propto \frac{\gamma T B_x}{1 + (\gamma T B_x)^2} \tag{2.5.6}$$

Evaluation of $V$ as a function of the magnetic field $B_x$ shows a dispersion curve

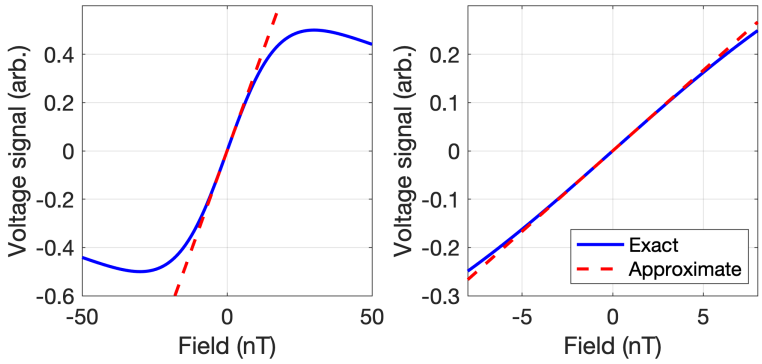



Figure 2.10: *Voltage signal measured by the OPMs following lock-in detection at the modulation frequency. Evaluation of the solution as a function of applied magnetic field is shown for the feild ranges ± 50 nT and ± 8 nT. The solution is approximately linear over a small field range around zero field. Large magnetic field values result in a decrease in linearity of the response and ultimately lead to a loss of sensitivity to magnetic field.*

response, which distinguishes between positive and negative fields in a region around zero field where $V(B_x)$ is approximately linear. The modulation shifts detection away from the low-frequencies avoiding the issues presented by the steady state solution. Taking the Taylor expansion of $V(B_x)$ gives the linear form of the equation in the regime where $\gamma B_x T << 1$ as

$$V \propto \gamma T B_x \tag{2.5.7}$$

This linearity allows for magnetic field to be easily interpreted by a simple field per unit voltage calculation. For QuSpin sensors, the range of this linear region is around ± 5 nT as is shown in Figure 2.10.

The bandwidth of the OPM is fundamentally determined by the relaxation time constant $T$ which for the QuSpin sensor is around 100 Hz. Whilst biomagnetic

signals generated by the brain exceeding 100 Hz in frequency are present, they are not usually investigated [Baillet, 2017]. Signals which pass through nerves in the spine with a frequency >1 kHz are of interest in magnetospinography (MSG) [Curio et al., 1991, MacKert et al., 1998].

Larger values of magnetic field push the magnetometer signal away from the linear region around zero magnetic field. At higher magnetic field the linear form of the equation is no longer accurate and errors in the measured magnetic field will be acquired. This is interpreted as a change in the sensor gain. For QuSpin sensors the sensor gain changes over a $\pm 1.5$ nT range by 5% [Boto et al., 2018]. Expanding this to $\pm 5$ nT affects the sensor gain even further inducing gain changes up to 10% [Shah et al., 2018].

## 2.6 Sensor array operation

Each QuSpin OPM is attached to an electronics unit (which is common to Gen-1 and Gen-2 sensors) as outlined in Figure 2.11. Interfacing with each sensor is achieved via a USB connection to a micro-controller built into the unit. QuSpin software initialises the OPM by applying current to a resistive heater around the vapour cell to achieve the required spin density, the laser is powered on and stabilised to the correct frequency and the modulation signal is generated. The voltage signal which gives a measure of magnetic field is measured from the analogue output of each unit.




Figure 2.11: *The OPM sensor and electronics, a 6.5 m cable attaches the sensor to an electronics unit (one unit per sensor). (a) Outputs the modulation signal to another sensor in the array. (b) Input of the modulation signal from another sensor in the array. (c) If the unit is a master unit the modulation used by the entire array is generated here. (d) The analogue output of the sensor which can be sample at high-frequency. (e) The USB connection to the electronics. (f) Programmer port used to update firmware and other system parameters. (g) Mains power connection. (h) Power switch. (i) Sensor indicator LEDs which show the laser status, cell temperature status and whether the field around the cell is zero. These indicators are mirrored in the software. (j) Sensor connector.*




Figure 2.12: *Master/slave configuration for array operation. The modulation signal as generated by the master unit is output to the slave unit using a series of audio cables. This 'daisy chaining' procedure is repeated along the array such that all OPMs use the same modulation field.*

For MEG, an array of multiple OPMs must simultaneously record magnetic fields at multiple positions around the head. In order to obtain meaningful data, the 923 Hz modulation signal must be common to all sensors, as slight differences in the amplitude or phase of the signals generated by different units could affect the recordings. This is achieved by passing the modulation signal generated by a single 'master' unit to all other units which are designated as 'slaves'. This setup is shown in Figure 2.12.

The voltage-to-field calibration must also be constant across sensors. To achieve this a known field is applied by the on-sensor coils to calibrate the analogue outputs. Three analogue output gain settings are available: the standard 1× gain is 2.7 V/nT which provides a dynamic range of ±1.5 nT over a ±4 V range. Additional settings of 3× gain (8.1 V/nT) and 0.33× gain (0.9 V/nT) gain are available with dynamic ranges of ±0.5 nT and ±4.5 nT, respectively. A lower output gain allows for a wider dynamic range, but (as the loss in analogue to digital converter (ADC) precision can be compensated for with an increased sampling rate) measuring larger magnetic fields may impact on the sensor gain

as the measurement moves away from the linear region of the response as shown in Figure 2.10.

Interference, commonly referred to as 'cross-talk', between sensors can arise when the field generated by the modulation coils on one sensor is detected by a nearby OPM. These signals have an effect on both the sensor gain and the sensitive direction, meaning a radial measurement of magnetic field may be slightly off-axis [Boto et al., 2018, Tierney et al., 2019]. Modelling this interference in order to remove its effects from measured data is possible, and improved coil designs with field profiles which decrease the size of the interference can reduce its effects [Nardelli et al., 2019]. Cross-talk was not considered for any of the measurements in this work.

Following the setup of a multi-channel array, measurements of the magnetic field can be obtained. The OPM sensors themselves can record data at a rate of 200 Hz through the USB connection. Higher frequency measurements can be made by sampling the analogue output of each sensor with an ADC. An estimate of the sensor noise-level can be obtained by recording magnetic fields from stationary sensors placed inside an empty MSR. Figure 2.13 shows an example recording on an array of 5 OPMs revealing their noise level to be <15 fT/$\sqrt{Hz}$ from around 5-100 Hz. Higher noise levels at lower frequencies are apparent in the data.

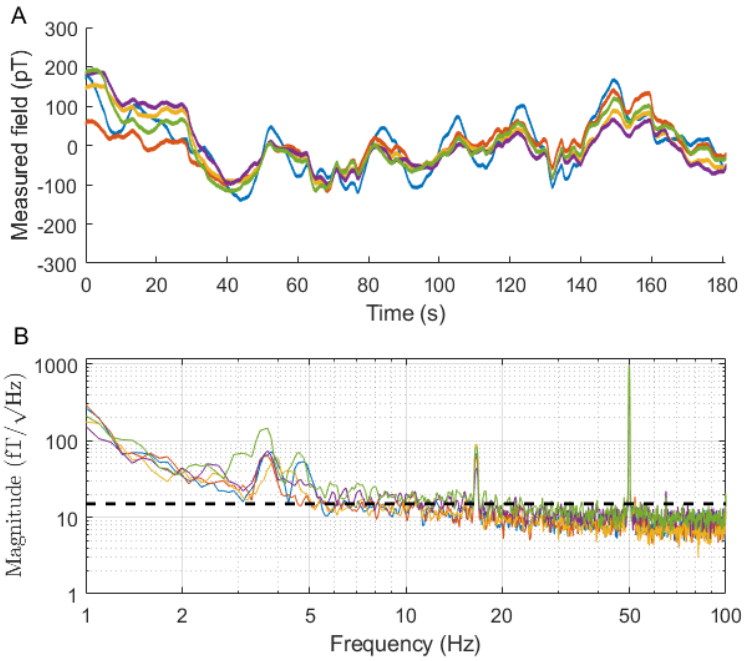



Figure 2.13: *Time-series data and power spectral density estimate from an array of five QuSpin OPMs operating inside an empty MSR. A) Three minutes of data recorded from the analogue output following sensor setup and calibration. Data were collected at 1200 Hz using a National Instruments (Austin, TX) 16-bit ADC. (B) The power-spectral density estimate was made by splitting the data into 10 s chunks and applying a flat top window before taking the fast Fourier transform of each chunk and averaging the results. The dashed black line indicates 15 $fT\sqrt{Hz}$. The 50 Hz mains frequency is visible in the data as well as an interfering source at 16 Hz generated by a nearby air-conditioning unit.*

## 2.7 Requirements for OPMs used in MEG

Considering all of the above, it is crucial that the sensor remains in an environment which is as close to zero field as possible. The QuSpin OPMs contain three electromagnetic coils for producing fields $B_x$, $B_y$ and $B_z$. When operating in 'field-zeroing mode' the sensor estimates the magnetic field which is experienced by the cell based on properties of the zero-field resonances [Shah and Hughes, 2015]. Coil currents which cancel out this field are then applied based on the known relationship of the produced field by the coil per unit current.

This process allows for fast and simple setup of the OPMs, but is limited to magnetic fields which are DC with a magnitude of 0 to 50,000 pT [Shah et al., 2018]. This is a small range when compared to the Earth's magnetic field strength of 40-60 $\mu$T, the effects of a positional change of the sensor and time varying changes in the magnetic field experienced by the cell also need to be compensated in order to maintain the zero-field environment.

Magnetic shielding of the sensors and the participant from external sources of magnetic field is commonly employed in current MEG systems, but these systems do not have the additional complication of a mobile sensor array. A combination of passive and active shielding of magnetic fields is required for OPM operation on a moving participant.

# Chapter 3

# Magnetic Shielding

## 3.1 Introduction

In order to achieve the sensitivity required to perform magnetoencephalography (MEG) QuSpin optically pumped magnetometers (OPMs) must be operated in the spin exchange relaxation free (SERF) regime around a zero field resonance. Commercial magnetically shielded rooms (MSRs) reduce the magnitude of static magnetic fields by a factor of roughly 1,000-2,000; leaving a remnant field of a few tens of nT in magnitude. QuSpin OPMs have on-board coils to compensate for static magnetic fields up to 50 nT in magnitude at a given sensor position and orientation.

However, further attenuation is required for OPM operation on a participant who freely moves through the spatially inhomogenous remnant field. Active shielding of magnetic fields utilising electromagnetic coils operating in feedback loops with an array of reference magnetic field sensors can be employed to provide improved and adaptable screening of static and dynamically varying magnetic fields.

In this chapter an overview of the physics of passive and active magnetic shielding

is presented. The characteristics required for the design of an active shielding system allowing OPM-MEG experiments to be performed on moving participants is also outlined.

## 3.2 Passive magnetic shielding

Passive shielding of magnetic fields refers to the use of materials which enclose a region over which a reduction in magnetic field magnitude is desired. Passive shielding of low-frequency (<1 kHz) electromagnetic fields originated from a desire to protect radio-receiving equipment. Its use became widespread following the adoption of cathode ray tube (CRT) display screens and it is still used to protect sensitive equipment and provide magnetically stable environments for high precision measurements, such as in MEG and the investigation of the neutron electric dipole moment [Hämäläinen et al., 1993, Altarev et al., 2014].

Typically, a region which requires magnetic shielding is completely enclosed by a material, or layers of material. The effectiveness, and the dominant physical mechanism of the shielding depends upon the material properties, and the frequency of the magnetic field being screened.

A quantitative assessment of the performance of a passive shield can be found via evaluation of the shielding factor. This factor is simply the ratio of the magnitude of the magnetic field measured at a single point in the absence of any shielding, $|\boldsymbol{B}_0|$ and the magnitude of the same field at the same position upon enclosure by a shielding material, $|\boldsymbol{B}_S|$ such that

$$SF = \frac{|\boldsymbol{B}_0|}{|\boldsymbol{B}_S|}. \tag{3.2.1}$$

Large values of $SF$ therefore indicate strong shielding and values close to unity indicate little to no shielding.

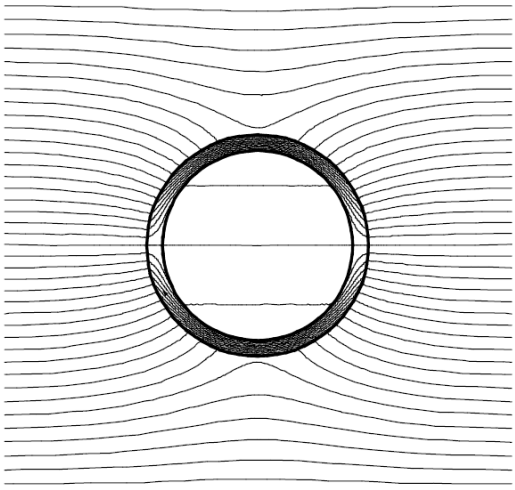


Figure 3.1: *Flux shunting mechanism for shielding of low frequency magnetic fields. Flux lines are drawn for a cross-section of a cylindrical shield. Adapted from [Celozzi et al., 2008].*

### 3.2.1 Flux shunting

For the shielding of low frequency magnetic fields (typically in the 0-10 Hz range, referred to as DC fields) a material with a large value of magnetic permeability is used and the dominant mechanism is flux shunting [Hoburg, 1995]. At a boundary between materials of different relative magnetic permeability, the following conditions apply: to obey Ampere's law the tangential component of the magnetic field $\boldsymbol{H}$ must be continuous across the surface, and to obey Gauss's law the normal component of $\boldsymbol{B}$ must also be continuous [Hoburg, 1995].

$\boldsymbol{B}$ takes the form $\boldsymbol{B} = \mu_0\mu_r\boldsymbol{H}$ inside the material and $\boldsymbol{B} = \mu_0\boldsymbol{H}$ in air. As $\mu_r$ can be >80,000 for common shielding materials such as mu-metal, whilst being roughly 1 in air, the field can abruptly change direction at an interface between air and mu-metal to satisfy the two boundary conditions. In particular on the air-side of the boundary the tangential components of the $\boldsymbol{B}$ and $\boldsymbol{H}$ fields must be approximately zero. The overall effect results in magnetic flux lines being 'pulled in' perpendicular to the material and then 'shunted' along its surface before being released back into the air as is shown in Figure 3.1. [Mager, 1970, Hoburg, 1995].

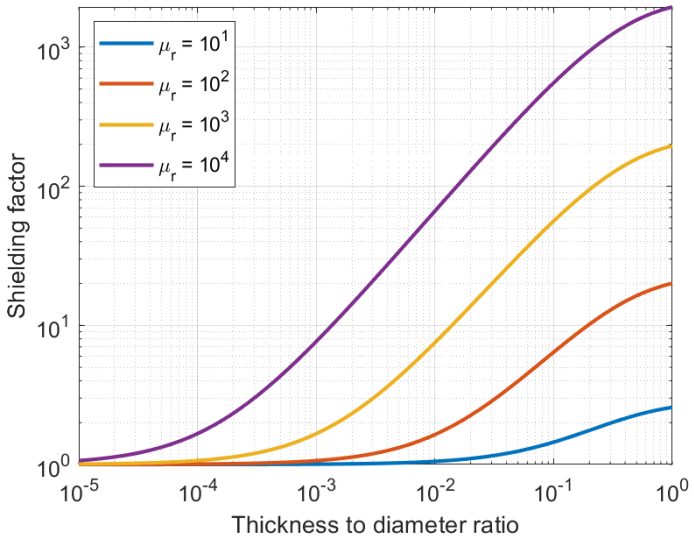



Figure 3.2: *The shielding factor obtained via the flux shunting mechanism for a spherical passive shield as a function of the ratio of the thickness of the shield material to the diameter of the sphere. Evaluation of the shielding factor is performed for various values of* $\mu_r$.

The effectiveness of such a shield depends strongly upon the value of $\mu_r$ of the material and the geometry of the shield. Assuming a shield taking the form of a spherical shell, flux is gathered over a region determined by the spherical diameter. The flux density within the shield material is then determined by the ratio of the shield diameter to material thickness, i.e. flux leakage can occur if a thin shield material encloses a large volume. Higher values of $\mu_r$ in the material prevent this leakage of flux.

Assuming a spherical shell of constant $\mu_r$ which has inner radius $a$ and outer radius $b$, for a uniform incident magnetic field the shielding factor will be the same everywhere inside the shell. Hoburg reports the shielding factor in this case to be [Hoburg, 1995]

$$SF = \frac{(\mu_r + 2)(2\mu_r + 1) - 2\frac{a^3}{b^3}(\mu_r - 1)^2}{9\mu_r}. \tag{3.2.2}$$

If $\mu_r >> 1$, the thickness of the shell $\Delta = b - a$ is small when compared to the

inner radius $a$ and the condition $\mu_r \frac{\Delta}{a} >> 1$ is met, then equation [3.2.2] can be simplified and expressed as [Mager, 1970, Cohen, 1970, Hoburg, 1995]

$$SF \approx \frac{4}{3}\mu_r \frac{\Delta}{a} + 1. \tag{3.2.3}$$

The effects of large values of $\Delta/a$ and $\mu_r$ to increase $SF$ are captured in this expression. Figure 3.2 shows evaluation of equation [3.2.2] to plot $SF$ as a function of the ratio $\Delta/a$ for varying values of $\mu_r$.

To further improve shielding effects, multiple layers of high-permeability material can be 'nested' with a spacing between shells to obtain higher shielding factors. In this case the shielding effect is evaluated using a series of matrices where both the distances between layers and the thickness to diameter ratios are crucial parameters [Schweizer, 1962, Kelhä et al., 1982]. An approximation for the shielding factor of a two layer sphere is given by Mager as

$$SF \approx S_i S_o \Big(1 - \frac{d_i^3}{d_o^3}\Big) + S_i + S_o + 1, \tag{3.2.4}$$

where $S_i$ and $S_o$ are the shielding factors of the two shells and $d_o$ and $d_i$ are the diameters of the outer and inner shells respectively [Mager, 1970].

Figure 3.3 shows the increase in shielding factor which can be achieved using a two-layer shield as a function of the outer shield diameter (from 1 to 100 m) for mu-metal ($\mu_r = 470,000$, value taken from mu-metal supplier available here - https://magneticshields.co.uk/technical/material-technical-data) of a fixed thickness (3 mm), and a fixed shell separation (20 cm, such that $D_i = D_o - 20$ cm). An improvement in the shielding factor by an order of magnitude or more is shown by nesting shields in this way. As a result commercial MSRs for MEG feature at least two layers of a high permeability material for the shielding of low-frequency magnetic fields.

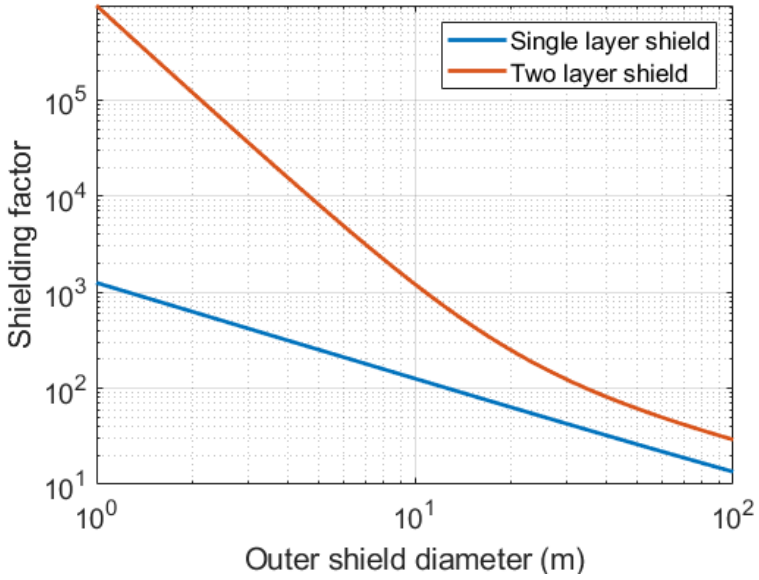



Figure 3.3: *The shielding factor obtained via the flux shunting mechanism for a two-layer spherical passive spherical shield as a function of the diameter of the outermost sphere. Evaluation of the shielding factor is performed for mu-metal ($\mu_r = 470,000$), a material thickness of 3 mm and a constant separation between the outer and inner layers of 20 cm.*

### 3.2.2 Eddy-current cancellation

For higher frequency magnetic fields (above 10 Hz, referred to as AC fields) eddy current cancellation becomes the dominant mechanism and a material with a high electrical conductivity is chosen [Mager, 1970, Hoburg, 1995]. As the material experiences a time varying magnetic field $\boldsymbol{B}(t)$ an electric field $\boldsymbol{E}(t)$ is induced according to Faraday's law

$$\nabla \times \boldsymbol{E(t)} = -\frac{\partial \boldsymbol{B}(t)}{\partial t}. \tag{3.2.5}$$

The electrical conductivity, $\sigma$ results in an induced current density in the material generating flux which opposes that of the incoming field. The net result is that the imposed flux is 'screened' away from the interface as is shown in Figure 3.4.

Eddy-current cancellation occurs only for time-varying magnetic fields and the

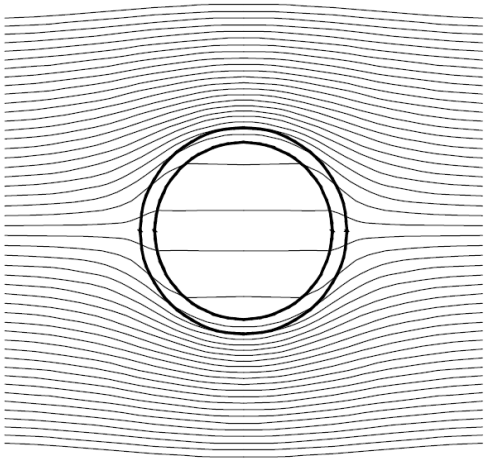


Figure 3.4: *Eddy current cancellation mechanism for shielding of high frequency magnetic fields. Flux lines are drawn for a cross-section of a cylindrical shield. Adapted from [Celozzi et al., 2008].*

induced current density decays exponentially into the material. For an AC source of angular frequency $\omega = 2\pi f$ the skin-depth, $\delta$ is given as [Hoburg, 1995]

$$\delta = \sqrt{\frac{2}{\omega \mu_0 \mu_r \sigma}} \tag{3.2.6}$$

where $\mu_r$ again is the relative magnetic permeability of the material. For materials where $\mu_r \approx 1$ such as copper or aluminium the skin depths at 60 Hz frequency are 8.5 and 11.8 mm respectively.

One would expect that $\delta << \Delta$ (the shield thickness) be a requirement for good shielding. However, increasing the size of the shield at a fixed thickness allows for current loops circulating over the material to induce large flux densities over the shielded region. Hence, good cancellation can be achieved even for shields where $\delta >> \Delta$.

For time varying effects, the shielding factor is a complex number. The magnitude of $SF$ reflects the magnitudes of the AC sources and the phase describes a phase difference between fields for shielded and unshielded cases. For a spherical enclosure of material with $\mu_r = 1$, $\delta >> \Delta$ and $\Delta << a$ the shielding factor can

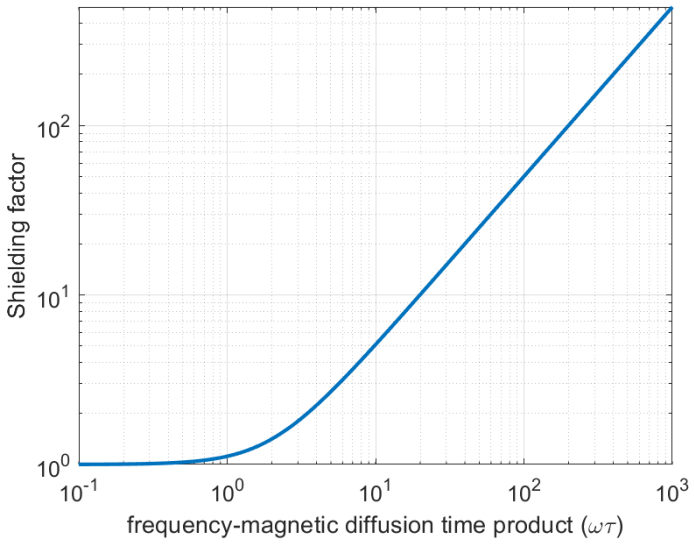



Figure 3.5: *The magnitude of the shielding factor obtained via the eddy-current cancellation mechanism for a spherical shell of radius $a$ and thickness $\Delta$ with $\mu_r = 1$ as a function of the product of the frequency of the source and magnetic diffusion time ($\tau = \mu_0\sigma a\Delta$).*

be expressed as [Hoburg, 1995]

$$SF = 1 + i\omega\frac{\mu_0\sigma a\Delta}{3}. \tag{3.2.7}$$

In this case, the shielding is improved with an increase in any of the terms $\sigma$, $a$ or $\Delta$ and good shielding can be achieved even when $\delta$ is large compared with $\Delta$. A plot of the magnitude of the shielding factor as a function of the product of $\omega$ and $\mu_0\sigma a\Delta$ (referred to as the frequency-diffusion time, $\tau$) is shown in Figure 3.5. Note the contrast to the flux shunting case, since here for a fixed $\Delta$ an increase in $a$ improves the shielding factor.

### 3.2.3 De-gaussing

The highly permeable materials used in passive magnetic shielding often consist of alloys of metals such as iron or nickel and are therefore ferromagnetic. Expo-

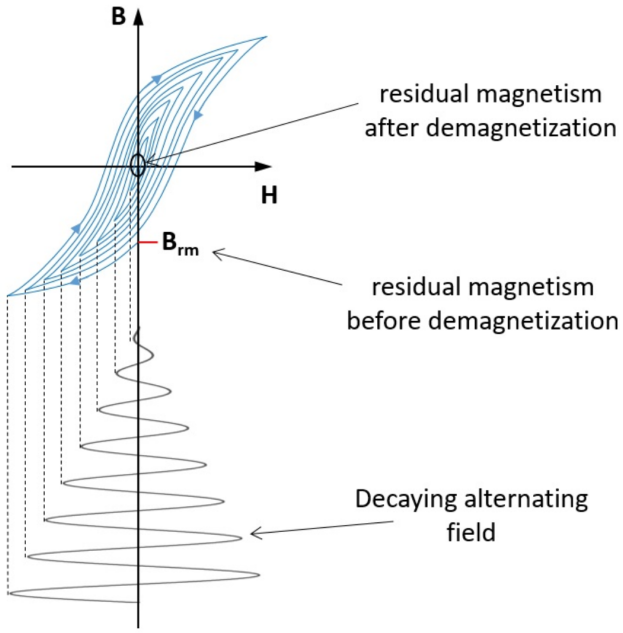



Figure 3.6: *Demagnetisation of a material by application of reversing magnetic field. The material is driven around its* $\boldsymbol{B}$*-*$\boldsymbol{H}$ *curve until the magnetisation reaches 0. Figure adapted from https://cestriom.com/en/technology/demagnetization-basics/.*

sure to magnetic fields either geomagnetically (e.g. moving the metal through the Earth's field) or otherwise (e.g. if the shield is situated inside an environment near to a MRI scanner) can leave a non-zero remnant magnetisation in the shielding enclosure. For mu-metal the saturation field is 0.75 T (data taken from the website of a mu-metal supplier, Magnetic Shields Limited, available here: https://magneticshields.co.uk/technical/b-h-curves-mumetal-50-nife).

The process of de-gaussing metals was developed to de-magnetise large ships to avoid damage by sea-mines with magnetic triggers [Kelly, 1946]. Large cables were wrapped around the ships and a large decaying sinusoidally oscillating current was applied. This de-magnetising pulse drives the metal around its hysteresis loop until the remnant magnetisation is close to zero. The process is outlined in Figure 3.6. Removing the remnant field allows for significant improvement of the shielding performance [Kelhä et al., 1982, Bryś et al., 2005, Voigt et al., 2013, Altarev et al., 2014]. Practically de-gaussing systems require advanced

modelling of the system and specialist hardware to obtain reproducible effects [Sun et al., 2016].

A similar technique where an oscillating magnetic field of constant amplitude is applied to the material to slightly increase its permeability is known as 'shaking' [Cohen, 1967]. This technique can however, create interference inside the shield [Kelhä et al., 1982].

### 3.2.4 Practical considerations

Engineering large spherical enclosures is impractical, and for MEG cuboidal structures are generally used. This and other compromises result in many issues, for example, sharp corners do not allow for neat passage of flux and result in significant flux leakage; doors for access and feed-through holes for equipment are often desired leaving discontinuities in the materials; the rooms are formed of several panels rather than one smooth sheet leading to 'gaps' with a discontinuity in $\mu_r$; the value of $\mu_r$ can vary within and between panels depending on the remnant magnetisation resulting in an inconsistent shielding effect throughout the material and the generation of spatial field gradients; de-gaussing equipment is expensive and requires good flux linkage throughout the enclosure. As a result commercial MSRs often leave a remnant field of a few tens of nT in magnitude with a high spatial variance in the centre of the room.

Evaluation of the flux-shunting and eddy-current cancellation mechanisms is possible for simple cases such as spheres, cylinders and infinite planes, but advanced modelling is required for other geometries and realistic structures. The complex geometries of the shield, as well as hysteresis/saturation effects and a non-constant value of permeability between sheets of metal will all impact on calculations. Specialist software, such as ANSYS (Ansys Inc., Canonsburg, PEN) can be used to perform finite element model (FEM) based analysis of complex

structures to aid the design of commercial shielded rooms.

Despite modelling complexities, high performance MSRs, such as the one constructed at the Physikalisch Technische Bundesanstalt (PTB) institute in Berlin can provide a passive shielding factor of $0.75 \times 10^6$ at 0.01 Hz [Bork et al., 1980]. The PTB room features seven layers of mu-metal and a single layer of aluminium. De-gaussing cables are installed within the metal layers.

Another application where low magnetic fields are required is investigation of the neutron electric dipole moment (EDM) [Pospelov and Ritz, 2005]. Highly stable background magnetic field with minimal spatial variation is required for these experiments. Fierlinger and colleagues constructed a two-layer room with de-gaussing capability leading to remnant field and field gradient values of $\approx$ 700 pT and 300 pT/m, respectively [Altarev et al., 2014]. This represents an improvement by a factor of around 100 on a standard commercial MSR.

Most MSRs employed in SQUID-based MEG have large internal dimensions due to the size of the helium dewar required for cooling the SQUIDs. This is not required in OPM-MEG and smaller, person sized shields can be employed instead. Borna and colleagues developed a 20-channel OPM-MEG system with dimensions comparable to that of the bore of an MRI scanner [Borna et al., 2017, Borna et al., 2019]. After degaussing, the remnant field around the OPMs was $\approx$ 1 nT and they were able to detect auditory and somatosensory evoked potentials [Borna et al., 2017]. Although systems operating inside smaller shields have both cost and siting advantages compared with those in larger rooms, the range of movement which can be afforded to the participant is limited.

## 3.3 Active shielding

The remnant magnetic field and its gradients inside a MSR a can be further compensated by using a series of electromagnetic coils to produce magnetic fields equal and opposite to those inside the shielding enclosure. From Maxwell's equations for magnetostatics the magnetic field obeys the following:

$$\nabla . \boldsymbol{B} = 0 \tag{3.3.1}$$

and

$$\nabla \times \boldsymbol{H} = \boldsymbol{J}, \tag{3.3.2}$$

where $\boldsymbol{J}$ denotes a current density. As $\boldsymbol{B} = \mu_0 \mu_r \boldsymbol{H}$ and within the air-filled region inside the shield there is no current flow and $\mu_r \approx 1$, it follows that

$$\nabla \times \boldsymbol{B} = 0. \tag{3.3.3}$$

Upon evaluation of these equations the magnetic field can be expressed as three vector components, $B_x$, $B_y$, $B_z$ which each obey Laplace's equation and so can be represented as a series of spherical harmonics. The lowest order terms in these series correspond to spatially uniform fields and field gradients. Upon evaluation of equations [3.3.1] and [3.3.3] there is a high degree of symmetry between gradient terms as

$$\begin{aligned} \frac{dB_z}{dx} &= \frac{dB_x}{dz} \\ \frac{dB_z}{dy} &= \frac{dB_y}{dz} \\ \frac{dB_x}{dy} &= \frac{dB_y}{dx} \\ \frac{dB_x}{dx} + \frac{dB_y}{dy} + \frac{dB_z}{dz} &= 0. \end{aligned} \tag{3.3.4}$$

Following measurement of the remnant field inside the MSR a linear combination of the vector components and the terms listed in equation [4.2.1] which best model the measured field can be used to generate a field which is equal and opposite to cancel the remnant field. These field variations are generated by electromagnetic coils. Higher order spatial variations can also be modelled.

### 3.3.1 Electromagnetic coils

The Biot-Savart law mathematically describes the magnetic field generated by a constant electrical current in a wire. For the calculation of a magnetic field at position $\boldsymbol{r}(x, y, z)$ generated by a current $I$ a line integral is evaluated over the elements $d\boldsymbol{l}$ in the current path C. The total field $\boldsymbol{B}(\mathbf{r})$ is then expressed as

$$\boldsymbol{B}(\boldsymbol{r}) = \frac{\mu_0}{4\pi} \int_C \frac{I d\boldsymbol{l} \times \boldsymbol{r}'}{|\boldsymbol{r}'|^3} \tag{3.3.5}$$

where $\boldsymbol{r}'$ is the vector between the line element and position $\boldsymbol{r}$. Coils of wire with constant currents can therefore be used to produce magnetic fields.

In order to generate the required cancellation field, electromagnetic coils are designed which produce single field components. Different current values can be applied to each coil to produce the required overall magnetic field.

The simplest case is that of a Helmholtz coil for producing a homogeneous magnetic field in one direction. A Helmholtz coil consists of two circular current loops

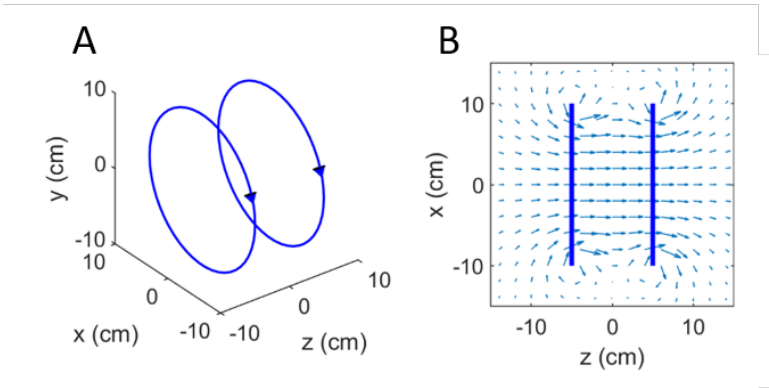



Figure 3.7: *A Helmholtz coil producing uniform field between two loops of wire. A) Two current carrying loops of radius a are separated in z. B) Vector plot of the magnetic field generated by the coil shows uniform field along the z direction.*

of radius $a$, positioned symmetrically in the $x-y$ plane and each carrying the same current, $I$. If the two loops are separated in the $z$ direction by a distance equal to their radius, then (through superposition of the magnetic field produced by each loop) the magnetic field component $B_z$ is highly homogeneous at the centre of the coils. Figure 3.7 shows this scenario. This arrangement can be rotated to form homogeneous fields along the two other Cartesian axes [Abbott, 2015]. A system based on this architecture is often referred to as a 'Helmholtz cage'.

To create a magnetic field gradient where the magnitude of the field in one direction varies linearly with its position, for example $dB_z/dz$, the current in one of the two circular loops can be reversed. The superposition of magnetic fields now results in a field which is zero at the centre of the coil pair and linearly increases/decreases based on position between the coils as shown in Figure 3.8. Again the structure can be rotated to produce gradients in the other dimensions. These field gradients, $dB_x/dx$, $dB_y/dy$ and $dB_z/dz$ where the field components vary with position along the same spatial dimensions are referred to as longitudinal field gradients. The remaining components are referred to as transverse field gradients. More complex wire-paths are required to produce these fields. Accurate coil design is crucial within the field of magnetic resonance imaging (MRI);

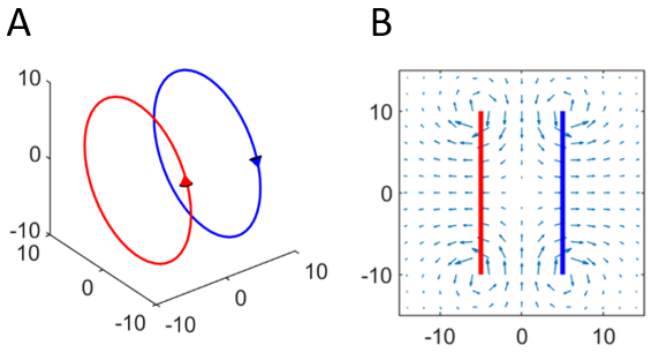



Figure 3.8: *A field gradient coil producing uniform field gradient between two loops of wire. A) Two current carrying loops of radius a placed a distance a apart in z. The loops carry the same magnitude current but with opposing circulation. B) Vector plot of the magnetic field generated by the coil shows uniform field gradient is generated along the z direction.*

high gradient homogeneity is desired to obtain optimal image quality, due to a requirement that the Larmor frequency of the nuclei be linearly dependent on position within the magnet. As a result, a wide array of techniques for designing electromagnetic coils whose wire-paths are formed on surfaces of multiple different geometry have been developed. Included in these design methods are optimisations which minimise the power dissipated within a coil set (to use as little current as possible), the inductance (crucial for rapidly switching gradients to minimise scan time) and balance the coil from large torques due to the main magnetic field of the scanner [Turner, 1993, Carlson et al., 1992]. All of this can be achieved with greater control if the wire-paths are 'distributed' over a surface, allowing for field gradient coils with very high homogeneity. Examples of distributed windings for MRI coils are shown in Figure 3.9.

Most relevant here (due to the cubic geometry of most MSRs) is the design of planar coil systems [Yoda, 1990, Martens et al., 1991]. Multiple design methods are available, with a common goal of minimising the variation of a single component of the field; coils which produce each of the eight required terms can therefore be designed and constructed to create an active shielding system suitable for use

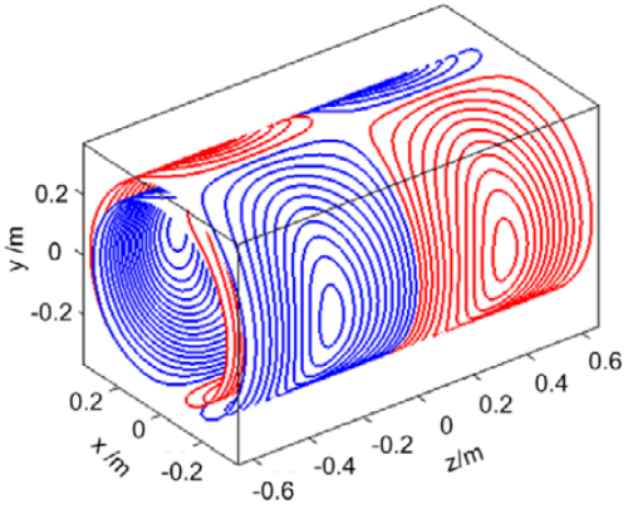



Figure 3.9: *A $dB_x/dz$ transverse field gradient coil featuring distributed windings. The coil was designed for use in MRI and features a cylindrical geometry. Figure adapted from [Hu et al., 2017].*

inside a MSR.

### 3.3.2 Feedback controllers

Feedback controllers are used to automatically control the electromagnetic coils employed in active shielding systems. For cancellation of the vector field components $B_x$, $B_y$ and $B_z$ inside the MSR a tri-axial magnetometer can be placed at the centre of the room. The output of this magnetometer can then be recorded and the measured field values used to inform a coil current, based on a known value of the coil field per unit of current in the coil. This system is referred to as a feedback controller.

Comparison of measurements recorded by a series of magnetometers at known locations around the MSR can provide estimates of the spatial variance (or gradients) of the magnetic field. These measurements can be passed to the field gradient coils and a similar feedback controller can be developed.

A more advanced controller is the proportional integral derivative (PID) con-

troller. PID control is utilised throughout science and industry. Its flexibility and adaptability make it a highly practical solution for complex systems [Åström and Hägglund, 1995, Ang et al., 2005]. For magnetic field cancellation, the PID controller applies a current to the coils whose value depends not only on the measurement, but also on the history of the system. A desired value, or 'setpoint' for the measurement is required, in the case of active magnetic shielding the measurement is the measured magnetic field, $b(t)$ which is to be driven towards zero. The error, $e(t)$ is then the difference between the measurement and setpoint ($sp$) and is computed as [Åström and Hägglund, 1995]

$$e(t) = b(t) - sp. \tag{3.3.6}$$

The basic expression for the current applied to the electromagnetic coil to alter the measured field, $I(t)$, as calculated by a PID controller, is given as the sum of three terms. The first term is proportional to the error in the system, the second varies with the integral of the error over time, and the third varies with the derivative of the error. The overall current is given as [Åström and Hägglund, 1995]

$$I(t) = K_p e(t) + K_i \int_0^t e(\tau) d\tau + K_d \frac{de(t)}{dt} \tag{3.3.7}$$

where $K_p$, $K_i$ and $K_d$ are the proportional, integral and derivative gains of the controller respectively. These gain terms can be adjusted either manually, or through automated methods, to provide a stable controller [Åström and Hägglund, 1995, Ang et al., 2005].

A well-tuned controller seeks to minimise the rise-time, which is the time taken for the measurement to go from 10% to 90% of the setpoint; overshoot, which is the amount by which the measurement exceeds the desired setpoint after rising;

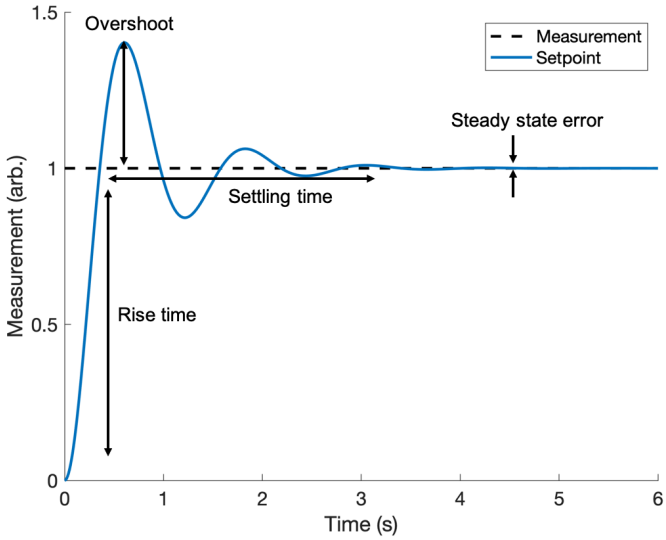



Figure 3.10: *PID controller response to a step change in setpoint. The controller varies a controllable parameter, e.g. temperature or electrical current to alter the system until a measurement reaches a desired setpoint. By varying the three gain terms $K_p$, $K_i$ and $K_d$ the rise time, overshoot, settling time and steady state error can be minimised providing a stable controller with a fast response to changes.*

the settling time, which is the time taken for the system to stabilise; the steady state error once the system has settled and the overall stability of the system. The overall PID response including these parameters is outlined in Figure 3.10 and the effects of altering either of $K_p$, $K_i$ or $K_d$ are summarised in Table 3.1.

Although in theory the inclusion of a derivative term $K_d$ produces a more stable controller, this term can act to amplify noise in the system [Ang et al., 2005].

| | Rise time | Overshoot | Settling time | Steady-state error | Stability |
|---|---|---|---|---|---|
| Increase $K_p$ | Decrease | Increase | Slight Increase | Decrease | Degrade |
| Increase $K_i$ | Slight decrease | Increase | Increase | Large Decrease | Degrade |
| Increase $K_d$ | Slight decrease | Decrease | Decrease | Little change | Improve |

Table 3.1: *Effect on system response to varying PID gain values whilst other parameters are fixed [Ang et al., 2005].*

As a result PI controllers are more commonly used. Controllers are implemented either using analogue circuits, where a combination of op-amps, resistors and capacitors are used to vary the applied current, or through software. Software based solutions such as implementation on a microprocessor are more flexible allowing for fast re-tuning of the system, but careful consideration of system-timing is required, as the loop rate will often be imprecise.

### 3.3.3 Practical considerations

Installation of an active compensation system for MEG requires careful consideration. It is crucial to design electromagnetic coils which do not restrict access to the room, do not produce unwanted magnetic interference and operate such that field inhomogeneities can be quickly and easily dealt with. The coils should also produce homogeneous field components over as large an area as possible. The placement of sensors for the feedback controller in order to fully characterise the disturbing fields needs to be considered such that coils can operate, without restricting the participant.

The choice of sensors to measure the static and dynamic variations of the remnant field inside the MSR is also crucial for feedback controller design. If the DC level of the field is too high then OPMs will not be able to operate in the SERF regime. If the temporal variation of the field is too high then the sensors may drift away from the linear portion of the response curve and sensor gain may be affected. Hardware and software which provides stable system gains with fast feedback loop times (exceeding the bandwidth of the sensor) need to be used.

The PTB room introduced previously, also includes an active compensation system featuring square coils placed outside the shielded room. At 0.01 Hz the shielding factor of the PTB room was increased from $0.75 \times 10^6$ with no active compensation to $2 \times 10^6$ with active compensation [Bork et al., 1980].

Iivanainen and colleagues developed an active cancellation system featuring a coil-cage type system, capable of compensating the remnant field inside a MSR, and its temporal variation. Reduction of the field from 70 nT to less than 1 nT was achieved. They also reduced the temporal variation of the field from a peak to peak drift of 1.3 nT to 0.4 nT [Iivanainen et al., 2019].

# Chapter 4

# Bi-planar coil active shielding system

## 4.1 Introduction

The magnetoencephalography (MEG) facility at the University of Nottingham was installed in 2007 and comprises a Canadian Thin Films (CTF, Coquitlam, BC, Canada) superconducting quantum interference device (SQUID) based system with 275 axial gradiometer channels. The system is housed in a magnetically shielded room (MSR) constructed by Vacuumschmelze (Vac, Hanau, Germany). The Vac room features two layers of mu-metal and one layer of aluminium.

The MSR is based at the Sir Peter Mansfield Imaging Centre, which also houses two 3 T magnetic resonance imaging (MRI) scanners and one 7 T MRI scanner (the 7 T scanner being around 30 m away from the MEG facility). No de-gaussing or active shielding systems were installed upon its construction. The remnant field at the centre of the MSR is around 25 nT in magnitude with field gradients in excess of 10 nT/m.

As a result of the high remnant field, the MSR is ill-suited to immediately allowing optically-pumped magnetometer (OPM) operation on a moving participant. The installation of an active field cancellation system to improve the shielding factor of the room by reducing the magnitude of the remnant magnetic field and its spatial variation is crucial to allowing OPM-MEG experiments to be performed on participants who are free to move.

This chapter describes the design, construction and evaluation of an active magnetic shielding system based on bi-planar coils that produce homogeneous magnetic fields and magnetic field gradients over a volume at the centre of the coils. Bi-planar coil designs provide a natural 'corridor', allowing easy access for participants and experimenters to the centre of the coils unlike a tri-axial 'Helmholtz-cage' system [Iivanainen et al., 2019].

The theory of bi-planar coil design is described by combining mathematics for bi-planar gradient coils used in MRI with a harmonic minimisation approach. The nulling performance is assessed via field mapping and by performing experiments involving controlled movements. A novel MEG paradigm which investigates the retinotopic organisation of the visual cortex is also presented, as well as a brief summary of additional experiments which have been realised using the bi-planar coil system.

The work described in this chapter was crucial to the development of an OPM-MEG system at the University of Nottingham and formed a key part of a recent publication in Nature [Boto et al., 2018]. A more detailed description of the system was published in NeuroImage and adapted for this chapter [Holmes et al., 2018].

## 4.2 Theory of bi-planar coil design

### 4.2.1 Magnetic field equation

Recalling the evaluation of a magnetic field in an air-filled region in which no current flows from Chapter 3, the lowest order terms in the magnetic field share a high degree of symmetry. As a result, a full description of the field and field gradients can be obtained using a series of eight components, instead of the expected twelve. Three coils can be designed to produce the uniform field components, $B_x$, $B_y$ and $B_z$ and a further five coils can be designed to produce the field gradients,

$$\begin{aligned} G_x &= \frac{dB_z}{dx} = \frac{dB_x}{dz} \\ G_y &= \frac{dB_z}{dy} = \frac{dB_y}{dz} \\ G_z &= \frac{dB_z}{dz} = -2\frac{dB_x}{dx} = -2\frac{dB_y}{dy} \\ G_{xy} &= \frac{dB_x}{dy} = \frac{dB_y}{dx} \\ G_{xx} &= \frac{dB_x}{dx} = -\frac{dB_y}{dy} - \frac{dB_z}{dz}. \end{aligned} \tag{4.2.1}$$

To produce designs for bi-planar coils, mathematics from planar coil design in MRI [Yoda, 1990] was incorporated into a harmonic minimisation approach [Carlson et al., 1992]. Initially an expression for the magnetic field generated by a given planar current distribution is required. Consider the magnetic vector potential $\boldsymbol{A}$ which is given by:

$$\boldsymbol{B} = \nabla \times \boldsymbol{A}. \tag{4.2.2}$$

Recalling that $\nabla \times \boldsymbol{B} = \mu_0 \boldsymbol{J}$ the vector potential can be re-written as:

$$\nabla \times (\nabla \times \boldsymbol{A}) = \nabla(\nabla \cdot \boldsymbol{A}) - \nabla^2 \boldsymbol{A} = \mu_0 \boldsymbol{J}. \tag{4.2.3}$$

This equation can be simplified as the divergence of $\boldsymbol{A}$ has no physical meaning. Adopting the Coulomb gauge such that $\nabla \cdot \boldsymbol{A} = 0$, reduces (4.2.3) to

$$\nabla^2 \boldsymbol{A} = -\mu_0 \boldsymbol{J}, \tag{4.2.4}$$

which is a form of Poisson's equation. Standard solutions to the Poisson equation exist, allowing the vector potential at a position $\boldsymbol{r}(x, y, z)$ to be expressed in terms of the current density $\boldsymbol{J}(\boldsymbol{r})$ as

$$\boldsymbol{A}(\boldsymbol{r}) = \frac{\mu_0}{4\pi} \int \frac{\boldsymbol{J}(\boldsymbol{r'})}{|\boldsymbol{r} - \boldsymbol{r'}|} d^3\boldsymbol{r'}. \tag{4.2.5}$$

We are interested in the situation where $\boldsymbol{J}(\boldsymbol{r'})$ is confined to the $x - y$ plane at $z = a$, and therefore perform the planar Green's function expansion of $|\boldsymbol{r} - \boldsymbol{r'}|^{-1}$ giving

$$\frac{1}{4\pi} \frac{1}{|\boldsymbol{r} - \boldsymbol{r'}|} = \frac{1}{4\pi^2} \int_{-\infty}^{\infty} dk_x \int_{-\infty}^{\infty} dk_y \; e^{ik_x(x-x')} \; e^{ik_y(y-y')} \; \frac{e^{-k_z(z_> - z_<)}}{2k_r}, \tag{4.2.6}$$

where $k_r = (k_x^2 + k_y^2)^{\frac{1}{2}}$ and $z_{>,<}$ is the greater or lesser of $z$ or $a$. The current density can then be rewritten in terms of its two-dimensional Fourier transform, $\widetilde{\boldsymbol{J}}(k_x, k_y)$,

$$\boldsymbol{J}(x, y) = \frac{1}{4\pi^2} \int_{-\infty}^{\infty} dk_x \int_{-\infty}^{\infty} dk_y \; \widetilde{\boldsymbol{J}}(k_x, k_y) \; e^{ik_x x'} \; e^{ik_y y'}. \tag{4.2.7}$$

Combining equations (4.2.5-4.2.7) allows the vector potential to be expressed as

$$\boldsymbol{A}(\boldsymbol{r}) = \frac{\mu_0}{2} \int_{-\infty}^{\infty} dk_x \int_{-\infty}^{\infty} dk_y \; \widetilde{\boldsymbol{J}}(k_x, k_y) \; e^{ik_x x} \; e^{ik_y y} \; \frac{e^{-k_z(z_> - z_<)}}{k_r}. \tag{4.2.8}$$

The surface current density $\boldsymbol{J}(\boldsymbol{r})$ can be defined using a two-dimensional, scalar, stream function $S(x, y)$ such that

$$\nabla S \times \hat{\boldsymbol{z}} = \boldsymbol{J}(\boldsymbol{r}) \tag{4.2.9}$$

(given the charge continuity equation $\nabla \cdot \boldsymbol{J} = 0$) [Carlson et al., 1992]. Combining this relation with the Fourier transform of equation (4.2.7) and integrating by parts reveals

$$\widetilde{\boldsymbol{J}}(k_x, k_y) = i\ [k_y \hat{\boldsymbol{x}} - k_x \hat{\boldsymbol{y}}]\ \widetilde{S}(k_x, k_y). \tag{4.2.10}$$

The vector potential can now be expressed in terms of the stream function as

$$\boldsymbol{A}(\boldsymbol{r}) = \frac{\mu_0}{2} \int_{-\infty}^{\infty} dk_x \int_{-\infty}^{\infty} dk_y\ e^{ik_x x}\ e^{ik_y y}\ \frac{e^{-k_z(z_> - z_<)}}{k_r}\ [k_y \hat{\boldsymbol{x}} - k_x \hat{\boldsymbol{y}}]\ \widetilde{S}(k_x, k_y). \tag{4.2.11}$$

A bi-planar coil includes an equal or opposite current distribution confined to the plane at $z = -a$, so that $S_{z'=a} = \pm S_{z'=-a}$. Through addition of the effects of the two current distributions the two-dimensional Fourier transform of the magnetic field over the $x - y$ plane at position $z$, $\widetilde{\boldsymbol{B}}(k_x, k_y, z)$, can be expressed as:

$$\widetilde{\boldsymbol{B}}(k_x, k_y, z) = \mu_0 \left[ (ik_x \hat{\boldsymbol{x}} + ik_y \hat{\boldsymbol{y}}) \begin{matrix}\sinh \\ \cosh\end{matrix}(k_r z) - \ k_r \hat{\boldsymbol{z}} \begin{matrix}\cosh \\ \sinh\end{matrix}(k_r z) \right] \widetilde{S}(k_x, k_y) e^{-k_r a}. \tag{4.2.12}$$

The upper/lower (sinh and cosh) terms refer to the cases where the stream function has the same/opposite sign on each plane. The real-space field variation, $\boldsymbol{B}(x, y, z)$ is then calculated via inverse Fourier transformation of equation [4.2.12].

### 4.2.2 Evaluating the stream function

To design a coil to produce a particular field variation, the stream function can be parameterised, and then the parameter values which yield optimal performance

based on a pre-defined functional can be identified [Carlson et al., 1992]. For the bi-planar coils considered here, the stream function is parameterised as a two-dimensional Fourier series which is confined to the region $|x|$, $|y| < L$ ($z = \pm a$) on the two coil planes, so that:

$$\begin{aligned} S(x,y) = \sum_{n=1}^{N} \Big[\alpha_n \cos\Big(\frac{\pi}{2}(2n-1)\frac{x}{L}\Big) + \beta_n \sin\Big(\frac{n\pi x}{L}\Big)\Big] \times \\ \sum_{m=1}^{M} \Big[\gamma_m \cos\Big(\frac{\pi}{2}(2m-1)\frac{y}{L}\Big) + \delta_m \sin\Big(\frac{m\pi y}{L}\Big)\Big]. \end{aligned} \tag{4.2.13}$$

the coefficients $\alpha_n$, $\beta_n$, $\gamma_n$ and $\delta_n$ are used to weight the different harmonics in the series in order to produce required variations in the magnetic fields. The fields and field gradients which are to be generated all have a high degree of symmetry and as a result only a sub-set of the harmonic combinations are needed when designing each coil.

For example, in the simple case of a $B_z$ coil the symmetry can be obtained by considering a Helmholtz coil. Two loops of wire spatially separated in the $z$ direction produce a uniform field along this axis. The shapes of the two loops are the same and the stream function is symmetric in $x$ and $y$. The two loops also carry the same current circulating in the same sense, i.e. the coil is symmetric in $z$. If the current is reversed in one of the loops, a field gradient is produced and the stream function becomes anti-symmetric in $z$. The symmetry conditions for the stream functions defining each coil are detailed in Table 4.1.

For the $B_x$ coil it is required that the stream function is anti-symmetric in $x$, symmetric in $y$ and anti-symmetric in $z$. Choosing the sine terms for anti-symmetric cases and cosine terms for symmetric cases allows the stream function for a $B_x$ coil to be written as:

$$S_{(B_x)} = \sum_{n=1}^{N}\sum_{m=1}^{M} \Big[\lambda_{nm} \sin\Big(\frac{n\pi x}{L}\Big) \cos\Big(\frac{\pi}{2}(2m-1)\frac{y}{L}\Big)\Big] \tag{4.2.14}$$

| Coil | $x$ symmetry | $y$ symmetry | $z$ symmetry |
|---|---|---|---|
| $B_x$ | A/S | S | A/S |
| $B_y$ | S | A/S | A/S |
| $B_z$ | S | S | S |
| $G_x$ | A/S | S | S |
| $G_y$ | S | A/S | S |
| $G_z$ | S | S | A/S |
| $G_{xy}$ | A/S | A/S | A/S |
| $G_{xx}$ | S | S | A/S |

Table 4.1: *Summary of stream functions required to produce a given magnetic field or field gradient. Symmetric (S) or Anti-Symmetryic (A/S) terms can be extracted from equation [4.2.13] based on $x$ and $y$ symmetry. The choice of* sinh *or* cosh *terms in equation [4.2.12] can be made using the $z$ symmetry.*

defining the $x$ and $y$ symmetry. The $z$ symmetry is defined by setting ($S_{z=a} = -S_{z=-a}$). The new constant, $\lambda_{nm}$ is defined as $\lambda_{nm} = \beta_n \gamma_m$.

The stream function equations can be re-written for ease of notation in the form

$$S = \sum_{j=1}^{N \times M} \lambda_j S_j. \tag{4.2.15}$$

with $j = (n-1)N + m$. Continuing with the case of the $B_x$ coil, the contribution to the magnetic field in the $x$-direction $b_{xj}(\boldsymbol{r}_i)$, from the $j^{th}$ component of the stream function is expressed using equation [4.2.12] as

$$b_{xj}(\boldsymbol{r}_i) = 2DFT\Big(i\mu_0 k_x \widetilde{S}_j e^{-k_r a} \cosh(k_r z_i)\Big)\Big|_{x_i, y_i}, \tag{4.2.16}$$

where $2DFT$ indicates the two-dimensional Fourier Transform.

Defining $\widetilde{S}_j$ in terms of the reduced variables $x' = x/L$, $y' = y/L$ ($k'_x = k_x L$, $k'_y = k_y L$) allows its expression as

$$\widetilde{S}_j(k'_x, k'_y) \propto \int_{-1}^{1} dx' \int_{-1}^{1} dy' \ \sin(nx'\pi) \ \cos\Big((2m+1)y'\frac{\pi}{2}\Big) \ e^{-ik'_x x'} e^{-ik'_y y'}. \tag{4.2.17}$$

Evaluating the integral gives

$$\begin{aligned}\widetilde{S}_j(k'_x, k'_y) = i\big[\operatorname{sinc}(n\pi - k'_x) - \operatorname{sinc}(n\pi + k'_x)\big]\times \\ \big[\operatorname{sinc}((m - {}^1\!/_2)\pi - k'_y) + \operatorname{sinc}((m - {}^1\!/_2)\pi + k'_y)\big]\end{aligned} \tag{4.2.18}$$

which can be substituted into (4.2.16) in order to find the magnetic field at position $\boldsymbol{r}_i$ due to each component of the stream function. Similar calculations can be performed for the other coils by imposing the symmetry conditions in Table 4.1 and the resulting stream functions are summarised in Table 4.2.

| Coil | $\widetilde{S}_j(k'_x, k'_y)$ |
|---|---|
| $B_x/G_x$ | $i\big[\operatorname{sinc}(n\pi - k'_x) - \operatorname{sinc}(n\pi + k'_x)\big]\times$ $\big[\operatorname{sinc}((m - {}^1\!/_2)\pi - k'_y) + \operatorname{sinc}((m - {}^1\!/_2)\pi + k'_y)\big]$ |
| $B_y/G_y$ | $\big[\operatorname{sinc}((n - {}^1\!/_2)\pi - k'_x) + \operatorname{sinc}((n - {}^1\!/_2)\pi + k'_x)\big]\times$ $i\big[\operatorname{sinc}(m\pi - k'_y) - \operatorname{sinc}(m\pi + k'_y)\big]$ |
| $B_z/G_z/G_{xx}$ | $\big[\operatorname{sinc}((n - {}^1\!/_2)\pi - k'_x) + \operatorname{sinc}((n - {}^1\!/_2)\pi + k'_x)\big]\times$ $\big[\operatorname{sinc}((m - {}^1\!/_2)\pi - k'_y) + \operatorname{sinc}((m - {}^1\!/_2)\pi + k'_y)\big]$ |
| $G_{xy}$ | $i\big[\operatorname{sinc}(n\pi - k'_x) - \operatorname{sinc}(n\pi + k'_x)\big]\times$ $i\big[\operatorname{sinc}(m\pi - k'_y) - \operatorname{sinc}(m\pi + k'_y)\big]$ |

Table 4.2: *Calculated values of $\widetilde{S}_j(k'_x, k'_y)$ for each of the eight coils. These expressions incorporate the x and y symmetry of the stream functions with the z symmetry defined by the choosing of* sinh *or* cosh *terms in equation [4.2.12].*

### 4.2.3 Harmonic Minimisation

Harmonic minimisation involves calculating optimal weights for the stream function that minimises a functional [Carlson et al., 1992]. It is desired to minimise the spatial deviation of the field that is produced from the desired field using the functional:

$$F = \sum_{i=1}^{I} \left| B(\boldsymbol{r}_i) - b(\boldsymbol{r}_i) \right|^2. \tag{4.2.19}$$

Here $B(\boldsymbol{r}_i)$ is the desired field at $\boldsymbol{r}_i$ and $b(\boldsymbol{r}_i) = \sum_{j=1}^{J} \lambda_j b_j(\boldsymbol{r}_i)$ is the calculated field at $\boldsymbol{r}_i$. The set of position vectors $\boldsymbol{r}_{i=1\ to\ I}$ define target points within the volume at which a homogeneous field or field gradient is required.

However, it is likely that the resulting coil would be formed of intricate windings which would be challenging to engineer accurately. In order to account for this, the power dissipation over the coil is also minimised.

### 4.2.4 Power dissipation term

MRI gradient coils are often designed with terms in the functional that act to minimise additional coil parameters, alongside the deviation of the magnetic field from the target distribution. These include the power dissipation, inductance and torque [Carlson et al., 1992, Turner, 1993, Jin, 1998].

The coils designed here do not need to generate rapidly time-varying fields and are not operated inside a large magnetic field, therefore inductance minimisation and torque balancing are unnecessary and only a power dissipation term needs to be included in the functional.

Considering a single element on a coil plane with current density $\boldsymbol{J}$, a resistivity $\rho$ and dimensions $dx \times dy \times t$ where $t$ is the thickness of the region in which current flows, the power dissipation in this element due to $\boldsymbol{J}$ is

$$dP = I^2 R = \frac{\rho}{t}(J_x^2 + J_y^2)\ dxdy. \tag{4.2.20}$$

Integrating across all elements to find the total power $P$ gives

$$P = \frac{\rho}{t} \int_{-L}^{L} dx \int_{-L}^{L} dy \ (J_x^2 + J_y^2). \tag{4.2.21}$$

Applying Parseval's relation gives

$$P = \Omega \int_{-\infty}^{\infty} dk_x \int_{-\infty}^{\infty} dk_y \ \left( \left| \widetilde{J}_x \right|^2 + \left| \widetilde{J}_y \right|^2 \right) \tag{4.2.22}$$

where $\Omega$ is introduced to represent the combined effect of all constants. This can be redefined by recalling the definition of the stream function, $\nabla S \times \hat{\boldsymbol{z}} = \boldsymbol{J}$ giving

$$P = \Omega \int_{-\infty}^{\infty} dk_x \int_{-\infty}^{\infty} dk_y \ k_r^2 \left| \widetilde{S} \right|^2. \tag{4.2.23}$$

$P$ is then weighted by a tuneable term $\omega$ before inclusion in the functional. Since the power is minimised by reducing large, local excursions in the amplitude of the stream function, higher values of $\omega$ result in simpler wire paths, but this is associated with a loss of field or gradient homogeneity. Lower values of $\omega$ result in more homogenous fields produced by more complex wire paths.

The functional can be re-defined to include the effect of power dissipation with the form

$$F = \sum_{i=1}^{I} \left| B(\boldsymbol{r}_i) - b(\boldsymbol{r}_i) \right|^2 + \omega P. \tag{4.2.24}$$

### 4.2.5 Optimising Stream Functions

When designing a coil in which the $x$-component of the field is targeted, the functional is minimised by choosing the weights $\lambda_j$ which satisfy the condition

$$\frac{dF}{d\lambda_j} = -\sum_{i=1}^{I} B_x(\boldsymbol{r}_i)\; b_{xj}(\boldsymbol{r}_i) + \sum_m \lambda_m \Big( \sum_{i=1}^{I} b_{xj}(\boldsymbol{r}_i) b_{xm}(\boldsymbol{r}_i) \; + \omega\Omega \int_{-\infty}^{\infty} dk_x \int_{-\infty}^{\infty} dk_y \; k_r^2 \widetilde{S}_j \widetilde{S}_m \Big) \tag{4.2.25}$$

This set of derivatives can be cast as a set of linear simultaneous equations in matrix form, $\boldsymbol{a} = \boldsymbol{B}\boldsymbol{\lambda}$ where

$$a_j = \sum_{i=1}^{I} B_x(\boldsymbol{r}_i)\; b_{xj}(\boldsymbol{r}_i) \tag{4.2.26}$$

and

$$B_{jm} = \sum_{i=1}^{I} b_{xj}(\boldsymbol{r}_i) b_{xm}(\boldsymbol{r}_i) \; + \omega\Omega \int_{-\infty}^{\infty} dk_x \int_{-\infty}^{\infty} dk_y \; k_r^2 \widetilde{S}_j \widetilde{S}_m \tag{4.2.27}$$

defining the vector $\boldsymbol{\lambda}$ whose solution is found by identifying the pseudo-inverse matrix $\boldsymbol{B}^{-1}$ allowing the optimal stream function coefficients to be expressed as

$$\boldsymbol{\lambda} = \boldsymbol{B}^{-1}\boldsymbol{a}. \tag{4.2.28}$$

The optimal stream function can then be formed and the wire paths of the coils can be extracted as contours of the optimised stream function.

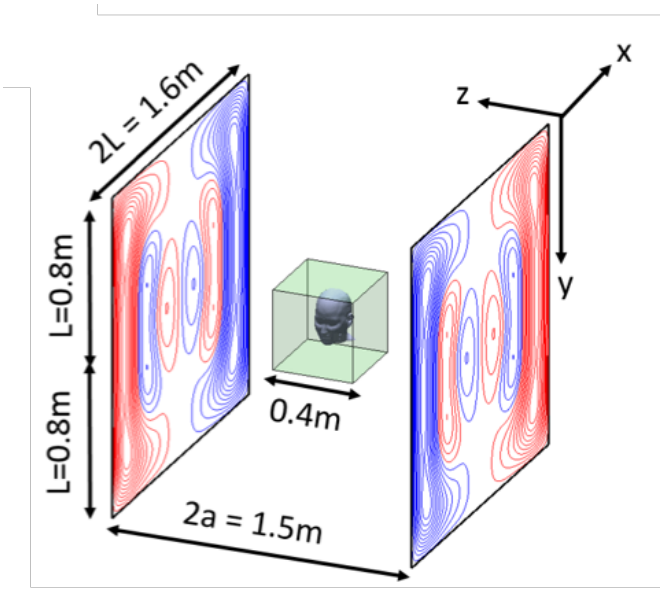



Figure 4.1: *The bi-planar geometry of the coil system. Two square planes of side length 2L = 1.6 m are placed a distance 2a = 1.5 m apart. Each coil produces a homogeneous field or field gradient (to within ±5%) inside the region highlighted by the green cube.*

## 4.3 Methods

### 4.3.1 Coil design and construction

Programmes were written in MATLAB (The MathWorks Inc.) to design bi-planar coils based on the mathematics outlined in section 4.2. The maximum dimensions of the coils were determined by the size and layout of the MSR which contains a 275-channel SQUID-based MEG system (CTF, Coquitlam, BC, Canada) and the need to produce homogeneous fields and field gradients over a central volume which would comfortably contain the head, and the OPM array, allowing for head-movements by a seated participant. Based on assessment of average adult head sizes and the size of the OPM-MEG scanner-cast it was determined that a $40 \times 40 \times 40$ cm$^3$ region over which the field or field gradient was homogeneous to within ±5% would be required.

The final dimensions which met both conditions were square planes with side length $2L = 1.6$ m and a separation of $2a = 1.5$ m. These are shown for a single coil in Figure 4.1. The $B_x$, $B_y$, $G_x$, $G_y$ and $G_{xy}$ coils were designed using 16 harmonics with $N = M = 4$ and the field was evaluated over $I = 320$ target points. The $B_z$ and $G_z$ coils were designed with 9 harmonics with $N = M = 3$ and the field was evaluated over $I = 75$ target points. Fewer harmonics and target points are required to limit the field variation for the $B_z$ and $G_z$ coils due to the high degree of rotational symmetry of these coils about the $z$ axis (as in a Helmholtz coil). Breaking the planar symmetries requires more harmonics and target points to produce fields with the same level of homogeneity.

Since the symmetry of the bi-planar arrangement needed to produce the $G_{xx}$ field gradient coil (symmetric in $x$ and $y$, but anti-symmetric in $z$) is the same as that of the coil arrangement that produces the field gradient $dB_z/dz$ additional steps have to be taken to force the field to follow the right spatial form. A breaking of the four-fold symmetry of the stream function for rotation about the $z$-axis is required, which can be achieved by removing the first component of the stream function in the $x$ dimension. The stream function components included are then $n = 2, 3, 4, 5$ and $m = 1, 2, 3, 4, 5$. The field was evaluated over $I = 320$ target points. In designing each coil the tuneable power dissipation parameter was manually adjusted to the minimum value that produced deviation of less than 5% of the field or gradient from uniformity within the $40 \times 40 \times 40$ cm$^3$ target region.

Six of the eight coils which were designed were constructed to allow nulling of the uniform field components $B_x$, $B_y$ and $B_z$ as well as three field gradients $G_x$, $G_y$, $G_z$. Designs for the remaining gradients $G_{xy}$ and $G_{xx}$ were not constructed. (The $G_{xy}$ coil was later constructed, but not used in the experiments described in this chapter). It was chosen to only construct gradient coils with field variation in the $z$ direction as this would allow for simple construction of a reference array,

see Section 4.3.2.

To allow construction of the coils from continuous wires, the number of contours of the optimised stream function was chosen to yield buildable coils with wire paths formed by manually inserting links between contours. Coils were mounted on two sheets of medium density fibreboard (MDF), measuring $1.8 \times 1.8$ m$^2$ which were each attached to a wooden support structure such that the centre of the coil set was raised by 1.1 m from the floor level of the MSR. This meant that with a seated subject the head-mounted OPMs would be located in the volume within which the coils generate uniform fields or field gradients. Coil designs were printed on paper sheets which were attached to the wooden boards using wallpaper paste. Enamelled copper wire of diameter 0.56 mm was laid on each printed path and fixed in place using masking tape. Additional coils were added in layers by repeating this procedure.

The two coils in each bi-planar coil pair were connected in series to a low-noise coil driver which produced a maximum voltage of ±4 V and were supplied by QuSpin. These drivers were controlled using a LabVIEW (National Instruments (NI) Corporation, programme interfaced to a NI-9264, 16-bit, ±10 V digital to analogue converter (DAC) voltage output module. An appropriately-sized resistor was added in series with each coil circuit so that a maximum field of around ±40 nT could be produced. The NI-9264 has a least significant bit (lsb) voltage of $^{20}/_{2^{16}} \approx 300$ $\mu$V, equivalent to a field step size of 30 pT. For field gradient coils a resistor was added such that around 25 nT/m could be produced (lsb size of 20 pT/m).

### 4.3.2 Automated field nulling procedure

To use the bi-planar coils to null the remnant magnetic field inside the MSR a reference array of four QuSpin OPMs was set up to sample the static field. Since

the OPMs have two sensitive axes of measurement, four OPMs could be used to measure the three field components, $B_x$, $B_y$, $B_z$ at two positions spatially separated in the $z$-direction by 30 cm. The magnitude of the field can be taken from single sensor outputs (or the mean of two measurements) and the field gradient can be estimated via subtraction of two measurements. The setup of the reference array is shown in Figure 4.2.

A LabVIEW-based controller was developed to interface with the reference array and the coil drivers. The sensors were operated in their field-zeroing mode where magnetic field in the range 0 to 50,000 pT are reported (as described in Chapter 2) [Shah and Hughes, 2015, Shah et al., 2018]. Estimates of the field and field gradient were passed to proportional integral derivative (PID) control loops which varied the voltage applied to each coil to drive the field and field gradient measurements towards zero (in practice reaching levels of around 10 pT and 50 pT/m respectively). Basic PID theory is described in Chapter 3.

Once nulling was completed the PIDs were switched off, and stable currents were applied to the coils. The nulling sensors could then be set up in their normal measurement mode and used as reference sensors: they were placed close enough to the head to monitor variations in the background interference during the course of an experiment, but far enough away to be relatively insensitive to magnetic fields generated by the brain. This meant that a synthetic gradiometer could be formed, by applying linear regression to the brain data using the outputs of the reference sensors as predictors [Boto et al., 2017].

### 4.3.3 Field mapping to assess nulling performance

The reductions in the fields, and field gradients afforded by the bi-planar coil set were quantified by mapping the field in a single plane before and after field nulling using the automated procedure described above. The field was mapped

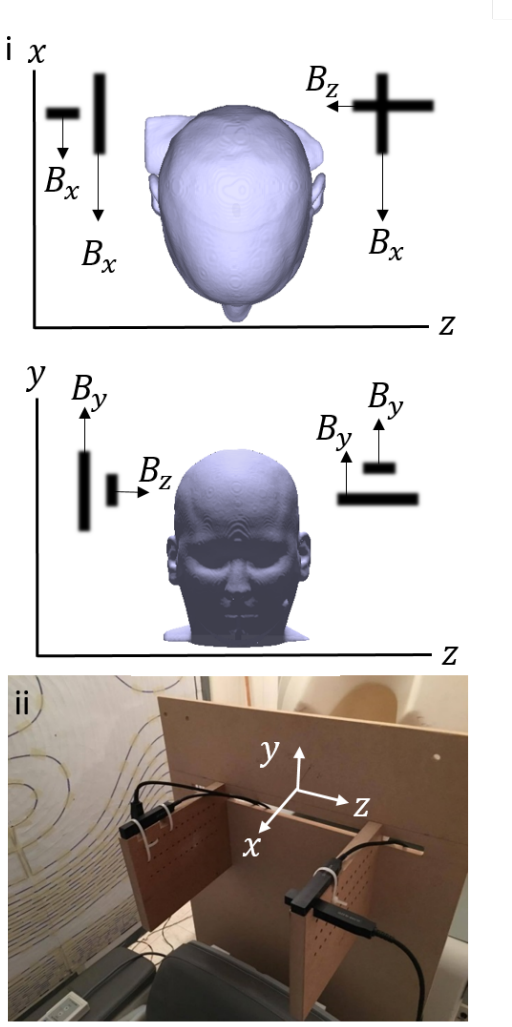



Figure 4.2: *Reference array setup for a MEG recording. i) The positions and orientations of the four OPMs used for reference measurements. The OPMs are positioned such that a measurement of each field component can be made at two different z-positions to provide a measure of the field gradients. ii) The reference array as set up for an experiment.*

over a central $20 \times 20$ cm$^2$ region in the $x$-$z$ plane which was centred between the reference sensors (separated by 30 cm in the $z$-direction). By recording the output of the OPM's on-sensor coils when operating in the field-zeroing mode, measurements of static background field were taken with a single OPM sensor.

The sensor was placed at two different orientations at each position on a 5-cm grid spanning the $20 \times 20$ cm$^2$ region to obtain a representation of the spatial variation of the three Cartesian components of the static magnetic field. The field was then nulled using the bi-planar coils and the process repeated. The data were interpolated onto a 1-cm resolution grid and displayed as field maps to show the reduction in field strength and spatial variation of the field over the $20 \times 20$ cm$^2$ plane, that was produced by the field nulling coils.

### 4.3.4 Stability of null over time

The stability of the field nulling over time is important to ensure accurate MEG measurements can be made. Although regression of reference sensor data can remove trends, it cannot account for gain changes in the sensors or recover information if the sensors go outside their dynamic range. As no correction of the coil currents to account for a time-varying background field was applied, an investigation into the stability of the field nulling as well as the level of the noise introduced by the coil drivers was performed.

An array of 7 OPMs was placed inside an empty scanner-cast positioned between the reference sensors. An initial measurement of the static background field was taken with the nulling system switched off. The field nulling was then performed as usual, and the currents in the bi-planar coils were set and then held constant. The magnitude of the static background field was measured every 5 minutes over a 30-minute period using the on-sensor coils of the 7 OPMs. The OPMs were then switched off and the door to the MSR opened (none of the experimental

equipment was displaced) for 30 minutes, while the currents in the bi-planar coils were still held constant. The sensors were then rebooted and the door to the MSR closed, the static field was again measured once every 5 minutes over an additional 30-minute period.

The power spectral density of OPM signals recorded inside an empty MSR was also investigated with the field nulling system on and off. A single OPM in the empty scanner-cast was chosen and recordings were completed over 60-s periods. For these measurements, only the radial component of the magnetic field was recorded using LabVIEW interfaced with a 16-bit NI-9205 Data Acquisition card sampling at 1200 Hz. Environmental interference is prominent in the recordings, as no interference-reduction methods were applied to these magnetometer data; any additional interference produced by the coils and their associated electronics is therefore easy to identify.

### 4.3.5 Demonstrating the allowed range of motions

The effects of controlled motions were investigated to demonstrate the wide range of head movements that a participant can make when the field nulling system is in operation, without causing any OPM sensor in a head-mounted array to go outside its ±1.5 nT operating range (when operating at the standard sensor gain setting of 2.7 V/nT).

To monitor the movement of the participant's head during experiments, motion data were captured using an OptiTrack V120:Duo camera system (NaturalPoint Inc., Corvallis) which provides sub-millimetre and sub-1-degree precision optical tracking of a rigid body with six degrees of freedom: translations ($x$, $y$, $z$) and rotations (*pitch*, *yaw*, *roll*) as shown in Figure 4.3A. The system comprises two cameras, each of which has an associated array of 15 infrared LEDs that are used to illuminate multiple, highly reflective markers, that were attached to the

scanner-cast as shown in Figure 4.3B. The camera system initially identifies the individual marker positions and uses their combined co-ordinates to define a rigid body; rotation and translation of the rigid body can then be monitored at the camera's 120 Hz frame rate. In these experiments, the rigid body was formed from 5 markers.

Thirteen visual marks (numbered from 0 to 12) were fixed either to a bench, placed 70 cm in front of the participant, or to the edges of the two coil planes, as shown in Figure 4.3C-D. Marks 0 - 4 were sited close to the centre of the participant's field of view when they were seated and looking directly forwards. Marks 5-8 were positioned so that the participant would have to rotate their head approximately $\pm 25^{\circ}$ from the centre point to bring them to the centre of their field of view. Marks 9 – 12 required larger head rotations of around $\pm 35^{\circ}$ from the centre point. The movements required to view marks 9 – 12 were at the limit of what was deemed comfortable for the participant to achieve without rotation of the body. To enable a controlled assessment of the effect of these motions on OPM recordings, the participant was first asked to focus on mark 0 (central) and then after 10 s the participant was instructed to switch their gaze to mark 1. After a further 10 s the participant was instructed to look at mark 2 and so on. After 4 markers had been viewed the participant was asked to return to viewing mark 0 before beginning the viewing of the next 4 marks. The full experiment lasted 160 s.

Magnetic field data were simultaneously recorded from an array of 18 OPMs which was mounted in the scanner-cast to provide good coverage of the visual cortex. Positioning the OPMs in the slots over the visual cortex in particular generates an exaggerated movement of the sensor locations at the back of the head during the head movements needed to view the different marks, hence providing the most challenging setting in terms of OPM movement.

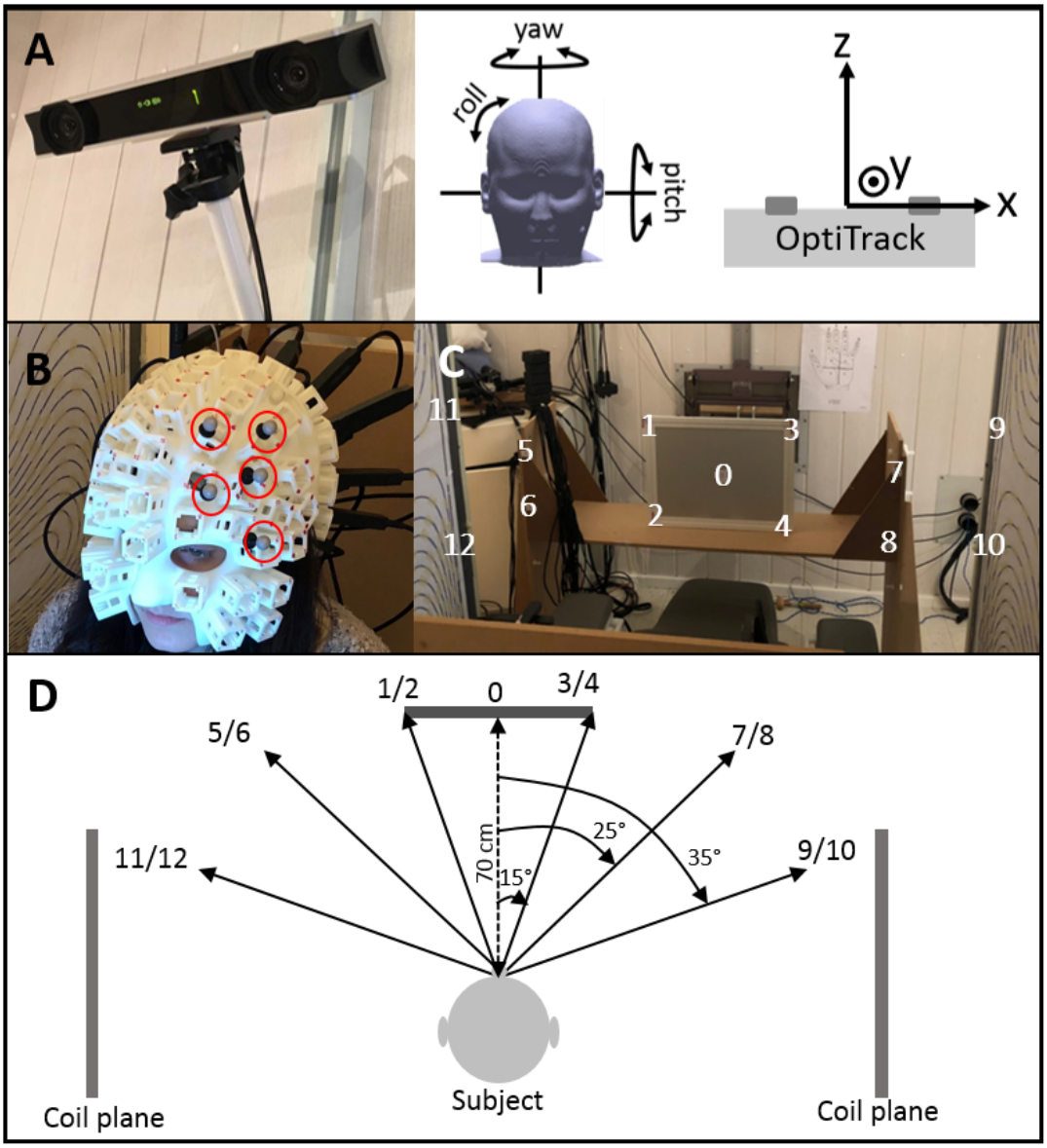



Figure 4.3: *Optical tracking of the head to measure OPM response to controlled movements. A) The OptiTrack V120:Duo optical tracking camera is used to measure subject movement. The translations (x, y, z) and rotations (pitch, yaw, roll) are measured in the camera's frame of reference. B) The system uses infra-red LEDs to illuminate a series of 5, highly reflective markers (circled in red) positioned on the surface of the scanner-cast. These markers are combined to form a single rigid-body which is tracked during an experiment. C) A series of 13 numbered marks were positioned within the field of view of the subject. The subject was instructed to shift their gaze to these marks. D) Approximate angular movements of the head required to shift the gaze to each mark.*

Recordings of the sensor analogue outputs were made using LabVIEW interfaced with a set of three 16-bit NI-9205 Data Acquisition cards sampling at 1,200 Hz. In these experiments, only the fields radial to the head surface were measured. At the start of the experiment, currents through the bi-planar coils were optimised to null the ambient fields as described previously. The residual fields at each sensor were then zeroed using the on-sensor coils. Following this, the MEG recording was initiated and the participant was instructed to start making the movements.

As the magnetic fields reported by the OPMs are affected by interference from fluctuating background fields, as well as field changes due to head motion in the remnant Earth's field, multiple linear regression analyses were used [Boto et al., 2017]. A design matrix of predictors was formed using the 6 motion parameters (up-sampled through linear interpolation to an effective sampling rate of 1200 Hz), as well as the signals from the 4 reference magnetometers. Regression was performed over the full dataset.

### 4.3.6 Measurement of retinotopy: data acquisition

To test the fidelity of the MEG data captured with head movement following field nulling, a novel means to exploit the retinotopic organisation of the visual cortex was devised. Traditionally in retinotopic mapping experiments the participant remains still with their gaze fixed centrally, while a stimulus is moved around the participant's field of view [Engel et al., 1997]. Analysis then reveals activation of the visual cortex in different locations depending on the position of the stimulus in the visual field. In the simplest case, a stimulus presented in the right visual hemifield will evoke activity in left visual cortex, and vice-versa. Here, taking advantage of the head movement allowed by the field-nulling bi-planar coil set, this simple aspect of retinotopic mapping is demonstrated by making measurements with the stimulus fixed in position while the participant physically moves

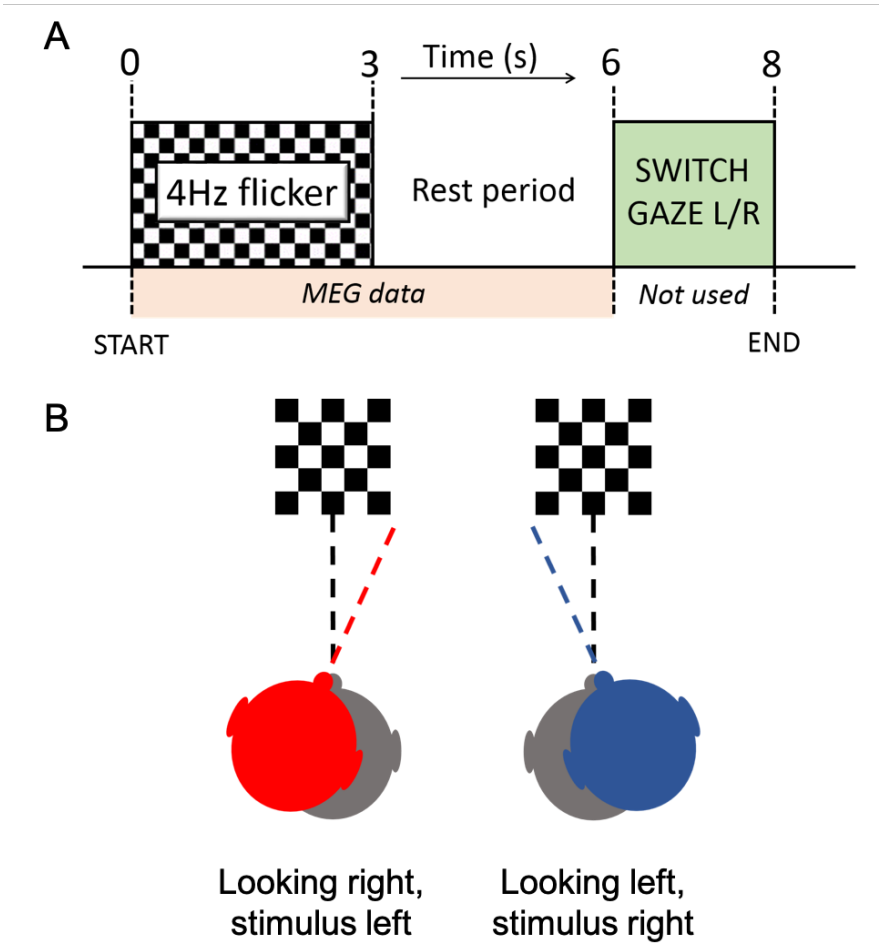



Figure 4.4: *Experimental structure for the measurement of retinotopy. A) The trial structure used for the retinotopy experiment. Data were analysed only from the stimulus and rest periods, during the switch-gaze period the participant was free to move their head or remain fixated. B) Approximate directions of subject gaze and corresponding stimulus locations for the two conditions.*

their gaze by head rotation/translation.

Presentation (Neurobehavioral Systems Inc., Berkeley, CA) was used to generate a checkerboard pattern reversing at 4 Hz, which was expected to produce a driven, 8 Hz, electrophysiological response in the visual cortex. This pattern was projected onto a screen positioned 50 cm away from the participant's eyes. The checkerboard had dimensions of 10 $\times$ 10 cm$^2$ and subtended a visual angle of 11° $\times$ 11°. Each check had dimensions of 2 $\times$ 2 cm$^2$ and subtended a visual angle of 2.3° $\times$ 2.3°.

Two crosses were placed on the top corners of the stimulus presentation screen as fixation points, so that when the participant fixed their gaze on these crosses the stimulus would be in either the lower right, or lower left, quadrant of their central visual field. Magnetic field data were recorded from an array of 18 OPMs that were mounted in a subject-specific 3D-printed scanner-cast to provide good coverage of the visual cortex [Boto et al., 2017]. Each sensor measured a single field component that was radial to the surface of the head and was operated with the standard sensor gain setting of 2.7 V/nT.

The timing of the stimulus was set such that a single trial lasted for 8 s. The reversing checkerboard was on for 3 s (16 cycles) followed by a 3 s rest period during which the screen showed only a central cross. In the final 2 s of each trial the words '*switch gaze*' were shown on the screen. The participant was instructed to choose whether to switch their gaze to the opposite side of the screen, or to remain still during this period. The trial structure is detailed in Figure 4.4. There were 80 trials in total, and importantly, at the time of acquisition, in any one trial it is not known upon which of the two crosses the participant was fixated (and hence it is not known in which visual hemifield the stimulus was located). To address this issue, the participant's head location and orientation were recorded throughout the experiment using the OptiTrack camera. Prior to MEG recording, a calibration measurement was performed in which the participant was simply asked to focus on the two crosses in turn.

### 4.3.7 Measurement of retinotopy: data analysis

The OPM-MEG data acquired during our retinotopy experiment were processed using a beamformer approach, as introduced in Chapter 1. Using information from the OptiTrack camera, the data were segmented into two sub-sets comprising trials where the stimulus appeared on the left, or on the right. Regression of

the data with motion parameters and the signals from the reference magnetometers was performed on a trial-by-trial basis. Data were then frequency-filtered between 4 Hz and 12 Hz. The resulting two subsets of data were averaged over trials. Data averaging prior to beamforming ensures that the weights are tuned to the trial-averaged steady state response of interest, i.e. any alpha modulation (e.g. a decrease in alpha power during visual stimulation) associated with the visual stimulus around the same frequency band as the driven response is averaged out [Brookes et al., 2010].

Three covariance matrices were derived from the time-averaged data during left visual stimulus presentation: $\boldsymbol{C_{la}}$ representing the data covariance in the (0 s $< t <$ 3 s) active window (when the stimulus was on), $\boldsymbol{C_{lc}}$ representing the data covariance in the (3 s $< t <$ 6 s) control time window (when the stimulus was off, but before any movement) and $\boldsymbol{C_l} = (\boldsymbol{C_{la}} + \boldsymbol{C_{lc}})/2$ which is the average of the two, representing the whole trial before gaze shifting. Three equivalent covariance matrices ($\boldsymbol{C_{ra}}$, $\boldsymbol{C_{rc}}$ and $\boldsymbol{C_r}$) were constructed for the right visual stimulus presentation.

The covariance matrices $\boldsymbol{C_l}$ and $\boldsymbol{C_r}$ were regularised using the Tikhonov method with a regularisation parameter which was 1% of the leading eigenvalue of the unregularised matrices. The regularised matrices $\boldsymbol{C}_{l_{reg}}$ and $\boldsymbol{C}_{r_{reg}}$ were used to form independent beamformer weights vectors $\boldsymbol{w_{l\Theta}}$ and $\boldsymbol{w_{r\Theta}}$ for a given source position and orientation $\Theta$ calculated for each sub-set of data as

$$\boldsymbol{w}_{l\Theta}^{T} = \frac{\boldsymbol{l}_{\Theta}^{T}\, \boldsymbol{C}_{l\ reg}^{-1}}{\boldsymbol{l}_{\Theta}^{T}\, \boldsymbol{C}_{l_{reg}}^{-1}\, \boldsymbol{l}_{\Theta}} \tag{4.3.1}$$

and

$$\boldsymbol{w}_{r\Theta}^{T} = \frac{\boldsymbol{l}_{\Theta}^{T}\, \boldsymbol{C}_{r\ reg}^{-1}}{\boldsymbol{l}_{\Theta}^{T}\, \boldsymbol{C}_{r_{reg}}^{-1}\, \boldsymbol{l}_{\Theta}} \tag{4.3.2}$$

where $\boldsymbol{l}_\Theta$ is the lead field vector. A spherically-symmetric conductor was assumed when calculating lead fields. The magnetic field outside the sphere due to a current dipole inside was calculated using the analytical formula introduced by Sarvas, as described in Chapter 1 [Sarvas, 1987]. Computing separate beamformer weights for each data subset maximises the spatial specificity of the resulting beamformer images [Barratt et al., 2018]. pseudo-T-stat values were calculated as

$$T_{l\Theta} = \frac{\boldsymbol{w}_{l\Theta}^T \boldsymbol{C_{la}} \boldsymbol{w}_{l\Theta} - \boldsymbol{w}_{l\Theta}^T \boldsymbol{C_{lc}} \boldsymbol{w}_{l\Theta}}{2\boldsymbol{w}_{l\Theta}^T \boldsymbol{w}_{l\Theta}} \tag{4.3.3}$$

and

$$T_{r\Theta} = \frac{\boldsymbol{w}_{r\Theta}^T \boldsymbol{C_{ra}} \boldsymbol{w}_{r\Theta} - \boldsymbol{w}_{r\Theta}^T \boldsymbol{C_{rc}} \boldsymbol{w}_{r\Theta}}{2\boldsymbol{w}_{r\Theta}^T \boldsymbol{w}_{r\Theta}}. \tag{4.3.4}$$

Based on these pseudo-T-statistical images, two locations of interest were selected (1 and 2) at the peaks of each image. Beamformer-reconstructed signals were calculated for both using the two data sub-sets where $\boldsymbol{m_l}(t)$ and $\boldsymbol{m_r}(t)$ represent the trial averaged MEG data recorded by the OPMs when the stimulus was in the left and right visual hemifields, respectively.

This resulted in four 'virtual electrode' time courses: $q_{r1}(t) = \boldsymbol{w}_{r1}^T \boldsymbol{m_r}(t)$ represents the time course of electrical activity at location 1, during right hemifield stimulation, $q_{r2}(t) = \boldsymbol{w}_{r2}^T \boldsymbol{m_r}(t)$ represents the time course of electrical activity at location 2, during right hemifield stimulation. Similarly, $q_{l1}(t) = \boldsymbol{w}_{l1}^T \boldsymbol{m_l}(t)$ represents the time course of electrical activity at location 1, during left hemifield stimulation, $q_{l2}(t) = \boldsymbol{w}_{l2}^T \boldsymbol{m_l}(t)$ represents the time course of electrical activity at location 2, during left hemifield stimulation.

These four time courses were Fourier transformed, and then tested for the expected peak at 8 Hz. It is expected that peak locations 1 and 2 would appear in

the contralateral (right and left) hemispheres in response to left-and-right-sided visual stimulation, respectively. It is also expected that the 8 Hz response would only be observed in contralateral, and not ipsilateral (same side as stimulation) visual cortex.

## 4.4 Results

### 4.4.1 Coil designs

Figures 4.6-4.20 show the optimised stream functions, extracted wire paths and contours of the spatial variation of the desired magnetic field or magnetic field gradient component produced by each of the eight coils ($B_x$, $B_y$, $B_z$, $G_x$, $G_y$, $G_z$, $G_{xy}$ and $G_{xx}$) that were designed. Red and blue colours denote opposite senses of current flow in the coil windings.

The variation in the magnetic field or magnetic field gradient which is produced by each coil was calculated by applying the elemental Biot-Savart expression to the digitised wire paths for a unit current. The variation of the field or field gradient relative to the value at the centre of the coils (or at a value positioned slightly off centre for field gradient coils since the field is zero at the centre for these coils) was then evaluated and contoured as a measure of the homogeneity of the produced field components. The deviation from the desired pattern of field variation was found to be less than 5% within a central region of $40 \times 40 \times 40$ $cm^3$ for all coils.

Table 4.3 shows the calculated and measured coil parameters for the six coils that were constructed and simulated parameters only for the $G_{xx}$ coil. Calculation of coil resistance values assumed that coils were wound using 0.56-mm-diameter copper wire. The coil inductances were calculated from the stream functions using previously published expressions [Martens et al., 1991].

| Coil | Wire length (m) | Resistance ($\Omega$) | Efficiency (nT/mA or nT/m/mA) | Inductance ($\mu$H) |
|---|---|---|---|---|
| $B_x$ | 170 | 11.9 (14.2) | 1.21 (1.13± 0.1) | 544 (619) |
| $B_y$ | 170 | 11.9 (13.3) | 1.21 (1.06± 0.1) | 544 (614) |
| $B_z$ | 186 | 13.0 (13.8) | 7.29 (7.90± 0.1) | 1520 (1290) |
| $G_x$ | 195 | 13.7 (16.1) | 6.75 (6.50± 0.2) | 843 (985) |
| $G_y$ | 195 | 13.7 (15.5) | 6.75 (6.33± 0.6) | 843 (984) |
| $G_z$ | 168 | 11.8 (12.8) | 14.4 (14.0± 1) | 968 (1090) |
| $G_{xy}$ | 97 | 6.83 (7.45) | 0.41 (0.39± 0.1) | 154 (180) |
| $G_{xx}$ | 173 | 12.1 | 0.4 | 562 |

Table 4.3: *Bi-planar coil characteristics. Theoretical results for each coil are shown with measured values in brackets where appropriate. The calculated values of resistance assume that 0.56-mm diameter copper wire was used in coil construction.*

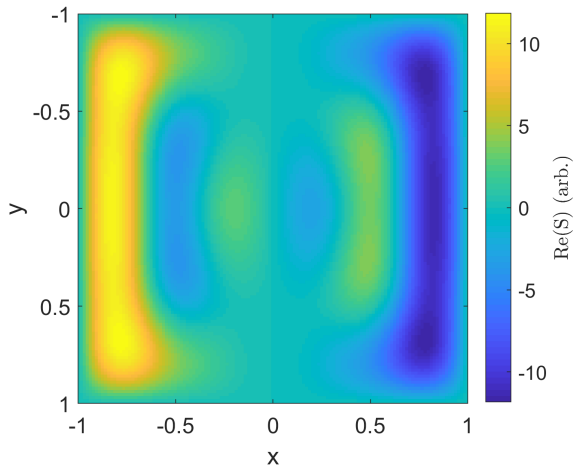



Figure 4.5: *The real part of the optimised stream function for the $B_x$ coil shown for a unit square side length.*

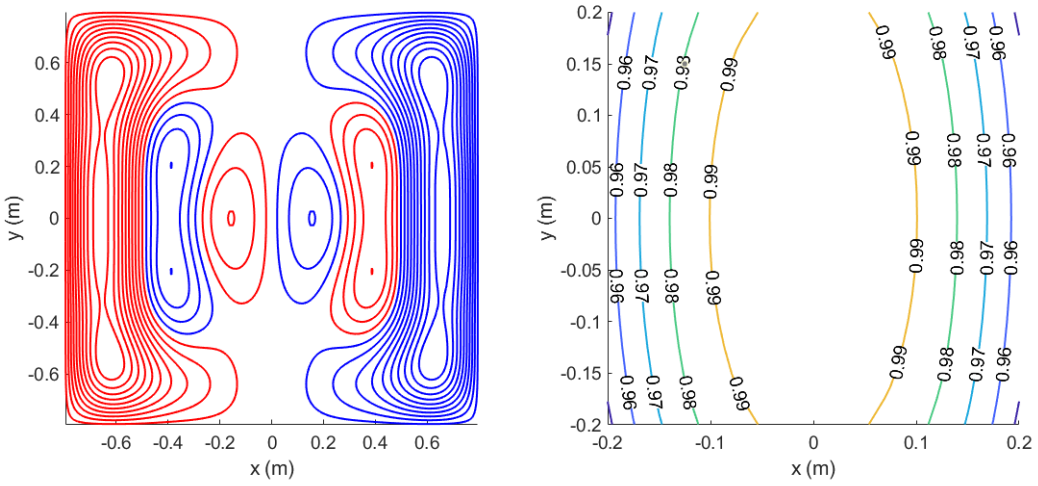



Figure 4.6: *The $B_x$ coil. Wire paths extracted as contours of the optimised stream function shown for a single plane, scaled to the true coil dimensions. Red and blue denote wires with opposite senses of current flow. The contours of the field component $B_x$ are shown in the plane at $z = 0$ m, for $|x|$, $|y| < 0.2$ m. The value of the magnetic field is normalised to the value at the centre of the two planes.*

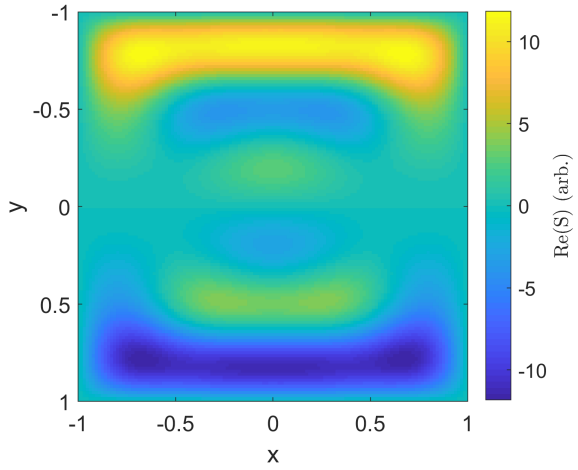



Figure 4.7: *The real part of the optimised stream function for the $B_y$ coil shown for a unit square side length.*

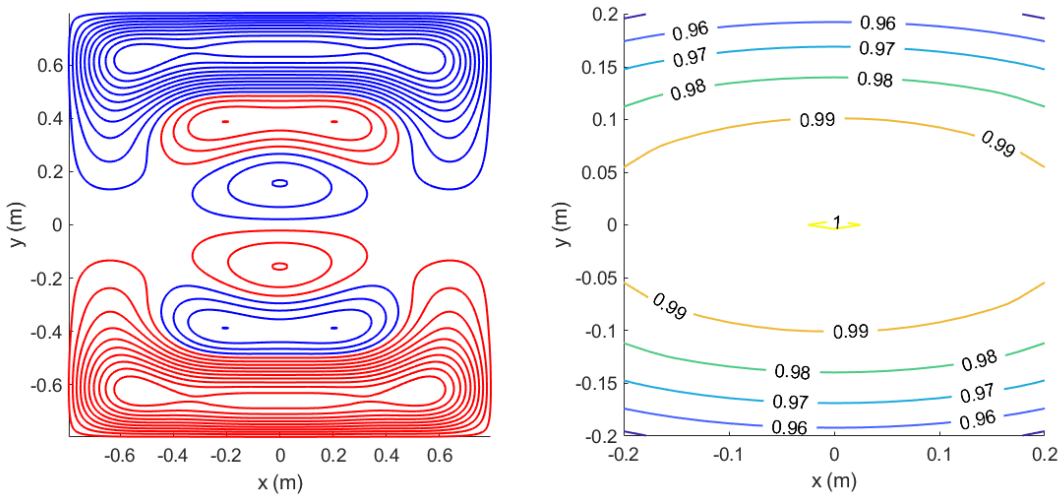



Figure 4.8: *The $B_y$ coil. Wire paths extracted as contours of the optimised stream function shown for a single plane, scaled to the true coil dimensions. Red and blue denote wires with opposite senses of current flow. The contours of the field component $B_y$ are shown in the plane at $z = 0$ m, for $|x|$, $|y| < 0.2$ m. The value of the magnetic field is normalised to the value at the centre of the two planes.*

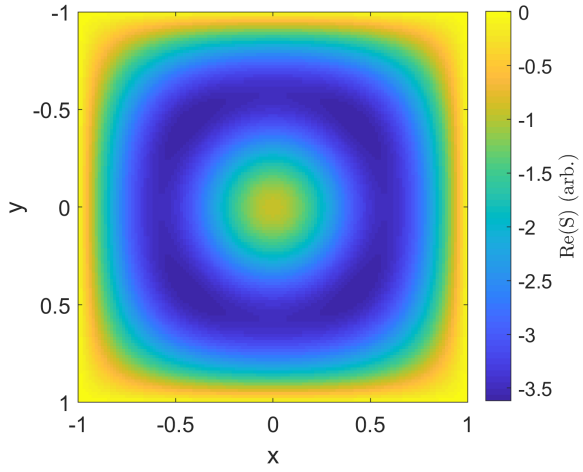



Figure 4.9: *The real part of the optimised stream function for the $B_z$ coil shown for a unit square side length.*

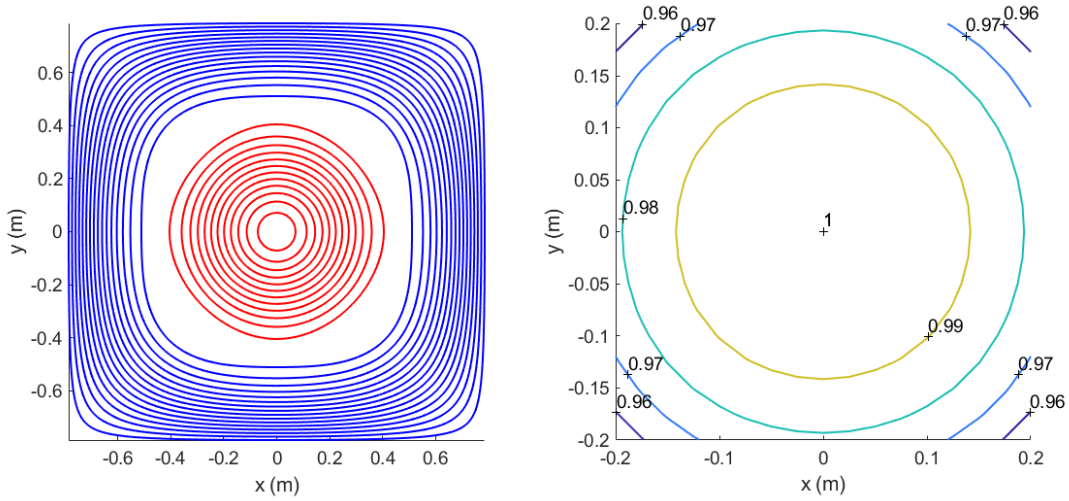



Figure 4.10: *The $B_z$ coil. Wire paths extracted as contours of the optimised stream function shown for a single plane, scaled to the true coil dimensions. Red and blue denote wires with opposite senses of current flow. The contours of the field component $B_z$ are shown in the plane at $z = 0$ m, for $|x|$, $|y| < 0.2$ m. The value of the magnetic field is normalised to the value at the centre of the two planes.*

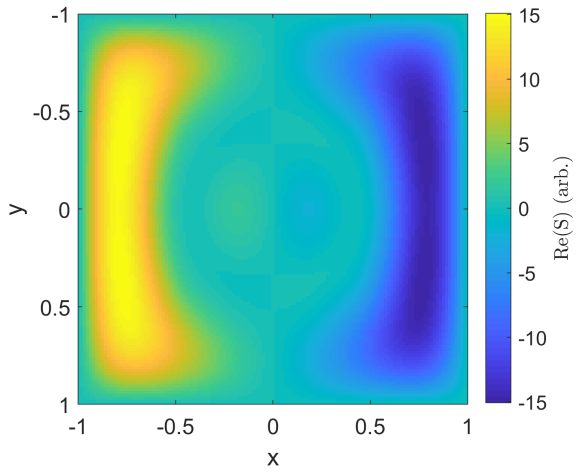



Figure 4.11: *The real part of the optimised stream function for the $G_x = dB_x/dz$ coil shown for a unit square side length.*

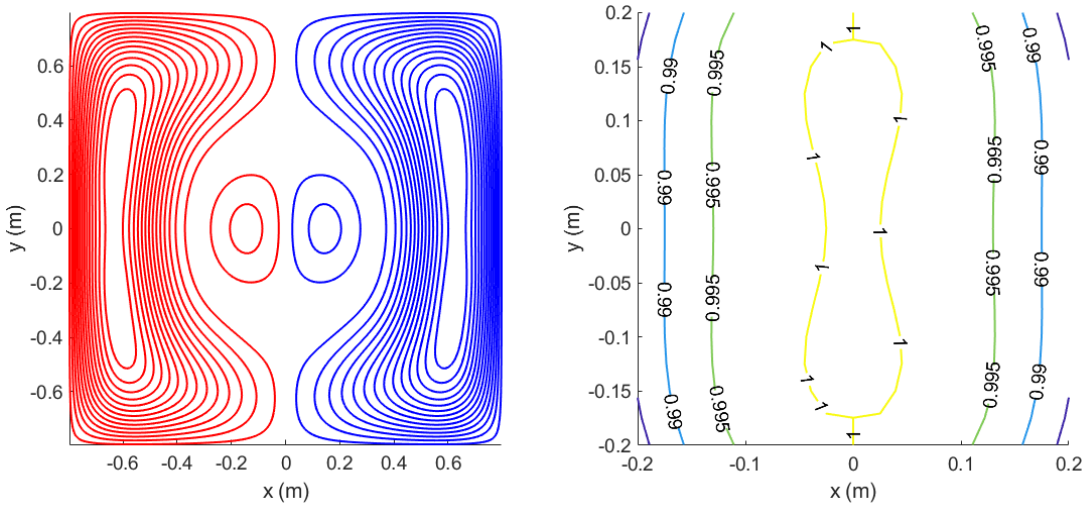



Figure 4.12: *The $G_x = dB_x/dz$ coil. Wire paths extracted as contours of the optimised stream function shown for a single plane, scaled to the true coil dimensions. Red and blue denote wires with opposite senses of current flow. The contours of the magnetic field gradient component are estimated as $B_x/z$ for each $z$ position and are shown in the plane at $z = 0$ m, for $|x|, |y| < 0.2$ m. The magnetic field was normalised to a value slightly off centre of the two planes.*

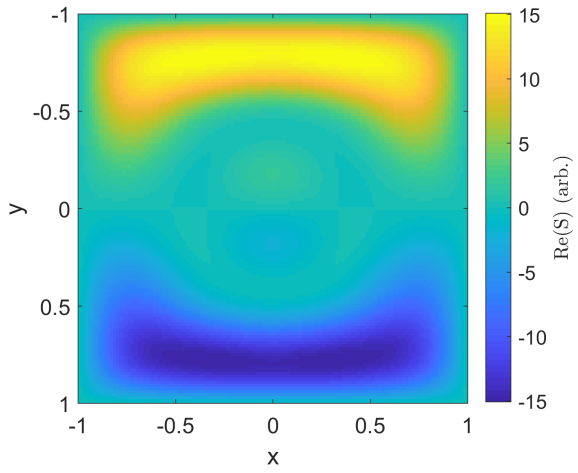



Figure 4.13: *The real part of the optimised stream function for the $G_y = dB_y/dz$ coil shown for a unit square side length.*

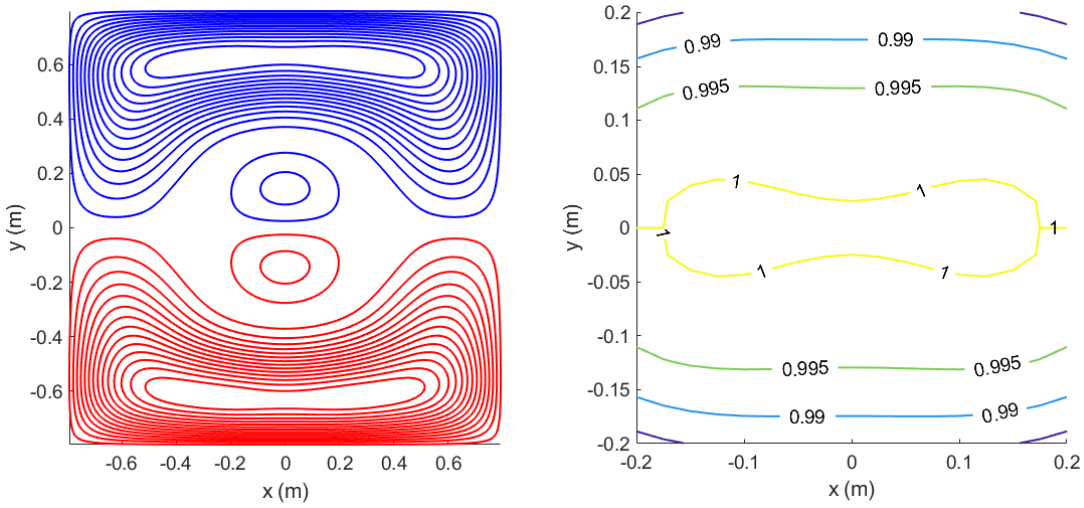



Figure 4.14: *The $G_y = dB_y/dz$ coil. Wire paths extracted as contours of the optimised stream function shown for a single plane, scaled to the true coil dimensions. Red and blue denote wires with opposite senses of current flow. The contours of the magnetic field gradient component are estimated as $B_y/z$ for each $z$ position and are shown in the plane at $z = 0$ m, for $|x|, |y| < 0.2$ m. The magnetic field was normalised to a value slightly off centre of the two planes.*

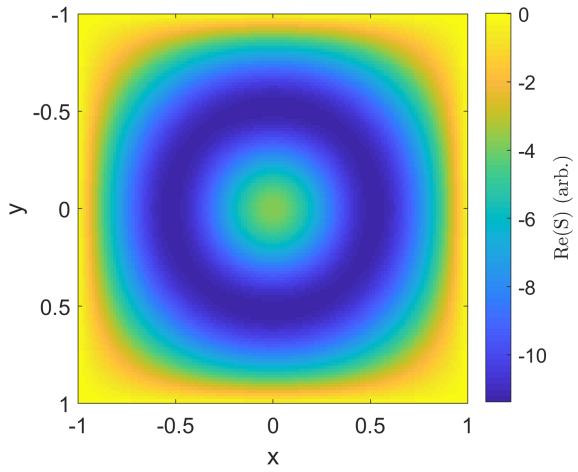



Figure 4.15: *The real part of the optimised stream function for the $G_z = dB_z/dz$ coil shown for a unit square side length.*

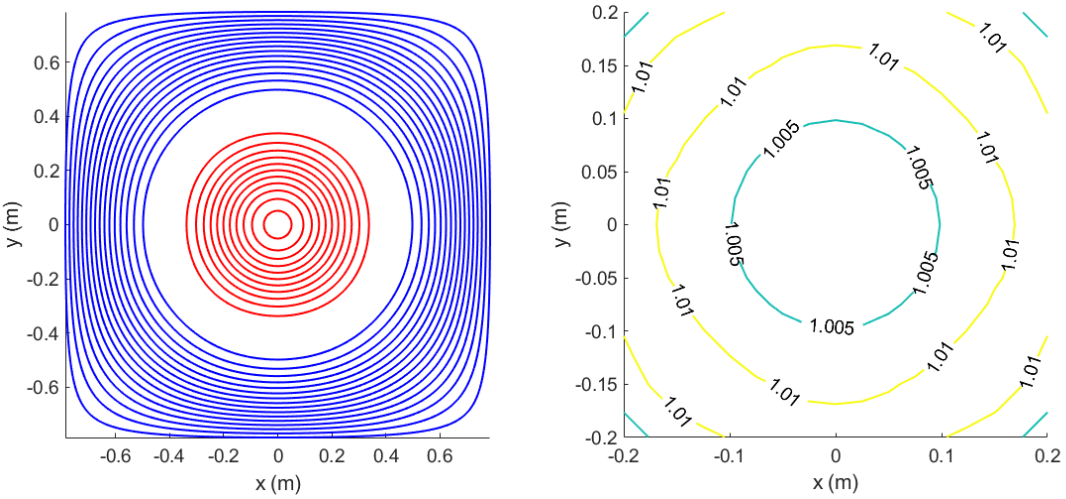



Figure 4.16: *The $G_z = dB_z/dz$ coil. Wire paths extracted as contours of the optimised stream function shown for a single plane, scaled to the true coil dimensions. Red and blue denote wires with opposite senses of current flow. The contours of the magnetic field gradient component are estimated as $B_z/z$ for each $z$ position and are shown in the plane at $z = 0.02$ m, for $|x|$, $|y| < 0.2$ m. The magnetic field was normalised to a value slightly off centre of the two planes.*

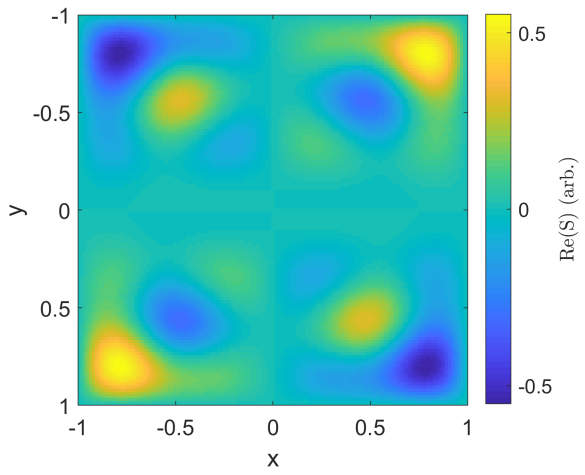



Figure 4.17: *The real part of the optimised stream function for the $G_{xy} = dB_x/dy$ coil shown for a unit square side length*

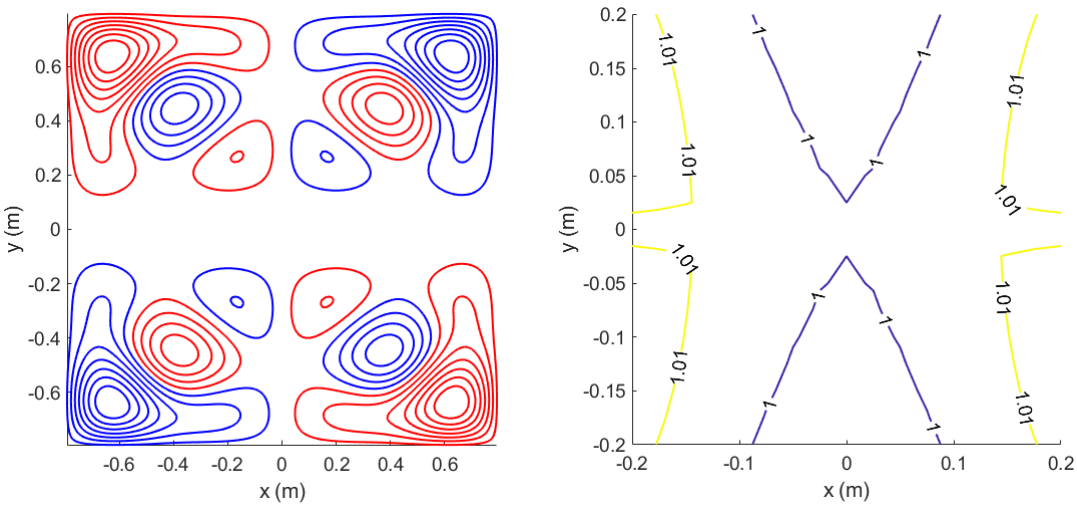



Figure 4.18: *The $G_{xy} = dB_x/dy$ coil. Wire paths extracted as contours of the optimised stream function shown for a single plane, scaled to the true coil dimensions. Red and blue denote wires with opposite senses of current flow. The contours of the magnetic field gradient component are estimated as $B_x/y$ for each $y$ position and are shown in the plane at $z = 0$ m, for $|x|$, $|y| < 0.2$ m. The magnetic field was normalised to a value slightly off centre of the two planes.*

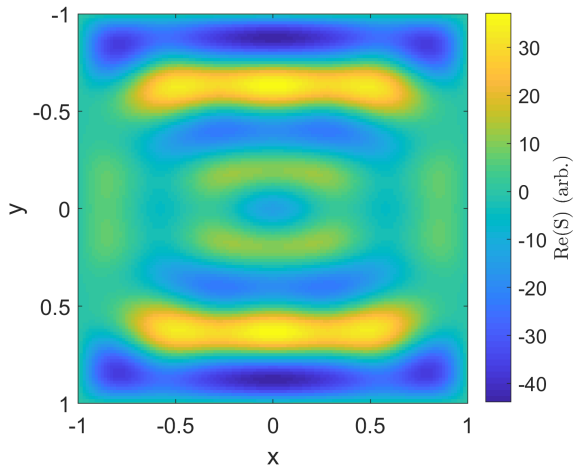



Figure 4.19: *The real part of the optimised stream function for the $G_{xx} = dB_x/dx$ coil shown for a unit square side length.*

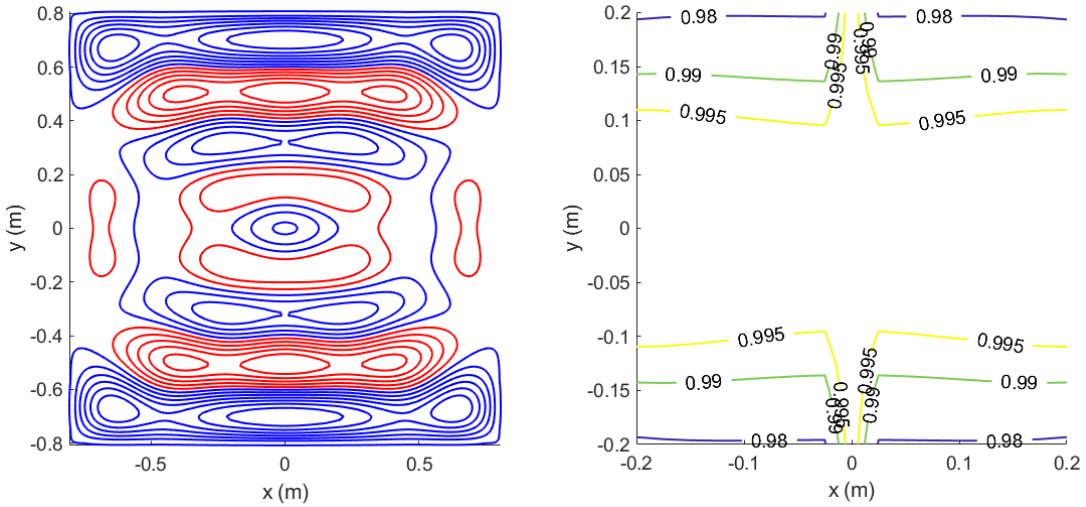



Figure 4.20: *The $G_{xx} = dB_x/dx$ coil. Wire paths extracted as contours of the optimised stream function shown for a single plane, scaled to the true coil dimensions. Red and blue denote wires with opposite senses of current flow. The contours of the magnetic field gradient component are estimated as $B_x/x$ for each $x$ position and are shown in the plane at $z = 0$ m, for $|x|$, $|y| <$ 0.2 m. The magnetic field was normalised to a value slightly off centre of the two planes.*

### 4.4.2 Coil construction

Figure 4.21A shows a $B_z$ coil design wallpapered to the wooden board. A completed $B_x$ coil panel is shown in Figure 4.21B where the masking tape used to hold the wire in place can be clearly seen. The $B_x$ panel was layered on top of the $B_z$ panel and the process repeated until all six coils were constructed. The bi-planar coils as setup for an experiment are shown in Figure 4.21C, the outermost panel is the $G_x$ coil. A seated participant is shown in front of the reference array wearing a scanner-cast containing an array of 13 OPMs, the cryogenic MEG system can be seen behind the reference array.

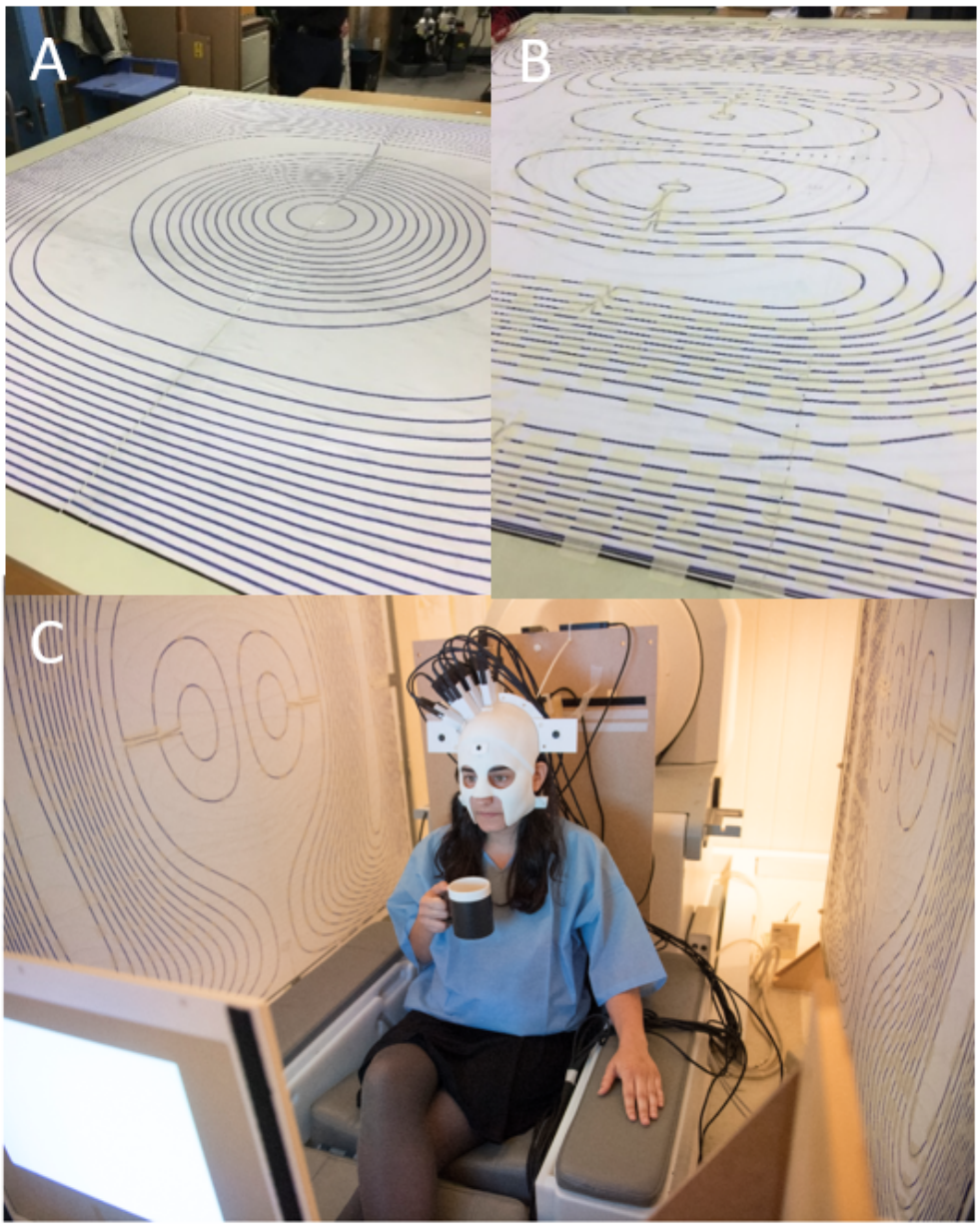



Figure 4.21: *Constructed bi-planar coil system. A) Coil design wallpapered to the wooden plane. B) Completed $B_x$ coil wound using masking tape to hold the wire in place. C) Seated participant wearing a scanner-cast containing an array of OPMs.*

### 4.4.3 Field mapping to assess nulling performance

Currents of less than 30 mA in each coil are required to cancel the 30 nT field and 10 nT/m field gradients (as the efficiency of each coil is within the range of 1 to 8 nT/mA and 6 to 14 nT/m/mA with a coil resistance of $< 10\ \Omega$). The maximum power dissipation is therefore less than 10 mW per coil.

Figure 4.22 shows field maps measured before (i) and after (ii) the automated nulling was applied along with a bar plot of reduction in average field strength (iii), as measured using the field-zeroing procedure with a single OPM sequentially sampling field components at different positions on a reference grid with 5-cm grid spacing.

The mean magnitude of the field vector $|\boldsymbol{B}| = (B_x^2 + B_y^2 + B_z^2)^{1/2}$ fell from 28.0 nT to 0.74 nT, corresponding to a reduction by a factor of 38 (averaged over the full 20 x 20 cm$^2$ plane studied). In terms of spatial field variation, the root mean square deviation from the mean value fell from 0.6 nT to 0.16 nT, a reduction by a factor of 4. The maximum magnitude of the field vector $|\boldsymbol{B}|$ is found to be 29 nT and 1.2 nT respectively. Reductions in each of the six coil field components are reported in Table 4.4.

| Field component | Nulling off (nT or nT/m) | Nulling on (nT or nT/m) | Reduction factor |
|---|---|---|---|
| $B_x$ | 21.8 | 0.47 | 46 |
| $B_y$ | 6.3 | 0.03 | 210 |
| $B_z$ | 16.4 | -0.49 | 33 |
| $G_x$ | 7.4 | 0.55 | 13 |
| $G_y$ | 2.8 | 0.5 | 6 |
| $G_z$ | 6.28 | 1.37 | 5 |

Table 4.4: *Field nulling performance for each field component. Mean values over the mapped region are shown from the field maps taken when nulling was off and on. The factor by which the field was reduced is also reported.*

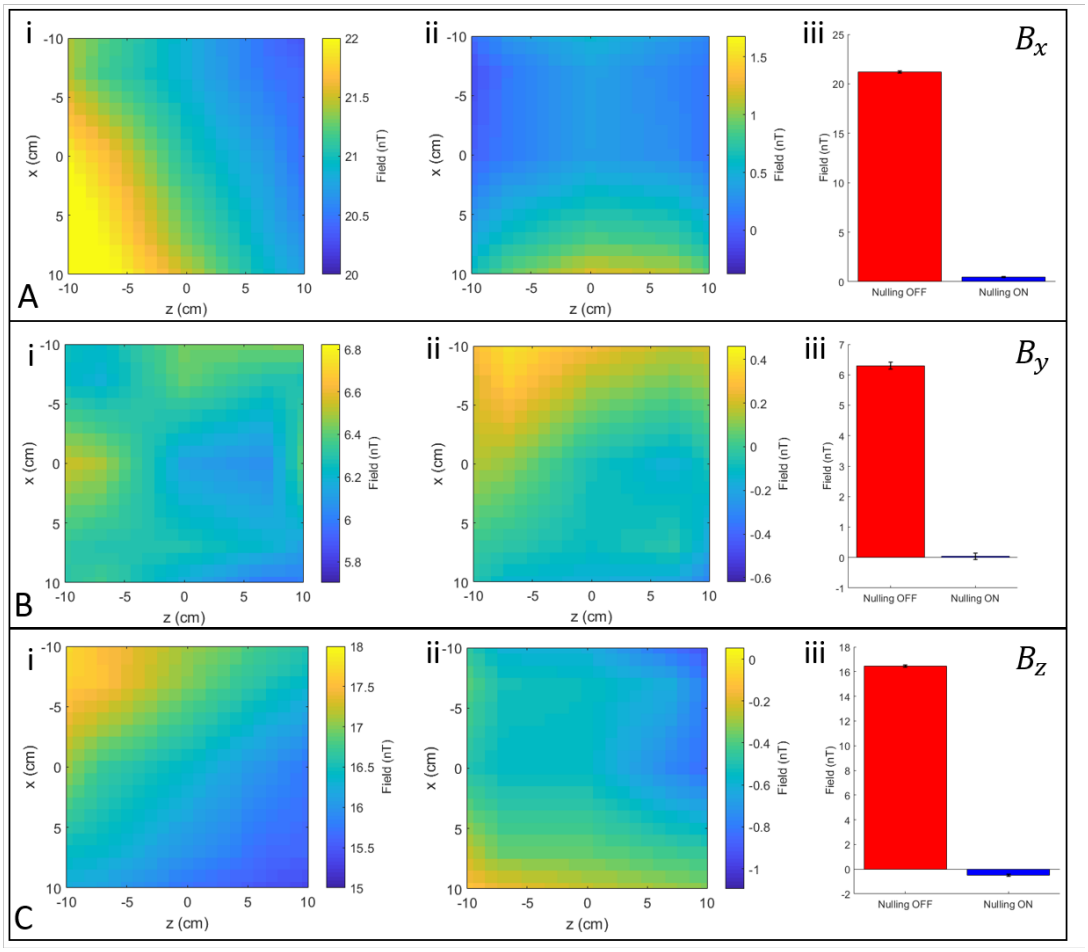



Figure 4.22: *Field nulling performance and maps of spatial variation. A) B) and C) show for $B_x$, $B_y$ and $B_z$ respectively i) a map of the field before nulling is applied ii) a map of the field after nulling is applied and iii) the average field magnitude with error-bars showing the standard deviation of measurement before (red) and after (blue) nulling is applied.*

### 4.4.4 Stability of null over time

The measured field magnitude is plotted as a function of time in Figure 4.23A for the experiment described in Section 4.3.4. Analysis of these data shows that the maximum change in field magnitude over the 90 minutes on any sensor was 0.50 nT, while the average (over all 7 sensors) of the standard deviation over time was $0.18 \pm 0.03$ nT.

These values are both smaller than the $\pm 1.5$ nT dynamic range of the OPMs (in their standard sensor gain setting), showing that the field nulling achieved was sufficiently stable over the duration of our experiments.

The power spectral density of the empty room OPM recordings evaluated using Welch's method in MATLAB with the field nulling on (red) and off (blue) are shown in Figure 4.23B. There is little difference in the two measurements when the OPMs remain still.

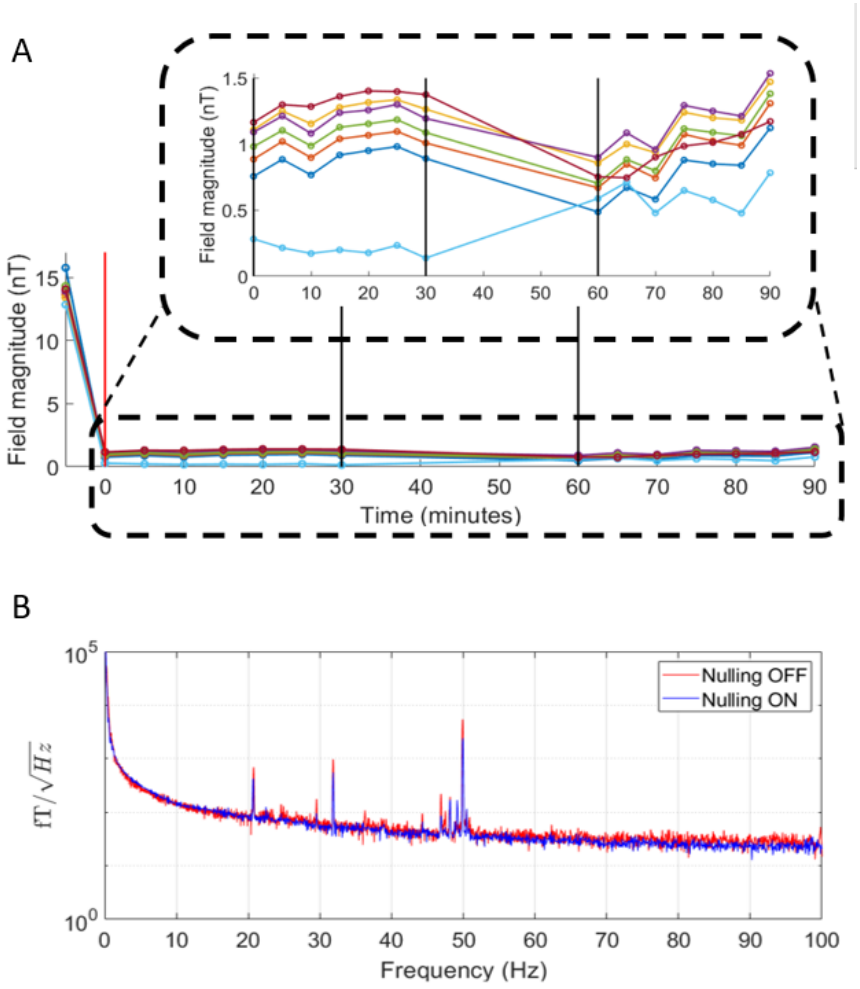



Figure 4.23: *Assessing the stability of the field nulling over time. A) The static field magnitude as reported by the on-sensor coils for an array of 7 OPM sensors at 5-minute intervals over a 30 minute period. The red line shows the results of recordings made when the field nulling was applied, the black lines show a period where the sensors were switched off, and the door to the MSR was left open. There followed an additional 30 minutes during which the door was closed and further field measurements were made. The bi-planar coil currents were held constant throughout the entire 90-minute experiment. B) The power spectra of a single OPM in this scanner-cast recorded with the field nulling OFF (red trace) and ON (blue trace).*

### 4.4.5 Demonstrating the allowed range of motions

Figure 4.24A shows the output of a single OPM (blue) as the subject moved their head. Measurements of the translation (in the $x$-direction) and rotation ($yaw$) of the head that were simultaneously recorded by the OptiTrack camera are also plotted in red and black, respectively, for comparison.

The output of the OPM following linear regression with the 6 motion parameters and the output of the 4 reference sensors is shown in green. It is evident that the sensors remain within their operational range (±1.5 nT in the standard sensor gain setting) even after the largest movements when field nulling is applied. Figure 4.24B-C show bar charts which describe the magnitude of the total rotations $\sqrt{pitch^2 + roll^2 + yaw^2}$ and translations $\sqrt{x^2 + y^2 + z^2}$ recorded by the OptiTrack for three subsets of marks (1-4, 5-8, 9-12). The associated root mean squared deviations from the mean for each case are also shown. Figure 4.24D shows the reduction in size of the measured field following regression at each subset of marks for the sensor which detected the largest positive field over the whole experiment. Figure 4.24E shows the reduction in standard deviation over time for the entire experiment following regression, averaged over all 18 sensors.

The largest head motion was produced when the subject viewed marks 9-12. This required a rotation of ±34.0 ± 0.9° and translation of ±9.2 ± 1.1 cm from the central position. This motion produced a maximum field artefact of approximate magnitude 1 nT, which was reduced following regression with the motion parameters to 0.037 nT.

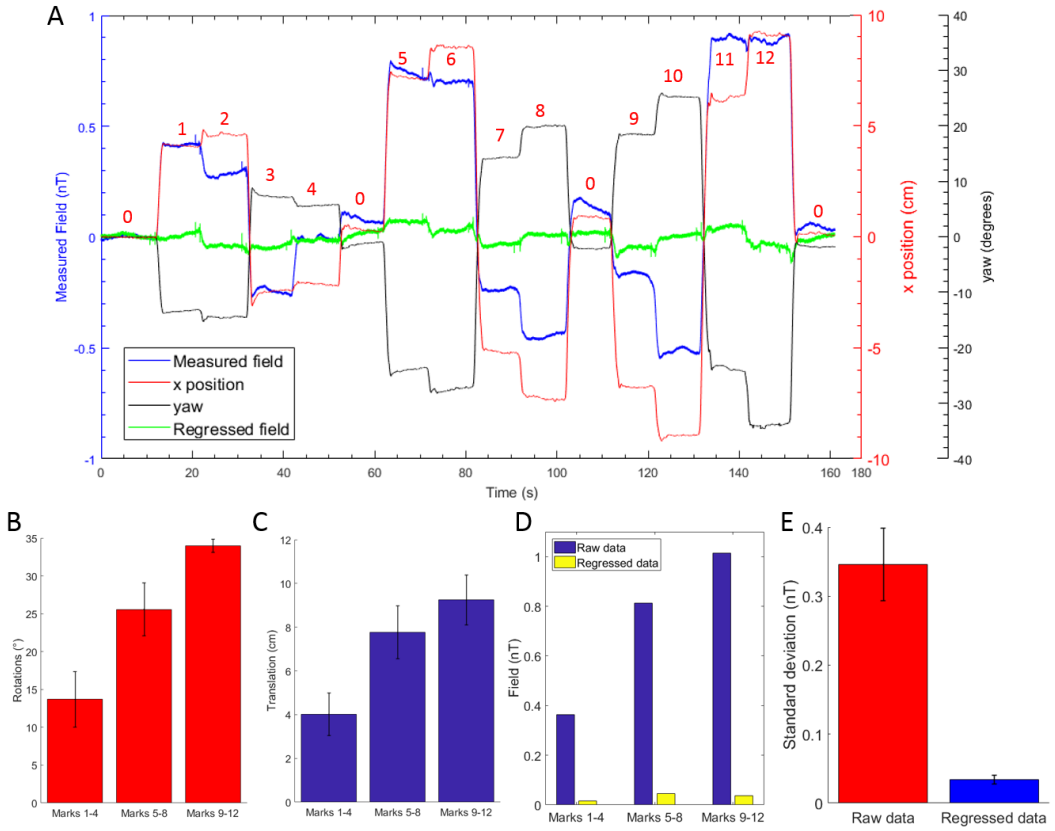



Figure 4.24: *Demonstrating the allowed range of participant motions. A) The output of a single OPM within an array of 18 worn by the participant is displayed in blue. The magnetic field data is compared with the x translation (red) and yaw rotation (black) of the rigid body. The text labels identify the order in which the positions were viewed during the experiment. The measured field following regression with motion parameters and the four reference magnetometers is shown in green. B) The magnitude of rotation required to move from mark 0 to each mark is averaged over the 3 subsets (each containing 4 marks). C) The magnitude of the translation required to move from mark 0 to each mark is averaged over 3 subsets. D) Reduction in field following regression at each subset of marks shown for the sensor which detected the largest (positive) field over the whole experiment. E) Reduction in the standard deviation over time of raw sensor outputs during the entire 160 s of the experiment following regression. Results are averaged over all 18 sensors in the scanner-cast.*

### 4.4.6 OPM-MEG demonstration: measurement of retinotopy

Figure 4.25 shows the pseudo-T-statistical images overlaid on an MRI scan of the participant's brain. The red/blue overlays are the beamformer images formed when the stimulus was on the left/right respectively (participant view for each case is the same as the red/blue diagrams in Figure 4.4). Evaluating motion data from the OptiTrack during the "switch-gaze" period for the trials where the subject moved revealed the average magnitude of translations and rotations to be 1.4 ± 0.04 cm and 5.9 ± 0.8°, respectively.

Figure 4.26A compares Fourier transforms of the virtual electrode time courses produced during stimulation and rest periods at location 1 when the stimulus was on the left ($q_{l1}(t)$) and on the right ($q_{r1}(t)$). Figure 4.26B compares Fourier transforms of the virtual electrode time courses produced during stimulation and rest periods at location 2 when the stimulus was on the left ($q_{l2}(t)$) and on the right ($q_{r2}(t)$).

As expected, the areas of largest 8 Hz response in the beamformer images for the two cases localise to opposite sides of the visual cortex. Inspecting the Fourier transforms, there are clear 8 Hz responses during periods of stimulus presentation in the corresponding cortex when compared to rest. Looking in the opposing cortex during stimulus presentation reveals no response.

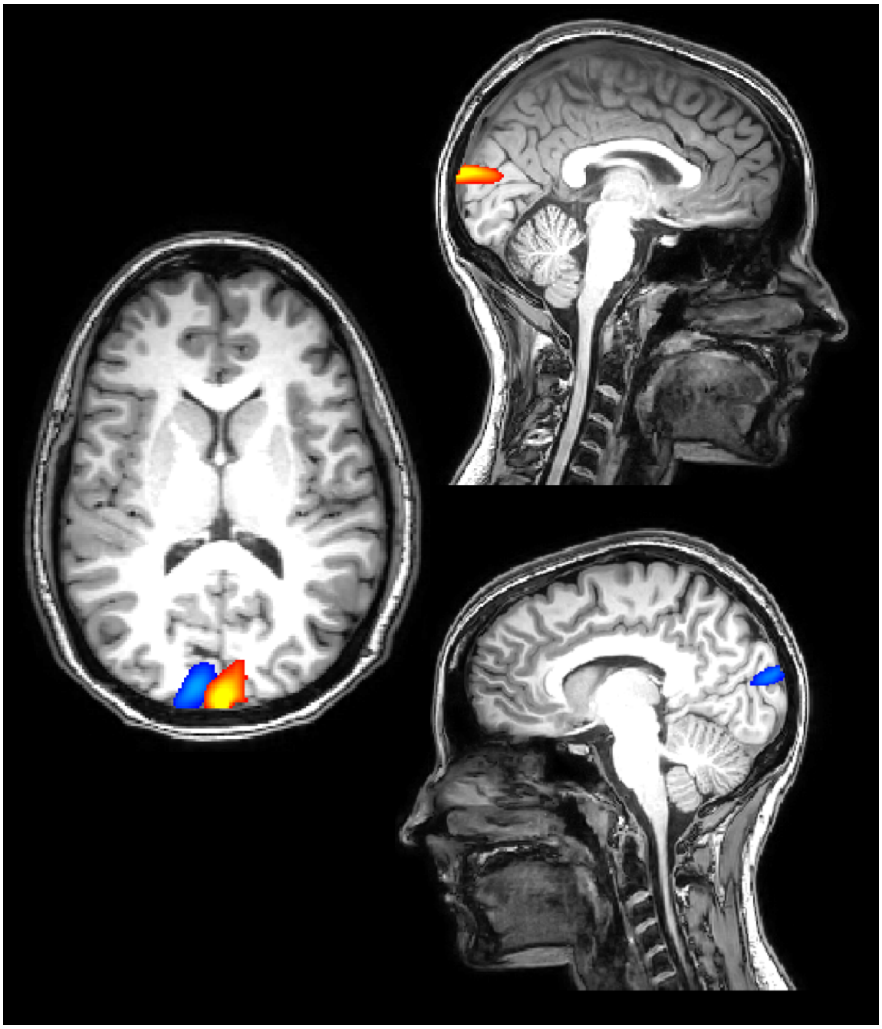


Figure 4.25: *Beamformer images from the retinotopy experiment. Pseudo-T-statistical images overlaid onto a MRI scan of the participant produced from the cases where the stimulus was in the left visual field (red overlay) or the right visual field (blue overlay). The images were thresholded between 1.5 and 1.8 and 1.1 and 1.6 for the red and blue images respectively.*

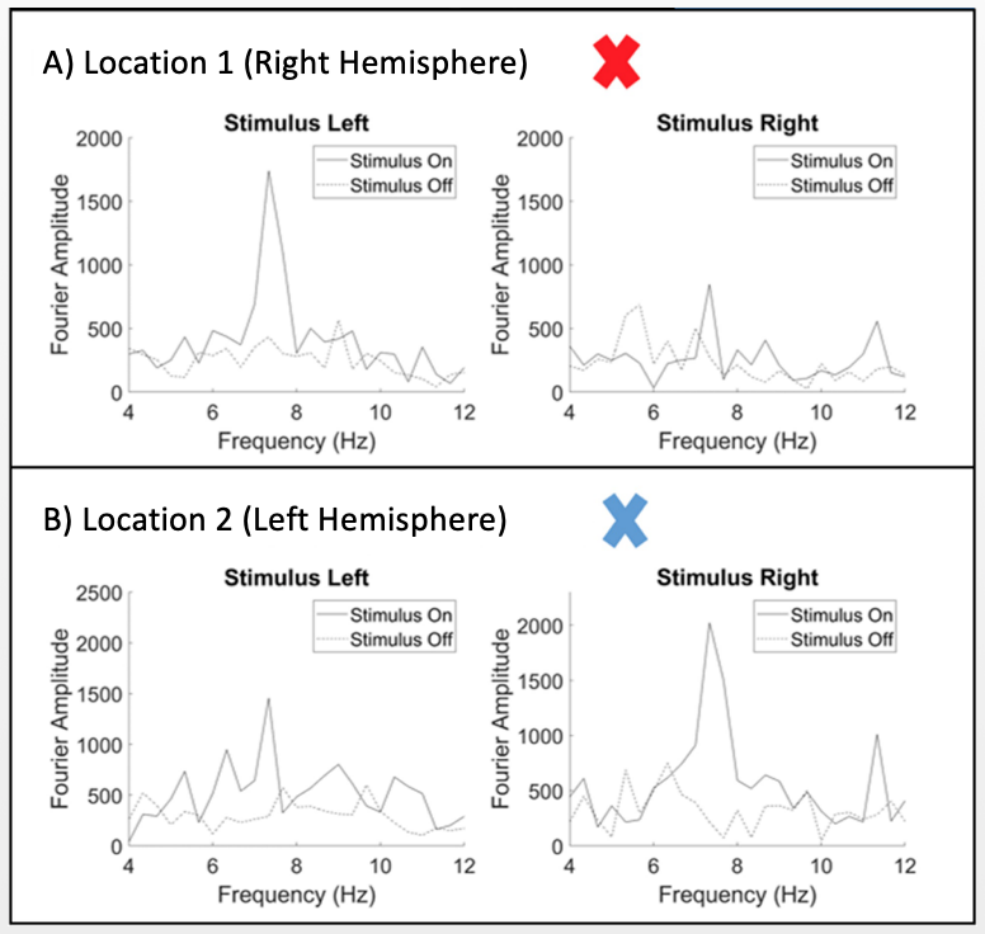



Figure 4.26: *Virtual electrode timecourses of the beamformed data. A) The Fourier transforms of virtual electrode time-courses compared during stimulation and rest. The electrode was positioned at the peak of the red overlay and compared for the cases where the stimulus was on the left and on the right. B) Comparing Fourier transforms of virtual electrodes positioned at the peak of the blue overlay and compared for the cases where the stimulus was on the left and on the right.*

## 4.5 Discussion

The six-coil bi-planar set designed here was tested and shown to provide an automated, stable cancellation of remnant field and field gradients which allows for MEG recordings to be made on an unconstrained seated participant. Here, several issues and suggested improvements to the system are discussed.

### 4.5.1 Coil design

Discrepancies between the predicted and measured coil parameters could arise due to interactions between the coils and the high-permeability walls of the MSR. These interactions were not taken into account during the design process and are more formally investigated in Chapter 5.

Further development of the field nulling technology will be required to allow full ambulatory motion during an experiment. To realise this aim, new designs could feature a larger region over which the homogeneous fields and field gradients are produced. Additional coils producing higher order spatial variations of the field could also be produced. The coils could also be built directly into the walls of the MSR. This would also require consideration of the interactions between the coils and the mu-metal, similar interactions have previously been accounted for in gradient coil design for MRI [Moon et al., 1999]. Increased performance is likely to come at the cost of increased complexity in wire patterns which may lead to further difficulties in engineering of coil systems.

Any increase in the volume within which the OPMs remain operational would immediately allow for wider ranges of motion, and potentially make possible the implementation of experiments involving spatial navigation and direct social interaction between individuals.

### 4.5.2 Coil construction

Manual winding using masking tape and wallpaper paste was used to construct the coils. Whilst this method is simple, the MDF boards on which the coils are mounted are not completely flat, and board positioning is done manually. This leads to errors in the alignment and separation of the set which could detract from the predicted performance. 3D printing or printed circuit board etching techniques could potentially be used to streamline the process of coil construction and to increase the correspondence of the actual wire paths to the coil designs.

However, it might be difficult to gain access to machines capable of constructing coils of this scale. As eight coils are needed per set, system construction is difficult and time-consuming. The weight and structural rigidity of the system need to be considered. The effects of manual construction and misalignment have not proven problematic, the choice of a PID based nulling algorithm hopefully accounts for some of these errors.

### 4.5.3 Field cancellation method

As well as the field mapping which was performed, the static fields reported by the on-sensor coils of the array of 18 OPMs in the scanner-cast were also recorded with and without field nulling before the start of the retinotopic mapping experiment while the subject viewed the centre of the screen. Taking the mean magnitude of the fields shows a decrease from 14.9 $\pm$ 5.2 nT to 1.61 $\pm$ 0.43 nT after the nulling was applied. The reduction in field is less on the head than was found during the field-mapping (a reduction in the mean magnitude from 28 nT to 0.74 nT). The reference array which is employed here sits slightly behind the head of the participant (to avoid protruding sensors from the scanner-cast bumping into reference sensors during an experiment) and as a result the head sensors are

displaced from the region of maximal field cancellation.

A re-designed reference array which includes sensors positioned to form a cube around the participant would allow for a better reduction in the field over the head sensors, the final two gradient coils $G_{xx}$ and $G_{xy}$ could then be added to form a full cancellation system. A larger reference array would however, require a more complex PID control system, more redundant sensors in terms of brain coverage and potentially restrict the participant if poorly sited. The $G_{xy}$ coil has been successfully constructed, but is yet to be routinely used.

An alternative approach could be to null the field over the head-mounted OPMs. For example, an approach in which the effect of each coil on each OPM is measured by pulsing individual coils in turn, and then a matrix inversion applied to find optimal currents to cancel remnant fields could be implemented. However, it would be important to ensure good sampling of all field components is possible. For example, in the retinotopic mapping paradigm the sensors were mounted over visual cortex and predominately pointing in the $x$-direction in which the nulling will be strongest.

Iivanainen and colleagues recently developed an active cancellation system featuring a coil-cage type system, capable of compensating the remnant field inside a MSR, and its temporal variation using the voltage outputs of three orthogonal QuSpin OPMs mounted on the head of a participant in a high-speed PID loop [Iivanainen et al., 2019]. Reduction of the field from 70 nT to less than 1 nT was achieved (reduction by a factor of 70). They also reduced the temporal variation of the field from a peak to peak drift of 1.3 nT to 0.4 nT to restrict any gain changes during an session. However, the participants were required to remain still inside a 'Helmholtz-cage' style system.

Despite these issues, and even with the significant head movements that were made in this experiment, none of the sensors went outside their operational range

during the experiments. The simplicity of the PID based approach, with reference sensors behind the subject allows for a fast and flexible scanning procedure.

### 4.5.4 Artefact reduction

The ability of the linear regression to de-trend magnetic field data shows that field measurements are highly correlated with the changes in head position data recorded by the OptiTrack camera and background field measurements recorded by the reference array. By applying the regression approach prior to further analysis with a beamformer (or other MEG processing technique) the resulting signals contain a better representation of the underlying brain data.

This regression could be further improved by implementing a non-linear solution as the regression weights that remove interference for one orientation will be different when the head is moved. A sliding window based approach could also be useful for when the rotations exceed small angle approximation and become non-linear.

However, none of these methods can compensate for the changing gain in the sensor at large magnetic field values. As outlined in Chapter 2, the linearity of the sensor response to magnetic field is such that over $\pm 1.5$ nT sensor gain varies by $\pm 5\%$. The regression methods outlined previously would not be able to readily compensate for this change. Dynamic control of the magnetic field cancellation system is required to keep all sensors at zero field throughout the experiment in order to compensate for these changes. The coil system developed by Iivanainen and colleagues was designed to allow OPM operation in a lightly shielded room with significant time-varying interfering magnetic fields. These drifts would cause significant gain changes and would have rendered OPM operation impossible without a field cancellation system. Development of a dynamic-nulling system which continuously updates currents in the bi-planar coils designed

here, accounting for temporal variations in the remnant magnetic field is detailed in Chapter 5 but was not required in the work presented here due to the high temporal stability of the remnant field inside the MSR (as shown in Figure 4.23).

Nevertheless, given the movements in the retinotopic mapping experiment were around 2 cm and 7° this would lead to a field change of  200 pT, equivalent to a sensor gain change of around 1% which is deemed small enough to be insignificant in our case.

## 4.6 Other demonstrations of OPM-MEG

Field nulling using the bi-planar coils has been crucial to the ongoing development of OPM-MEG, allowing experiments which would be impractical in conventional systems to be performed. A brief summary of standout work in which data was collected using the Nottingham system with the bi-planar coils is provided here.

**The 'Ping-Pong' experiment**

The work developing OPM-based MEG where participants are free to move was described in a publication in Nature. As well as showing the constructed system had a performance similar to that of a cryogenic system (even during movements of $\pm 10$ cm) the movement allowed by field nulling using the bi-planar coil system was utilised further to measure oscillatory dynamics in the brain of a participant bouncing a ping-pong ball on a bat as shown in Figure 4.27 [Boto et al., 2018]. Tasks involving rapid, unpredictable motions such as this could be used to investigate motor-learning, connectivity and brain plasticity.

**Language lateralisation**

Tierney and colleagues used the system to perform a cognitive test to locate the eloquent cortex of three participants using a simple verb-generation task [Tierney et al., 2018]. This method when compared to the invasive WADA test [Loring, 1997] or the claustrophobia of a functional MRI approach holds promise for providing clinically useful information during pre-surgical planning for epilepsy patients.

**Virtual reality**

Roberts and colleagues used the capability to measure OPM-MEG with head movement to perform experiments in virtual reality (VR) using an Oculus Rift

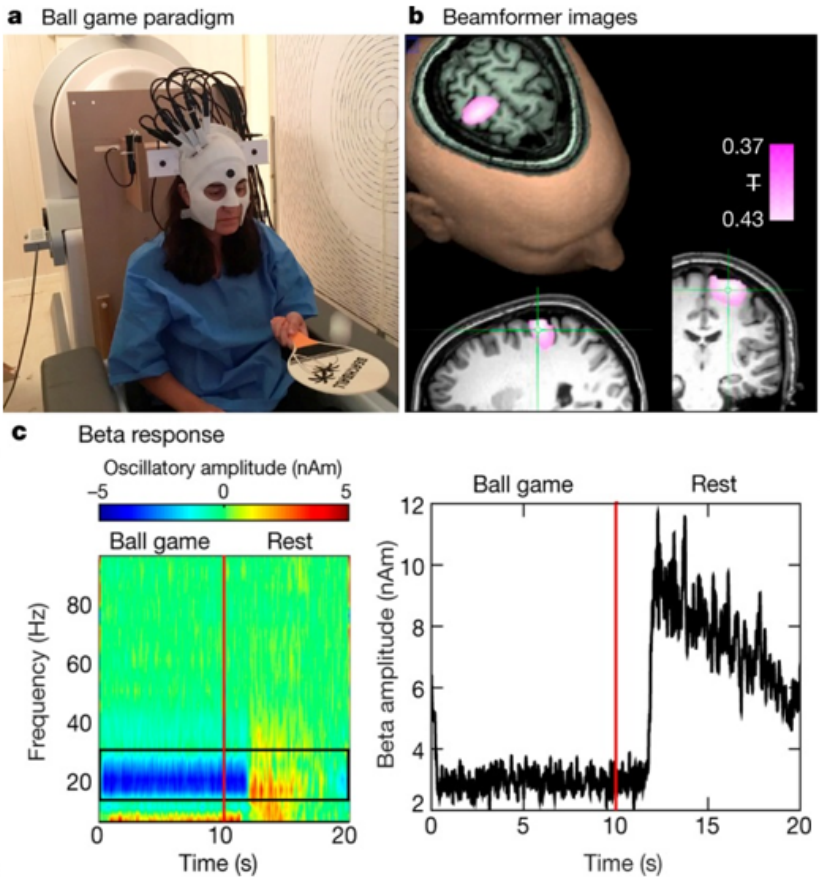



Figure 4.27: *The 'ping-pong' experiment. a) Seated subject wearing a 3D-printed subject-specific scanner-cast containing 13 OPMs positioned over the motor cortex. The participant bounced the ball on a bat for 10 s followed by 10 s of rest, repeating 29 times. b) Beamformer images show the response in the motor cortex. c) Virtual electrode timecourses show the decrease in oscillatory power in the beta-band (13 - 30 Hz) during movement and a post-stimulus beta rebound following movement cessation. The response is similar to that shown in Chapter 1 where the beta rebound is diminished in schizophrenia patients. Figure taken from [Boto et al., 2018].*

(Oculus VR LLC, Menlo Park, CA.) head mounted display unit to project stimuli [Roberts et al., 2019]. Changes in alpha power as well as evoked and driven neural responses were observed over visual cortex. These experiments provide more naturalistic stimuli than are available in conventional neuroimaging systems and their continued development will allow for new avenues to be explored such as social interaction and spatial navigation.

**Lifespan-compliance**

Work by Hill and colleagues is being performed to measure brain activity in children as young as 3 years of age using adapted scanner-casts to give life-long compliance [Hill et al., 2019]. The coil system allows the children to remain comfortable and watch television on a screen whilst the scan occurs. The OptiTrack camera was utilised to develop uncued experiments, useful for children who would find adhering to a rigid task structure difficult.

**Deep sources**

The majority of MEG studies are focused on the cerebrum due to coverage limitations in conventional systems, and a decrease in signal arising from deeper sources. The cerebellum and hippocampus are of significant interest to neuroscientists as they contribute to motor control and memory. The ability to flexibly place OPMs allowed Lin and colleagues to measure evoked responses occuring in the cerebellum as a response to an air-puff stimulus [Lin et al., 2019]. Work by Barry and colleagues showed hippocampal activity in response to an imagination paradigm [Barry et al., 2019].

The continued development of coil systems to allow participant movements during experiments is crucial to the continued success of wearable MEG devices, with widespread potential already being exploited as a result of the bi-planar coil system described here.

# Chapter 5

# Balanced, bi-planar field and field gradient coils

## 5.1 Introduction

The previous chapter showed that the remnant magnetic field in a magnetically shielded room (MSR) can be further nulled using a set of six, bi-planar coils mounted on large planes of dimensions 1.6 x 1.6 $m^2$, separated by 1.5 m, which compensate $B_x$, $B_y$ and $B_z$ as well as the three dominant first-order spatial field gradients $G_x = dB_x/dz$, $G_y = dB_y/dz$ and $G_z = dB_z/dz$. In summary, these coils were used in a MSR (Vacuumschmelze, Hanau, Germany) comprised of two layers of mu-metal and one layer of aluminium to reduce the dominant static field component, $B_x$, by a factor of 46 from 21.8 ± 0.2 nT to 0.47 ± 0.08 nT, and the dominant gradient, $G_x$, by a factor of 13 from 7.4 nT/m to 0.55 nT/m [Holmes et al., 2018, Boto et al., 2018].

The integration of these coils with a scalp-mounted array of optically pumped magnetometers (OPMs) allowed high quality magnetoencephalography (MEG) data to be recorded whilst the participant made large (±10 cm and ±35°) head

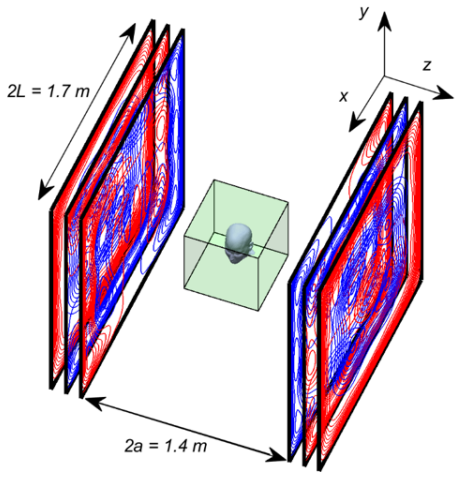



Figure 5.1: *Geometry of the balanced bi-planar coil system. Two square planes of side length* $2L = 1.7$ *m placed a distance* $2a = 1.4$ *m apart. Each coil pair is simultaneously designed to produce homogeneous field and field gradient over a region at the centre of the coils. The three coil layers on each plane are spaced by* $\approx$ *1 mm in the constructed system.*

movements [Holmes et al., 2018]. Without the additional field nulling provided by the coils small movements and rotations of only a few degrees would saturate sensor outputs and cause significant sensor gain changes [Iivanainen et al., 2019].

The bi-planar coils thus form a crucial element of an OPM-based MEG system, but their construction is time-consuming due to the large size of the coils and the significant number of coil layers that are required. The distribution of the weight of the current-carrying wires and structural rigidity of the coil-set have to be taken into account during coil construction and siting. In this chapter it is shown that by exploiting the natural symmetry shared by pairs of coils ($B_x$ and $G_x$, $B_y$ and $G_y$ and $B_z$ and $G_z$), the number of coils that need to be constructed to produce a simple field-nulling system can be reduced from six to three, as illustrated in Figure 5.1.

The harmonic-minimisation approach that allows optimisation of planar current distributions to produce both homogeneous fields and spatial field gradients is

described; the performance of coils generated using the joint design method is compared with that of coils designed to produce only a uniform field or field gradient. A proportional integral derivative (PID) control method, which nulls the static field and field gradients automatically by independently optimising the currents in each plane based on reference measurements is also shown. The static field compensation achieved using this method is quantified by comparing field maps measured in a single plane in the MSR before and after field compensation.

The previous six-coil system provided only static field compensation with coil currents fixed during an experimental session. As well as the large static field components, significant temporal variation of the remnant magnetic field by as much as 10's of nT over the period of a single experiment (10-20 minutes) can occur, depending on the environment. This drifting background field level has a detrimental effect on the open-loop OPM sensor gain, which varies by more than 10% over the full QuSpin OPM dynamic range of $\pm 5$ nT [Boto et al., 2018, Shah et al., 2018]. For accurate MEG measurements it is desirable that the sensor gain varies as little as possible, as a result dynamic compensation of the background magnetic field can also be required for sensor operation.

The three coils here were designed for integration into an OPM-MEG system sited at University College London. This city-centre site is located directly above a London Underground railway line which produces unpredictable, temporally varying magnetic fields large enough and frequent enough to make even a 10-minute scan unfeasible. To correct for this, a dynamic PID-based feedback controller was developed to continually update coil currents during a session in order to null reference measurements of $B_x$, $B_y$ and $B_z$. Empty room recordings with and without the dynamic nulling were compared whilst noting the number of trains which passed beneath the lab during these recordings.

Discrepancies between the predicted and measured coil performance which were

briefly discussed in the previous chapter may be caused by interactions between the coils and the high-permeability mu-metal walls of the MSR. It has been shown that this interaction can be modelled by using a method of images approach. Here, the method of images was utilised to simulate the effects of interactions with the mu-metal walls on the efficiency and homogeneity of the designed coils when operated inside a MSR [Juhas et al., 2014, Qinjie et al., 2018]. Results are compared to the measured performance and the impact this may have on future coil designs is discussed.

The work described here was crucial to the development of an OPM-based MEG system at University College London. A detailed description of the system was published in Nature Scientific Reports and adapted for this chapter [Holmes et al., 2019]. Researchers at the Wellcome Institute for Neuroimaging are working to develop neuroscientific experiments which fully exploit the potential of the OPM-based MEG. Through collaboration with Great Ormond Street Hospital epilepsy patients are being scanned using this system.

## 5.2 Design theory

As shown in Chapter 4 a current distribution $\boldsymbol{J}(x, y)$ that is confined to an $x$-$y$ plane using a two-dimensional stream function $S(x, y)$ can be characterised, where $\nabla S(x, y) \times \hat{\boldsymbol{z}} = \boldsymbol{J}(x, y)$ (since $\nabla . \boldsymbol{J}(x, y) = 0$). The wire paths of a coil design that represents the current distribution correspond to the contours of the stream function. Planar current distributions which produce a uniform field along one of the Cartesian axes have shared symmetry with current distributions that generate specific field gradients, and this sharing of symmetry also applies to the stream functions.

For example, in the simple case of a Helmholtz coil, two co-axial loops of radius $a$ carrying the same current and placed a distance $a$ apart in $z$ will produce a uniform field $B_z$ along the $z$ direction as shown in Figure 5.2 (i-ii). In this instance the stream function required to produce the field is symmetric in $x$ and $y$, and also symmetric in $z$ (as the two loops carry the same current which circulates in the same sense in both coils). If the current in one of the loops is reversed with respect to the other (so the stream function is now anti-symmetric in $z$, and symmetric in $x$ and $y$) then the result is a gradient in $B_z$ along the $z$ direction (i.e. a $dB_z/dz$ coil) as shown in Figure 5.2 (iii-iv). If the two loops are driven independently the currents can be set to produce both a field, and a field gradient simultaneously as shown in Figure 5.2 (v-vi). This involves applying the sum of the currents needed to produce a field and a field gradient to one loop and the difference to the other loop.

Considering the symmetry of the coil stream functions required to generate each of the three uniform fields (referring to Table 4.1), the $x$-$y$ symmetry is the same for $B_x$ (anti-symmetric in $x$, symmetric in $y$ and anti-symmetric in $z$) and $G_x$ (anti-symmetric in $x$, symmetric in $y$ and symmetric in $z$) coils, $B_y$ (symmetric

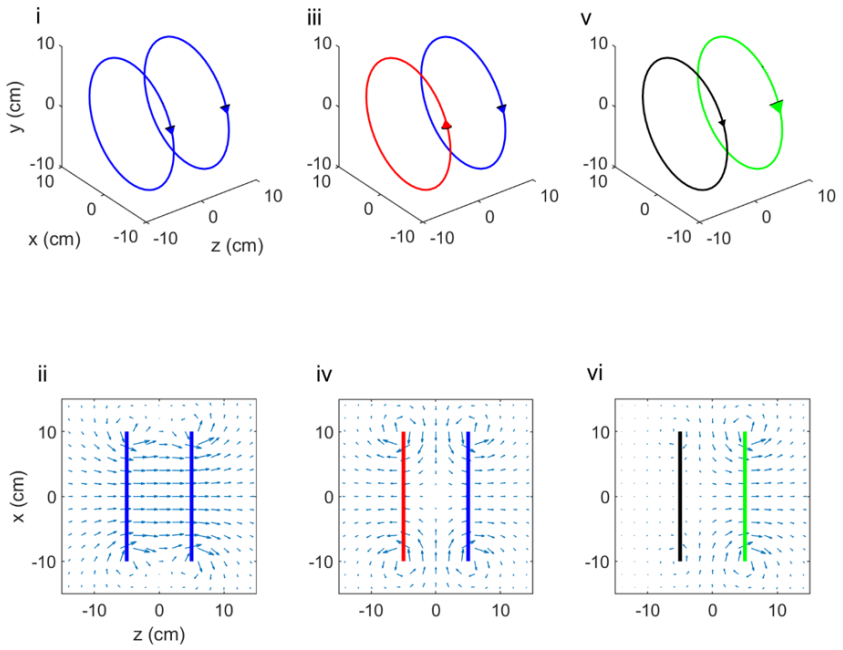



Figure 5.2: *The field produced by a pair of co-axial loops varies with the strength and direction of the applied currents. (i) The Helmholtz coil consists of two current-carrying loops. The same current is applied to each loop making the stream function symmetric in $x$, $y$ and $z$. (ii) A homogeneous field $B_z$ is produced through the centre of the loops. (iii) The current applied to one of the loops is reversed (now making the stream function anti-symmetric in $z$) (iv) In this case a $B_z$ field which linearly varies with $z$ position (constant $dB_z/dz$) is produced. (v-vi) By independently driving the two loops, a desired field and gradient can be simultaneously produced.*

in $x$, anti-symmetric in $y$ and anti-symmetric in $z$) and $G_y$ (symmetric in $x$, anti-symmetric in $y$ and symmetric in $z$) coils, and $B_z$ (symmetric in $x$, symmetric in $y$ and symmetric in $z$) and $G_z$ (symmetric in $x$, symmetric in $y$ and anti-symmetric in $z$) coils. Through a combined design process and careful control of the applied currents, three coil pairs can therefore be used simultaneously to generate the three uniform fields and the associated longitudinal gradients. The remaining two components, $dB_x/dy = dB_y/dx$ and $dB_x/dx$ have no shared symmetry and would have to be constructed separately.

The coil pairs were designed by applying a harmonic minimisation approach based on expressions used for designing planar magnetic field gradient coils for use in MRI [Yoda, 1990, Carlson et al., 1992, Turner, 1993]. The two-dimensional Fourier transform of the magnetic field, $\tilde{\boldsymbol{B}}(k_x, k_y, z)$ over the $x$-$y$ plane produced by current distributions on two planes positioned at $z = a$ and $z = -a$, at a position $z$ in the region $-a < z < a$ (as derived in section 4.2) can be written as:

$$\widetilde{\boldsymbol{B}}(k_x, k_y, z) = \mu_0 \left[ (ik_x\hat{\boldsymbol{x}} + ik_y\hat{\boldsymbol{y}}) \begin{matrix}\sinh\\\cosh\end{matrix}(k_r z) - k_r\hat{\boldsymbol{z}} \begin{matrix}\cosh\\\sinh\end{matrix}(k_r z) \right] \widetilde{S}(k_x, k_y) e^{-k_r a}. \tag{5.2.1}$$

where $k_r = (k_x^2 + k_y^2)^{1/2}$ and $\tilde{S}(k_x, k_y)$ is the two-dimensional Fourier transform of the stream function. The upper/lower terms define the $z$-symmetry where the stream function has the same (symmetric in $z$)/opposite (anti-symmetric in $z$) sign on each plane.

The stream function is parameterised again as a two-dimensional Fourier series confined to the region $|x|$, $|y| < L$ ($z = a$) on the two coil planes, so that [Carlson et al., 1992]:

$$\begin{aligned} S(x, y) = \sum_{n=1}^{N} \left[ \alpha_n \cos\left(\frac{\pi}{2}(2n-1)\frac{x}{L}\right) + \beta_n \sin\left(\frac{n\pi x}{L}\right) \right] \times \\ \sum_{m=1}^{M} \left[ \gamma_m \cos\left(\frac{\pi}{2}(2m-1)\frac{y}{L}\right) + \delta_m \sin\left(\frac{m\pi y}{L}\right) \right]. \end{aligned} \tag{5.2.2}$$

where coefficients $\alpha_n$, $\beta_n$, $\gamma_m$ and $\delta_m$ are used to weight the different harmonics in the series. By applying symmetry conditions to the stream function, a sub-set of the harmonic combinations in equation [5.2.2] can be used to design each coil. For example, in the case of a balanced $B_x$ and $G_x$ coil, the stream function is required to be anti-symmetric in $x$ and symmetric in $y$. These constraints allow the stream function to be written as

$$S_{(B_x/G_x)} = \sum_{n=1}^{N}\sum_{m=1}^{M}\left[\lambda_{nm}\sin\left(\frac{n\pi x}{L}\right)\cos\left(\frac{\pi}{2}(2m-1)\frac{y}{L}\right)\right] \tag{5.2.3}$$

where sine terms are chosen for the anti-symmetric cases and cosine terms for the symmetric cases. The $z$ symmetry for this case is defined by setting ($S_{z=a} = \pm S_{z=-a}$). The new constant $\lambda_{nm} = \beta_n\gamma_m$.

The stream function equations can be re-written for ease of notation in the form

$$S = \sum_{j=1}^{N\times M}\lambda_j S_j. \tag{5.2.4}$$

with $j = (n-1)N+m$ (see Equation [5.2.3]). Continuing with the case of the balanced $B_x/G_x$ coil, the contribution to the field $B_x$ at position $\boldsymbol{r}_i(x,y,z)$, $b_{xj}(\boldsymbol{r}_i)$, due to the $j^{th}$ component of the stream function can be expressed (defining the $z$-symmetry to be antisymmetric, i.e. choosing cosh in equation [5.2.1]) as

$$b_{xj}(\boldsymbol{r}_i) = 2DFT\Big(i\mu_0 k_x \widetilde{S}_j e^{-k_r a}\cosh(k_r z_i)\Big)\Big|_{x_i,y_i} \tag{5.2.5}$$

where 2DFT denotes the two-dimensional Fourier transform. The contribution to the field from the gradient component $G_x$ at position $\boldsymbol{r}_i(x,y,z)$ in the $x$-direction, $g_{xj}(\boldsymbol{r}_i)$, from the $j^{th}$ component of the stream function can also be expressed (defining the $z$-symmetry to be symmetric, i.e. we choose sinh in equation [5.2.1]) as

$$g_{xj}(\boldsymbol{r}_i) = 2DFT\Big(i\mu_0 k_x \widetilde{S}_j e^{-k_r a}\sinh(k_r z_i)\Big)\Big|_{x_i,y_i}. \tag{5.2.6}$$

Defining $\tilde{S}_j$ in terms of the reduced variable $x' = x/L$, $y' = y/L$ ($k'_x = k_x L$, $k'_y = k_y L$) allows expression of the Fourier transform of equation [5.2.3] as

$$\widetilde{S}_j(k'_x, k'_y) \propto \left[\operatorname{sinc}((m - {}^1\!/_2)\pi - k'_y) + \operatorname{sinc}((m - {}^1\!/_2)\pi + k'_y)\right] \times \left[\operatorname{sinc}(n\pi - k'_x) - \operatorname{sinc}(n\pi + k'_x)\right] \tag{5.2.7}$$

This can be substituted into equations [5.2.5] and [5.2.6] to find the field at position $\boldsymbol{r}_i$ due to each component of the stream function. Similar calculations can be performed by imposing the symmetry conditions needed for the other coils.

$\lambda$-coefficients are then chosen to minimise a functional containing three parts [Carlson et al., 1992]: the spatial deviation of the field term ($B_x$) over an array of target points, the spatial deviation of the field gradient term ($G_x$) and the power dissipated in the coil. The functional is written as:

$$F = \sum_{i=1}^{I} \left| B_t(\boldsymbol{r}_i) - b_x(\boldsymbol{r}_i) \right|^2 + \alpha \sum_{i=1}^{I} \left| g_t z_i - g_x(\boldsymbol{r}_i) \right|^2 + \omega P. \tag{5.2.8}$$

Here, from the $B_x$ term $B_t(\boldsymbol{r}_i)$ is the desired (or target) field at position $\boldsymbol{r}_i$ and $b_x(\boldsymbol{r}_i) = \Sigma_j \lambda_j b_x j(\boldsymbol{r}_i)$ is the calculated field at $\boldsymbol{r}_i$. For the $G_x$ term $g_t z_i$ is the desired (or target) field chosen to vary linearly with position $z_i$ and $g_x(\boldsymbol{r}_i) = \Sigma_j \lambda_j g_x j(\boldsymbol{r}_i)$ is the calculated field at $\boldsymbol{r}_i$. The set of position vectors $\boldsymbol{r}_{(i=1\ to\ I)}$ define target points within the volume at which a homogeneous field or field gradient is required. The linear weighting $\alpha$ applied to the field gradient minimisation can be altered to balance the strength of the field and gradient terms. $P$ is a tuneable power dissipation term which can be upweighted by increasing the weighting coefficient to reduce the complexity of the designed coils as described in section 4.2.4.

Here the functional is minimised by choosing the weights $\lambda_j$ which satisfy $dF/d\lambda_j = 0$. The set of derivatives can be cast as a set of linear simultaneous equations in matrix form, whose solution is found by identifying the pseudo-inverse matrix as

shown in section 4.2.5. The wire paths of the coils are then extracted as contours of the optimised stream function.

## 5.3 Methods

### 5.3.1 Coil design and construction

MATLAB (The MathWorks Inc.) was used to produce designs for three coils allowing simultaneous compensation of $B_x$ and $G_x$, $B_y$ and $G_y$ and $B_z$ and $G_z$. The dimensions of the system were limited by the size and layout of the MSR which also contains a SQUID-based MEG system (CTF, Coquitlam, BC, Canada). Final bi-planar coil dimensions were chosen to be $a = 0.7$ m and $L = 0.85$ m as shown in Figure 5.1.

The number of harmonics, and the power and field/gradient term weightings were chosen manually to produce homogeneous fields and field gradients (to within $\pm 5\%$) over a central volume of $40 \times 40 \times 40$ cm$^3$. The magnetic field for each coil was evaluated over a 2.5-cm-resolution, 3D grid using the elemental Biot-Savart law. A numerical value of the field, or field gradient homogeneity, $H$ was computed by assigning a value of 1 to every element in the 3D grid where the homogeneity condition was met, and a 0 where it was not. The homogeneity is then reported as a percentage of the number of 1's versus the total number of grid points. The balanced $B_x/G_x$ and $B_y/G_y$, coils were designed using 36 harmonics with $N = M = 6$, and the field was evaluated over $I = 320$ target points. The balanced $B_z/G_z$ coil was designed with 36 harmonics with $N = M = 6$ and the field was evaluated over $I = 256$ target points. Fewer target points are required to limit the field variation in the $B_z/G_z$ coil due to the high degree of rotational symmetry of these coils about the $z$-axis.

Contours of the optimised stream function were connected to form continuous wire paths. The coils were mounted on two sheets of medium-density fibreboard (MDF) measuring $1.8 \times 1.8$ m$^2$ with legs which place the centre of the coils

1.1 m from floor level. Coil designs were printed and then hand-traced onto thin paper sheets. These sheets were then attached to the board with wallpaper paste. Copper wire (enamelled, diameter of 0.56 mm) was laid on each path and fixed in place using masking tape. The total thickness of each coil layer is around 1 mm. The three coils were layered by repeating these steps.

Each planar coil unit was connected to a QuSpin coil driver (4 V, low-noise, six drivers in total, one per coil unit), which was controlled using a 16-bit NI-9264 DAC voltage output module interfaced with LabVIEW (National Instruments (NI) Corporation, Austin, TX). Resistors were added in series to each coil unit so that fields of around 40 nT or field gradients of around 25 nT/m could be produced from a 4 V output.

Prior to their use in balanced mode, the coils were connected in standard, bi-planar arrangements (with equal or equal and opposite current in each plane as in Chapter 4) to test their performance when producing each of $B_x$ and $G_x$, $B_y$ and $G_y$ and $B_z$ and $G_z$. The coil efficiencies (field or field gradient per unit current) were measured by using an array of three Gen-1 QuSpin OPMs operating in radial measurement mode. These OPMs were then oriented in order to measure the field component of interest.

A linearly increasing current was applied to each bi-planar coil and the change in field measured as a function of this applied current. For $B_x/G_x$ and $B_y/G_y$ measurements the OPMs were positioned approximately at the centre of the bi-planar coils and spatially separated by 8 cm in the $z$ direction (such that the field was measured at roughly $z$ = -8 cm, 0 cm and +8 cm, at $x = 0$ cm, $y = 0$ cm). For the $B_z/G_z$ measurements, the long axes of the sensors were lined up in the measurement plane, which meant that the field had to be sampled at locations with a greater spatial separation in the $z$ direction (field measured at $z$ = -17 cm, $z = 0$ cm and $z = +17$ cm at $x = 0$ cm, $y = 0$ cm). For comparison, the

fields and gradients produced by the bi-planar coils were also calculated using the elemental Biot-Savart law. These measurements were carried out in the MSR at the University of Nottingham (Vacuumschmelze, Hanau, Germany) which is comprised of two layers of mu-metal and one layer of aluminium.

### 5.3.2 Comparing design methods

To compare the performance of the balanced coils designed using the combined method to that of coils designed just to produce a uniform field or field gradient, three different coils were compared via simulations: a coil designed to produce $B_x$; a coil designed to produce $G_x$; a coil designed to produce $B_x$ and $G_x$ (i.e. comparing simulated results from the coil design method used in Chapter 4 to this balanced method). For each case the number and location of target points and the weighting of the power dissipation term were kept constant. The dimensions of the coils were fixed at $a = 0.7$ m and $L = 0.85$ m as above. The field and gradient produced by these coils in a bi-planar arrangement were calculated using the elemental Biot-Savart law. Fields were then normalised to their values at the origin to allow evaluation of the deviation of the field and gradient over a 40 $\times$ 40 $\times$ 40 cm$^3$ volume (evaluated over a 2.5 cm resolution 3D grid). The homogeneity $H$ is also reported for each case, using the measure described in section 3.1. As before, less than $\pm$5% deviation over the full volume is desired.

### 5.3.3 Static field nulling

As described in section 4.3.2, a reference array of four Gen-1 QuSpin OPMs operating in field-zeroing mode was used to measure the three vector field components, at two positions spatially separated in the z-direction by 40 cm, as shown in Figure 5.3A. The measurements from the sensors are combined to form

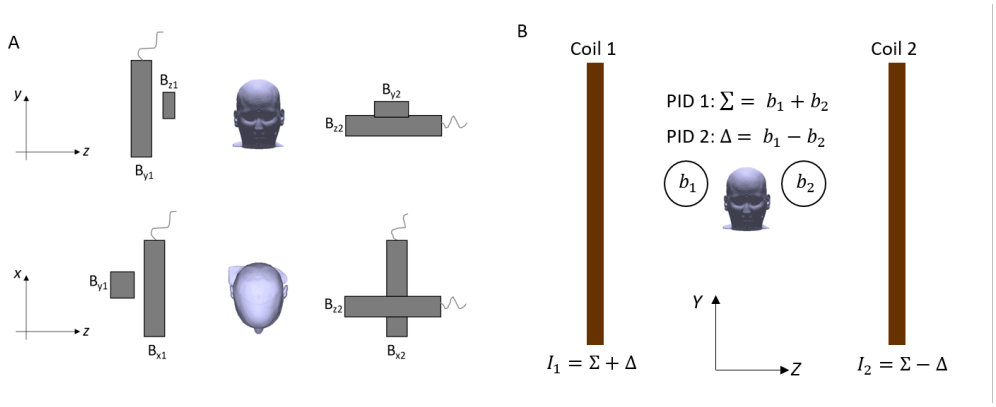



Figure 5.3: *Automated field nulling based on reference measurements. (A) A reference array of four Gen-1 QuSpin OPMs is used to measure the vector field components $B_x$, $B_y$ and $B_z$ at two locations separated in the z direction. (B) Two PID controllers are used to drive each coil. One uses $\Sigma$ to drive the sum of the field at the two locations (driving for example the $B_x$ field down towards zero). The second PID uses $\Delta$ to drive the difference of the field at the two locations (the gradient $G_x$) towards zero. Currents which are the sum and difference of these values are then applied to the planes.*

estimates of the magnitudes of $B_x$, $B_y$ and $B_z$ and of $G_x$, $G_y$ and $G_z$ (for example, $G_x$ is found through subtraction of two measurements of $B_x$).

To automatically null the field over the reference array, two proportional integral derivative (PID) controllers (see section 3.3.2) are driven in tandem and used to identify the optimal currents to pass through the coil windings in each plane. Taking the example of nulling the $B_x$ and $G_x$ fields, the reference array produces two measures of $B_x$ ($b_{x1}$ and $b_{x2}$) at locations which are spatially separated in $z$. The first controller varies a parameter $\Delta$ in order to reduce $b_{x1} - b_{x2}$, which provides a measure of the field gradient $G_x$. The second controller varies a parameter $\Sigma$ in order to reduce $b_{x1} + b_{x2}$, which provides a measure of $B_x$. Currents $I_1$ and $I_2$ are then supplied to the two different coil planes, where $I_1 = \Sigma + \Delta$ and $I_2 = \Sigma - \Delta$. The balancing of the terms results in simultaneous reduction of the field and field gradient towards zero.

A LabVIEW-based controller was developed to implement this algorithm by link-

ing to the reference array and coil drivers. Once nulling is completed the PIDs are switched off, and stable currents are applied to the coils. This process is outlined in Figure 5.3B.

### 5.3.4 Field mapping

In order to quantify the reduction in field and field gradient, field maps were taken over a single plane before and after the coils were used for field nulling as described previously in section 4.3.3,. A 40 × 40 $cm^2$ region in the $x$-$z$ plane lying between the reference sensors (which were separated by 40 cm in $z$) was mapped. By taking two measurements using the field-zeroing mode of a single Gen-1 QuSpin OPM at each position on a 10-cm grid (changing the orientation of the sensor to allow the field to be measured in three dimensions) over the plane, a representation of the static field can be obtained. The data were linearly interpolated (using the MATLAB interp2 function) onto a 1-cm resolution grid for visualisation, and field maps produced to show changes in magnitude and spatial variation.

The average field is calculated as the mean over each point in the interpolated grid with the associated standard deviation given as the error. A measure of the gradient is found from the difference in field divided by the difference in $z$ position. The difference of the field values measured at $z$ = -20 cm and $z$ = +20 cm were taken. These measurements were again carried out in the MSR at the University of Nottingham.

### 5.3.5 Dynamic field nulling

The balanced bi-planar coils described here were intended for use in an OPM-MEG system to be operated inside a MSR (Vacuumschmelze, Hanau, Germany)

comprised of two layers of mu-metal and one layer of aluminium, which is sited in the basement of the Wellcome Centre for Neuroimaging at University College London (UCL). This city centre site is close to the Piccadilly Line of the London Underground as it runs between Russell Square and Holborn underground stations at a depth of around 33 m (maps generated from Transport for London data available here - https://www.dansilva.co.uk/down-underground). As a consequence of proximity to the passing underground trains the background magnetic field in the MSR varies by several nT over a 10-minute period. This drift pushes the OPMs close to the edge of their dynamic range and causes gain changes.

In order to address this issue, a dynamic PID controller was developed that could be used to control the currents in the balanced, bi-planar coils to keep the ambient field within the sensors' operational range during recordings, minimising any impact on their performance. In contrast to the static-field nulling PID controller this controller uses the sensor voltage signal, not the field-zeroing values, as the process variable.

An array of 15, Gen-2 QuSpin OPMs was placed in an empty 3D printed scanner-cast [Boto et al., 2017]. Three of these sensors, which were placed in slots oriented in the $x$, $y$ and $z$ directions so that they measured the field components $B_x$, $B_y$ and $B_z$ along their radial axes, were selected as reference sensors. The sensors were operated in single-axis measurement mode with the dynamic range set to $\pm 5$ nT and data were recorded using a National Instruments 16-bit NI-9205 ADC interfaced with a LabVIEW controller. The voltage outputs from LabVIEW for driving the coils were controlled using the NI-9264 DAC. The controller sampled data from all 15 sensors at a 6,000 Hz sampling rate and the data was saved in chunks of 50 samples. For each of these 50-sample chunks the data from the three reference sensors was selected and passed to a digital, first-order, low-pass Butterworth filter with a 1 Hz cut-off frequency (chosen such that the controller

was addressing only the low frequency fluctuations in the remnant magnetic field). The average of these 50 samples was then taken.

The averaged values were then fed into three PID controllers (one for controlling each of the $B_x$, $B_y$ and $B_z$ fields). These controllers were manually tuned by observing the system response to variation in the proportional and integral gains (derivative gains were set to zero) to provide stable nulling without interfering with each other, as cross-talk can be introduced between the coils and reference sensors. For example, the effect of poor coil or reference sensor positioning could lead to a measurable effect of the $B_x$ coil on the $B_y$ reference sensor, in turn leading to an over-correction on the $B_y$ coil which impacts on the $B_x$ reference sensor and so on. A well-tuned loop can readily compensate for these 'cross-talk' effects. The PID output voltages were applied to the coils on the two planes such that uniform field components were produced (i.e. voltages of the same sign were applied to the coils for generating $B_z$, and of opposite sign for producing $B_x$ and $B_y$). Data from the remaining 12 sensors were also recorded. During each recording, data was taken from the Transport for London website for trains which ran on either of two routes: Eastbound from Holborn to Russell Square and Westbound from Russell Square to Holborn. Whilst this does not provide the exact time that trains came in closest proximity to the MSR, it does indicate the number of trains that crossed beneath the lab during the recordings.

A recording with the nulling off was taken between 17:22 and 17:32, while a recording with nulling- on was made between 17:35 and 17:45. These times fall during the 'rush hour', during which there is heavy train activity (trains arrive roughly every 2 minutes on the Piccadilly Line around this time), providing a challenging environment for the measurements.

### 5.3.6 Investigating interactions with the shielded room

The fields that are produced by the coils may interact with the high-permeability material used when constructing the MSR and result in deviations from the predicted performance. As described in Chapter 3, the following conditions apply: at a boundary between materials of different relative magnetic permeability $\mu_r$, to obey Ampere's law the tangential component of the magnetic field $\boldsymbol{H}$ must be continuous across the surface, and to obey Gauss's law the normal component of $\boldsymbol{B}$ must also be continuous [Hoburg, 1995]. Since $\boldsymbol{B}$ takes the form $\boldsymbol{B} = \mu_0\mu_r\boldsymbol{H}$ inside the material and $\mu_r$ can be >80,000 for mu-metal, while $\mu_r \approx 1$ in air, the field must abruptly change direction at an interface between air and mu-metal to satisfy the two boundary conditions [Hoburg, 1995], and in particular on the air-side of the boundary the tangential components of the $\boldsymbol{B}$ and $\boldsymbol{H}$ fields must be approximately zero.

Under these circumstances the field variation within the MSR can be evaluated by addition of a set of virtual mirror currents produced by simple reflection of current-carrying elements of the coils at each of the walls of the room. For magnetostatics' problems, this 'method of images' approach is not very sensitive to the exact value of $\mu_r$, just requiring that $\mu_r >> 1$ since deviations from the field variation it predicts scale as $(\mu_r)^{-1}$ which is negligible for mu-metal [Hammond, 1960, Roshen, 1990]. To ensure that the boundary conditions are properly fulfilled, reflections have to be calculated recursively so that the mirrored currents are themselves mirrored. Here, the effect that the mu-metal walls have on the form of the field produced by the balanced coils operating inside the MSR has been modelled via the addition of a truncated set of these mirror currents [Juhas et al., 2014, Qinjie et al., 2018].

Considering a single current element, reflections are made at each of the internal faces of the shielded room and the direction $d\boldsymbol{l}$ reversed according to $d\boldsymbol{l} = d\boldsymbol{l} -$

$2(d\boldsymbol{l}.\hat{\boldsymbol{n}})$ where $\hat{\boldsymbol{n}}$ is the unit vector perpendicular to the plane in which the element was reflected.

After consideration of each internal face of the MSR, this results in the production of 6 mirrored current elements. Each of these mirrored elements is then also mirrored by reflection at the five walls of the MSR that were not involved in the original reflection. This process should be repeated ad infinitum to satisfy the boundary conditions on the magnetic fields at the MSR's internal walls. Accounting for redundancies there are 6 first order mirror elements, 18 second order mirrors, 38 third order mirrors and so on. Example mirrored elements up to third order in two dimensions are shown in Figure 5.4. The additional field produced by each of the mirrored elements is calculated using the elemental Biot-Savart law. Here, only reflections up to third order were considered. This order was chosen as the change in coil efficiency (at the centre of the planes) with reflections up to second order was found to be around 30%, while the additional contribution from third order mirrors only modified the efficiency by a further $\approx$ 5%.

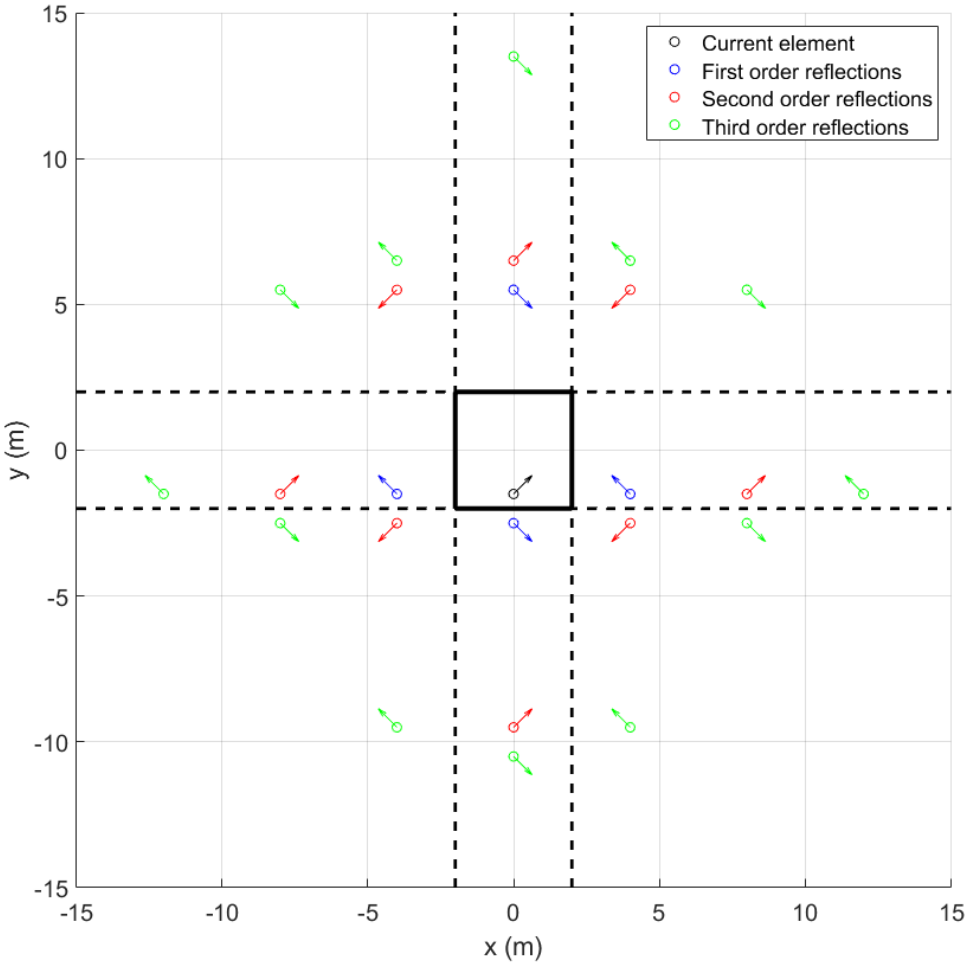



Figure 5.4: *Using virtual 'mirror currents' to simulate the effects of high-permeability materials on magnetic fields produced by electromagnetic coils. A single current element (black circle) is positioned at $x = 0$ m, $y = -1.5$ m, $z = 0$ m with an orientation $dx = 1/\sqrt{2}$, $dy = 1/\sqrt{2}$, $dz = 0$ inside a cube of high-permeability material (solid black lines) of side length 2 m. The method of mirror images can be used to evaluate a series of virtual mirror currents via reflections in the walls of the cube and their extended planes (dashed black lines) with the direction $d\boldsymbol{l}$ reversed according to $d\boldsymbol{l} = d\boldsymbol{l} - 2(d\boldsymbol{l}.\hat{\boldsymbol{n}})$ to describe interactions with the high-permeability material. The first-order, second-order and third-order reflections are calculated for this single element and plotted over a two-dimensional plane at $z = 0$ m in blue, red and green, respectively.*

A simple experiment to verify the mirroring method was conducted in the UCL MSR, which has internal dimensions of 3.85 × 2.4 × 3 $m^3$. A single coil plane was placed parallel, and as close as possible, to one of the 3.85 × 2.4 $m^2$ walls of the MSR. The coil plane was offset from the centre of the MSR by 0.6 m and -0.2 m in the $x$ and $y$ directions and due to the legs of the wooden support structure the centre of the coil was displaced by 25 cm in the $z$-direction from the proximal wall of the MSR. A 0.1 Hz sinusoidally oscillating voltage with amplitude of 1 V (equivalent to 8.1 mA current, $R = 125\ \Omega$) was applied to the $B_z/G_z$ coil on this plane and the $z$-component of the magnetic field was measured at a position 5 cm displaced from the centre of the coil in the $z$-direction away from the proximal wall of the MSR (but centred in $x$ and $y$) using a single-axis fluxgate magnetometer (Fluxmaster, Stefan Mayer Instruments, Dinslaken, Germany). The coil plane and fluxgate magnetometer were then further displaced from the wall in steps of 20 cm in the $z$-direction until the setup could not be moved any further due to the presence of a cryogenic MEG system (CTF, Coquitlam, BC, Canada). A final displacement of 85 cm from the wall was achieved. At each position the fluxgate magnetometer was similarly positioned relative to the coil. For comparison the $z$-component of the field was calculated, with, and without the effect of mirroring by applying the elemental Biot-Savart law to the $B_z/G_z$ coil and its reflections.

The effects of the interactions on the bi-planar coils was then investigated by simulation. The field was calculated over a 40 × 40 × 40 $cm^3$, 2.5 cm resolution 3D grid at the centre of the two coil planes and the results compared to measurements of the coil field or field gradient per unit current. Three cases were studied: first, when no mirrors were considered, second when the coils were positioned centrally in the MSR at the University of Nottingham and mirrors up to third order were included, and finally when the coils were positioned as they are during an experimental session and mirrors up to third order were considered. For each case a box plot of the full range of fields calculated at all grid positions

was produced to show the effects of the mirror currents on both the homogeneity and the mean level of the produced field.

The effects were investigated for the three coil pairs when producing $B_x$, $B_y$ and $B_z$. The MSR considered here has internal dimensions of 3.85 $\times$ 2.4 $\times$ 3 $m^3$ and during an experiment the centre of the bi-planar coil set is displaced from the centre of the room by +0.2 m in $y$ and -0.25 m in $x$ (with zero offset in $z$).

## 5.4 Results

### 5.4.1 Coil designs

Figure 5.5 shows wire paths (i) for the (A) $B_x$ and $G_x$, (B) $B_y$ and $G_y$ and (C) $B_z$ and $G_z$ coils, respectively. The elemental Biot-Savart law was applied to the wire-paths to evaluate the spatial variation of the field (ii) or field gradient (iii) produced, when the coils are wound in a bi-planar arrangement. The field was calculated over a 3D array of points covering a region of 40 × 40 × 40 cm$^3$. Contours are shown over a plane at $z = 0$ m; $|x|$, $|y| < 0.2$ m for the case of $B_x$, $B_y$, $B_z$, $G_x$, and $G_y$ and over the plane at $z = 0.025$ m; $|x|$, $|y| < 0.2$ m for the $G_z$ case. The fields were normalised to the value at the centre of the two planes (or a value positioned slightly off-centre when the field is zero at the centre). The homogeneity measure for all the fields produced over this volume was $H = 100\%$.

Table 5.1 shows calculated and measured values for the bi-planar coil efficiencies and single plane inductances. The errors quoted for the field generating coils are the standard deviation from the mean measured across three OPMs spatially separated in $z$, while the errors in the gradient generating coils are the differences in the two gradient values calculated from the three OPM measurements. The inductances were calculated from the stream functions using previously published expressions [Martens et al., 1991].

| Coil | Efficiency as field coil nT/mA | Efficiency as field gradient coil nT/m/mA | Single plane inductance $\mu$H |
|---|---|---|---|
| $B_x$ and $G_x$ | 0.74 (0.57± 0.01) | 1.20 (1.11± 0.02) | 169 (192) |
| $B_y$ and $G_y$ | 0.74 (0.47± 0.02) | 1.20 (0.98± 0.02) | 169 (193) |
| $B_z$ and $G_z$ | 3.9 (3.6± 0.3) | 4.7 (4.5± 0.7) | 379 (385) |

Table 5.1: *Comparing theoretical and measured values (in brackets) of the efficiency and inductances for the coil designs when wound as field and gradient coils.*

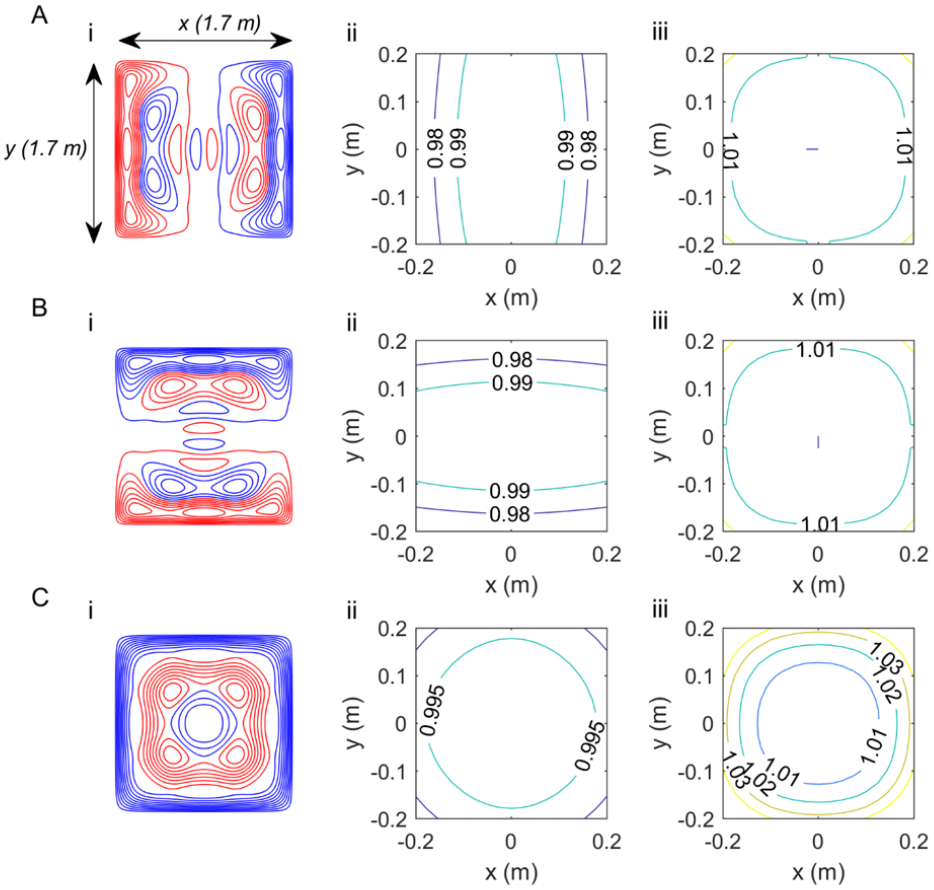



Figure 5.5: *Final coil designs and simulated fields. Wire paths (i) and field (ii) or field gradient contours (iii) for the: A) $B_x$ and $G_x$ coil, B) $B_y$ and $G_y$ coil and C) $B_z$ and $G_z$ coil, respectively. Red and blue denote wires with opposite senses of current flow. The contours of the field or field gradient in the plane at $z = 0$ m, for $|x|$, $|y| < 0.2$ m ($z = 0.025$ m, for $|x|$, $|y| < 0.2$m for $G_z$) are shown. The field values are normalised to the field at the centre of the plane or a value slightly off-centre when the central field is zero.*

### 5.4.2 Comparing design methods

Figure 5.6 shows (i) designs for coils, (ii) contours of $B_x$ and (iii) contours of $G_x$ for coils optimised to produce (A) $B_x$, (B) $G_x$ and (C) and both $B_x$ and $G_x$. The field and gradient variation is calculated using the elemental Biot-Savart law and is plotted over a plane at $z = 0.20$ m; $|x|$,$|y| < 0.20$ m. This plane is deliberately chosen to be off-centre to highlight the decrease in homogeneity with distance from the centre of the region between the two coil planes.

Comparing the homogeneity of the non-optimised field (e.g. the $G_x$ variation produced by the $B_x$ coil) shows the combined method improves homogeneity, but with an increase in design complexity. The $B_x$ coil had a $G_x$ homogeneity of $H = 76\%$ and the $G_x$ coil had $B_x$ homogeneity of $H = 78\%$ compared to $H = 100\%$ for the optimised field components. The largest deviations of the field and gradient at $z = 0.20$ m in Figure 5.6A (ii-iii) are +2% and -13% respectively. The field and gradient in Figure 5.6B (ii-iii) deviate by -9% and +2% respectively. The field and gradient in Figure 5.6C (ii-iii) deviate by +3% and -4% respectively. Only the combined design satisfies the condition that both the field and field gradient should be homogeneous to within 5% over a central $40 \times 40 \times 40$ cm$^3$ cubic region.

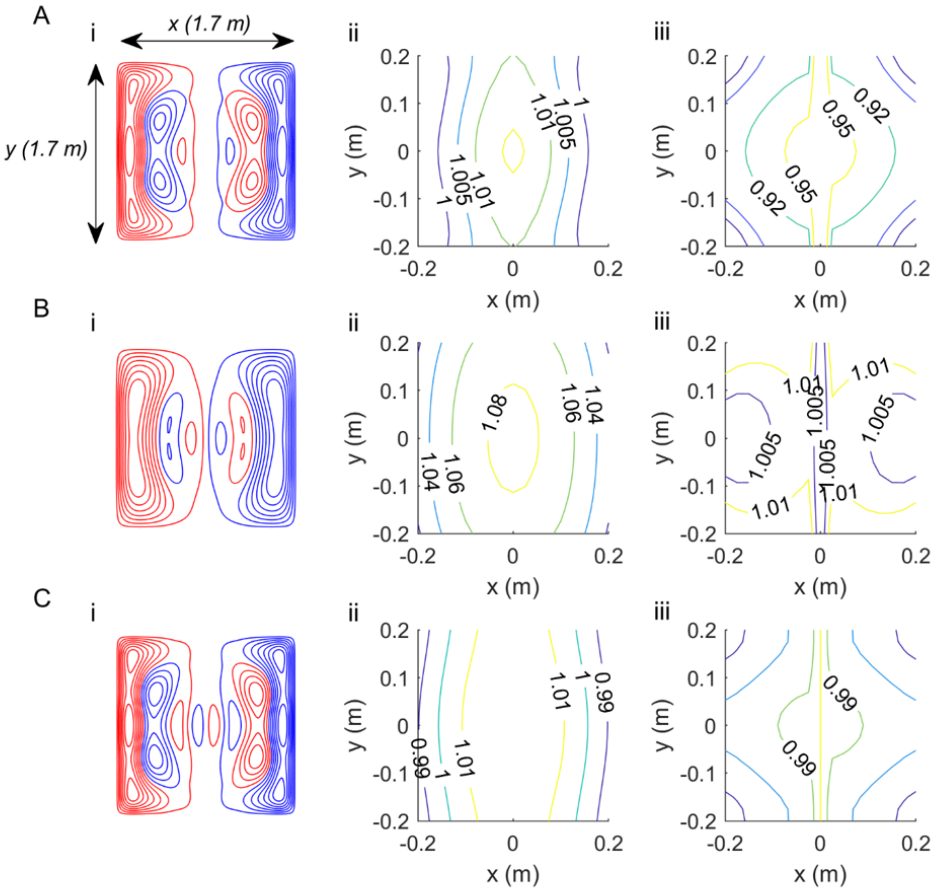



Figure 5.6: *Investigating the performance of the joint design method versus only producing a single field component. A) B) and C) show for coils optimised to produce $B_x$, $G_x$ and both $B_x/G_x$ respectively: i) coil wire paths (red and blue denote wires with opposite senses of current flow); ii) contours of the variation of $B_x$ produced by these coils; iii) contours of the variation of $G_x$ produced by these coils. Contours are shown for the plane $z = 0.20$ m, for $|x|, |y| < 0.20$ m. The field values are normalised to the field at the centre of the plane or a value slightly off-centre when the central field is zero.*

### 5.4.3 Field mapping

Figure 5.7 shows maps of the spatial field variation in (A) $B_x$, (B) $B_y$ and (C) $B_z$ inside the MSR before (i) and after (ii) the automated nulling process was applied, along with a bar chart (iii) showing the reduction in average field strength. The mean magnitude of the field vector was reduced by a factor of 26 from 23 nT to 0.9 nT. The reduction in the measured individual field components with the associated standard deviation from the mean is shown in Table 5.2. The maps of the field variation are not as smooth as are expected to be found in a source-free region, as a result of inaccuracies in manually setting the sensor position and orientation, and the limited accuracy of measurement that can be achieved when operating the QuSpin sensors in field-zeroing mode.

| Field component | Nulling off (nT or nT/m) | Nulling on (nT or nT/m) | Reduction factor |
|---|---|---|---|
| $B_x$ | 16.0 ± 0.1 | 0.3 ± 0.04 | 53 (46) |
| $B_y$ | 2.9 ± 0.1 | 0.11 ± 0.13 | 26 (210) |
| $B_z$ | 17 ± 0.2 | 0.49 ± 0.15 | 35 (33) |
| $G_x$ | 6.1 ± 0.9 | 0.9 ± 0.4 | 7 (13) |
| $G_y$ | 2.5 ± 0.9 | 1.8 ± 0.9 | 1.4 (6) |
| $G_z$ | 3.4 ± 0.8 | 1.3 ± 0.3 | 3 (5) |

Table 5.2: *Field nulling performance on each field component. Mean values over the mapped region are shown from the field maps taken when nulling was off and on. Errors are standard deviation from the mean. The factor by which the mean value of each field component was reduced is also reported, with the values obtained using the six-coil system described in Chapter 4 quoted in brackets.*

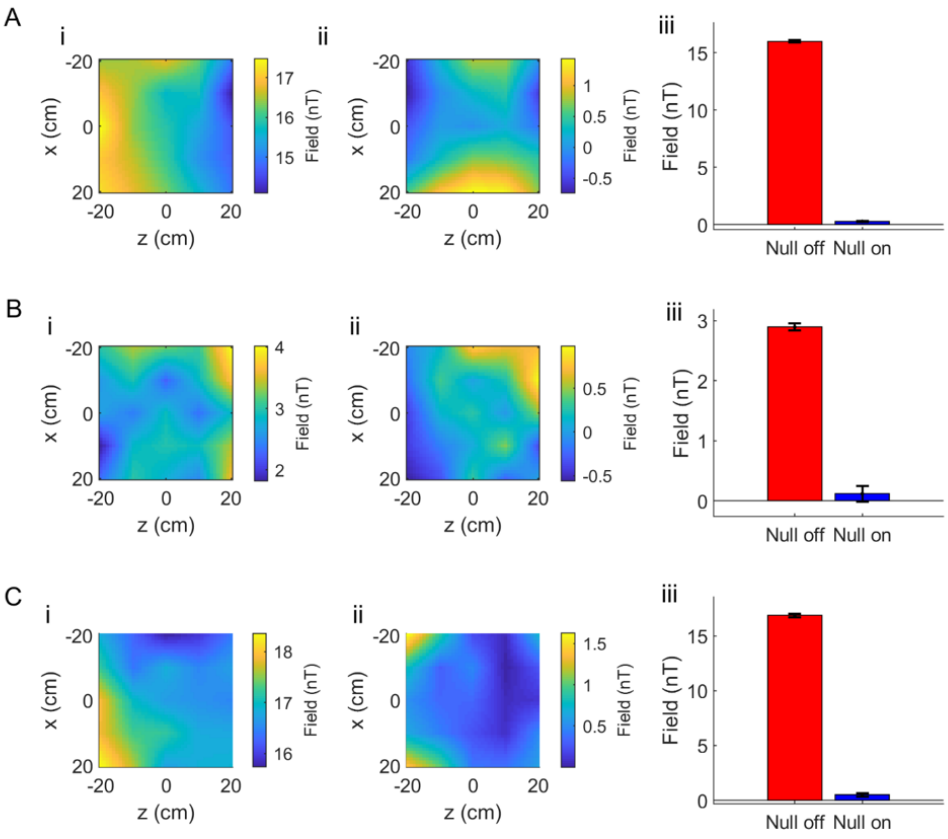



Figure 5.7: *Quantifying the coil performance by measuring the field in a single plane. A) B) and C) show for $B_x$, $B_y$, and $B_z$ respectively: i) a map of the field before nulling is applied; ii) a map of the field after nulling is applied; iii) the average field magnitude with error-bars showing the spatial standard deviation of measurement before (red) and after (blue) nulling is applied.*

### 5.4.4 Dynamic field nulling

Figure 5.8A-B show the time-series data from the 15 sensors placed in an empty scanner-cast inside the empty MSR. Figure 5.8A shows data recorded over a 10-minute period with the dynamic nulling off, while Figure 5.8B shows data recorded with dynamic nulling on. Vertical lines show the approximate times that a train arrived at either Russell Square or Holborn stations during the two different recording periods, thick lines show two trains arriving at the same time. During the nulling-off recording, 10 trains were reported in the 10-minute period, while for the nulling-on recording 7 trains were reported.

The maximum peak-to-peak variation of the time-series data across the 15 sensors was reduced from 2.37 nT to 0.13 nT by the dynamic nulling. The maximum standard deviation from the mean of the sensor outputs across sensors was reduced from 0.501 nT to 0.012 nT.

Figure 5.8C shows the median power spectral density estimate across all 15 sensors. To compute this estimate, the data were split into three non-overlapping sections of 200-s duration. For each section, flat-top windowing (using the MATLAB function flattopwin) was applied prior to calculation of the power spectral density via fast Fourier transformation. The results were then averaged over the three sections for each sensor and the median taken across all 15 sensors. No additional processing (e.g. forming synthetic gradiometers or linear regression) was applied to the raw magnetometer traces to remove other sources of interference. As a result, the noise spectra are mostly dominated by interference sources, which exceed the noise level specifications of the OPM sensors (https://quspin.com/products-qzfm/).

Figure 5.8D shows the shielding factor of the system computed as the ratio of the PSDs shown in Figure 5.8C for the nulling-off and nulling-on cases. The shielding

factor is reported in decibels (dB) and is 40 dB at 0.01 Hz.

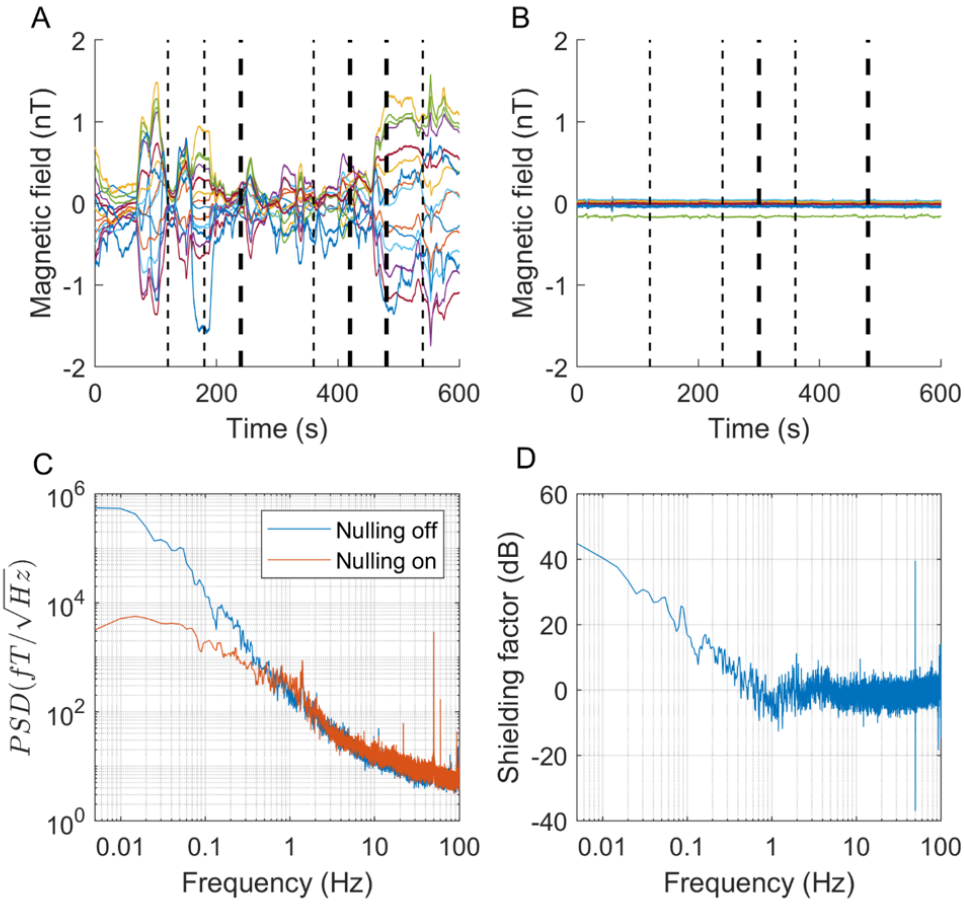



Figure 5.8: *Assessing the performance of dynamic nulling. A) The time-series data from a series of 15 OPMs placed in an empty scanner-cast in an empty MSR with no dynamic nulling applied. Here and in (B), vertical dashed lines show the approximate times that a train arrived at either Russell Square or Holborn stations, thick lines indicate two trains arriving at approximately the same time. B) Time-series data from the same OPMs with the dynamic nulling switched on. C) The median power spectral density of the sensor outputs for the two cases across all sensors. D) The shielding factor of the system.*

### 5.4.5 Investigating interactions with the shielded room

Figure 5.9 shows the measured $B_z$-field amplitude as a function of the $z$ displacement of the coil plane from the wall of the MSR, errorbars are calculated as the standard deviation of the amplitude over ten cycles. The expected enhancement of the measured field amplitude with proximity to the wall of the MSR is seen. Good agreement with the calculated data is also evident, indicating that the mirroring method provides a reasonable model of the interaction between the coils and the walls of the MSR.

Figure 5.10 shows box plots representing the mean and spatial variation over a central 40 × 40 × 40 $cm^3$ volume of the calculated (A) $B_x$, (B) $B_y$ and (C) $B_z$ fields per unit current (i.e. coil efficiencies) for three cases, where: (i) no mirror currents were considered; (ii) the bi-planar coils were assumed to be centrally positioned within the MSR and mirror currents up to third order were considered; (iii) the bi-planar coils were positioned off-centre, as they would be during an experiment, and mirror currents up to third order were considered. The measured experimental value of the efficiency and its associated standard deviation is shown as a red star with error bar for each case. As indicated previously, the experimental values of $B_x$, $B_y$ and $B_z$ were averaged over three OPMs spatially separated in z. If the experimental value lies within the range of the box plots this is a good indication of the model being broadly accurate. High spatial homogeneity is desirable for producing a controlled field over the subject.

For the case of the $B_x$ coil with no mirroring of currents, the median calculated field over the grid was 0.72 nT/mA with a range of 0.05 nT/mA (maximum value 0.7 nT/mA and minimum value 0.75 nT/mA). Positioning the coils at the centre of the MSR and adding mirror currents reduced the median calculated field to 0.64 nT/mA with a range of 0.06 nT/mA (max/min 0.61/0.67 nT/mA). Realistic positioning of the coils within the MSR and accounting for current mirroring

further reduced the median efficiency to 0.62 nT/mA with a range of 0.21 nT/mA (max/min 0.67/0.46 nT/mA). The measured value of the efficiency of 0.57 ± 0.01 nT/mA lies within the increased range of field values. The simulations show that the field homogeneity decreases when the effect of the MSR is included. The maximum deviation of the field over the 40 x 40 x 40 $cm^3$ volume that was considered increases from 5% with no consideration of mirror currents to 26% when the effects of the mirror currents are included for the realistically positioned coils.

Similar results were obtained for the $B_y$ coil with the median simulated field decreasing from 0.66 nT/mA with a range of 0.05 nT/mA (max/min 0.64/0.69 nT/mA) when mirror currents were not considered to 0.54 nT/mA with a range of 0.17 nT/mA (max/min 0.6/0.43 nT/mA) when the coils were realistically positioned and the effects of the mirror currents were included. This range includes the measured value of 0.47 ± 0.02 nT/mA. The field inhomogeneity is increased from 5% to 22% for this coil when the mirror currents are included

Finally, in the case of the $B_z$ coil, the median field increased from 3.90 nT/mA with a range of 0.11 nT/mA (max/min 3.97/3.86 nT/mA) to 4.27 nT/mA with a range of 0.61 nT/mA (max/min 4.45/3.84 nT/mA) on inclusion of mirror currents with realistic coil positioning. The upper bound of the error on the experimentally measured value of 3.60 ± 0.30 nT/mA lies within this range, but the general trend of an increased efficiency is not observed. The inhomogeneity is increased from 5% to 10% for this coil when the effect of the mirror currents is taken into account.

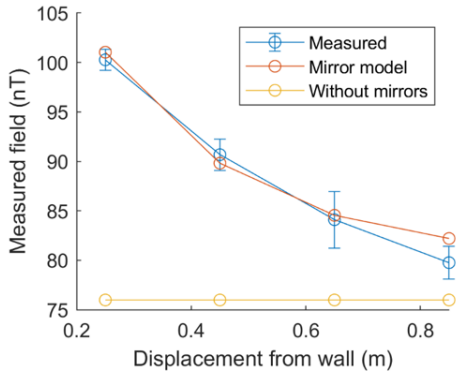



Figure 5.9: *Experimental test of the mirroring approach to modelling coil interactions with high-permeability materials. The measured amplitude of a sinusoidally varying $B_z$ magnetic field produced by a single coil is plotted as a function of displacement from the wall of the MSR. Simulated data both with and without the mirroring is provided for comparison.*

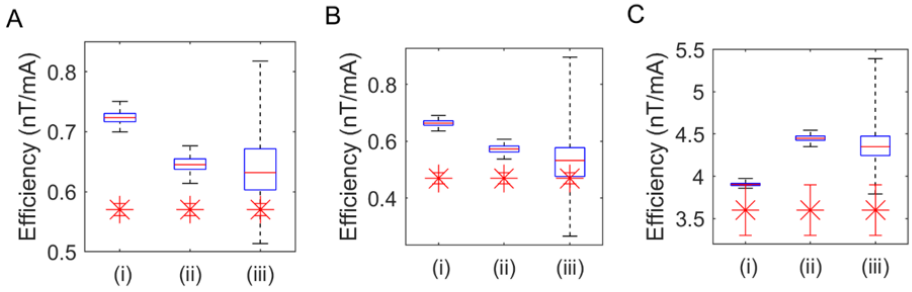



Figure 5.10: *Investigating the effects of interactions of the coils with the mu-metal walls on the efficiency and homogeneity of the produced fields. A) B) and C) show for $B_x$, $B_y$, and $B_z$ respectively: i) a boxplot of the full range of fields calculated over a 40 $\times$40 $\times$ 40$cm^3$ grid when the coils are operating in free space, ii) when the bi-planar coils are centred in the room and mirror currents up to third order are included and iii) when the coils are positioned as they would be during an experiment. The red stars shows the measured efficiency and standard deviation of each coil when setup for an experiment. Experimental values of $B_x$ and $B_y$ were averaged over three OPMs spatially separated in z at z = -8 cm, z = 0 cm and z = +8 cm. For the $B_z$ measure the sensors were positioned at z = -17 cm, z = 0 cm and z = +17 cm for the $B_z$ measurement.*

## 5.5 Discussion

### 5.5.1 Coil design and construction

By introducing a design and control method to produce coils which provide field nulling of six field terms using only three coil designs, construction of a field nulling system for use in wearable MEG is considerably simplified. The performance of the new field-nulling system is comparable to that obtained previously using the six-coil system described in the previous chapter.

Although simpler coil designs such as the 'Helmholtz-cage' style system described by Iivanainen and colleagues do not require complex wirepaths or use of large biplanar coils the subject has to remain fixed within a cubic enclosure [Iivanainen et al., 2019]. A compromise has to be made upon system design between the freedom of motion and the quality of the MEG data which is obtained. Shielded rooms with larger remnant fields and gradients and larger temporally varying fields will pose a greater challenge for field nulling and as a result a fixed system may be simpler to implement. Additional compensation of higher order terms as well as improved dynamic nulling could allow for subject movement in poorer shielded environments.

To fully compensate for the uniform field and field gradients 8 terms (3 uniform fields and 5 gradients) are required, as the divergence and curl of the field are both zero in the current-free region between the planes. The system described here only produces 6 field terms. In this bi-planar arrangement the additional $dB_x/dy$ and $dB_x/dx$ terms have no shared symmetry with the uniform coils (or with one another) and would have to be individually constructed. Designs for these coils are detailed in Chapter 4 but they were not constructed.

Although the number of coils that have to be wound is halved with this approach,

the process of manual construction is still a cumbersome task and will likely result in errors such as inaccurate wire placement, misalignment from the wallpapering of the coils and warping of the wood.

Although the PID approach allows for some of these errors to be taken into account, and the field nulling performs well, 3D printing, printed circuit board etching or water cutting techniques could potentially be used to increase the accuracy of coil winding and decrease labour requirements. With these techniques, the complexity of wire paths that could be produced would also increase.

### 5.5.2 Static and dynamic field nulling

Though the system described here provides nulling which allows for movements by a seated subject, additional coils could also be constructed to provide better nulling and potentially allow a greater range of movements. These could include coils to generate the remaining two field gradients ($dB_x/dx$ and $dB_x/dy$), individual, higher order spherical harmonics or more complex local patterns of field variation. Dynamic nulling of uniform field components was successfully implemented using the balanced bi-planar coils, allowing the OPMs to be operated continually in a magnetically noisy environment, meaning that experiments could be completed without saturation of sensor outputs due to interference from a nearby underground railway line.

The relatively low mutual inductance ($M$) and self-inductance ($L$) of the coils (all $< 400$ $\mu$ H) and the low frequency of operation ($< 120$ Hz) meant that the effects of inductance were not important when driving the coils since $MdI/dt$ and $LdI/dt$ were both always much smaller than $IR$ (where $I$ is the current and $R$ is the coil resistance).

The slight increase in noise level which is introduced in the nulling-on case (see

Figure 5.8C-D) produces a negative shielding factor at some frequencies above 1 Hz. This noise results from the limited dynamic range of the field nulling electronics used here. To compensate for the remnant static field components the field nulling system has to be able to produce tens of nT; the NI-9264 DAC module has a ±10 V dynamic range and a 16-bit resolution, the least significant bit is therefore equivalent to $20/2^{16} \approx 0.3$ mV. In an example system, where 40 nT is required from 10 V this is equivalent to a field of roughly 1 pT. Rounding errors in setting the voltage in dynamic nulling consequently lead to additional field variation at the pT level at the sensor. In the low frequency range (<1 Hz) the environmental field variation is much larger than 1 pT and the dynamic nulling performs well, producing a significant shielding factor. However, at higher frequencies the environmental field noise is lower in magnitude and the additional field noise from the limited dynamic range of the nulling system becomes the dominating factor. This additional noise is apparent in the presented data, but as the effects are systematic and picked up by all sensors, synthetic gradiometry could be used to attenuate them.

To attenuate these effects in future field nulling systems a 24-bit DAC could be used to increase the dynamic range. The development of a two-circuit driver, one optimised for static nulling (producing e.g. 40 nT from 10 V) and one for dynamic nulling (producing e.g. 4 nT from 10 V) with the sum of the currents applied to the coils could be developed.

The speed of the LabVIEW based controller is fundamentally limited by the loop rate of the software. More advanced controllers, such as field programmable gate array microcontrollers or analogue solutions will be required for increased nulling performance at higher frequencies.

Although, here, the reference sensors were mounted in a scanner-cast during the MEG recording they would have to be placed behind the subject as shown in

Figure 5.3 in a real experiment, since with head-mounted reference sensors subject movements would reorient the reference sensors away from the $x$, $y$ and $z$ directions. This setup would allow the dynamic nulling to be readily expanded to include compensation of the field gradients $G_x$, $G_y$ and $G_z$ through measurement of the full vector field on both sides of the head. This has not yet been implemented due to the limited number of sensors available for use in the reference array. A more complex arrangement of the reference array and feedback mechanism will most likely be required to provide an optimal dynamic null over an entire head array of OPMs. Flexible arrays, body mounted reference sensors and prior knowledge of the static magnetic field at different points combined with optical tracking could be used to provide a stable null as the subject moves within the MSR. Such improvements in the performance of coil technology for field compensation will be needed to facilitate new avenues of OPM-MEG research, such as experiments involving spatial navigation and direct social interaction between individuals.

### 5.5.3 Interactions with the shielded room

Our brief investigation of the use of mirror currents to model interactions with the MSR revealed a change in median efficiency and reduction in homogeneity of the produced field which broadly agreed with the experimental measurements (Figures 5.9 and 5.10). The results imply the need to incorporate the effects of the high-permeability mu-metal into future coil designs, but it should be noted that the PID approach to both static and dynamic field nulling will seek to find the best solution without relying on a priori information.

Comparison of the boxplots in Figure 5.10 shows that, for all three coils, the effect of the MSR on the field homogeneity is much less when the coils are positioned at the centre of the room. The off-centre positioning of the coil results

in an asymmetric distribution of the additional field components from the mirror currents which make the field inhomogeneity larger than the ±5% condition targeted at the design stage. This asymmetry will also affect the efficiency and homogeneity of the gradient components, distorting the spatial distribution of the produced field. Unfortunately, the coils cannot be positioned centrally in the MSRs at UCL and the University of Nottingham, as a cryogenic MEG system which weighs around 500 kg is sited at the centre of each room. Increased displacement of the coils from the centre of the MSR in the $x$ and $y$ directions would further affect the spatial distribution of the mirrored current elements; the closer a coil plane is to the wall, the greater the asymmetry of the resulting field distribution.

The experimental values were taken over single lines with a 16 cm spread for the $B_x$ and $B_y$ cases and a 34 cm spread for the $B_z$ case instead of being measured over the entire 40 x 40 x 40 $cm^3$ region. This may account for some of the discrepancy between experimental and theoretical measurements. In general, the interaction between the coils and the mu-metal walls should be more thoroughly investigated in order to incorporate the effect of the MSR when designing future coils. A more thorough experimental test of the range of validity of the simple mirror approach for static and dynamically-varying fields would also be worthwhile, complemented by electromagnetic calculations using finite element analysis software.

# Chapter 6

# Matrix coils

## 6.1 Introduction

Chapters 4 and 5 described bi-planar coil systems which produce uniform magnetic fields, or magnetic field gradients over a central volume of interest. To better realise the potential of optically pumped magnetometers (OPMs) in magnetoencephalography (MEG) the capability to measure with participants undergoing full ambulatory motion is desired.

Following the successes of the development of OPM-based MEG (as aided by the bi-planar coil systems), a second magnetically shielded room (MSR) has been installed at the University of Nottingham by Magnetic Shields Limited (Kent, UK). This room has internal dimensions of $3 \times 2.4 \times 3$ m$^3$ but does *not* contain a cryogenic MEG system, meaning a large area is available for participant motion. The room is constructed from two layers of mu-metal and one layer of copper for shielding of high-frequency magnetic fields (aluminium was used in the MSRs described previously). A degaussing system (see Chapter 3) was installed which reduces the remnant field from 30 nT to $< 2$ nT in magnitude with field gradients of $\sim 2$ nT/m.

The size and position of the region of homogenous field produced by a bi-planar coil set is restricted by the fixed wire paths. As a result the strength of the magnetic field produced by each coil can be varied, but not its pattern of spatial variation. Without physically translating the coils, the field-cancellation region consequently cannot be moved to different positions inside a magnetically shielded room (MSR).

Interactions of the magnetic fields produced by the coils with the high-permeability materials used in construction of a MSR were briefly investigated in Chapter 5, but not considered when designing the coils. Using a method of images approach, with recursive mirroring to correctly fulfil boundary conditions, two key results were shown: an enhancement in the efficiency of field production of a single plane of a bi-planar coil when it was placed close to the wall, and a degrading of the homogeneity which is highly dependent on the position of the coil set within the MSR (as off-centre placement results in an asymmetric distribution of mirror components).

In this chapter, a coil design is described where adjustable currents are applied to a series of small unit coils to approximate a variety of current distributions. Such a system would be able to flexibly incorporate interactions with high-permeability materials, and move the field-nulling volume around the MSR allowing a wider range of participant motion. The design theory of this so-called 'matrix coil' is outlined and the simulated performance of a 48-coil prototype system is presented. Ongoing work to construct the prototype system is reported. A simulated matrix coil system where 60 coils are wound directly onto the walls of a MSR is also described.

## 6.2 Background

A multi-coil approach has previously been employed when designing shimming coils in magnetic resonance imaging (MRI). The application of such coils in this context is briefly summarised here.

Poor homogeneity in the large magnetic field inside the bore of a MRI scanner, $B_0$, has adverse effects on image quality. Position in an MR image is obtained from an assumed linear dependency of the Larmor frequency on the local magnetic field, and small changes in $B_0$ can therefore lead to image distortions.

The homogeneity of the superconducting magnet will be affected by imperfections and tolerances during the manufacturing process, environmental factors and the introduction of a participant. These inhomogenities can be alleviated by the process of shimming [Brown et al., 2014]. Passive shimming involves the positioning of small pieces of ferromagnetic metals at well-chosen locations to remove local field distortions. A more adaptable approach is through the use of active shimming coils [Gruetter, 1993].

Often, several coils are installed inside a scanner to produce 3 field gradient terms and 5 second order variations in the magnetic field, as described by the first and second order spherical harmonic functions [Roméo and Hoult, 1984]. A map of the field inhomogeneity is obtained and the optimal coil currents to remove field distortions are calculated. This shimming can be done at the start of a scan, or updated dynamically during scanning. Shimming coils are a standard component of an MRI scanner, enabling experiments ranging from structural and functional imaging to spectroscopic measurements of chemical concentrations within biological tissue.

Higher values of $B_0$ allow for increased spatial and temporal resolution, but at the

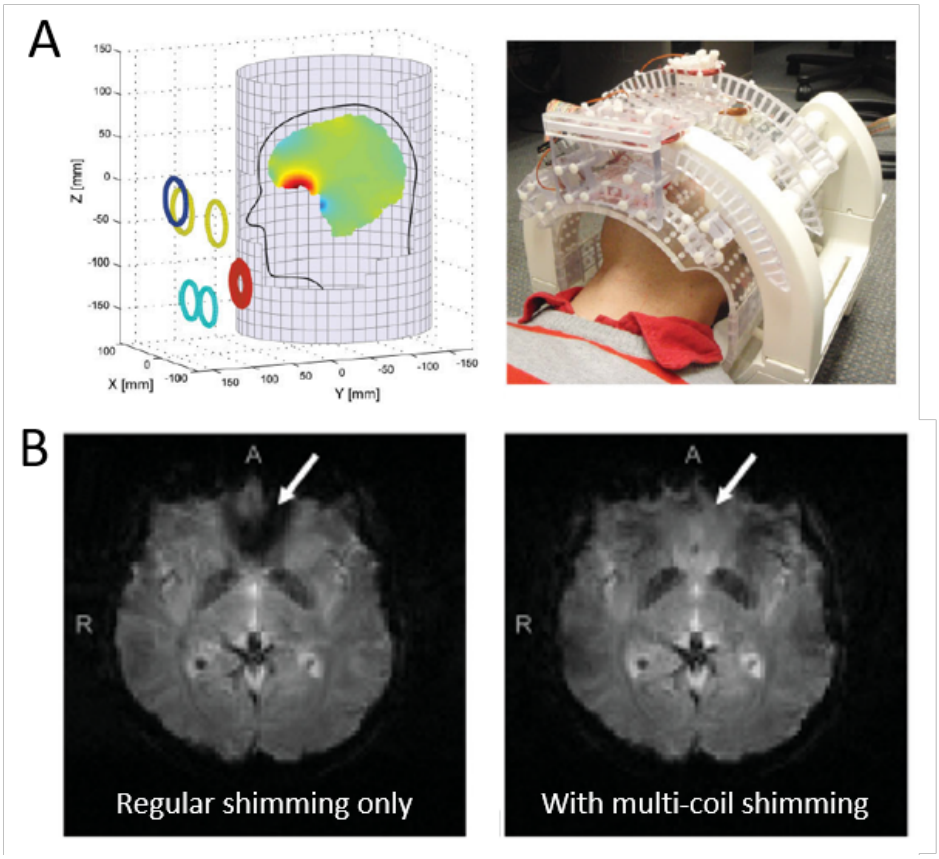



Figure 6.1: *Multi-coil shimming system. A) Layout and experimental setup of 6 coils to provide additional shimming to the prefrontal cortex. B) MRI images showing signal recovery from an increase in $B_0$ homogeneity over prefrontal cortex when applying multi-coil shimming to aid the regular shimming coils. Figure adapted from [Juchem et al., 2010a].*

cost of increasing the challenge of obtaining suitable $B_0$ homogeneity. For example, Juchem and colleagues note the complexity of obtaining high-quality fMRI data from the prefrontal cortex, where highly localised distortions are caused by large magnetic susceptibility differences between air-filled cavities and bones around the sinuses [Juchem et al., 2010a]. The temporal lobes are also areas which prove difficult to accurately shim. To address this problem they initially developed a multi-coil shimming technique using 6 small coils positioned above the head of a participant. These coils were used in conjunction with the standard shimming coils (which produce field components up to the full set of second order terms). Improvement of field homogeneity (in a 4 T MRI scanner) over prefrontal

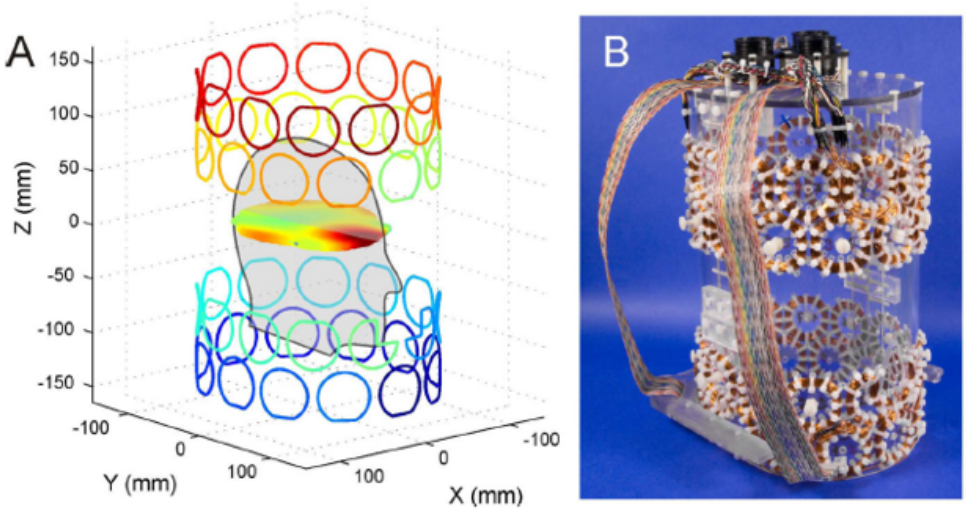



Figure 6.2: *48-coil shimming system. A) Layout of 48 coils to provide shimming over the full brain, the gap in the middle of the two 'bands' is to accommodate the radio frequency coil. B) Experimental realisation of the 48 coil system. Figure adapted from [Juchem et al., 2011b].*

cortex was achieved without impacting on the field homogeneity in the rest of the brain as shown in Figure 6.1 [Juchem et al., 2010a].

More complex multi-coil designs based on 48 coils have been used (without a standard shim system) to perform shimming of the brain of a mouse, where the small object size results in susceptibility variations causing highly localised and complex field inhomogeneities. Signal gains of up to 50% when compared to standard shimming techniques were achieved (9.4 T magnet using gradient echo scanning) [Juchem et al., 2011a]. Dynamic multi coil technique (DYNAMITE) shimming of the whole human brain at 7 T was also achieved using the 48 coil system shown in Figure 6.2 [Juchem et al., 2011b, Juchem et al., 2015].

Use of this kind of multi (or matrix) coil system for cancellation of the remnant magnetic fields inside a MSR could have multiple advantages over the bi-planar systems described previously:

- Bi-planar coils have a fixed region over which the field is homgoeneous; without physically translating the coils this region cannot easily be moved.

- The coils are wound on large planes, making their engineering, transportation and siting, challenging.

- Although interactions with high-permeability materials could be accounted for in the design stage, these interactions will vary with the geometry of the MSR and coil locations (as outlined in Chapter 5).

A matrix coil system has the potential to address these issues, since:

- Coil currents which best produce a given target field (at multiple locations away from the centre of the system) can be calculated. These cancellation currents can be found from knowledge of the field produced by each unit coil at each position, and of the remnant field at these locations.

- The design could be modular, with multiple small units placed wherever space inside the MSR is available. All units can then be connected to the driving electronics.

- Interactions could readily be taken into account through modelling of the field produced by each coil including the effect of mirrored images.

To develop matrix coil systems, calculation of physically sensible currents which meet power dissipation constraints, whilst producing accurate magnetic fields is crucial. Modelling investigations [Juchem et al., 2010b, Juchem et al., 2013] and linear algebra approaches [Garda and Galias, 2012, Garda and Galias, 2014, Garda and Galias, 2015] have previously been used to derive the individual coil currents which best produce a given target field within physical constraints. Here, these methods were used to create a mathematical formalism for matrix coil designs for field nulling inside a MSR.

## 6.3 Theory

A linear algebra method was used to develop mathematics for the matrix coil designs. By modelling the field of each coil at a set of target field positions when a unit current is applied, appropriate weightings can be chosen to produce a desired field pattern [Garda and Galias, 2014].

### 6.3.1 Matrix equation formulation

The magnetic field is evaluated over a set of target field points. The field produced by coil $m$ (from a set of $M$ coils), when carrying a unit current at target point $\boldsymbol{r}_n(x, y, z)$, is given as $\boldsymbol{b}_m(\boldsymbol{r}_n)$. The total field, $\boldsymbol{B}(\boldsymbol{r}_n)$ at this target point from all of the coils in the system, with the $m^{th}$ coil carrying a current $I_m$ (from $m = 1$ up to coil $m = M$), is then given as the vector sum of field contributions i.e.

$$\boldsymbol{B}(\boldsymbol{r}_n) = \sum_{m=1}^{M} I_m \boldsymbol{b}_m(\boldsymbol{r}_n). \tag{6.3.1}$$

By splitting the vector field into its Cartesian components $\boldsymbol{B} = b_x\hat{\boldsymbol{x}} + b_y\hat{\boldsymbol{y}} + b_z\hat{\boldsymbol{z}}$ the field produced at each of the target field points by each coil containing distinct currents can be expressed in matrix form as

$$\begin{bmatrix} b_{x11} & b_{x12} & b_{x13} & \cdots & b_{x1M} \\ b_{y11} & b_{y12} & b_{y13} & \cdots & b_{y1M} \\ b_{z11} & b_{z12} & b_{z13} & \cdots & b_{z1M} \\ b_{x21} & b_{x12} & b_{x13} & \cdots & b_{x2M} \\ b_{y21} & b_{y12} & b_{y13} & \cdots & b_{y2M} \\ b_{z21} & b_{z12} & b_{z13} & \cdots & b_{z2M} \\ \vdots & \vdots & \vdots & \ddots & \vdots \\ b_{xN1} & b_{xN2} & b_{xN3} & \cdots & b_{xNM} \\ b_{yN1} & b_{yN2} & b_{yN3} & \cdots & b_{yNM} \\ b_{zN1} & b_{zN2} & b_{zN3} & \cdots & b_{zNM} \end{bmatrix} \begin{bmatrix} I_1 \\ I_2 \\ I_3 \\ \vdots \\ I_M \end{bmatrix} = \begin{bmatrix} B_{x1} \\ B_{y1} \\ B_{z1} \\ B_{x2} \\ B_{y2} \\ B_{z2} \\ \vdots \\ B_{xN} \\ B_{yN} \\ B_{zN} \end{bmatrix} \tag{6.3.2}$$

using the standard linear algebra format $\boldsymbol{Ax} = \boldsymbol{b}$. Here $\boldsymbol{A}$ is a matrix with dimensions of $3N$ rows (each of the three Cartesian field components for each of $n = 1$ to $N$ target field locations) by $M$ columns (for each of the $m = 1$ to $M$ coils). The vector $\boldsymbol{x}$ has dimensions $M$ rows by 1 column and contains the current $I_m$ applied to each coil. Finally, the target field vector $\boldsymbol{b}$ has dimensions $3N$ rows and 1 column and contains the desired field components due to all coils at each of the target field points.

Similarly, a matrix equation for designing magnetic field gradient coils was also derived using each of the 9 terms in the gradient tensor

$$\begin{bmatrix} B_{xx} & B_{xy} & B_{xz} \\ B_{yx} & B_{yy} & B_{yz} \\ B_{zx} & B_{zy} & B_{zz} \end{bmatrix} = \begin{bmatrix} dB_x/dx & dB_x/dy & dB_x/dz \\ dB_y/dx & dB_y/dy & dB_y/dz \\ dB_z/dx & dB_z/dy & dB_z/dz \end{bmatrix} \tag{6.3.3}$$

as

$$\begin{bmatrix} b_{xx11} & b_{xx12} & b_{xx13} & \cdots & b_{xx1M} \\ b_{xy11} & b_{xy12} & b_{xy13} & \cdots & b_{xy1M} \\ b_{xz11} & b_{xz12} & b_{xz13} & \cdots & b_{xz1M} \\ b_{yx11} & b_{yx12} & b_{yx13} & \cdots & b_{yx1M} \\ b_{yy11} & b_{yy12} & b_{yy13} & \cdots & b_{yy1M} \\ b_{yz11} & b_{yz12} & b_{yz13} & \cdots & b_{yz1M} \\ b_{zx11} & b_{zx12} & b_{zx13} & \cdots & b_{zx1M} \\ b_{zy11} & b_{zy12} & b_{zy13} & \cdots & b_{zy1M} \\ b_{zz11} & b_{zz12} & b_{zz13} & \cdots & b_{zz1M} \\ \vdots & \vdots & \vdots & \ddots & \vdots \\ b_{xxN1} & b_{xxN2} & b_{xxN3} & \cdots & b_{xxNM} \\ b_{xyN1} & b_{xyN2} & b_{xyN3} & \cdots & b_{xyNM} \\ b_{xzN1} & b_{xzN2} & b_{xzN3} & \cdots & b_{xzNM} \\ b_{yxN1} & b_{yxN2} & b_{yxN3} & \cdots & b_{yxNM} \\ b_{yyN1} & b_{yyN2} & b_{yyN3} & \cdots & b_{yyNM} \\ b_{yzN1} & b_{yzN2} & b_{yzN3} & \cdots & b_{yzNM} \\ b_{zxN1} & b_{zxN2} & b_{zxN3} & \cdots & b_{zxNM} \\ b_{zyN1} & b_{zyN2} & b_{zyN3} & \cdots & b_{zyNM} \\ b_{zzN1} & b_{zzN2} & b_{zzN3} & \cdots & b_{zzNM} \end{bmatrix} \begin{bmatrix} I_1 \\ I_2 \\ I_3 \\ \vdots \\ I_M \end{bmatrix} = \begin{bmatrix} B_{xx1} \\ B_{xy1} \\ B_{xz1} \\ B_{yx1} \\ B_{yy1} \\ B_{yz1} \\ B_{zx1} \\ B_{zy1} \\ B_{zz1} \\ \vdots \\ B_{xxN} \\ B_{xyN} \\ B_{xzN} \\ B_{yxN} \\ B_{yyN} \\ B_{yzN} \\ B_{zxN} \\ B_{zyN} \\ B_{zzN} \end{bmatrix} \tag{6.3.4}$$

again, using the standard linear algebra format $\boldsymbol{Ax} = \boldsymbol{b}$. Here $\boldsymbol{A}$ is a matrix with dimensions of $9N$ rows (each of the nine field gradient components for each of $n = 1$ to $N$ target field locations) by $M$ columns (for each of the $m = 1$ to $M$ coils). The vector $\boldsymbol{x}$ has dimensions $M$ rows by 1 column and contains the current $I_m$ applied to each coil. Finally, the target field gradient vector $\boldsymbol{b}$ has dimensions $9N$ rows and 1 column and contains the desired field gradient components due to all coils at each of the target field points.

In each case, it is required that the vector $\boldsymbol{x}$ be found through inversion of the

matrix $\boldsymbol{A}$, forming a solution $\boldsymbol{x} = \boldsymbol{A}^{-1}\boldsymbol{b}$ of coil currents which produce a desired field or field gradient.

### 6.3.2 Matrix regularisation and inversion

In this context, matrix $\boldsymbol{A}$ is unlikely to be square or 'fat' (more columns than rows). As a result the matrix may not have full rank (number of linearly independent columns) and finding a stable and physically manageable solution requires an additional constraint. For example, a simple least-squares solution of the Euclidean norm of $\|\boldsymbol{A}\boldsymbol{x} - \boldsymbol{b}\|_2^2$ will likely find infinite solutions, characteristic of an overdetermined, ill-posed, inverse problem (comparison can be made to the MEG inverse solution, and the beamformer method described in Chapter 1 and applied in Chapter 4).

If a condition which minimises $\|\boldsymbol{A}\boldsymbol{x} - \boldsymbol{b}\|_2^2$ is added, whilst simultaneously minimising $\|\boldsymbol{x}\|_2^2$ the resulting values for $\boldsymbol{x}$ also have a minimised norm and are likely to be more physically realisable. Mathematically the least squares minimum-norm solution, $\boldsymbol{x}_{ls}$ is given by

$$\boldsymbol{x}_{ls} = \boldsymbol{A}^T(\boldsymbol{A}\boldsymbol{A}^T)^{-1}\boldsymbol{b}. \tag{6.3.5}$$

However, no constraint on the system is possible with this simple form. Here, it is desireable to have tuneable control over the the properties of $\boldsymbol{x}$. For example, in order to not exceed a given current limit per coil or total power dissipation over the full set.

Often, the matrix $\boldsymbol{A}$ will contain small singular values, inversion in these cases can result in the increase of noise in the system. Tikhonov regularisation is a commonly applied method for finding stable solutions to ill-posed inverse problems through the introduction of a new matrix, $\boldsymbol{\Gamma}$. This matrix acts as a tuneable

regularisation term. Solutions which operate within given constraints can then be obtained by varying the parameters. The term to be minimised is

$$\|\boldsymbol{A}\boldsymbol{x} - \boldsymbol{b}\|_2^2 + \|\boldsymbol{\Gamma}\boldsymbol{x}\|_2^2 \tag{6.3.6}$$

and the matrix $\boldsymbol{\Gamma}$ is commonly a multiple of the identity matrix such that $\boldsymbol{\Gamma} = \alpha\boldsymbol{I}$. With this definition of $\boldsymbol{\Gamma}$, the solution $\boldsymbol{x}_{tik}$ can be obtained via singular value decomposition of the matrix $\boldsymbol{A}$. Following singular value decompositon $\boldsymbol{A}$ can be expressed as

$$\boldsymbol{A} = \boldsymbol{U}\boldsymbol{\Sigma}\boldsymbol{V}^T. \tag{6.3.7}$$

If $\boldsymbol{A}$ is a $m \times n$ matrix then $\boldsymbol{U}$ is a $m \times m$ matrix whose columns contain the eigenvectors of $\boldsymbol{A}\boldsymbol{A}^T$, and $\boldsymbol{V}$ is a $n \times n$ matrix whose columns contain the eigenvectors of $\boldsymbol{A}^T\boldsymbol{A}$ where $\boldsymbol{A}^T$ denotes the transpose of $\boldsymbol{A}$. The non-zero singular values of the matrix are arranged in descending order on the diagonal of the $m \times n$ matrix $\boldsymbol{\Sigma}$ whose off-diagonal values are all zero.

The regularisation is performed by introducing a matrix $\boldsymbol{D}$ containing diagonal values

$$D_{ii} = \frac{\sigma_i}{\sigma_i^2 + \alpha^2} \tag{6.3.8}$$

where $\sigma_i$ are the singular values of $\boldsymbol{\Sigma}$ and $\alpha$ is the tuneable regularisation term. The solution $\boldsymbol{x}_{tik}$ is then found as

$$\boldsymbol{x}_{tik} = \boldsymbol{V}\boldsymbol{D}\boldsymbol{U}^T\boldsymbol{b}. \tag{6.3.9}$$

### 6.3.3 Choosing optimal regularisation parameter

Although manual tuning of $\alpha$ can be used to find a solution, it is important to choose a balanced value which is large enough to meet the constraints of the system, but as small as possible to allow $\|\boldsymbol{A}\boldsymbol{x} - \boldsymbol{b}\|_2^2$ to dominate the solution. In order to choose the optimal regularisation parameter $\alpha$, a bisection algorithm is employed [Garda and Galias, 2014].

The algorithm requires two values of $\alpha$. The first, $\alpha_{min}$ is set to zero and a guess at the second $\alpha_{max}$ is made such that the solution $\boldsymbol{x}_{tik}$ meets the constraints of the system (a common choice being $1 - 10\%$ of the leading singular value of $\boldsymbol{A}$). Upon each iteration a new value $\alpha = 0.5\ (\alpha_{min} + \alpha_{max})$ is tested. If the resulting solution $\boldsymbol{x}_{tik}$ meets the condition then $\alpha_{max}$ is set $= \alpha$. If the constraints are not met then $\alpha_{min}$ is set $= \alpha$. The process is repeated until $|\alpha_{min} - \alpha_{max}|$ reaches a suitably small value. An example of the operation of this alogorithm is shown in Figure 6.3.

As the energy dissipated by the coil is a quantity directly related to the size of the current applied to each coil ($P = I^2R$) the Tikhonov method addresses power dissipation in a constrained manner using the bisection algorithm to obtain the highest quality of solution.

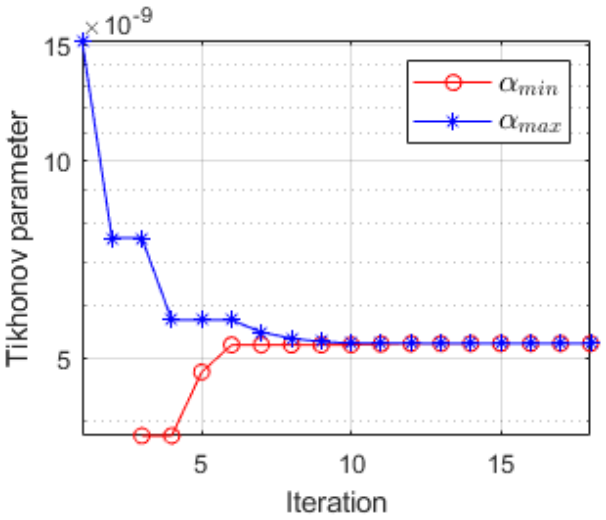



Figure 6.3: *Bisectional algorithm for choosing an optimal regularisation parameter. Values of $\alpha_{min}$ and $\alpha_{max}$ are adjusted until their difference meets a required tolerance.*

## 6.4 Methods

As described previously, the remnant field in the MSR can be approximated as a linear combination of three uniform field components and five field gradients. For comparison to the bi-planar coil systems described before, the matrix coil system should be able to produce these components over a large volume.

The design of a prototype matrix coil system is outlined, and simulations to assess its performance are described. These simulations include the effect of moving the homogenous region to a range of different locations between the coils, and also of adding interactions with the high-permeability walls of the MSR.

### 6.4.1 Prototype matrix coil design

A prototype matrix coil system was designed to be mounted in a bi-planar arrangement with dimensions the same as those used for the six-coil system described in Chapter 4 (two square planes of side length 1.6 m separated by 1.5 m) allowing for performance comparison. For ease of eventual construction, square unit coils were chosen.

To reduce the complexity of the electronics, 48 coils were to be mounted on the two planes, forming a $4 \times 4$ grid of coils with an overlapping $3 \times 3$ grid of coils displaced by half the square coil side length in the $x$ and $y$ directions. Each coil occupied a square region of side length 0.4 m. The central position of each $3 \times 3$ grid was left unoccupied. The coil design is shown in Figure 6.4. Each coil was to be formed of 20 turns of 0.56 mm diameter copper wire.

All simulations were evaluated in MATLAB (The MathWorks Inc.) based on this design. The magnetic field per unit current of each coil is calculated by applying the elemental Biot-Savart law to the coil wire-paths. The number of turns on

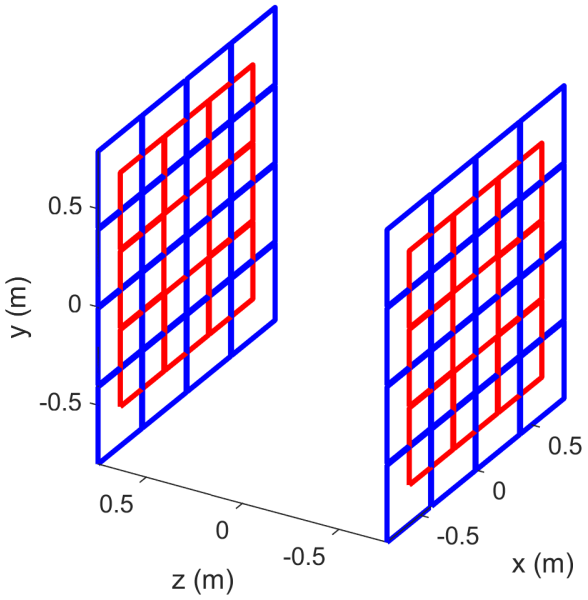



Figure 6.4: *The design and layout for the 48 coil prototype system. Two 1.6 × 1.6 m$^2$ area planes, each containing 24 square coils of square side length 40 cm are placed 1.5 m apart. Red and blue colours are used to distinguish between the 4 × 4, and the overlapping 3 × 3, grids of coils.*

each coil is taken account of by multiplying the field strength for a single loop by the desired number of turns. Tikhonov regularisation with the bisectional algorithm was incorporated with a current limit of ±1 A per coil.

### 6.4.2 Comparison to bi-planar coil designs

Comparison to the designs obtained in Chapters 4 and 5 is made by calculating current values to produce each of the eight terms: $B_x$, $B_y$, $B_z$, $G_x = B_{xz} = B_{zx}$, $G_y = B_{yz} = B_{zy}$, $G_z = B_{zz} = -2B_{xx} = -2B_{yy}$, $G_{xx} = B_{xx} = -B_{yy} - B_{zz}$ (choosing a case where $B_{yy} = 0$) and $G_{xy} = B_{xy} = B_{yx}$ over a $0.4 \times 0.4 \times 0.4$ m$^3$ region at the centre of the two planes. No interactions with high-permeability materials in the walls of the MSR were considered.

The target field points were placed at the nodes of a regular 0.05 m resolution 3D grid which spanned the full region. Figure 6.5 shows the organisation of these

target field points as a series of nine $z-y$ planes each separated by 0.05 m in the $x$ direction. A colour is assigned to each plane for identification. Each of these $z-y$ planes is a 9 $\times$ 9 grid containing 81 points where point 1 is at $z = -0.2$ m, $y = -0.2$ m, point 2 is at $z = -0.15$ m, $y = -0.2$ m and so on leading to a total of 729 target field points. The current required in each coil to produce a homogeneous field, or field gradient value of 2 nT or 2 nT/m strength (typical for the magnetic field inside the new MSR following degaussing), respectively, was calculated. The absolute maximum current applied to a single coil, $|I_{max}|$ and the total magnitude of current applied to the whole system, $\sum_{m=1}^{M} |I_m|$, were extracted for each calculation.

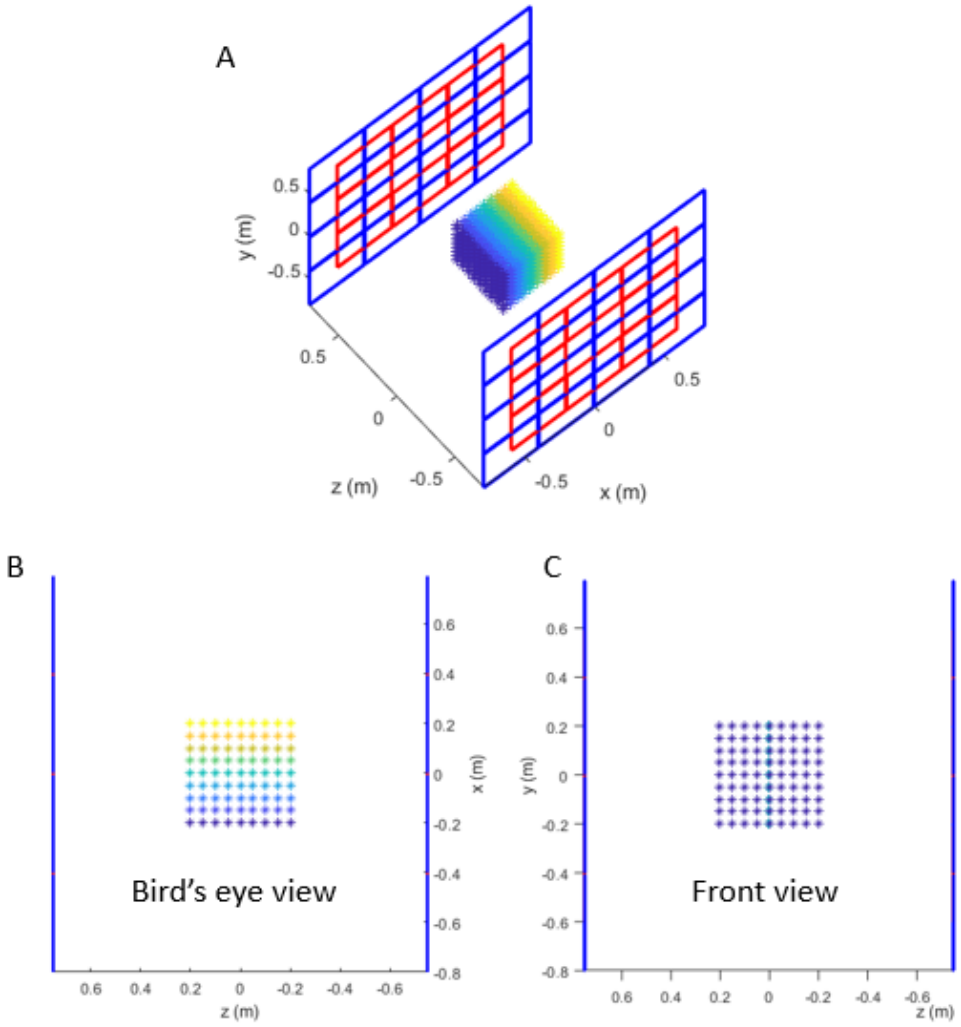



Figure 6.5: *Organisation of target field points for matrix coil calculations when comparing designs to the bi-planar system. A) A 5 cm resolution regular grid of points spanning a* $0.4 \times 0.4 \times 0.4$ *cm*$^3$ *region at the centre of the coils is shown. There are nine* $z-y$ *planes each with its own colour. B) A bird's eye view* ($z-x$ *plane) of the setup. C) Front view* ($z-y$ *plane) of the setup.*

### 6.4.3 Moving the homogeneous region

The ability of the prototype system to produce homogeneous magnetic fields or field gradients at locations away from the centre of the region spanned by the coil planes was also investigated. The space between the two planes can be split into 8 cubic octants. A single octant was chosen (from the symmetry of the system, the performance will be the same in all octants) and this was further split into 27 regions each with dimensions $0.2 \times 0.2 \times 0.2$ m$^3$. A 0.025 m resolution grid of 729 target points was used over each region, structured similarly to the arrangement shown in Figure 6.5. The centre of the first region was placed at the origin, ($x$, $y$, $z$) = (0 m, 0 m, 0 m) and the centre of the 27$^{\text{th}}$ region was sited at ($x$, $y$, $z$) = (0.4 m, 0.4 m, 0.4 m). These regions and the numbering system used to describe them are shown in Figure 6.6. The symmetry of the setup gives an effective total volume of 1 $\times$ 1 $\times$ 1 m$^3$ over which each of the magnetic field components can be created between the two planes.

For each region, the current values required to produce a 2 nT $B_x$ or 2 nT/m $G_x$ magnetic field were calculated. No interactions with high-permeability materials were considered. The homogeneity of the produced field in each region is investigated as a measure of performance. The absolute maximum current applied to a single coil, $|I_{max}|$ and the total magnitude of current applied to the whole system, $\sum_{m=1}^{M} |I_m|$, were extracted for each region.

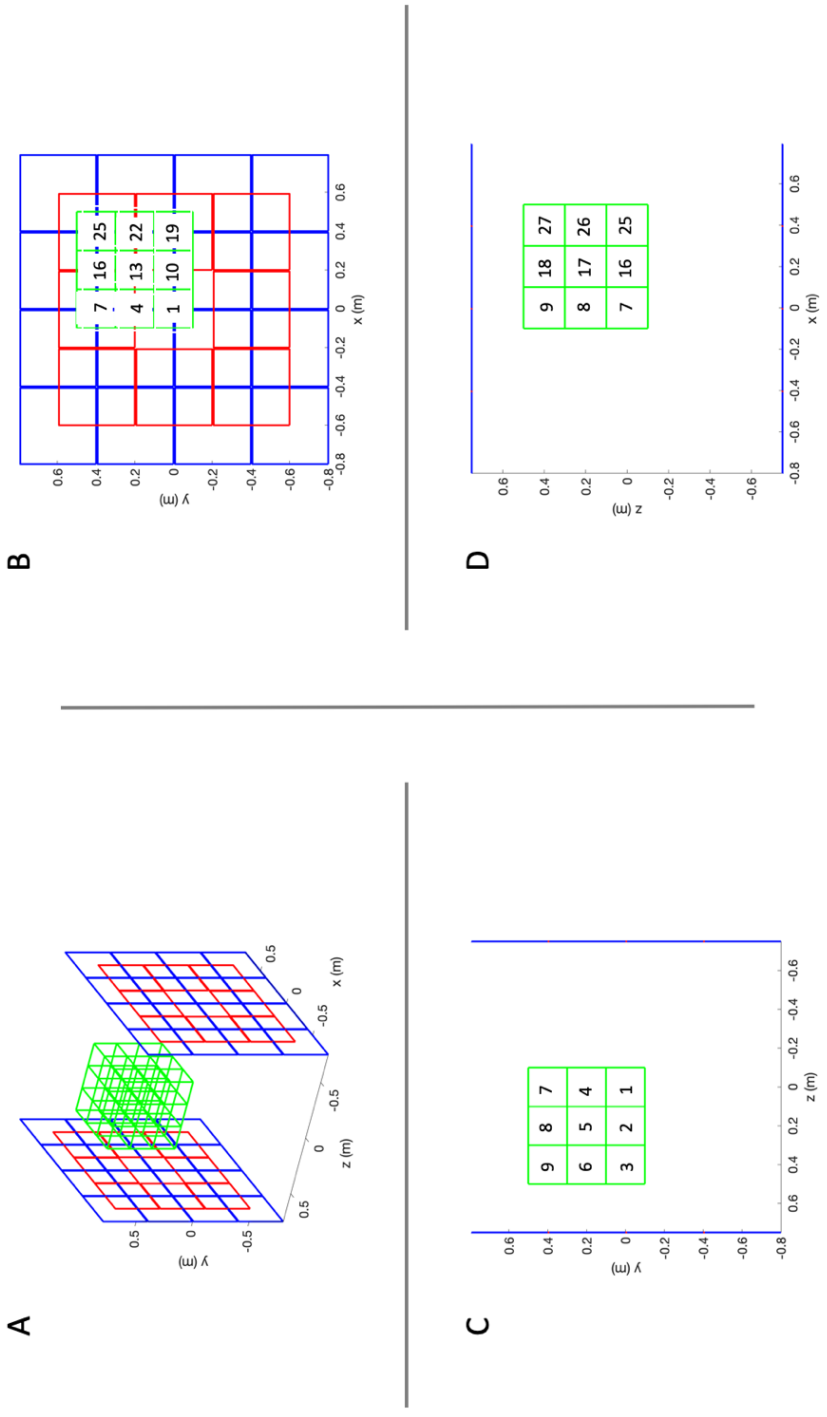



Figure 6.6: *Position of the 27 different regions over which coil currents to generate homogeneous field and field gradient components were calculated. Each region has a volume of* $0.2 \times 0.2 \times 0.2$ $m^3$. *A) Green boxes show region locations within one octant of a* $1 \times 1 \times 1$ $m^3$ *volume centred between the two planes. B) The region numbering system in the* $x - y$ *plane. C) Numbering in the* $z - y$ *plane. D) Numbering in the* $x - z$ *plane.*

### 6.4.4 Mu-metal interactions

The simulations outlined in the previous sections (calculating applied currents which produce each of the eight field components, and moving the homogeneous region over a series of 27 regions between the planes) were repeated with interactions with the MSR taken into account during the design stage. The 48-channel prototype system was assumed to be positioned at the centre of a MSR which has dimensions of $(x \times y \times z)$ 3 $\times$ 2.4 $\times$ 3 m$^3$. Mirror currents up to third-order were included in the designs, as described in Chapter 5, using the elemental Biot-Savart law.

For each coil design and each of the 27 regions the coil currents required to produce a 2 nT field, or 2 nT/m field gradient, were calculated. The homogeneity of the produced fields was again investigated as a measure of performance. The absolute maximum current applied to a single coil, $|I_{max}|$ and the total magnitude of current applied to the whole system, $\sum_{m=1}^{M} |I_m|$, were extracted for each simulation.

### 6.4.5 Building coils into the MSR

The prototype bi-planar arrangement described so far, with a regular grid of coils confined to $x-y$ planes, has natural $z$-axis symmetry; producing fields or field gradients with $x$ or $y$ axis variation requires the overlapping grid of coils to produce field cancellation effects. Adding coils on the walls of the MSR forming $x-z$ and $y-z$ planes should allow for these changes to the field to be more easily compensated. Variation of the size of the unit coils within the system can also readily be accounted for in the mathematical framework described previously.

To address this, a simulation study of a coil system which could be easily constructed using cables mounted directly onto the mu-metal on the six faces of

the MSR is also investigated. A high-resolution grid (similar to the 48-channel design) could be considered (e.g. placing 0.4 m side length unit coils over all the faces of the MSR), but the practicality of operating the large number of independent current sources this requires would be a significant challenge. Instead, different shaped coils were strategically chosen based on the desired field characteristics.

Two square coils with square side length close to the full length of the MSR walls were placed on each wall. The resulting Helmholtz-style design should allow for generation of uniform field components and the longitudinal field gradients. Four, thin rectangular coils were then added towards the edges of each wall along with four square coils forming a grid in the centre of each face to address the transverse field gradients. The ten coils required on each wall of the MSR leads to a 60-channel system. Instead of driving each coil set individually, the current applied to each coil is optimised for homogeneity and interactions with the high-permeability materials using the matrix-coil approach.

The simulated MSR was a cubic structure with internal dimensions of 2.5 $\times$ 2.5 $\times$ 2.5 $m^3$. The large square coils were centred on each wall with square side lengths of 2.125 m and 2.5 m as shown in Figure 6.7A (coil numbers 1 to 12). The rectangular coil dimensions were 0.125 $\times$ 2.4375 $m^2$ and were placed 0.1 m away from the edge of the walls as shown in Figure 6.7B (coil numbers 13 to 36). The grid of four square coils was centred on each wall with a square side length of 0.75 m, the centre of each square was displaced by 0.125 m in the planar dimensions to form the grid as shown in Figure 6.7C (coil numbers 37 to 60). The complete system is shown in 6.7D.

Currents required to produce each of the eight field components, whilst considering interactions with the mu-metal were calculated. The 1331 target field points were the nodes of a 0.1 m resolution 1 $\times$ 1 $\times$ 1 $m^3$ grid at the centre of the room.

The setup of this grid is similar to that shown in Figure 6.5. Field strengths of 50 nT and field gradients of 50 nT/m were chosen as a system of this design could be used inside a lightly-shielded enclosure. Each coil was formed of 20 turns.

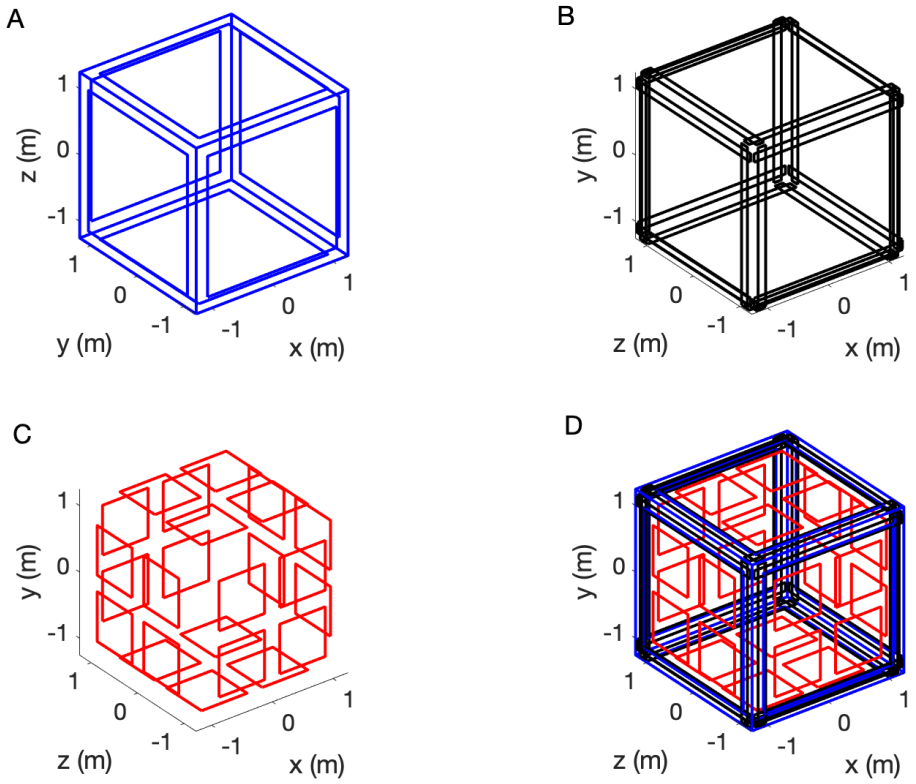



Figure 6.7: *Matrix coil system built into the walls of a MSR. A) Six large square coils to provide uniform field and and longitudinal field gradient compensation. B-C) Thin, rectangular coils and a grid of square coils to provide transverse field gradients and other correction terms. D) The complete 60-coil system.*

## 6.5 Results

### 6.5.1 Comparison to bi-planar coil designs

Figures 6.8-6.15 show simulated results for production of $B_x$, $B_y$, $B_z$, $G_x$, $G_y$, $G_z$, $G_{xy}$ and $G_{xx}$ field components over a $0.4 \times 0.4 \times 0.4$ m$^3$ volume which is centred between the two planes of the prototype system. Current values which produce a homogeneous magnetic field of strength 2 nT or a homogeneous magnetic field gradient strength of 2 nT/m were found. As with previous designs, current values which produce field components to within $\pm 5\%$ of the target field are desired.

The current applied to each of the 48 coils is shown for each field component. The approximated current densities should be compared to Figures 4.6-4.20, highlighting the similarities to the current distributions found when designing bi-planar coils via harmonic minimisation. The percentage deviation from the modelled field at each of the 729 target points (with position relative to the coil planes as outlined in Figure 6.5) is also shown.

The maximum magnitude of current applied to one of the 48 unit coils, the total magnitude of the applied current across all coils and the maximum percentage deviation from the modelled field are summarised in Table 6.2 for all field components.

Analysis for the $G_{xx}$ component shows poor performance, with a maximum deviation from homogeneity of 13.5%. As described in Chapter 4 the requirement that the four-fold symmetry of the coil design be broken is restricted by the relatively coarse resolution that can be achieved with the 48-channel matrix design. Considering the field variation over a smaller, $0.3 \times 0.3 \times 0.3$ m$^3$ volume produces field variation with a deviation of $< 5\%$.

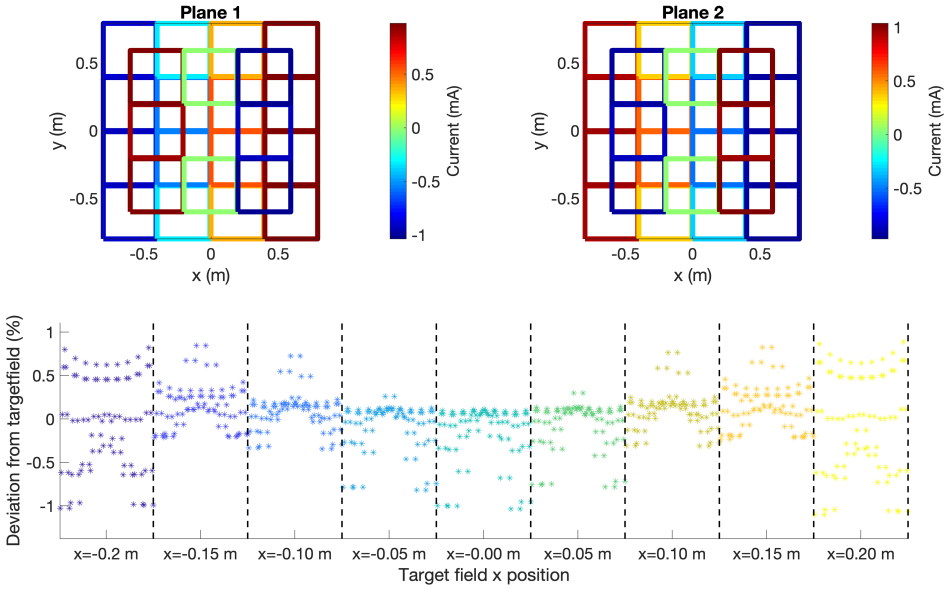



Figure 6.8: *The currents applied to each coil to produce a homogeneous 2 nT, $B_x$-field. Red represents positive current circulation in the loop and blue negative current circulation with magnitude indicated by the colorbar. The approximate current distribution which is formed reflects that of a bi-planar $B_x$ coil, the stream function being anti-symmetric in $x$ and $z$, but symmetric in $y$. The deviation from the desired field at each of the 729 target points is shown, and sectioned for each of the nine $z-y$ planes with colour and label corresponding to the $x$ position of each plane.*

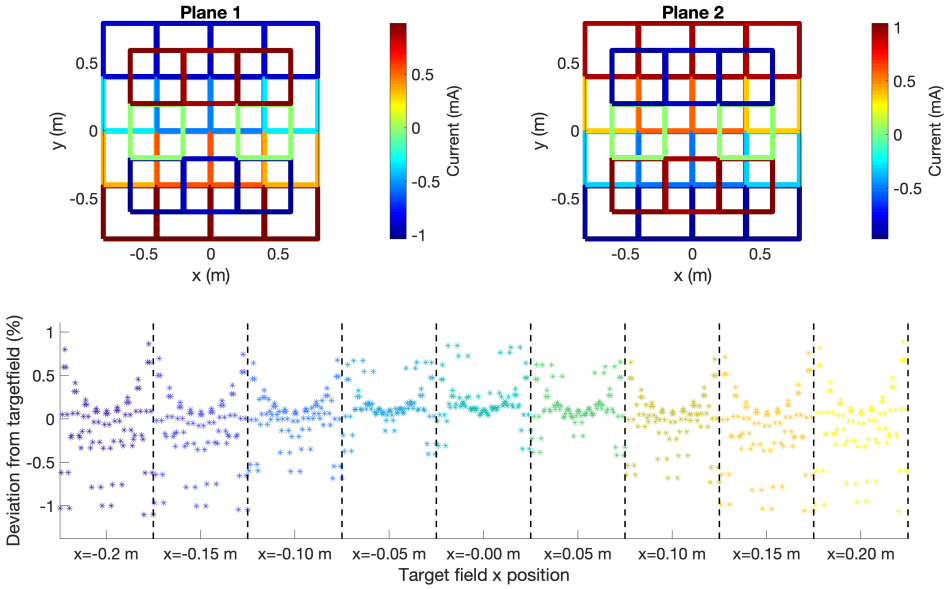



Figure 6.9: *The currents applied to each coil to produce a homogeneous 2 nT, $B_y$-field. Red represents positive current circulation in the loop and blue negative current circulation with magnitude indicated by the colorbar. The approximate current distribution which is formed reflects that of a bi-planar $B_y$ coil, the stream function being anti-symmetric in $y$ and $z$, but symmetric in $x$. The deviation from the desired field at each of the 729 target points is shown, and sectioned for each of the nine $z-y$ planes with colour and label corresponding to the $x$ position of each plane.*

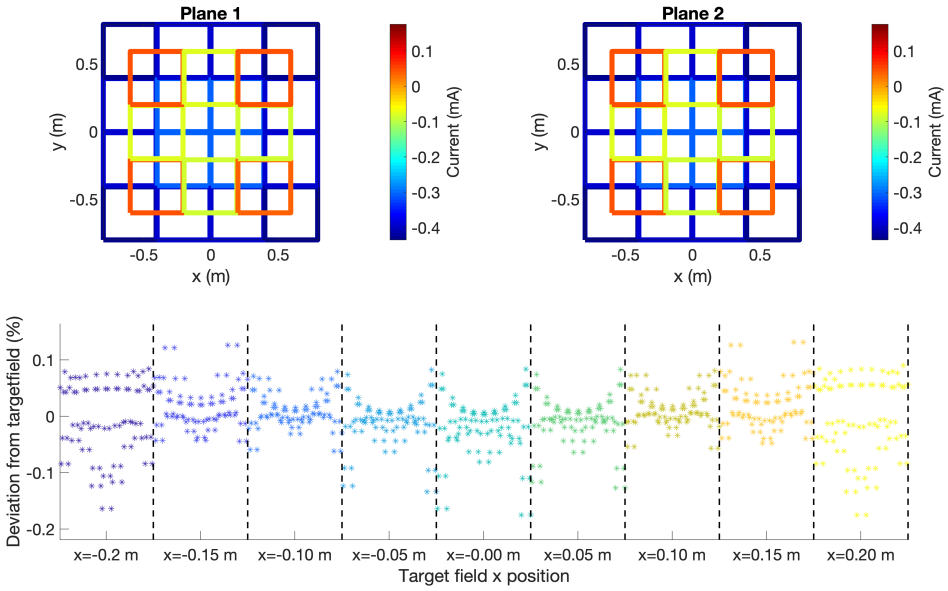



Figure 6.10: *The currents applied to each coil to produce a homogeneous 2 nT, $B_z$-field. Red represents positive current circulation in the loop and blue negative current circulation with magnitude indicated by the colorbar. The approximate current distribution which is formed reflects that of a bi-planar $B_z$ coil, the stream function being symmetric in $x$, $y$ and $z$. The deviation from the desired field at each of the 729 target points is shown, and sectioned for each of the nine $z-y$ planes with colour and label corresponding to the $x$ position of each plane.*

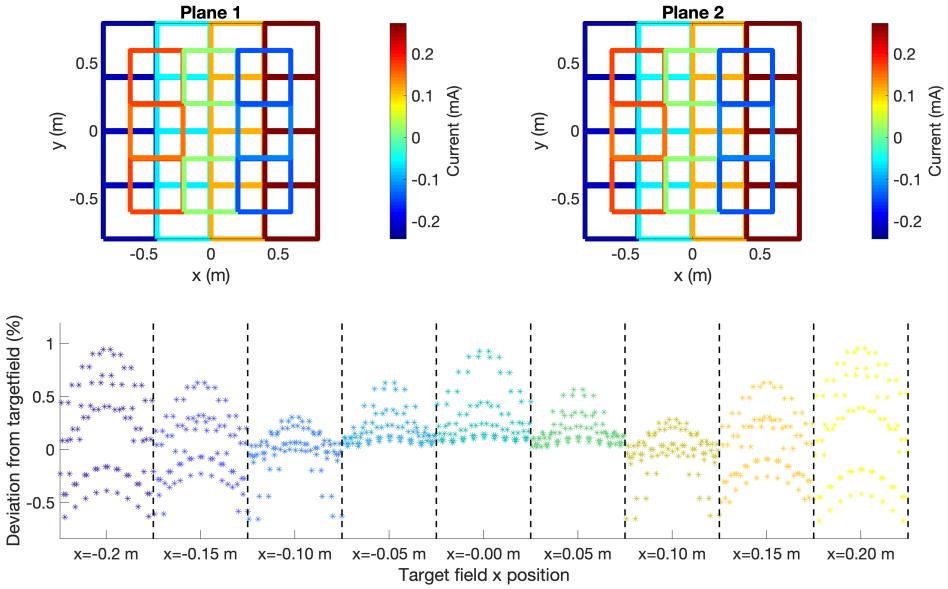



Figure 6.11: *The currents applied to each coil to produce a homogeneous 2 nT/m, $G_x$-field gradient. Red represents positive current circulation in the loop and blue negative current circulation with magnitude indicated by the colorbar. The approximate current distribution which is formed reflects that of a bi-planar $G_x$ coil, the stream function being anti-symmetric in $x$, but symmetric in $y$ and $z$. The deviation from the desired field gradient at each of the 729 target points is shown, and sectioned for each of the nine $z-y$ planes with colour and label corresponding to the $x$ position of each plane.*

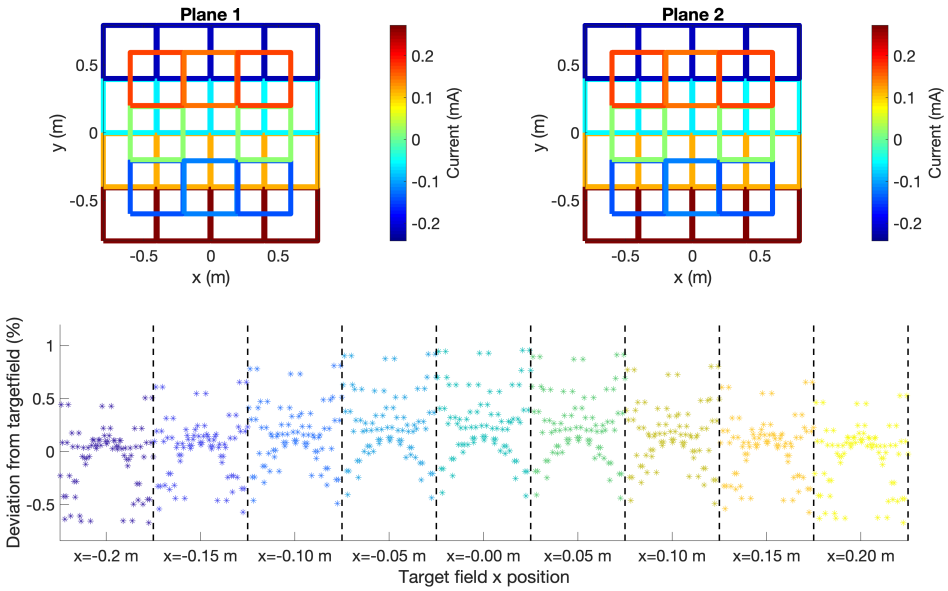



Figure 6.12: *The currents applied to each coil to produce a homogeneous 2 $nT/m$, $G_y$-field gradient. Red represents positive current circulation in the loop and blue negative current circulation with magnitude indicated by the colorbar. The approximate current distribution which is formed reflects that of a bi-planar $G_y$ coil, the stream function being anti-symmetric in $y$, but symmetric in $x$ and $z$. The deviation from the desired field gradient at each of the 729 target points is shown, and sectioned for each of the nine $z-y$ planes with colour and label corresponding to the $x$ position of each plane.*

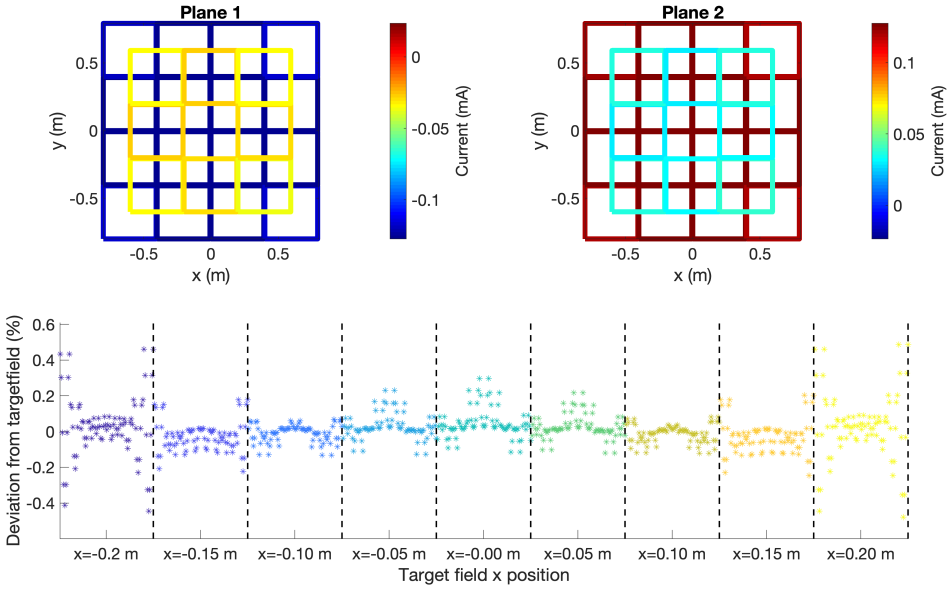



Figure 6.13: *The currents applied to each coil to produce a homogeneous 2 nT/m, $G_z$-field gradient. Red represents positive current circulation in the loop and blue negative current circulation with magnitude indicated by the colorbar. The approximate current distribution which is formed reflects that of a bi-planar $G_z$ coil, the stream function being anti-symmetric in $z$, but symmetric in $x$ and $y$. The deviation from the desired field gradient at each of the 729 target points is shown, and sectioned for each of the nine $z-y$ planes with colour and label corresponding to the $x$ position of each plane.*

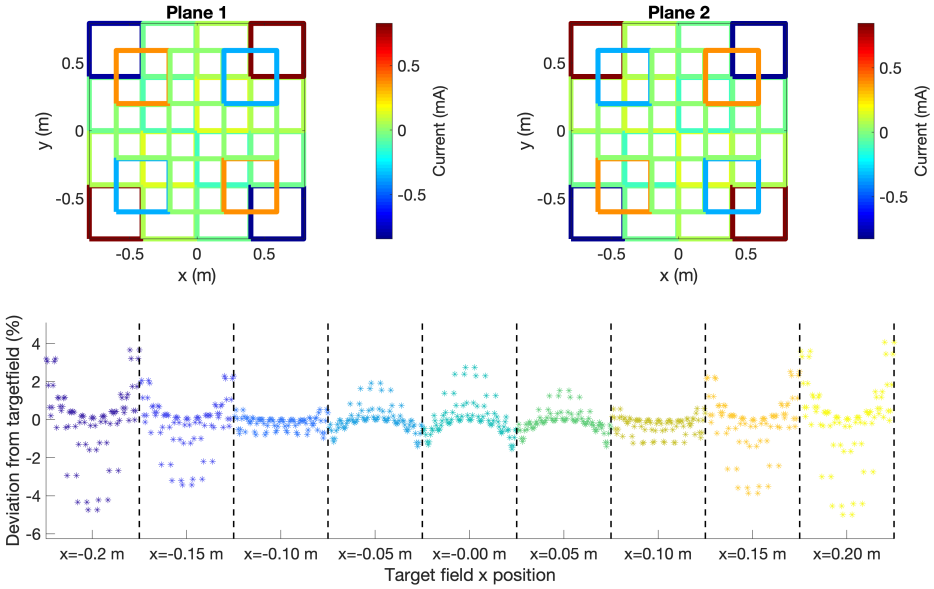



Figure 6.14: *The currents applied to each coil to produce a homogeneous 2 nT/m, $G_{xy}$-field gradient. Red represents positive current circulation in the loop and blue negative current circulation with magnitude indicated by the colorbar. The approximate current distribution which is formed reflects that of a bi-planar $G_{xy}$ coil, the stream function being anti-symmetric in $x$, $y$ and $z$. The deviation from the desired field gradient at each of the 729 target points is shown, and sectioned for each of the nine $z-y$ planes with colour and label corresponding to the $x$ position of each plane.*

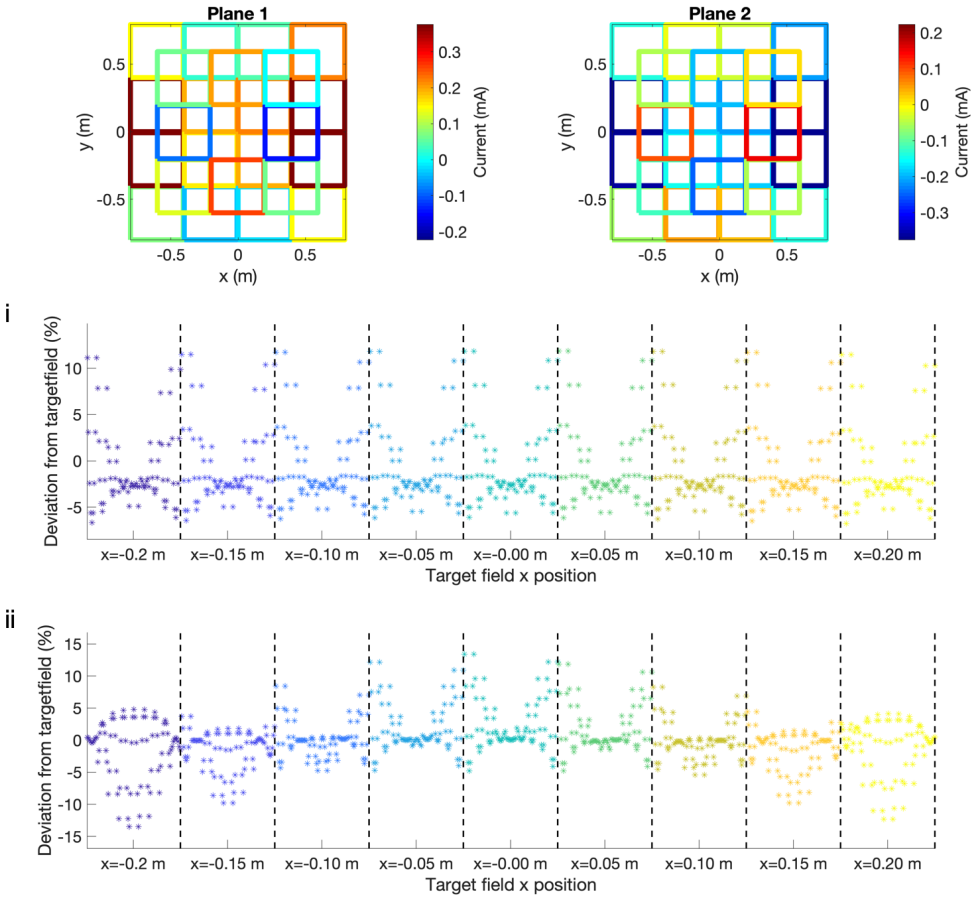



Figure 6.15: *The currents applied to each coil to produce a homogeneous 2 nT/m $G_{xx}$ field gradient. Red represents positive current circulation in the loop and blue negative current circulation with magnitude indicated by the colorbar. The approximate current distribution which is formed reflects that of a bi-planar $G_{xx}$ coil, the stream function being anti-symmetric in $z$, but symmetric in $x$ and $y$. The deviation from the two desired field gradient components i) $dB_x/dx$ and ii) $dB_z/dz$ at each of the 729 target points is shown, and sectioned for each of the nine $z-y$ planes with colour and label corresponding to the $x$ position of each plane.*

| Field Component | Max deviation (%) | Absolute max current (mA) | Total current (mA) |
|---|---|---|---|
| $B_x$ | 1.1 | 1.04 | 33.7 |
| $B_y$ | 1.1 | 1.04 | 33.7 |
| $B_z$ | 0.2 | 0.43 | 10.9 |
| $G_x$ | 1.0 | 0.27 | 7.2 |
| $G_y$ | 1.0 | 0.27 | 7.2 |
| $G_z$ | 0.5 | 0.13 | 3.7 |
| $G_{xy}$ | 5 | 0.84 | 11.4 |
| $G_{xx}$ | 11.4 (13.5) | 0.38 | 6.42 |

Table 6.1: *Simulated performance of matrix coils for each field component when producing uniform fields of 2 nT or field gradients of 2 nT/m over the central volume. The maximum deviation from the desired field or field gradient (shown for both components in the case of the $G_{xx}$ coil), the absolute maximum current applied to any one coil and the total current magnitude applied to all coils are shown.*

### 6.5.2 Moving the homogeneous region

Figures 6.16-6.23 show simulated results for producing $B_x$, $B_y$, $B_z$, $G_x$, $G_y$, $G_z$, $G_{xy}$ and $G_{xx}$ field components over a $0.2 \times 0.2 \times 0.2$ cm$^3$ volume which is moved over 27 regions within one octant between the two planes. The region number corresponds to the numbering system outlined in Figure 6.6.

Figures show the maximum percentage deviation from the desired field in each region, the absolute maximum current that was applied to a single coil and the total current magnitude applied to the 48 coils. The maximum field deviation, total current and number of times the current limit of $\pm 1$ A per coil is hit are summarised in Table 6.2 for all field components.

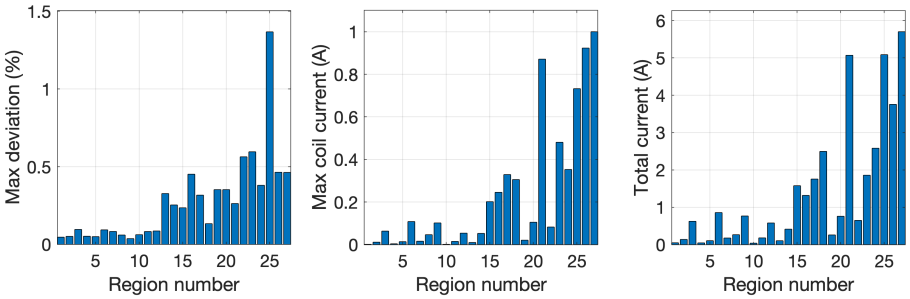



Figure 6.16: *Producing a $B_x$-magnetic field of strength 2 nT in 27 regions, each with volume 0.2 × 0.2 × 0.2 $m^3$. The maximum deviation from homogeneity, the maximum current magnitude applied to a single coil in the system and the total current magnitude over all 48 units are shown for each region.*

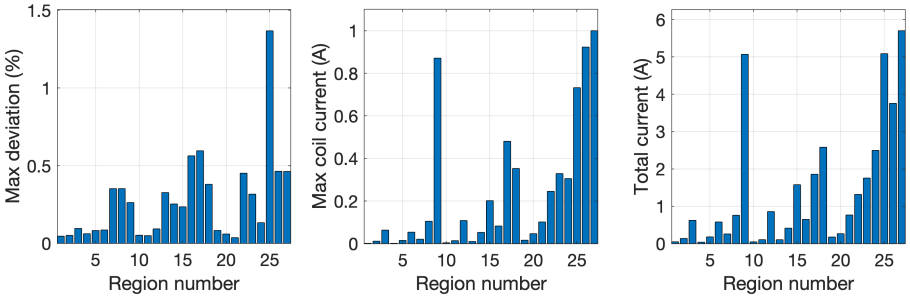



Figure 6.17: *Producing a $B_y$-magnetic field of strength 2 nT in 27 regions, each with volume 0.2 × 0.2 × 0.2 $m^3$. The maximum deviation from homogeneity, the maximum current magnitude applied to a single coil in the system and the total current magnitude over all 48 units are shown for each region.*

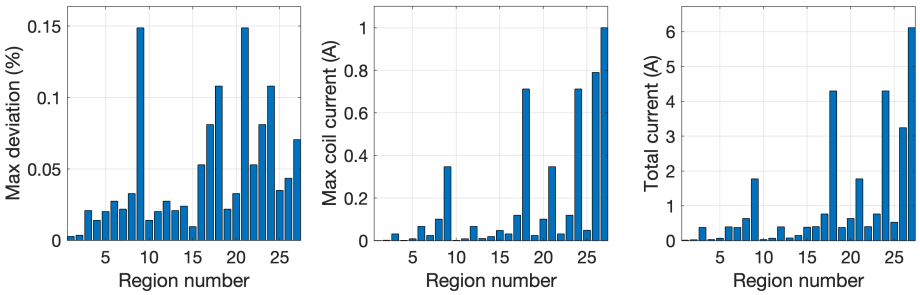



Figure 6.18: *Producing a $B_z$-magnetic field of strength 2 nT in 27 regions, each with volume 0.2 × 0.2 × 0.2 $m^3$. The maximum deviation from homogeneity, the maximum current magnitude applied to a single coil in the system and the total current magnitude over all 48 units are shown for each region.*

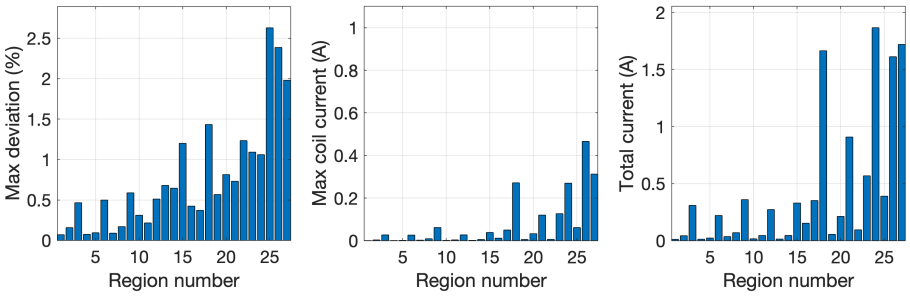



Figure 6.19: *Producing a $G_x$-magnetic field gradient of strength 2 nT/m in 27 regions, each with volume 0.2 × 0.2 × 0.2 $m^3$. The maximum deviation from homogeneity, the maximum current magnitude applied to a single coil in the system and the total current magnitude over all 48 units are shown for each region.*

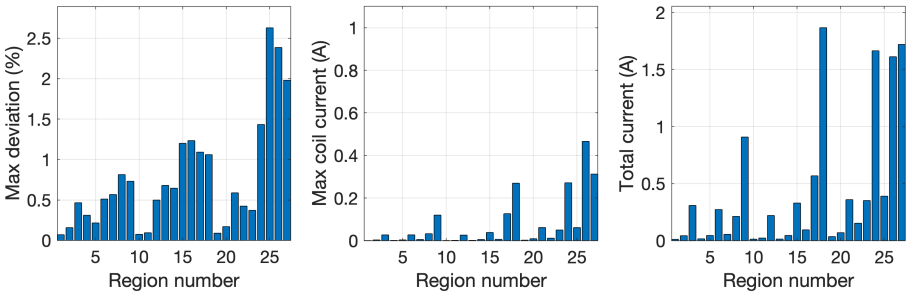



Figure 6.20: *Producing a $G_y$-magnetic field gradient of strength 2 nT/m in 27 regions, each with volume 0.2 × 0.2 × 0.2 $m^3$. The maximum deviation from homogeneity, the maximum current magnitude applied to a single coil in the system and the total current magnitude over all 48 units are shown for each region.*

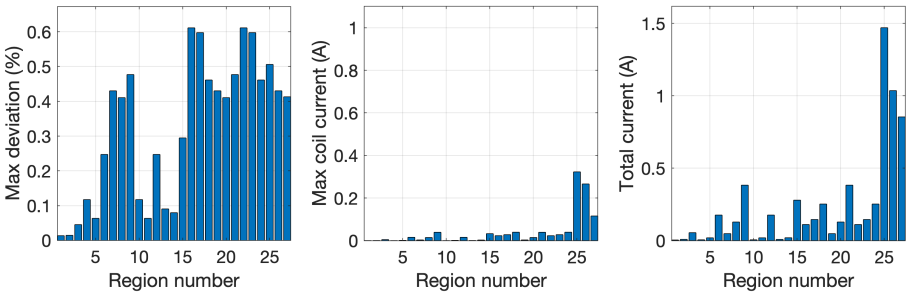



Figure 6.21: *Producing a $G_z$-magnetic field gradient of strength 2 nT/m in 27 regions, each with volume 0.2 × 0.2 × 0.2 $m^3$. The maximum deviation from homogeneity, the maximum current magnitude applied to a single coil in the system and the total current magnitude over all 48 units are shown for each region.*

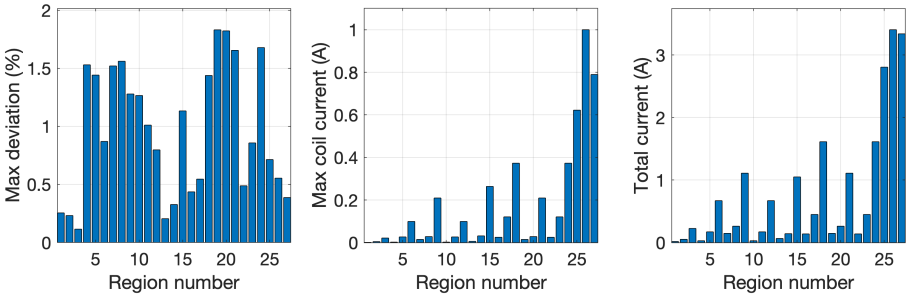



Figure 6.22: *Producing a $G_{xy}$-magnetic field gradient of strength 2 $nT/m$ in 27 regions, each with volume 0.2 × 0.2 × 0.2 $m^3$. The maximum deviation from homogeneity, the maximum current magnitude applied to a single coil in the system and the total current magnitude over all 48 units are shown for each region.*

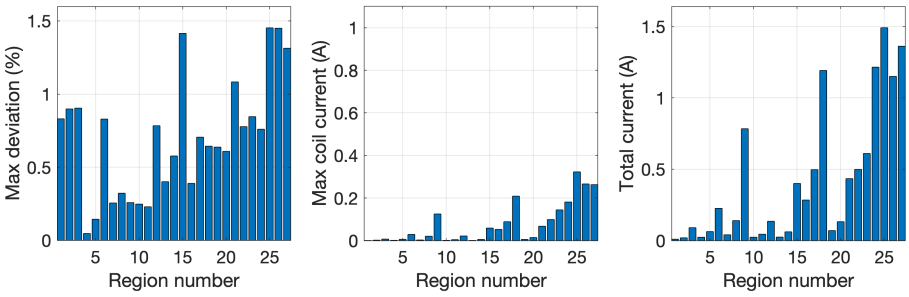



Figure 6.23: *Producing a $G_{xx}$-magnetic field gradient of strength 2 $nT/m$ in 27 regions, each with volume 0.2 × 0.2 × 0.2 $m^3$. The maximum deviation from homogeneity, the maximum current magnitude applied to a single coil in the system and the total current magnitude over all 48 units are shown for each region.*

| Field Component | Max deviation (%) | Total current (A) | Current limit hit count |
|---|---|---|---|
| $B_x$ | 1.4 | 5.7 | 1/27 |
| $B_y$ | 1.4 | 5.7 | 1/27 |
| $B_z$ | 0.15 | 6.1 | 1/27 |
| $G_x$ | 2.63 | 1.87 | 0/27 |
| $G_y$ | 2.63 | 1.87 | 0/27 |
| $G_z$ | 0.61 | 1.47 | 0/27 |
| $G_{xy}$ | 1.83 | 3.41 | 1/27 |
| $G_{xx}$ | 1.45 | 1.49 | 0/27 |

Table 6.2: *Summarised results showing the maximum deviation, maximum total applied current and the number of regions for which the current limit of $\pm 1$ A was hit.*

### 6.5.3 Mu-metal interactions

#### Coil designs

Figures 6.24-6.31 show simulated coil designs when the coil-system is positioned at the centre of a MSR with dimensions $3 \times 2.4 \times 3$ m$^3$ when interactions with the mu-metal are included in the calculations. Eight fields were designed to produce $B_x$, $B_y$, $B_z$, $G_x$, $G_y$, $G_z$, $G_{xy}$ and $G_{xx}$ field components over a $0.4 \times 0.4 \times 0.4$ m$^3$ volume which is centred between the two planes (and also centred inside the MSR). Current values were found to produce a homogeneous magnetic field of strength 2 nT, or a homogeneous magnetic field gradient strength of 2 nT/m. As with previous designs, current values which produce field components to within $\pm 5\%$ of the target field are desired.

The current applied to each of the 48 coils is shown. The percentage deviation from the modelled field at each of the 729 target points (with position relative to the coil planes as outlined in Figure 6.5) is also shown.

The maximum magnitude of current applied to any of the 48 unit coils, the total magnitude of the applied current and the maximum percentage deviation from the modelled field are summarised in Table 6.3 for all field components. Comparison of these results with Table 6.1, where interactions were not considered, shows the loss of shared parameters between the $B_x/B_y$ and $G_x/G_y$ fields when interactions are included. This is due to the square sides of the MSR being $3 \times 3$ m$^2$ in $x$ and $2.4 \times 2.4$ m$^2$ in $y$ resulting in an asymmetry between the mirrored components for the different fields.

In general the system still performs within the homogeneity tolerances when interactions are taken into account. A slight worsening of the homogeneity is observed over each field component which is most notable in the gradient terms $G_{xx}$ where an increase from 13.5% to 15.7% is seen. The maximum current and

total current remained broadly similar for the two cases.

### Moving the homogeneous region

Figures 6.32-6.39 show simulated results for producing $B_x$, $B_y$, $B_z$, $G_x$, $G_y$, $G_z$, $G_{xy}$ and $G_{xx}$ field components over a $0.2 \times 0.2 \times 0.2$ cm$^3$ volume which is moved over 27 regions within one octant between the two planes. The region number corresponds to the numbering system outlined in Figure 6.6.

Figures show the maximum percentage deviation from the desired field in each region, the absolute maximum current that was applied to a single coil and the total current magnitude applied to the 48 coils. The maximum field deviation, total current and number of times the current limit of $\pm 1$ A per coil is hit are summarised in Table 6.4 for all field components.

Comparing these results to those in Table 6.2, where interactions were not considered, shows an slight worsening in the maximum reported deviation for each component, most significantly in the case of the $G_x$ field, where an increase from 2.6% to 4.3% is shown. The current limit was also hit more frequently suggesting the regularisation has a larger impact on the produced results in the case where interactions are considered. Despite issues over high current requirements for the system, the maximum deviation remained within the $\pm 5\%$ range for each component in each region.

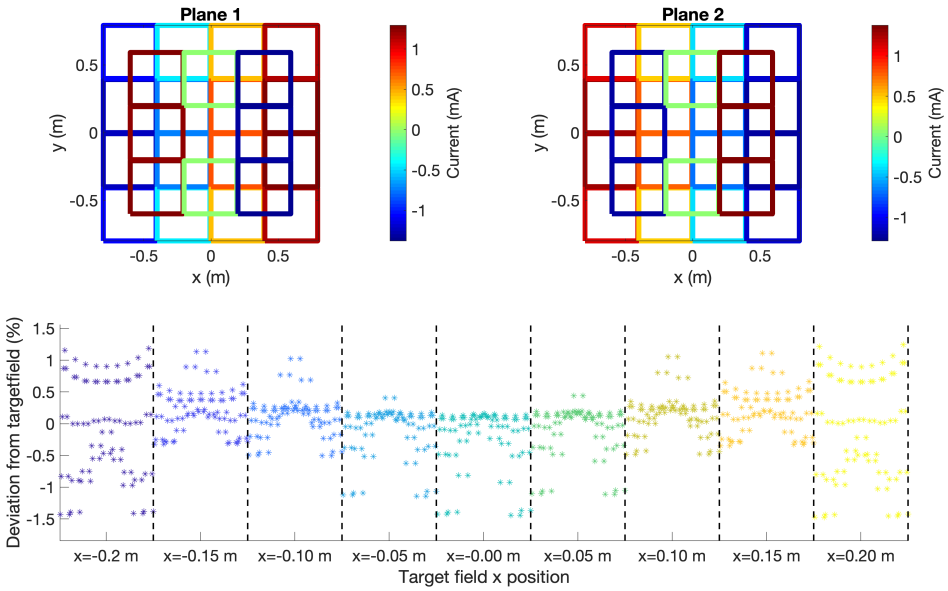



Figure 6.24: *The currents applied to each coil to produce a homogeneous 2 nT, $B_x$-field when interactions with the MSR are considered. Red represents positive current circulation in the loop and blue negative current circulation with magnitude indicated by the colorbar. The deviation from the desired field at each of the 729 target points is shown, and sectioned for each of the nine $z-y$ planes with colour and label corresponding to the $x$ position of each plane.*

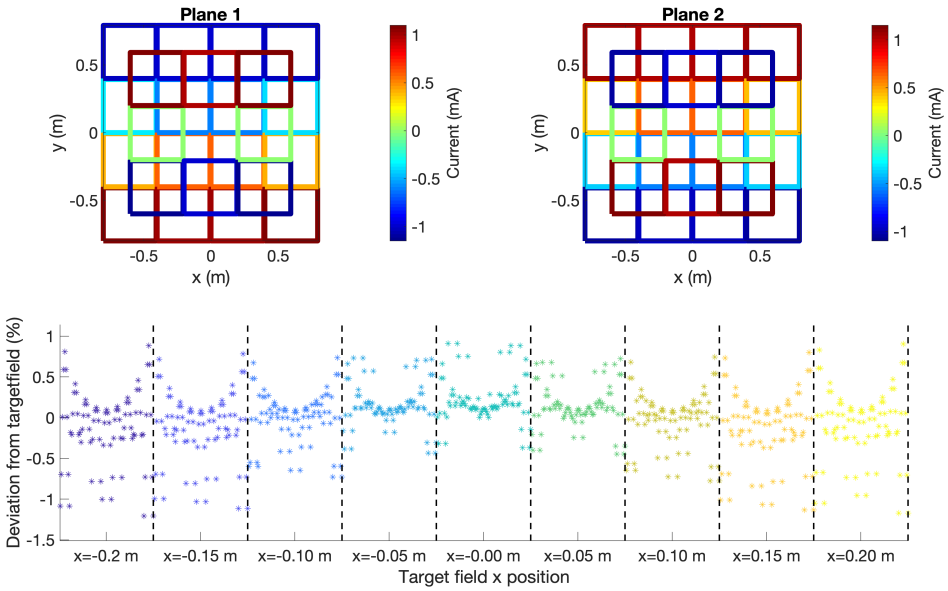



Figure 6.25: *The currents applied to each coil to produce a homogeneous 2 nT, $B_y$-field when interactions with the MSR are considered. Red represents positive current circulation in the loop and blue negative current circulation with magnitude indicated by the colorbar. The deviation from the desired field at each of the 729 target points is shown, and sectioned for each of the nine $z-y$ planes with colour and label corresponding to the $x$ position of each plane.*

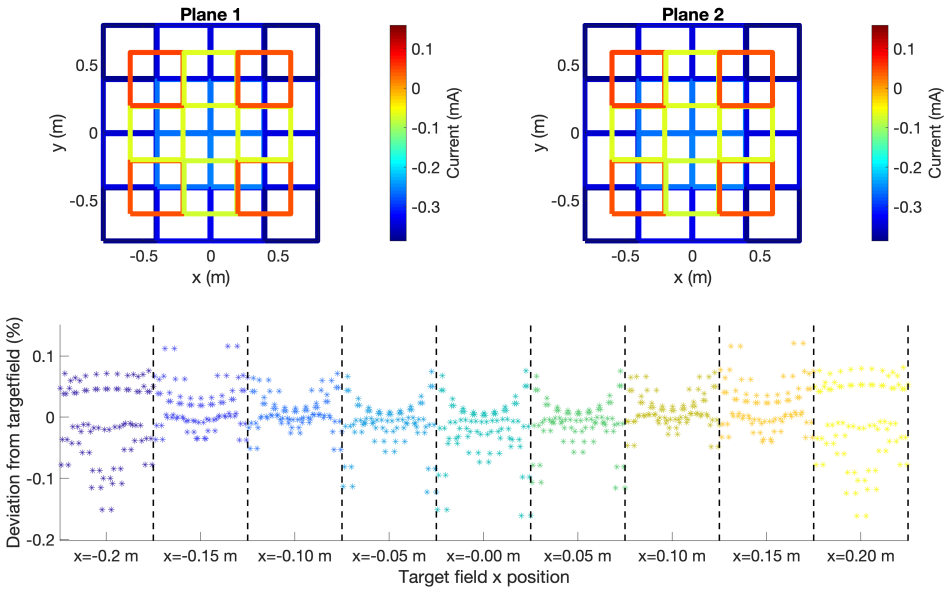



Figure 6.26: *The currents applied to each coil to produce a homogeneous 2 nT, $B_z$-field when interactions with the MSR are considered. Red represents positive current circulation in the loop and blue negative current circulation with magnitude indicated by the colorbar. The deviation from the desired field at each of the 729 target points is shown, and sectioned for each of the nine $z-y$ planes with colour and label corresponding to the $x$ position of each plane.*

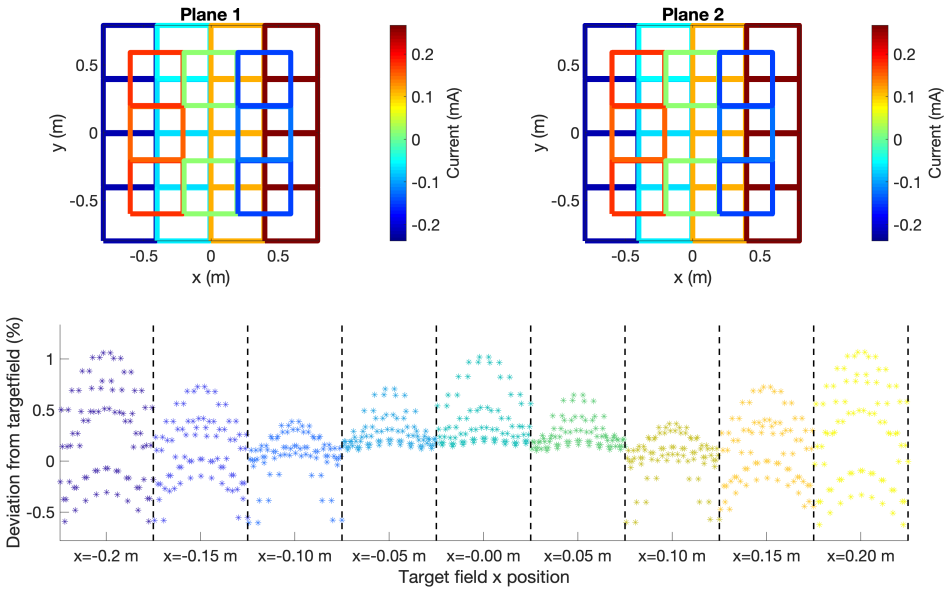



Figure 6.27: *The currents applied to each coil to produce a homogeneous 2 nT/m, $G_x$-field gradient when interactions with the MSR are considered. Red represents positive current circulation in the loop and blue negative current circulation with magnitude indicated by the colorbar. The deviation from the desired field gradient at each of the 729 target points is shown, and sectioned for each of the nine $z-y$ planes with colour and label corresponding to the $x$ position of each plane.*

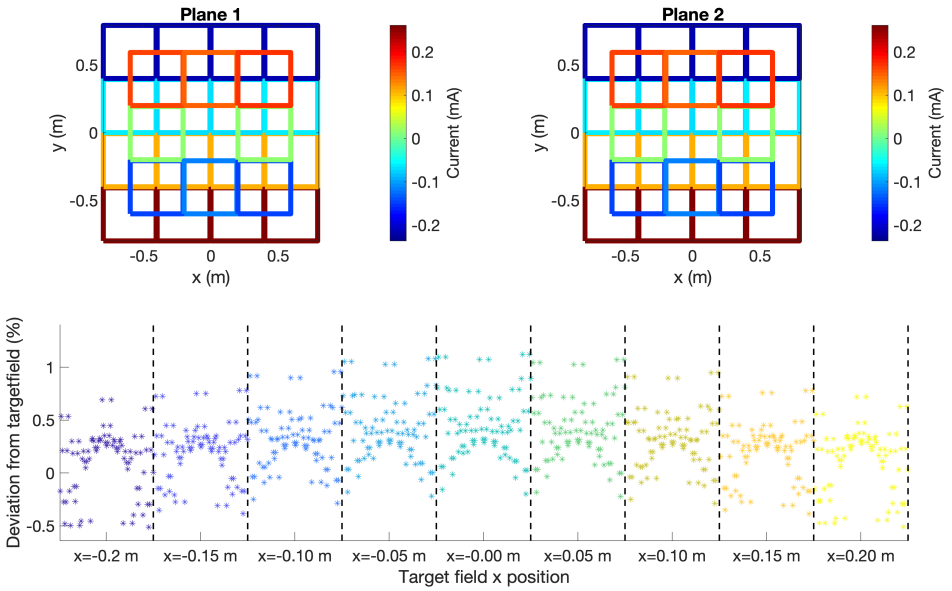



Figure 6.28: *The currents applied to each coil to produce a homogeneous 2 nT/m, $G_y$-field gradient when interactions with the MSR are considered. Red represents positive current circulation in the loop and blue negative current circulation with magnitude indicated by the colorbar. The deviation from the desired field gradient at each of the 729 target points is shown, and sectioned for each of the nine $z-y$ planes with colour and label corresponding to the $x$ position of each plane.*

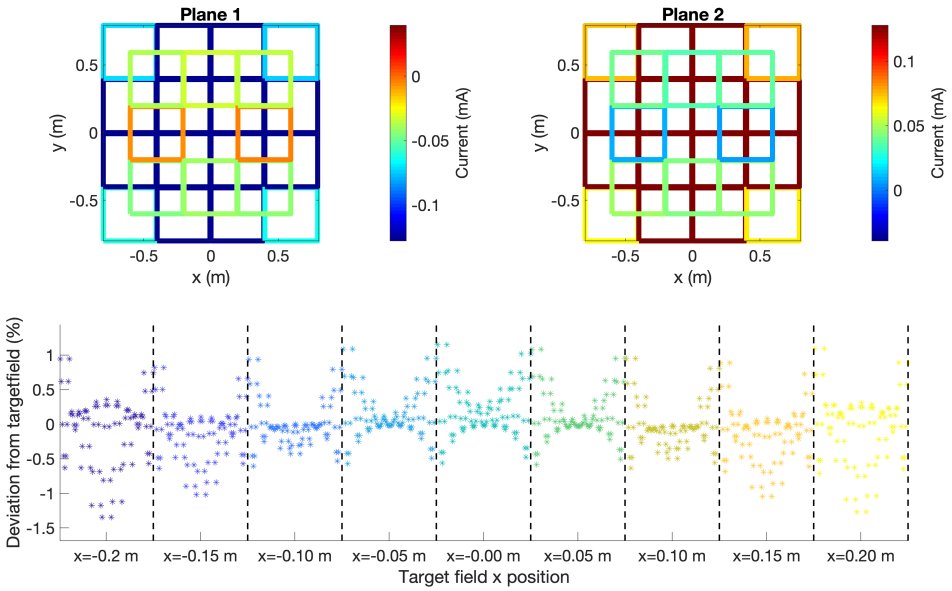



Figure 6.29: *The currents applied to each coil to produce a homogeneous 2 nT/m, $G_z$-field gradient when interactions with the MSR are considered. Red represents positive current circulation in the loop and blue negative current circulation with magnitude indicated by the colorbar. The deviation from the desired field gradient at each of the 729 target points is shown, and sectioned for each of the nine $z-y$ planes with colour and label corresponding to the $x$ position of each plane.*

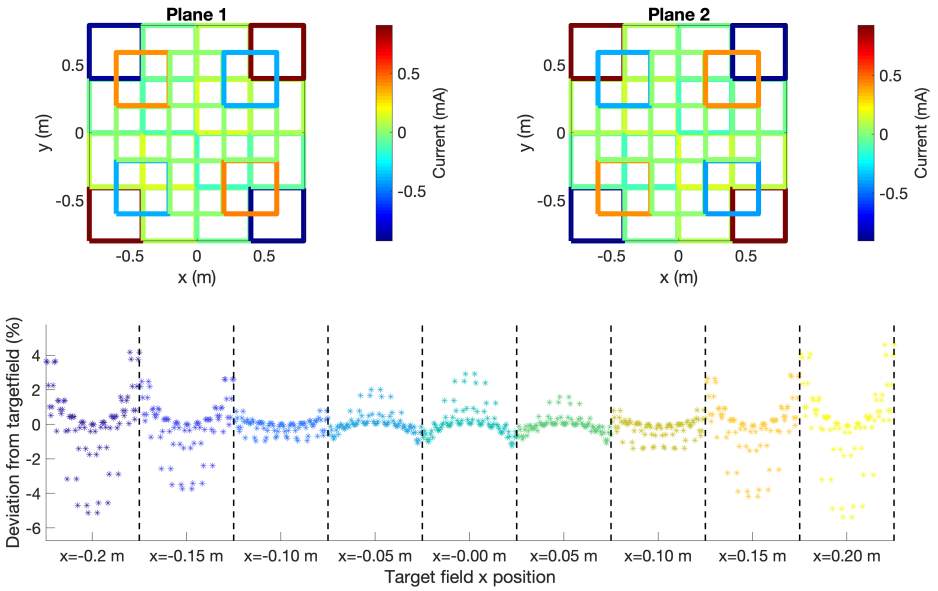



Figure 6.30: *The currents applied to each coil to produce a homogeneous 2 $nT/m$, $G_{xy}$-field gradient when interactions with the MSR are considered. Red represents positive current circulation in the loop and blue negative current circulation with magnitude indicated by the colorbar. The deviation from the desired field gradient at each of the 729 target points is shown, and sectioned for each of the nine $z-y$ planes with colour and label corresponding to the $x$ position of each plane.*

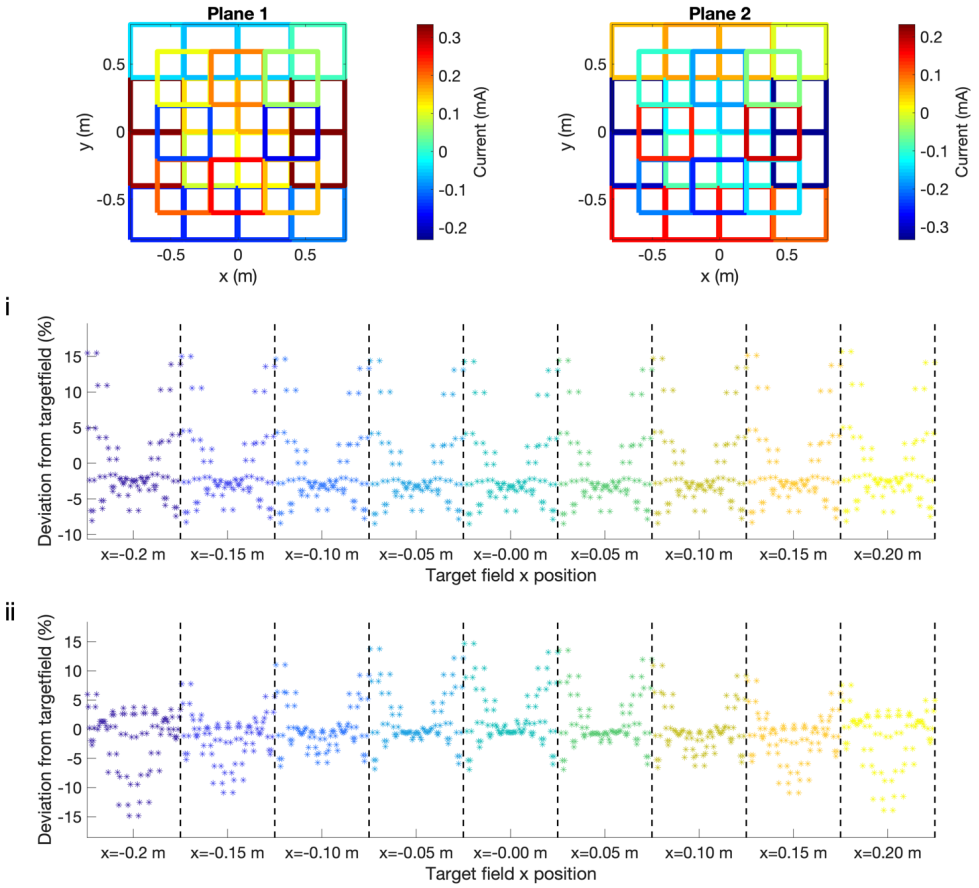



Figure 6.31: *The currents applied to each coil to produce a homogeneous 2 nT/m, $G_{xx}$-field gradient when interactions with the MSR are considered. Red represents positive current circulation in the loop and blue negative current circulation with magnitude indicated by the colorbar. The deviation from the desired field gradient i) $dB_x/dx$ and ii) $dB_z/dz$ at each of the 729 target points is shown, and sectioned for each of the nine $z-y$ planes with colour and label corresponding to the $x$ position of each plane.*

| Field Component | Max deviation (%) | Absolute max current (mA) | Total current (mA) |
|---|---|---|---|
| $B_x$ | 1.2 | 1.15 | 37.2 |
| $B_y$ | 1.5 | 1.38 | 44.1 |
| $B_z$ | 0.2 | 0.39 | 9.49 |
| $G_x$ | 1.1 | 0.26 | 7.12 |
| $G_y$ | 1.1 | 0.27 | 7.27 |
| $G_z$ | 1.3 | 0.13 | 2.88 |
| $G_{xy}$ | 5.4 | 0.92 | 12.6 |
| $G_{xx}$ | 15.7 (14.8) | 0.33 | 12.6 |

Table 6.3: *Simulated performance of matrix coils for each field component when producing uniform fields of 2 nT or field gradients of 2 nT/m over the central volume when interactions with the MSR are considered.*

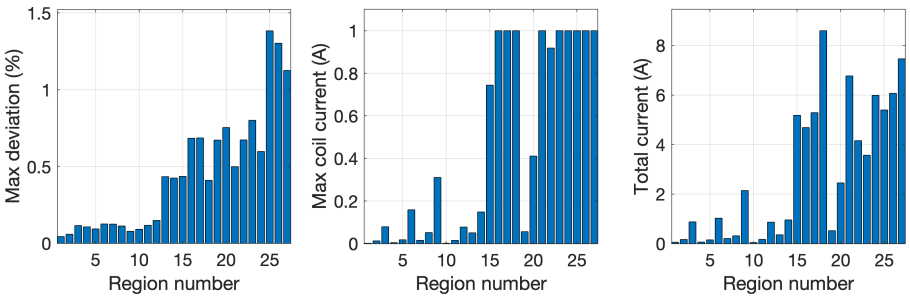



Figure 6.32: *Producing a $B_x$-magnetic field of strength 2 nT in 27 regions, each with volume 0.2 × 0.2 × 0.2 $m^3$ when interactions with the MSR are considered. The maximum deviation from homogeneity, the maximum current magnitude applied to a single coil in the system and the total current magnitude over all 48 units are shown for each region.*

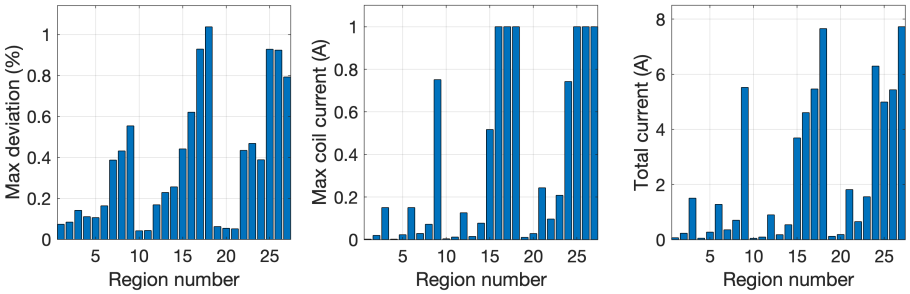



Figure 6.33: *Producing a $B_y$-magnetic field of strength 2 nT in 27 regions, each with volume 0.2 × 0.2 × 0.2 $m^3$ when interactions with the MSR are considered. The maximum deviation from homogeneity, the maximum current magnitude applied to a single coil in the system and the total current magnitude over all 48 units are shown for each region.*

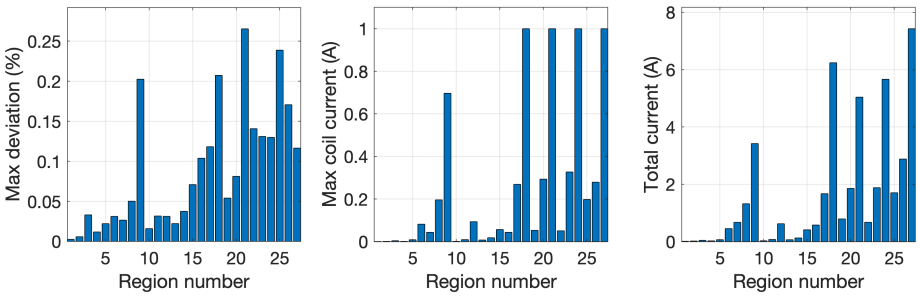



Figure 6.34: *Producing a $B_z$-magnetic field of strength 2 nT in 27 regions, each with volume 0.2 × 0.2 × 0.2 m$^3$ when interactions with the MSR are considered. The maximum deviation from homogeneity, the maximum current magnitude applied to a single coil in the system and the total current magnitude over all 48 units are shown for each region.*

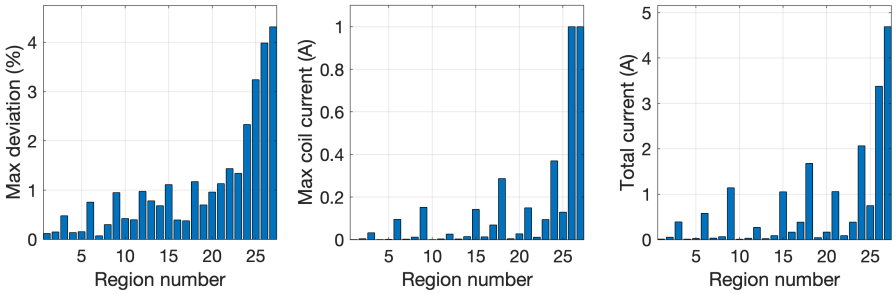



Figure 6.35: *Producing a $G_x$-magnetic field gradient of strength 2 nT/m in 27 regions, each with volume 0.2 × 0.2 × 0.2 m$^3$ when interactions with the MSR are considered. The maximum deviation from homogeneity, the maximum current magnitude applied to a single coil in the system and the total current magnitude over all 48 units are shown for each region.*

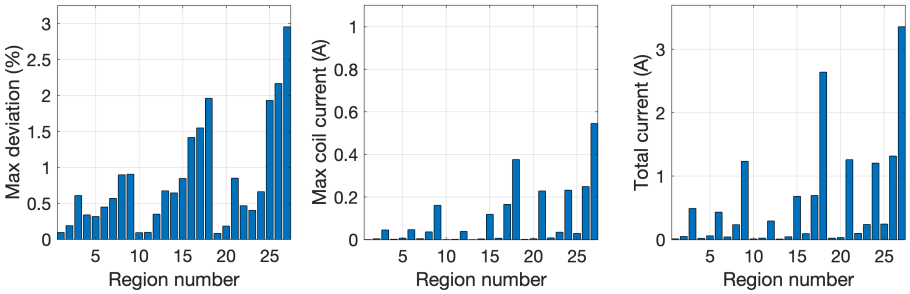



Figure 6.36: *Producing a $G_y$-magnetic field gradient of strength 2 nT/m in 27 regions, each with volume $0.2 \times 0.2 \times 0.2$ m$^3$ when interactions with the MSR are considered. The maximum deviation from homogeneity, the maximum current magnitude applied to a single coil in the system and the total current magnitude over all 48 units are shown for each region.*

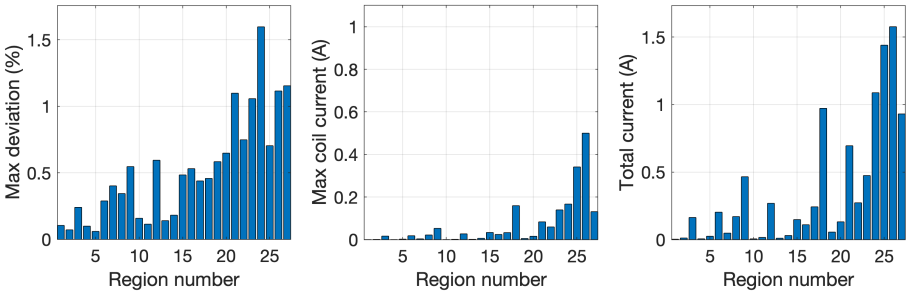



Figure 6.37: *Producing a $G_z$-magnetic field gradient of strength 2 nT/m in 27 regions, each with volume $0.2 \times 0.2 \times 0.2$ m$^3$ when interactions with the MSR are considered. The maximum deviation from homogeneity, the maximum current magnitude applied to a single coil in the system and the total current magnitude over all 48 units are shown for each region.*

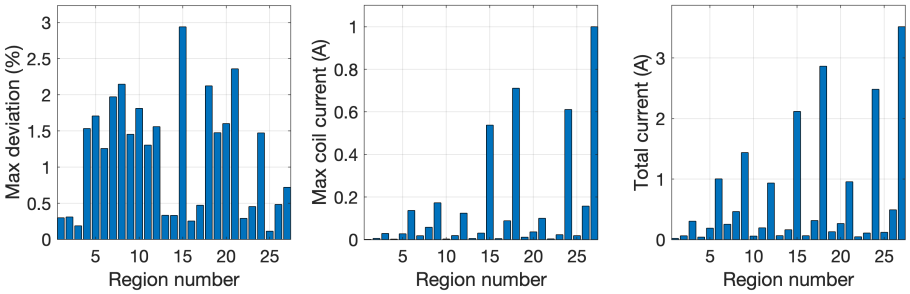



Figure 6.38: *Producing a $G_{xy}$-magnetic field gradient of strength 2 nT/m in 27 regions, each with volume 0.2 × 0.2 × 0.2 m$^3$ when interactions with the MSR are considered. The maximum deviation from homogeneity, the maximum current magnitude applied to a single coil in the system and the total current magnitude over all 48 units are shown for each region.*

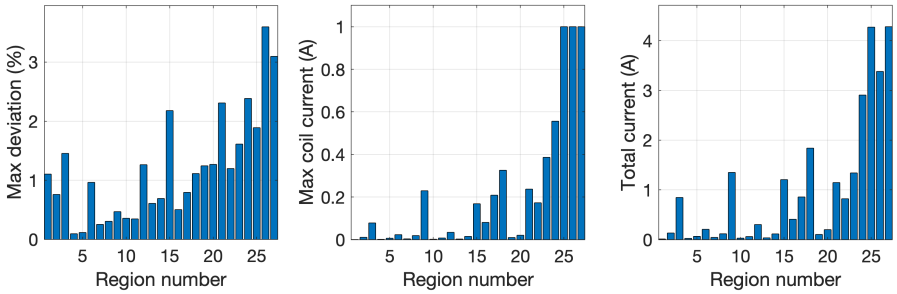



Figure 6.39: *Producing a $G_{xx}$-magnetic field gradient of strength 2 nT/m in 27 regions, each with volume 0.2 × 0.2 × 0.2 m$^3$ when interactions with the MSR are considered. The maximum deviation from homogeneity, the maximum current magnitude applied to a single coil in the system and the total current magnitude over all 48 units are shown for each region.*

| Field Component | Max deviation (%) | Total current (A) | Current limit hit count |
|---|---|---|---|
| $B_x$ | 1.4 | 8.6 | 9/27 |
| $B_y$ | 1.0 | 7.7 | 6/27 |
| $B_z$ | 0.3 | 7.4 | 4/27 |
| $G_x$ | 4.3 | 4.69 | 2/27 |
| $G_y$ | 3.0 | 3.35 | 0/27 |
| $G_z$ | 1.6 | 3.35 | 0/27 |
| $G_{xy}$ | 2.9 | 3.51 | 1/27 |
| $G_{xx}$ | 3.6 | 4.28 | 3/27 |

Table 6.4: *Summarised results showing the maximum deviation, maximum total applied current and the number of regions for which the current limit of $\pm 1$ A was hit. Coils were designed taking into account interactions with the MSR.*

### 6.5.4 Combining coils with the MSR

Figure 6.40 shows the required coil currents for each of the 60 coils in the system to produce a uniform $B_z$ field of strength 50 nT over a $1 \times 1 \times 1$ m$^3$ volume at the centre of the MSR when 60 coils are mounted on the inner walls of the MSR as shown in Figure 6.7. The error at each of the 1331 target field points is also shown. Figure 6.41 shows the required coil currents and error when producing a $G_z$ longitudinal magnetic field gradient of strength 50 nT/m. Figure 6.42 shows the required coil currents and error when producing a $G_x$ transverse magnetic field gradient of strength 50 nT/m.

For each design, the effects of interactions of the coils with the mu-metal were considered. As the coils are positioned very close to the edges of the walls the sharp corners of the cubic enclosure result in a dense concentration of mirrored current elements.

Good performance is shown for producing the uniform field and longitudinal field gradient components, with a maximum deviation of 0.4% and 1.5% respectively. The transverse gradient performs worse with a maximum deviation of 8.8%. Currents of <20 mA are reported for each coil.

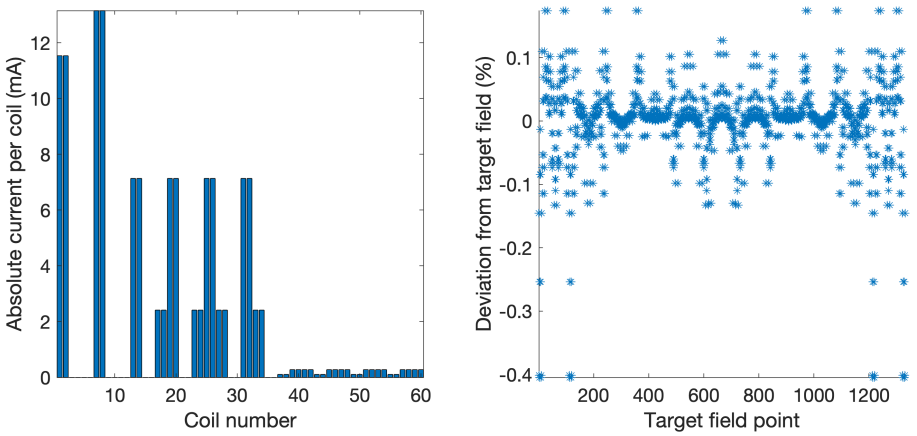



Figure 6.40: *Producing a $B_z$ magnetic field of strength 50 nT over a central 1 × 1 × 1 $m^3$ volume when interactions with the MSR are considered. The current magnitude applied to each coil and the deviation from homogeneity at each target point are shown.*

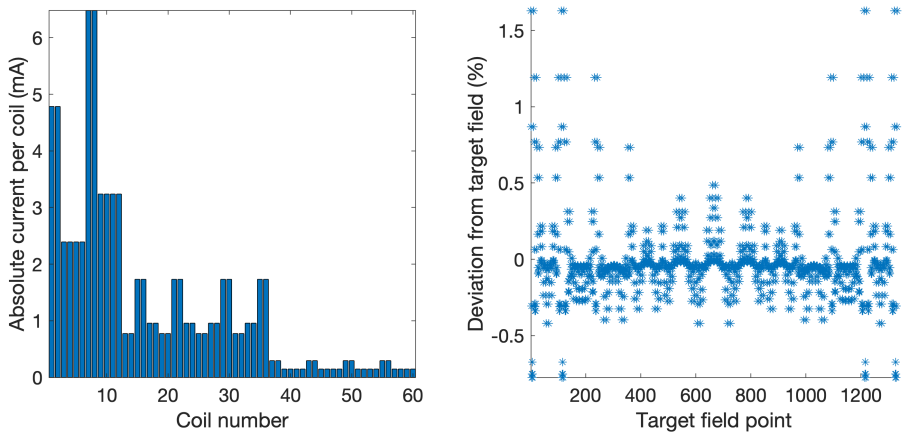



Figure 6.41: *Producing a $G_z$ magnetic field gradient of strength 50 nT/m over a central 1 × 1 × 1 $m^3$ volume when interactions with the MSR are considered. The current magnitude applied to each coil and the deviation from homogeneity at each target point are shown.*

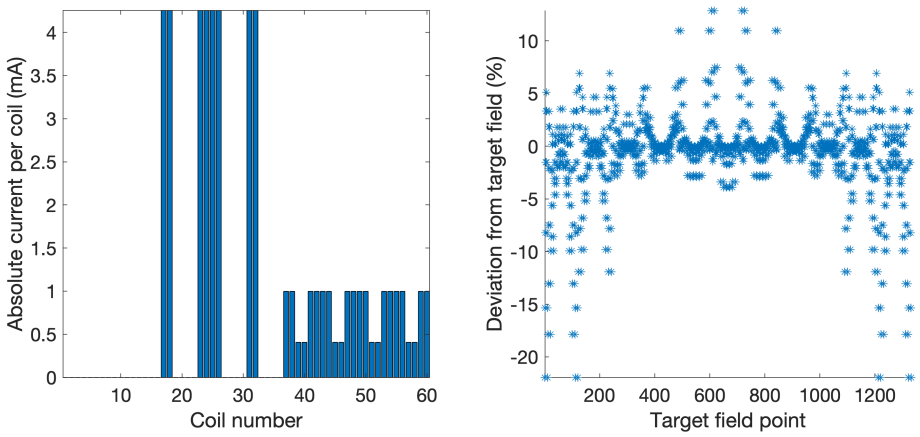



Figure 6.42: *Producing a $G_x$ magnetic field gradient of strength 50 $nT/m$ over a central $1 \times 1 \times 1$ $m^3$ volume when interactions with the MSR are considered. The current magnitude applied to each coil and the deviation from homogeneity at each target point are shown.*

## 6.6 Discussion

### 6.6.1 Comparison to six-coil system

The prototype 48-channel coil system successfully produces the 3 field and 5 field gradient components over the central region of interest when no interactions are considered. The small current values required for each field component ($<$ 120 mA over the system) suggests that superposition of coil currents to produce a desired combination required for field nulling would be possible at reasonably low total power values.

The bi-planar systems required currents of tens of mA per coil to produce the desired nulling. Here (based on Table 6.1) hundreds of mA of total current will be required making the total system less efficient. More turns per unit coil could be added to the design to produce the same strength magnetic field, with smaller applied current, but increased weight, resistance, inductance and engineering difficulty would have to be accounted for.

The distribution of currents over matrix elements of the designs correspond highly with those found for the bi-planar coils designed with harmonic minimisation. The maximum deviations from homogeneity are comparable given the harmonic minimisation design process was restricted to manual tuning of a power-dissipation parameter, and there was a desire to produce wirepaths which could be easily linked. A larger number of smaller matrix-coils would allow for more complex current distributions to be approximated and potentially allow for more homogeneous coils to be designed.

### 6.6.2 Moving the homogeneous region

The design method is reasonably successful at producing homogeneous fields when the region of interest is moved to different locations between the two planes. However, a change in the centre of the homogeneous region results in a loss of the natural symmetry in the designs. This makes the matrices more difficult to invert, leading to an increase in the regularisation parameter and a subsequent increased likelihood of hitting the current limits. This, coupled with high values (up to a maximum of 48 A) of total current magnitude in the system, impacts upon the matrix coils ability to superimpose currents in order to produce different field components when providing field nulling at variable locations.

The number of turns per coil could be increased to allow for a greater efficiency, thus reducing the number of times the current limit would be hit. However, it is more likely that better performance could again be achieved using a larger number of coil elements at a higher resolution around the region of interest. More coils would lead to a high total current value, but the current per coil could be decreased.

### 6.6.3 Mu-metal interactions

Although, as discussed in Chapter 5, interactions could be included in the harmonic minimisation design method, an adaptable solution cannot be readily achieved unless the coils are to be permanently fixed in position in the MSR and a limited array of participant motions are allowed. The mirror-current model of interactions was successfully incorporated into the optimisation of the matrix coil currents, providing a flexible solution. As these coils are positioned relatively far away from the walls and the coil system is centred within the MSR, their effects are not as prominent as if they were placed directly onto the walls (or the coil

set was positioned off-centre with respect to the centre of the room).

When moving the homogeneous region between the two planes, the current limit was not hit in any region. The additional field contributed by the mirrored current elements provides field spatial variation and magnitude that allows components to be produced with a lower error and power than previously.

Positioning the coil off-centre in the MSR would result in a more challenging situation than that which was investigated here, which would result in a loss of symmetry in the coil designs. Nonetheless, given the system flexibility when moving the centre of the homogeneous region, this should be easily incorporated. Again, the main challenge is the lack of $x-y$ field control afforded by the bi-planar design.

### 6.6.4 Combining coils with the MSR

The coils in the simulated 60-channel system were placed directly onto each of the walls. Although this situation provides symmetric field variation from coils in all three directions, their proximity to the sharp corners of the cubic enclosure increases the effect of the mirror currents compared to previous investigations. At such proximity, it is crucial that the mirror model be further verified through comparison with experimental data and advanced modelling using finite-element analysis.

To address the poorer performance of the transverse field gradients a movable, smaller volume could be considered and applied as before, instead of the large volume which was simulated. Optimal coil shapes and position could also be incorporated into the simulation, such that a series of $M$ coils are required to be shaped and sited over the shielding volume to produce the desired fields. More coils could be added to produce a finer resolution of correction terms, but the

scalability of the system will rely on stable current sources which can be adjusted at high-speed.

## 6.7 Prototype construction

It is clear from the simulations that the prototype 48-channel matrix coil system will not allow full ambulatory movement of a participant to be achieved. An increase in volume from $0.4 \times 0.4 \times 0.4$ m$^3$ to an effective $1 \times 1 \times 1$ m$^3$ volume will still allow for the development of new experiments where participants can take small steps. Given the engineering challenges of the prototype that are yet to be overcome it is clear that this system will be invaluable in the development of the matrix coil technology to expand the region even further. Construction work and engineering completed up to now is detailed here.

### 6.7.1 Coil construction

To construct the matrix coil, the $4 \times 4$ and $3 \times 3$ grids were marked out onto wooden boards of square length $1.8 \times 1.8$ m$^2$ using a grid of plastic wire-guides bolted at the corners of each square unit coil. Each guide had four rounded edges to smoothly make the square corners and a plastic nut to stop the wire from lifting away. The construction method resulted in a final unit coil square side length of 38.5 cm due to spacings on the wire guides. A test piece featuring 5 unit coils is shown in Figure 6.43.

Each coil was formed from 20 turns of enameled copper wire (diameter 0.56 mm) wound with inputs and outputs fed around the outside of the plane in twisted pairs down to a series of connector blocks at the base. These connector blocks each contain the input and output for 4 coils wired to an 8-core cable with a connector.

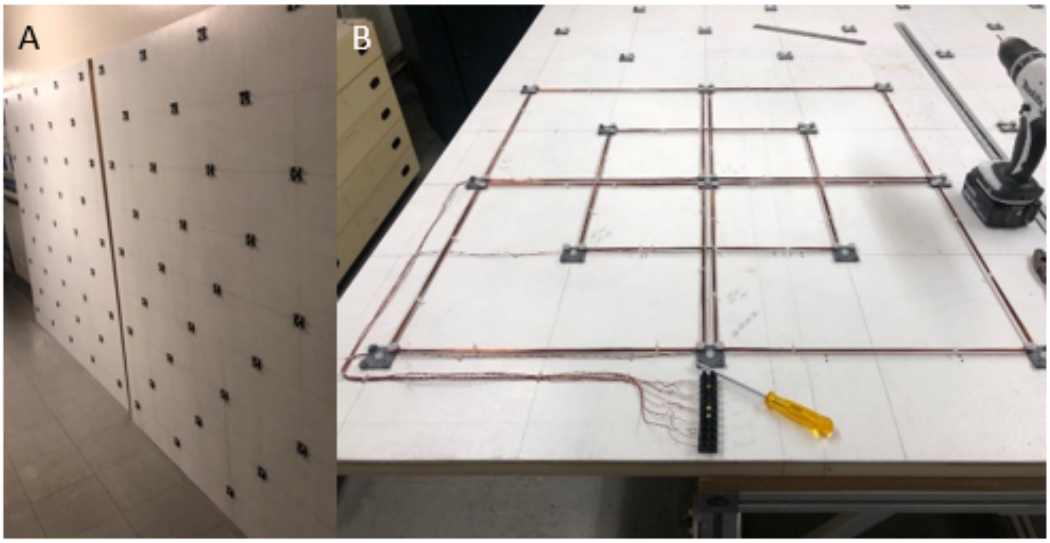



Figure 6.43: *Construction of the 48-channel prototype matrix coil. A) Two wooden boards with plastic wire guides to house the coils. B) Completed winding of 5 unit coils.*

### 6.7.2 Electronics system

To inform on the design of an electronics system a single test unit was built to assess the inductance and resistance of each unit. Copper wire of diameter 0.56 mm was used to wind the coil. Coil resistance was 2.15 Ω and coil inductance was 596 $\mu$H. With a maximum current limit of ± 1 A per coil there is a maximum power dissipation of less than 2.15 W per coil and 103 W total over the full system.

QuSpin provided low-noise voltage driver circuits for the bi-planar coil systems, but due to potential need for large current values it was decided that bespoke current amplifiers were better suited for use with the matrix coil system. An amplifier which could drive 4 unit coils from a single board was designed and constructed by the electronics support team in the School of Physics and Astronomy at the University of Nottingham.

Each amplifier features a AD5686 (Analog Devices, MA, USA) 4-channel 16-Bit digital to analogue converter (DAC) with serial peripheral interface (SPI).

The driver is designed to produce ±1.5 A from the 0-5 V range of the DAC. The least significant bit of the DAC is $5/2^{16} = 76.3$ $\mu$V which is equivalent to 38 $\mu$A through the coil. The DAC SPI can be controlled using an Arduino (or other similar micro-controller) and multiple DACs can be 'daisy-chained' for simultaneous operation from a single master unit.

### 6.7.3 Field nulling methods

In order to calculate coil currents for field nulling the mathematics developed here requires prior knowledge of the remnant magnetic field inside the MSR. It also requires knowledge of the effect of a unit current applied to each coil at each position. Two methods to gather this information are discussed here.

#### 6.7.3.1 Field mapping and optical tracking

Given that the magnitude of the remnant field is likely to be several nT this could be measured by using a suitably precise magnetometer. A tri-axial vector magnetometer could be moved around the room, recording the sensor's position and orientation with an optical tracking system (such as the OptiTrack camera described previously in Chapter 4). A map of the magnetic field at each position can then be formed as the target field vector. Maps of the field produced by each unit coil can also be obtained by applying a known current to one coil at a time.

Coil currents that best cancel the remnant magnetic field at each position can be calculated and stored. If the location of the participant is continually tracked during an experiment then currents can be constantly updated via a lookup table. This method would therefore allow the participant to move freely between the planes.

However, a stable remnant field, high precision magnetometer and precise optical

tracking are required. The mapping should also be simple to implement such that regular updates can be made. Dynamic nulling of the field would also need to be dealt with, possibly by further tracking of the head of the participant to find the orientation of head-mounted reference sensors. Measured fields could be used as inputs to PID controllers as described in Chapter 5.

#### 6.7.3.2 Reference array

A series of tri-axial magnetometers could be placed around the participant to form the corners of a cube. The 8 sensors could feed information from these points to form a sparse map of the remnant magnetic field. By pulsing each unit coil in turn a measure of the field produced by each coil at the 8 positions could be found. A matrix inversion could then be applied to find the currents which null the remnant field at each of the 8 points.

This method is entirely data-driven and does not rely on any modelling or field mapping to be performed. Dynamic control of the coil currents to correct for temporal fluctuations in the remnant field would be simple to implement from the fixed coil to sensor couplings. However, the sparsely sampled reference array may not generate as accurate a null over the participant. It also restricts participant motion to the volume which is enclosed by the reference sensors.

# Conclusion

This thesis has presented the development of a series of active magnetic shielding systems. The primary aim was to allow magnetoencephalography (MEG) recordings to be made with optically-pumped magnetometers (OPMs) on moving participants. However, the techniques are translateable to other magnetometers and shielding applications.

Chapter 4 described the design and construction of a bi-planar coil system capable of cancelling the three uniform field components, as well as three dominant field gradients. The six coil system allowed the first unrestrained MEG recordings to be made. Static field shielding factors of up to 46 for the uniform field and 13 for the largest field gradient were achieved. With this system, head motions of $\pm 10$ cm and $\pm 35^{\circ}$ could be tolerated whilst high-quality MEG data comparable to that of a cryogenic system was obtained. This was demonstrated by a measurement of retinotopy, where the neuromagnetic response to visual stimuli presented to the left and right sides of the central field of vision could be spatially resolved in the brain.

Chapter 5 described an adapted coil design method exploiting the shared symmetry of pairs of coils. This allowed the same performance as the six-coil system to be achieved with only three coil layers. A set of coils designed using this approach were installed at a city-centre site close to a London Underground railway line. Dynamic control of the coil-currents to cancel the low-frequency, time-varying

magnetic fields induced by passing of trains was required. A dynamic shielding factor of 40 dB at 0.01 Hz was achieved over a 10-minute period. The limited dynamic range of the coil electronics impacted on the performance of the dynamic nulling, as the least-significant-bit voltage of the hardware that was used, produced a magnetic field which was larger than the magnitude of the interfering fields at frequencies >1 Hz. Development of the electronics to prevent the addition of noise at high-frequency will be required for optimal performance. Interactions of the magnetic fields produced by the coils with the high-permeability walls of the shielded room were modelled as a series of image currents. The interactions were shown to alter the efficiency and degrade the homogeneity of the coils from predicted values both in simulation and measurement. These interactions should be taken into account in future coil designs to achieve the best performance of any coil system operating inside an enclosure of high-permeability material.

The second magnetically shielded room (MSR) which was installed at the University of Nottingham by Magnetic Shields Limited (Kent, UK) does *not* contain a cryogenic MEG system, meaning a large volume is available for participants to move within. With a bi-planar coil arrangement the participant is restricted to movements over a region at the centre of the two planes. The designs are inflexible and difficult to construct; adapting the setup to paradigms where a different range of participant motion is required would only be achieved by physically translating the coils.

Chapter 6 outlined an alternative in the form of the matrix coil system. Individually controllable currents applied to a series of small unit coils can be used to move the nulling volume around, allowing a wider range of participant motions. The development of this system requires significant further work, but will be essential to allow full exploitation of the available space inside the new MSR. A prototype unit featuring 48-channels is under construction. Consideration of

the electronics' challenges, incorporating the mu-metal interactions and ensuring the participant is continually tracked to allow dynamical updating of the coil currents will be required. With a completed system, spatial navigation tasks, virtual reality experiences and hyperscanning (in which multiple individuals are simultaneously scanned) will be possible.

Coil sets based on the work described in Chapter 4 and Chapter 5 are now commercially available following licensing of the technology to Magnetic Shields Limited. The commercial availability of bi-planar coil systems will allow other MEG centres to develop OPM-based systems by retrofitting their existing MSRs. However, coils (bi-planar or matrix systems) which are built into the walls of new MSRs and do not limit the available space inside the shielded enclosure would be a more practical solution.

Development of a lightweight MSR which combines passive shielding with integrated coil systems is ongoing through collaboration between the University of Nottingham, Magnetic Shields Limited, University College London and Young Epilepsy (a specialist school for young children and adults with epilepsy). The aim of the project is to develop a commercially available MSR with lower weight and smaller external dimensions, making it suitable for installation in most rooms, with minimal building work and a short installation time.

Young Epilepsy operates a small clinical facility, where epilepsy monitoring with electroencephalography (EEG) is routinely performed. Successful completion of the project would see a state-of-the-art MSR that is optimised for OPM-based MEG recordings on epilepsy patients to be installed at this facility. Reducing the cost and siting challenges of MSRs by integrating active shielding systems, whilst demonstrating clinically relevant applications could help to stimulate an increase in the number of new MEG facilities. A growing community of OPM-MEG researchers will contribute significantly to furthering our understanding of

the human brain.

# Bibliography

[Abbott, 2015] Abbott, J. J. (2015). Parametric design of tri-axial nested Helmholtz coils. *Review of Scientific Instruments*, 86(5).

[Ahlfors et al., 1992] Ahlfors, S. P., Ilmoniemi, R. J., and Hämäläinen, M. S. (1992). Estimates of visually evoked cortical currents. *Electroencephalography and Clinical Neurophysiology*.

[Allred et al., 2002] Allred, J. C., Lyman, R. N., Kornack, T. W., and Romalis, M. V. (2002). High-Sensitivity Atomic Magnetometer Unaffected by Spin-Exchange Relaxation. *Physical Review Letters*.

[Altarev et al., 2014] Altarev, I., Babcock, E., Beck, D., Burghoff, M., Chesnevskaya, S., Chupp, T., Degenkolb, S., Fan, I., Fierlinger, P., Frei, A., Gutsmiedl, E., Knappe-Grüneberg, S., Kuchler, F., Lauer, T., Link, P., Lins, T., Marino, M., McAndrew, J., Niessen, B., Paul, S., Petzoldt, G., Schläpfer, U., Schnabel, A., Sharma, S., Singh, J., Stoepler, R., Stuiber, S., Sturm, M., Taubenheim, B., Trahms, L., Voigt, J., and Zechlau, T. (2014). A magnetically shielded room with ultra low residual field and gradient. *Review of Scientific Instruments*.

[Andersen et al., 2017] Andersen, L. M., Oostenveld, R., Pfeiffer, C., Ruffieux, S., Jousmäki, V., Hämäläinen, M., Schneiderman, J. F., and Lundqvist, D. (2017). Similarities and differences between on-scalp and conventional in-helmet magnetoencephalography recordings. *PLoS ONE*.

[Ang et al., 2005] Ang, K. H., Chong, G., and Li, Y. (2005). PID control system analysis, design, and technology. *IEEE Transactions on Control Systems Technology*.

[Appelt et al., 1998] Appelt, S., Ben-Amar Baranga, A., Erickson, C. J., Romalis, M. V., Young, A. R., and Happer, W. (1998). Theory of spin-exchange optical pumping of3He and129Xe. *Physical Review A - Atomic, Molecular, and Optical Physics*.

[Åström and Hägglund, 1995] Åström, K. J. and Hägglund, T. (1995). *PID Controllers - Theory, Design, and Tuning (2nd Edition)*.

[Baillet, 2017] Baillet, S. (2017). Magnetoencephalography for brain electrophysiology and imaging.

[Bardeen et al., 1957] Bardeen, J., Cooper, L. N., and Schrieffer, J. R. (1957). Theory of Superconductivity. *Phys. Rev.*, 108(5):1175–1204.

[Barratt et al., 2018] Barratt, E. L., Francis, S. T., Morris, P. G., and Brookes, M. J. (2018). Mapping the topological organisation of beta oscillations in motor cortex using MEG. *NeuroImage*.

[Barry et al., 2019] Barry, D. N., Tierney, T. M., Holmes, N., Boto, E., Roberts, G., Leggett, J., Bowtell, R., Brookes, M. J., Barnes, G. R., and Maguire, E. A. (2019). Imaging the human hippocampus with optically-pumped magnetoencephalography. *NeuroImage*.

[Batie et al., 2018] Batie, M., Bitant, S., Strasburger, J. F., Shah, V., Alem, O., and Wakai, R. T. (2018). Detection of Fetal Arrhythmia by Using Optically Pumped Magnetometers.

[Bell and Bloom, 1957] Bell, W. E. and Bloom, A. L. (1957). Optical detection of magnetic resonance in alkali metal vapor. *Physical Review*.

[Bell and Bloom, 1961] Bell, W. E. and Bloom, A. L. (1961). Optically driven spin precession. *Physical Review Letters*.

[Berger, 1934] Berger, H. (1934). Über das Elektrenkephalogramm des Menschen. *Deutsche Medizinische Wochenschrift*.

[Bison et al., 2009] Bison, G., Castagna, N., Hofer, A., Knowles, P., Schenker, J. L., Kasprzak, M., Saudan, H., and Weis, A. (2009). A room temperature 19-channel magnetic field mapping device for cardiac signals. *Applied Physics Letters*.

[Bloch, 1953] Bloch, F. (1953). The principle of nuclear induction. *Science*.

[Bork et al., 1980] Bork, J., Hahlbohm, H., Klein, R., and Schnabel, A. (1980). The 8-layered magnetically shielded room of the PTB : Design and construction. *Biomag 2000, Proceedings of the 12th International Conference on Biomagnetism*, pages 970–973.

[Borna et al., 2019] Borna, A., Carter, T. R., Derego, P., James, C. D., and Schwindt, P. D. (2019). Magnetic Source Imaging Using a Pulsed Optically Pumped Magnetometer Array. *IEEE Transactions on Instrumentation and Measurement*.

[Borna et al., 2017] Borna, A., Carter, T. R., Goldberg, J. D., Colombo, A. P., Jau, Y. Y., Berry, C., McKay, J., Stephen, J., Weisend, M., and Schwindt, P. D. (2017). A 20-channel magnetoencephalography system based on optically pumped magnetometers. *Physics in Medicine and Biology*, 62(23):8909–8923.

[Boto et al., 2016] Boto, E., Bowtell, R., Krüger, P., Fromhold, T. M., Morris, P. G., Meyer, S. S., Barnes, G. R., and Brookes, M. J. (2016). On the potential of a new generation of magnetometers for MEG: A beamformer simulation study. *PLoS ONE*, 11(8).

[Boto et al., 2018] Boto, E., Holmes, N., Leggett, J., Roberts, G., Shah, V., Meyer, S. S., Muñoz, L. D., Mullinger, K. J., Tierney, T. M., Bestmann, S., Barnes, G. R., Bowtell, R., and Brookes, M. J. (2018). Moving magnetoencephalography towards real-world applications with a wearable system. *Nature*, 555(7698):657–661.

[Boto et al., 2017] Boto, E., Meyer, S. S., Shah, V., Alem, O., Knappe, S., Kruger, P., Fromhold, T. M., Lim, M., Glover, P. M., Morris, P. G., Bowtell, R., Barnes, G. R., and Brookes, M. J. (2017). A new generation of magnetoencephalography: Room temperature measurements using optically-pumped magnetometers. *NeuroImage*.

[Brookes et al., 2010] Brookes, M. J., Zumer, J. M., Stevenson, C. M., Hale, J. R., Barnes, G. R., Vrba, J., and Morris, P. G. (2010). Investigating spatial specificity and data averaging in MEG. *NeuroImage*, 49(1):525–538.

[Brown et al., 2014] Brown, R. W., Cheng, Y.-C. N., Haacke, E. M., Thompson, M. R., and Venkatesan, R. (2014). *Magnetic ressonance imaging: Physical Principles ans Sequence Design*.

[Bryś et al., 2005] Bryś, T., Czekaj, S., Daum, M., Fierlinger, P., George, D., Henneck, R., Kasprzak, M., Kirch, K., Kuźniak, M., Kuehne, G., Pichlmaier, A., Siodmok, A., Szelc, A., Tanner, L., Assmann, C., Bechstein, S., Drung, D., Schurig, T., Ciofi, C., and Neri, B. (2005). Magnetic field stabilization for magnetically shielded volumes by external field coils. *Nuclear Instruments and Methods in Physics Research, Section A: Accelerators, Spectrometers, Detectors and Associated Equipment*.

[Budker and Jackson Kimball, 2011] Budker, D. and Jackson Kimball, D. F. (2011). *Optical magnetometry*.

[Carlson et al., 1992] Carlson, J. W., Derby, K. A., Hawryszko, K. C., and Weideman, M. (1992). Design and evaluation of shielded gradient coils. *Magnetic Resonance in Medicine*, 26(2):191–206.

[Celozzi et al., 2008] Celozzi, S., Araneo, R., and Lovat, G. (2008). *Electromagnetic Shielding*.

[Churchill et al., 2004] Churchill, J. D., Tharps, J. A., Wellman, C. L., Sengelaub, D. R., and Garraghty, P. E. (2004). Morphological correlates of injury-induced reorganization in primate somatosensory cortex. *BMC Neuroscience*.

[Cohen, 1967] Cohen, D. (1967). Enhancement of ferromagnetic shielding against low-frequency magnetic fields. *Applied Physics Letters*.

[Cohen, 1968] Cohen, D. (1968). Magnetoencephalography: evidence of magnetic fields produced by alpha rhythm currents.

[Cohen, 1970] Cohen, D. (1970). Large-volume conventional magnetic shields. *Revue de Physique Appliquée*.

[Cohen, 1972] Cohen, D. (1972). Magnetoencephalography: Detection of the brain's electrical activity with a superconducting magnetometer. *Science*.

[Cohen-Tannoudji et al., 1970] Cohen-Tannoudji, C., Dupont-Roc, J., Haroche, S., and Laloë, F. (1970). Diverses résonances de croisement de niveaux sur des atomes pompés optiquement en champ nul. I. Théorie. *Revue de Physique Appliquée*.

[Curio et al., 1991] Curio, G., Erné, S. N., Sandfort, J., Scheer, J., Stehr, R., and Trahms, L. (1991). Exploratory mapping of evoked neuromagnetic activity from human peripheral nerve, brachial plexus and spinal cord. *Electroencephalography and Clinical Neurophysiology/ Evoked Potentials*.

[Dale and Morley, 2017] Dale, M. W. and Morley, G. W. (2017). Medical applications of diamond magnetometry: commercial viability. pages 1–10.

[Donner and Siegel, 2011] Donner, T. H. and Siegel, M. (2011). A framework for local cortical oscillation patterns.

[Dupont-Roc et al., 1969] Dupont-Roc, J., Haroche, S., and Cohen-Tannoudji, C. (1969). Detection of very weak magnetic fields (109gauss) by 87Rb zero-field level crossing resonances. *Physics Letters A*, 28(9):638–639.

[Engel et al., 2013] Engel, A. K., Gerloff, C., Hilgetag, C. C., and Nolte, G. (2013). Intrinsic Coupling Modes: Multiscale Interactions in Ongoing Brain Activity.

[Engel et al., 1997] Engel, S. A., Glover, G. H., and Wandell, B. A. (1997). Retinotopic organization in human visual cortex and the spatial precision of functional MRI. *Cerebral Cortex*, 7(2):181–192.

[Garda and Galias, 2012] Garda, B. and Galias, Z. (2012). Non-negative least squares and the Tikhonov regularization methods for coil design problems. In *2012 International Conference on Signals and Electronic Systems, ICSES 2012 - The Conference Proceedings*.

[Garda and Galias, 2014] Garda, B. and Galias, Z. (2014). Tikhonov regularization and constrained quadratic programming for magnetic coil design problems. *International Journal of Applied Mathematics and Computer Science*.

[Garda and Galias, 2015] Garda, B. and Galias, Z. (2015). Synthesis of the Magnetic Field Using Transversal 3D Coil System. *International Journal of Electronics and Telecommunications*.

[Geselowitz, 1967] Geselowitz, D. B. (1967). On Bioelectric Potentials in an Inhomogeneous Volume Conductor. *Biophysical Journal*.

[Gross et al., 2013] Gross, J., Baillet, S., Barnes, G. R., Henson, R. N., Hillebrand, A., Jensen, O., Jerbi, K., Litvak, V., Maess, B., Oostenveld, R., Parkko-

nen, L., Taylor, J. R., van Wassenhove, V., Wibral, M., and Schoffelen, J. M. (2013). Good practice for conducting and reporting MEG research.

[Gruetter, 1993] Gruetter, R. (1993). Automatic, localized in Vivo adjustment of all first-and second-order shim coils. *Magnetic Resonance in Medicine*.

[Hämäläinen et al., 1993] Hämäläinen, M., Hari, R., Ilmoniemi, R. J., Knuutila, J., and Lounasmaa, O. V. (1993). Magnetoencephalography theory, instrumentation, and applications to noninvasive studies of the working human brain. *Reviews of Modern Physics*, 65(2):413–497.

[Hammond, 1960] Hammond, P. (1960). Electric and magnetic images. *Proceedings of the IEE Part C: Monographs*, 107(12):306.

[Hansen et al., 2010] Hansen, P., Kringelbach, M., and Salmelin, R. (2010). *MEG: An introduction to methods*.

[Happer, 1972] Happer, W. (1972). Optical pumping. *Reviews of Modern Physics*.

[Hari et al., 1993] Hari, R., Karhu, J., Hämäläinen, M., Knuutila, J., Salonen, O., Sams, M., and Vilkman, V. (1993). Functional Organization of the Human First and Second Somatosensory Cortices: a Neuromagnetic Study. *European Journal of Neuroscience*.

[Hari et al., 1987] Hari, R., Pelizzone, M., Mäkelä, J. P., Hällström, J., Leinonen, L., and Lounasmaa, O. V. (1987). Neuromagnetic responses of the human auditory cortex to on- and offsets of noise bursts. *International Journal of Audiology*.

[Hipp et al., 2012] Hipp, J. F., Hawellek, D. J., Corbetta, M., Siegel, M., and Engel, A. K. (2012). Large-scale cortical correlation structure of spontaneous oscillatory activity. *Nature Neuroscience*.

[Hoburg, 1995] Hoburg, J. F. (1995). Principles of Quasistatic Magnetic Shielding with Cylindrical and Spherical Shields.

[Holmes et al., 2018] Holmes, N., Leggett, J., Boto, E., Roberts, G., Hill, R. M., Tierney, T. M., Shah, V., Barnes, G. R., Brookes, M. J., and Bowtell, R. (2018). A bi-planar coil system for nulling background magnetic fields in scalp mounted magnetoencephalography. *NeuroImage*.

[Holmes et al., 2019] Holmes, N., Tierney, T. M., Leggett, J., Boto, E., Mellor, S., Roberts, G., Hill, R. M., Shah, V., Barnes, G. R., Brookes, M. J., and Bowtell, R. (2019). Balanced, bi-planar magnetic field and field gradient coils for field compensation in wearable magnetoencephalography. *Scientific Reports*.

[Hounsfield, 1973] Hounsfield, G. N. (1973). Computerized transverse axial scanning (tomography): I. Description of system. *British Journal of Radiology*.

[Hu et al., 2017] Hu, Y., Wang, Q., Hu, X., Zhu, X., Crozier, S., Wang, Y., and Liu, F. (2017). A simulation study on the design of gradient coils in MRI for the imaging area above the patient bed. *Measurement Science and Technology*.

[Huang et al., 1999] Huang, M. X., Mosher, J. C., and Leahy, R. M. (1999). A sensor-weighted overlapping-sphere head model and exhaustive head model comparison for MEG. *Physics in Medicine and Biology*.

[Iivanainen et al., 2017] Iivanainen, J., Stenroos, M., and Parkkonen, L. (2017). Measuring MEG closer to the brain: Performance of on-scalp sensor arrays. *NeuroImage*, 147:542–553.

[Iivanainen et al., 2019] Iivanainen, J., Zetter, R., Grön, M., Hakkarainen, K., and Parkkonen, L. (2019). On-scalp MEG system utilizing an actively shielded array of optically-pumped magnetometers. *NeuroImage*.

[Jaklevic et al., 1964] Jaklevic, R. C., Lambe, J., Silver, A. H., and Mercereau, J. E. (1964). Quantum interference effects in Josephson tunneling. *Physical Review Letters*.

[Jin, 1998] Jin, J.-M. (1998). Electromagnetics in magnetic resonance imaging. *IEEE Antennas and Propagation Magazine*, 40(6):7–22.

[Johnson et al., 2010] Johnson, C., Schwindt, P. D., and Weisend, M. (2010). Magnetoencephalography with a two-color pump-probe, fiber-coupled atomic magnetometer. *Applied Physics Letters*, 97(24).

[Johnson et al., 2013] Johnson, C. N., Schwindt, P. D., and Weisend, M. (2013). Multi-sensor magnetoencephalography with atomic magnetometers. *Physics in Medicine and Biology*, 58(17):6065–6077.

[Josephson, 1962] Josephson, B. D. (1962). Possible new effects in superconductive tunnelling. *Physics Letters*.

[Juchem et al., 2011a] Juchem, C., Brown, P. B., Nixon, T. W., McIntyre, S., Rothman, D. L., and De Graaf, R. A. (2011a). Multicoil shimming of the mouse brain. *Magnetic Resonance in Medicine*.

[Juchem et al., 2013] Juchem, C., Green, D., and De Graaf, R. A. (2013). Multicoil magnetic field modeling. *Journal of Magnetic Resonance*.

[Juchem et al., 2011b] Juchem, C., Nixon, T. W., McIntyre, S., Boer, V. O., Rothman, D. L., and De Graaf, R. A. (2011b). Dynamic multi-coil shimming of the human brain at 7 T. *Journal of Magnetic Resonance*.

[Juchem et al., 2010a] Juchem, C., Nixon, T. W., McIntyre, S., Rothman, D. L., and De Graaf, R. A. (2010a). Magnetic field homogenization of the human prefrontal cortex with a set of localized electrical coils. *Magnetic Resonance in Medicine*.

[Juchem et al., 2010b] Juchem, C., Nixon, T. W., McIntyre, S., Rothman, D. L., and Graaf, R. A. (2010b). Magnetic field modeling with a set of individual localized coils. *Journal of Magnetic Resonance*.

[Juchem et al., 2015] Juchem, C., Umesh Rudrapatna, S., Nixon, T. W., and de Graaf, R. A. (2015). Dynamic multi-coil technique (DYNAMITE) shimming for echo-planar imaging of the human brain at 7 Tesla. *NeuroImage*.

[Juhas et al., 2014] Juhas, A., Pekari, N., and Toepfer, H. (2014). Magnetic Field of Rectangular Current Loop with Sides Parallel and Perpendicular to the Surface of High-permeability Material. 11(4):701–717.

[Kamada et al., 2012] Kamada, K., Ito, Y., and Kobayashi, T. (2012). Human MCG measurements with a high-sensitivity potassium atomic magnetometer. *Physiological Measurement*.

[Kamada et al., 2015] Kamada, K., Sato, D., Ito, Y., Natsukawa, H., Okano, K., Mizutani, N., and Kobayashi, T. (2015). Human magnetoencephalogram measurements using newly developed compact module of high-sensitivity atomic magnetometer. *Japanese Journal of Applied Physics*, 54(2).

[Kastler, 1973] Kastler, A. (1973). The Hanle effect and its use for the measurements of very small magnetic fields. *Nuclear Instruments and Methods*, 110(C):259–265.

[Kelhä et al., 1982] Kelhä, V. O., Pukki, J. M., Peltonen, R. S., Penttinen, A. J., Ilmoniemi, R. J., and Heino, J. J. (1982). Design, Construction, and Performance of a Large-Volume Magnetic Shield. *IEEE Transactions on Magnetics*.

[Kelly, 1946] Kelly, H. W. (1946). Degaussing.

[Knappe et al., 2010] Knappe, S., Sander, T. H., Kosch, O., Wiekhorst, F., Kitching, J., and Trahms, L. (2010). Cross-validation of microfabricated atomic

magnetometers with superconducting quantum interference devices for biomagnetic applications. *Applied Physics Letters*.

[Kominis et al., 2003] Kominis, I. K., Kornack, T. W., Allred, J. C., and Romalis, M. V. (2003). A subfemtotesla multichannel atomic magnetometer. *Nature*.

[Kornack, 2005] Kornack, T. W. (2005). A test of CPT and Lorentz symmetry using a K-3He co-magnetometer. *PhD Thesis*.

[Lauterbur, 1973] Lauterbur, P. C. (1973). Image formation by induced local interactions: Examples employing nuclear magnetic resonance. *Nature*.

[Ledbetter et al., 2008] Ledbetter, M. P., Savukov, I. M., Acosta, V. M., Budker, D., and Romalis, M. V. (2008). Spin-exchange-relaxation-free magnetometry with Cs vapor. *Physical Review A - Atomic, Molecular, and Optical Physics*.

[Lin et al., 2019] Lin, C.-H., Tierney, T. M., Holmes, N., Boto, E., Leggett, J., Bestmann, S., Bowtell, R., Brookes, M. J., Barnes, G. R., and Miall, R. C. (2019). Using optically-pumped magnetometers to measure magnetoencephalographic signals in the human cerebellum. *The Journal of Physiology*.

[Loring, 1997] Loring, D. W. (1997). Neuropsychological Evaluation in Epilepsy Surgery. *Epilepsia*.

[MacKert et al., 1998] MacKert, B. M., Curio, G., Burghoff, M., Trahms, L., and Marx, P. (1998). Magnetoneurographic 3D localization of conduction blocks in patients with unilateral S1 root compression. *Electroencephalography and Clinical Neurophysiology - Electromyography and Motor Control*.

[Mager, 1970] Mager, A. J. (1970). Magnetic Shields. *IEEE Transactions on Magnetics*.

[Mansfield and Grannell, 1973] Mansfield, P. and Grannell, P. K. (1973). Nmr 'diffraction' in solids?

[Martens et al., 1991] Martens, M. A., Petropoulos, L. S., Brown, R. W., Andrews, J. H., Morich, M. A., and Patrick, J. L. (1991). Insertable biplanar gradient coils for magnetic resonance imaging. *Review of Scientific Instruments*, 62(11):2639–2645.

[Moon et al., 1999] Moon, C. H., Park, H. W., and Lee, S. Y. (1999). A design method for minimum-inductance planar magnetic-resonance-imaging gradient coils considering the pole-piece effect. *Measurement Science and Technology*, 10(12).

[Muthukumaraswamy, 2013] Muthukumaraswamy, S. D. (2013). High-frequency brain activity and muscle artifacts in MEG/EEG: A review and recommendations.

[Nardelli et al., 2019] Nardelli, N. V., Krzyzewski, S. P., and Knappe, S. A. (2019). Reducing crosstalk in optically-pumped magnetometer arrays. *Physics in Medicine and Biology*.

[Nenonen et al., 2012] Nenonen, J., Nurminen, J., Kičić, D., Bikmullina, R., Lioumis, P., Jousmäki, V., Taulu, S., Parkkonen, L., Putaala, M., and Kähkönen, S. (2012). Validation of head movement correction and spatiotemporal signal space separation in magnetoencephalography. *Clinical Neurophysiology*, 123(11):2180–2191.

[Ogawa et al., 1990] Ogawa, S., Lee, T. M., Kay, A. R., and Tank, D. W. (1990). Brain magnetic resonance imaging with contrast dependent on blood oxygenation. *Proceedings of the National Academy of Sciences of the United States of America*.

[Pfeiffer et al., 2019] Pfeiffer, C., Ruffieux, S., Jönsson, L., Chukharkin, M. L., Kalaboukhov, A., Xie, M., Winkler, D., and Schneiderman, J. F. (2019). A 7-channel high-Tc SQUID-based on-scalp MEG system. *bioRxiv*.

[Pfurtscheller and Lopes Da Silva, 1999] Pfurtscheller, G. and Lopes Da Silva, F. H. (1999). Event-related EEG/MEG synchronization and desynchronization: Basic principles.

[Pospelov and Ritz, 2005] Pospelov, M. and Ritz, A. (2005). Electric dipole moments as probes of new physics. *Annals of Physics*.

[Purves et al., 2004] Purves, D., Augustine, G. J., Fitzpatric, D., Hall, W. C., LaMantia, A.-S., McNamara, J. O., and Williams, S. M. (2004). *Neuroscience 3rd Ed.*

[Qinjie et al., 2018] Qinjie, C., Donghau, P., Ji, L., Yinxi, J., Zhiyin, S., Shengxin, L., Guijie, Y., and Liyi, L. (2018). Optimization of a Coil System for Generating Uniform Magnetic Fields inside a Cubic. *Energies*, 11(3):608.

[Riaz et al., 2017] Riaz, B., Pfeiffer, C., and Schneiderman, J. F. (2017). Evaluation of realistic layouts for next generation on-scalp MEG: Spatial information density maps. *Scientific Reports*.

[Roberts et al., 2019] Roberts, G., Holmes, N., Alexander, N., Boto, E., Leggett, J., Hill, R. M., Shah, V., Rea, M., Vaughan, R., Maguire, E. A., Kessler, K., Beebe, S., Fromhold, M., Barnes, G. R., Bowtell, R., and Brookes, M. J. (2019). Towards magnetoencephalography in a virtual reality environment. *NeuroImage*.

[Robson et al., 2016] Robson, S. E., Brookes, M. J., Hall, E. L., Palaniyappan, L., Kumar, J., Skelton, M., Christodoulou, N. G., Qureshi, A., Jan, F., Katshu, M. Z., Liddle, E. B., Liddle, P. F., and Morris, P. G. (2016). Abnormal visuomotor processing in schizophrenia. *NeuroImage: Clinical*, 12:869–878.

[Roméo and Hoult, 1984] Roméo, F. and Hoult, D. I. (1984). Magnet field profiling: Analysis and correcting coil design. *Magnetic Resonance in Medicine*.

[Rondin et al., 2014] Rondin, L., Tetienne, J. P., Hingant, T., Roch, J. F., Maletinsky, P., and Jacques, V. (2014). Magnetometry with nitrogen-vacancy defects in diamond.

[Roshen, 1990] Roshen, W. A. (1990). Effect of Finite Thickness of Magnetic Substrate on Planar Inductors. *IEEE Transactions on Magnetics*, 26(1):270–275.

[Rossini and Rossi, 1998] Rossini, P. M. and Rossi, S. (1998). Clinical applications of motor evoked potentials. *Electroencephalography and Clinical Neurophysiology*.

[Sander et al., 2012] Sander, T. H., Preusser, J., Mhaskar, R., Kitching, J., Trahms, L., and Knappe, S. (2012). Magnetoencephalography with a chip-scale atomic magnetometer. *Biomedical Optics Express*, 3(5):981.

[Sarvas, 1987] Sarvas, J. (1987). Basic mathematical and electromagnetic concepts of the biomagnetic inverse problem. *Physics in Medicine and Biology*, 32(1):11–22.

[Savukov and Romalis, 2005] Savukov, I. M. and Romalis, M. V. (2005). Effects of spin-exchange collisions in a high-density alkali-metal vapor in low magnetic fields. *Physical Review A - Atomic, Molecular, and Optical Physics*.

[Schweizer, 1962] Schweizer, F. (1962). Magnetic shielding factors of a system of concentric spherical shells. *Journal of Applied Physics*.

[Schwindt et al., 2007] Schwindt, P. D. D., Lindseth, B., Knappe, S., Shah, V., Kitching, J., and Liew, L. A. (2007). Chip-scale atomic magnetometer with improved sensitivity by use of the Mx technique. *Applied Physics Letters*.

[Seltzer, 2008] Seltzer, S. J. (2008). *Developments in Alkali-Metal Atomic Magnetometry*. PhD thesis.

[Shah and Hughes, 2015] Shah, V. and Hughes, J. K. (2015). Method for detecting zero-field resonance.

[Shah et al., 2007] Shah, V., Knappe, S., Schwindt, P. D., and Kitching, J. (2007). Subpicotesla atomic magnetometry with a microfabricated vapour cell. *Nature Photonics*.

[Shah et al., 2018] Shah, V., Osborne, J., Orton, J., and Alem, O. (2018). Fully integrated, standalone zero field optically pumped magnetometer for biomagnetism. *Steep Dispersion Engineering and Opto-Atomic Precision Metrology XI*, (February):51.

[Shah and Romalis, 2009] Shah, V. and Romalis, M. V. (2009). Spin-exchange relaxation-free magnetometry using elliptically polarized light. *Physical Review A - Atomic, Molecular, and Optical Physics*.

[Shah and Wakai, 2013] Shah, V. K. and Wakai, R. T. (2013). A compact, high performance atomic magnetometer for biomedical applications. *Physics in Medicine and Biology*, 58(22):8153–8161.

[Shi et al., 2015] Shi, F., Zhang, Q., Wang, P., Sun, H., Wang, J., Rong, X., Chen, M., Ju, C., Reinhard, F., Chen, H., Wrachtrup, J., Wang, J., and Du, J. (2015). Single-protein spin resonance spectroscopy under ambient conditions. *Science*.

[Stenroos et al., 2014] Stenroos, M., Hunold, A., and Haueisen, J. (2014). Comparison of three-shell and simplified volume conductor models in magnetoencephalography. *NeuroImage*.

[Sun et al., 2016] Sun, Z., Reisner, M., Fierlinger, P., Schnabel, A., Stuiber, S., and Li, L. (2016). Dynamic modeling of the behavior of permalloy for magnetic shielding. *Journal of Applied Physics*.

[Taulu et al., 2005] Taulu, S., Simola, J., and Kajola, M. (2005). Applications of the Signal Space Separation Method. *October*, 53(9):3359–3372.

[Tierney et al., 2019] Tierney, T. M., Holmes, N., Mellor, S., López, J. D., Roberts, G., Hill, R. M., Boto, E., Leggett, J., Shah, V., Brookes, M. J., Bowtell, R., and Barnes, G. R. (2019). Optically pumped magnetometers: From quantum origins to multi-channel magnetoencephalography. *NeuroImage*.

[Tierney et al., 2018] Tierney, T. M., Holmes, N., Meyer, S. S., Boto, E., Roberts, G., Leggett, J., Buck, S., Duque-Muñoz, L., Litvak, V., Bestmann, S., Baldeweg, T., Bowtell, R., Brookes, M. J., and Barnes, G. R. (2018). Cognitive neuroscience using wearable magnetometer arrays: Non-invasive assessment of language function. *NeuroImage*, 181:513–520.

[Turner, 1993] Turner, R. (1993). Gradient coil design: A review of methods.

[Van Veen and Buckley, 1988] Van Veen, B. D. and Buckley, K. M. (1988). Beamforming: A Versatile Approach to Spatial Filtering. *IEEE ASSP Magazine*.

[Van Veen et al., 1997] Van Veen, B. D., Van Drongelen, W., Yuchtman, M., and Suzuki, A. (1997). Localization of brain electrical activity via linearly constrained minimum variance spatial filtering. *IEEE Transactions on Biomedical Engineering*.

[Voigt et al., 2013] Voigt, J., Knappe-Grüneberg, S., Schnabel, A., Körber, R., and Burghoff, M. (2013). Measures to reduce the residual field and field gradient inside a magnetically shielded room by a factor of more than 10. *Metrology and Measurement Systems*.

[Vrba, 2000] Vrba, J. (2000). Multichannel SQUID Biomagnetic Systems. In *Applications of Superconductivity*.

[Vrba and Robinson, 2001] Vrba, J. and Robinson, S. E. (2001). Signal processing in magnetoencephalography. *Methods*.

[Wang et al., 2019] Wang, P., Chen, S., Guo, M., Peng, S., Wang, M., Chen, M., Ma, W., Zhang, R., Su, J., Rong, X., Shi, F., Xu, T., and Du, J. (2019). Nanoscale magnetic imaging of ferritins in a single cell. *Science Advances*.

[Wehner et al., 2008] Wehner, D. T., Hämäläinen, M. S., Mody, M., and Ahlfors, S. P. (2008). Head movements of children in MEG: Quantification, effects on source estimation, and compensation. *NeuroImage*, 40(2):541–550.

[Xia et al., 2006] Xia, H., Ben-Amar Baranga, A., Hoffman, D., and Romalis, M. V. (2006). Magnetoencephalography with an atomic magnetometer. *Applied Physics Letters*, 89(21).

[Yoda, 1990] Yoda, K. (1990). Analytical design method of self-shielded planar coils. *Journal of Applied Physics*, 67(9):4349–4353.

[Zimmerman et al., 1970] Zimmerman, J. E., Thiene, P., and Harding, J. T. (1970). Design and operation of stable rf-biased superconducting point-contact quantum devices, and a note on the properties of perfectly clean metal contacts. *Journal of Applied Physics*.